Switched Flux Permanent Magnet Brushless Machines for Electric Vehicles

Mahir M. Jabir Al-Ani

A thesis submitted for the degree of Doctor of Philosophy

Department of Electronic and Electrical Engineering
University of Sheffield
20 September 2014

Abstract

This thesis investigates different topologies of switched flux permanent magnet (SFPM) machines and variable flux (VF) methods for high speed applications.

Although several novel topologies of SFPM machines have been proposed and investigated recently, their torque-speed capability has not been studied systematically. Therefore, the torque-speed capability as well as the open circuit and electromagnetic performance of conventional SFPM machines with three different stator/rotor pole combinations, i.e. 12/10, 12/13 and 12/14, and three novel SFPM machine topologies, i.e. multi-tooth, E-core and C-core are analysed and investigated by the finite element (FE) method and experiments. Moreover, in order to improve the flux-weakening capability of these machines a variable flux method using flux adjusters (FAs) is employed and the corresponding electromagnetic performance of the machines are investigated, analysed and compared. Both FE and measured results show when the FAs are used the torque-speed capability of the three conventional machines can be improved significantly, while no improvement is shown in the three novel topologies primarily due to the large winding inductances.

The technique of using flux adjusters has been improved by reducing the number of FAs. Thus, a new mechanical variable-flux machine topology, which uses only half of FAs outside the stator at alternative stator poles, is proposed, developed and analysed. Open circuit results, electromagnetic performance and torque- and power-speed curves of the 12/10, 12/13 and 12/14 stator/rotor pole SFPM machines with alternative FAs are predicted and compared by 2D and 3D-FE, and experimentally validated.

Furthermore, a novel SFPM machine topology with radial and circumferential PMs is proposed, investigated and optimized. This topology reduces the stator flux leakage and offers high magnetic utilization. Moreover, this topology can also be developed as a mechanical variable flux machine.

Finally, three SFPM machines with variable flux techniques, i.e. mechanically movable flux adjusters (MMFA), mechanically rotatable permanent magnet set (MRMS) and hybrid excitation with backside DC coils (HEBC) are analysed. Their open circuit results and electromagnetic performance with emphasis on torque-speed characteristic are investigated and compared. Additionally, the required power to switch between flux weakening and

strengthening states, flux weakening capability and permanent magnet demagnetization withstand capability are predicted, analysed and compared.

The influence of end-effect on the torque-speed capability in the conventional, multi-tooth, E-core and C-core SFPM machines is investigated. Measurements and 3D-FE are performed to obtain the torque-speed curve in order to validate the findings of the research. The 3D-FE predicted results match well with the measured results, while the 2D-FE predicted results are lower due to the high end-effect in the SFPM machines.

Acknowledgements

First I would like to thank my supervisor Professor Zi-Qiang Zhu for his continued invaluable encouragement, advice and support throughout this PhD study. Many thanks to the former and current members of the Electrical Machines and Drives Group who have offered help and support, in particular Dr Ziad Azar, Dr Lijian Wu and Dr Xu Liu for the many helpful assistance and discussions which have provided significant improvement in my research knowledge. Also I would like to thank Mr Beomseok Lee for his help in carrying out the dynamic tests. Finally, I would like to thank Mr John Wilkinson and Mr Lawrence Obodo for their work on constructing the prototype machines.

Unlimited thanks to my family, my mother, father and sister, for their continued financial and moral support throughout my university studying years. Without their support I would not be able to continue this work and achieve this degree.

"Love all, trust a few, do wrong to none"

William Shakespeare

Contents

List of Symbols

BLPM	Brushless Permanent Magnet
PM	Permanent Magnet
DSPM	Doubly Salient Permanent Magnet
FRPM	Flux Reversal Permanent Magnet
SFPM	Switched Flux Permanent Magnet
BLAC	Brushless Alternative Current
VFPM	Variable Flux Permanent Magnet
N_s	Number of stator pole number
N_r	Number of rotor pole number
m	Number of phases
$K_{1,2}$	Integer number
K_w	Winding factor
K_d	Distribution factor
K_p	Pitch factor
A	Back-EMF vectors
v	Order of harmonics
α	Angle between two adjacent vectors
T_e	Electromagnetic torque
Ψ_{pm}	Permanent magnet flux-linkage
I_d	D-axis current
I_q	Q-axis current
L_d	D-axis inductance
L_q	Q-axis inductance
I_{max}	Maximum phase current
U_{max}	Maximum phase voltage
U_d	D-axis voltage
U_q	Q-axis voltage
ω	Motor speed
ω_{max}	Motor maximum speed
K_{fw}	Flux weakening factor

N_a	Number of turns per phase
B_m	Magnetic loading
A_m	Magnet cross section area
J_s	Current density
A_{slot}	Slot area
K_{pa}	Packing factor
Ψ_d	D-axis flux linkage
I_a	Phase current
A_{wire}	Area of the wire cross-section
B_r	Airgap flux density
l_g	Airgap length
l_m	Magnet excitation length
ω_{base}	Motor base speed
FWR	Flux Weakening Region
FSR	Flux Strengthening Region
L	Inductance
E	Back-EMF
U_a	Phase voltage
Φ_{gap}	Airgap flux
Φ_{pm}	Magnet flux
Φ_a	Armature flux
β	Current angle
MMF	Magneto-Motive Force
FEA	Finite Element Analysis
LCM	Least Common Multiple
I_{ph}	Phase current
$V_{link\text{-}DC}$	DC link voltage
I_{test}	DC testing current
FAs	Flux Adjusters
all	Flux Adjusters in All Stator Teeth
alt	Flux Adjusters in Alternative Stator Teeth
CSFPM	Conventional Switched Flux Permanent Magnet
PMc	Circumferential Permanent Magnet Set

PMr	Radial Permanent Magnet Set
GA	Genetic Algorithm
h_{PMc}, l_{cm}	Circumferential permanent magnet height/ magnetic excitation height
h_{PMr}, l_{rm}	Radial permanent magnet height/ magnetic excitation height
H_{cm}	Circumferential permanent magnet coercivity
H_{rm}	Radial permanent magnet coercivity
h_{fr}	Laminated ring frame thickness
h_{bi}	Back-iron thickness
w_{PMc}	Circumferential permanent magnet width
h_{stator}	Stator outer radius
w_{s}	Stator tooth width
h_{rotor}	Rotor outer radius
w_{r}	Rotor tooth width
h_{r}	Rotor tooth height
h_{slot}	Slot height
w_{slot}	Slot width
w_{PMr}	PMr height
L_{a}	Axial length
L_{gap}	Airgap length
Bo_{r}	Bore radius
P_{cu}	Copper loss
B_{rpm}	Permanent magnet remanence
μ_r	Permanent magnet permeability
I_{rated}	Rated current
GCD	Greatest Common Divider
MMFA	Mechanically Movable Flux Adjusters
MRMS	Mechanically Rotatable Magnet Set
HEBC	Hybrid Excitation with Backside DC Coils
FSS	Flux Strengthening State
FWS	Flux Weakening State
I_{DC}	DC excitation current
Ψ_{DC}	DC excitation flux-linkage
L_{DC}	DC excitation inductance

P_{DC}	DC excitation copper loss
R_{DC}	DC excitation resistance
N_{DC}	DC excitation number of turns
l_{DC}	DC excitation coil length
A_{DC}	DC excitation slot area
K_{paDC}	DC excitation packing factor
ρ_{cu}	Copper resistivity
$\Psi_d(I_d, I_q)$	D-axis flux linkage under the influence of d- and q-axis current
$\Psi_q(I_d, I_q)$	Q-axis flux linkage under the influence of d- and q-axis current
$\Psi_d(I_d)$	D-axis flux linkage under the influence of d-axis current
$\Psi_{PM}(I_q)$	Q-axis flux linkage under the influence of q-axis current
$\Psi_{PM}(I_q)$	PM flux linkage under the influence of the q-axis current

1. General Introduction

1.1. Introduction

The significant achievements in the fields of magnetic materials, power electronics and controlling methods in the last four decades led to a further development in brushless permanent magnet (BLPM) machines. Various types of permanent magnet (PM) machines which contain the PMs on the rotor were developed, e.g. surface-mounted (SPM), inset, interior and radial interior (IPM). Moreover, based on the flux switching method, three new types of PM machines where the magnets and the armature windings are both located on the stator were proposed. These machines are doubly salient (DSPM), flux reversal (FRPM), and switched flux (SFPM), all of which have a simple salient pole rotor without any active parts, i.e. windings or magnets.

SFPM machines have several advantages which make them suitable for many industrial applications, such as automotive, aerospace and wind power. The location of the magnets and armature windings on the stator leads to simple and robust rotor, as well as easy and efficient cooling. In addition, high torque and power density can be exhibited in SFPM machines due to the utilization of flux focusing. Moreover, although concentrated winding is used, sinusoidal back-EMF waveform still can be achieved. Overall, the merits of the SFPM machine can be summarised as:

- Simple and robust rotor, suitable for high speed applications
- Magnets and armature windings are located on the stator, easy management of the temperature as well as easy to identify demagnetized magnets
- High power and torque density due to flux focusing
- Sinusoidal back-EMF waveform suitable for brushless AC (BLAC) applications
- Concentrated winding leads to low copper usage and consequently copper loss

However, the inductance of the conventional SFPM machine is relatively low when PM flux linkage is high and electric loading is low. Therefore, the SFPM machines suffer from short operating speed range and low flux weakening capability. Nevertheless, another advantage of the SFPM machine is the ability to modify the machine structure in order to include additional components to introduce variable flux ability while the machine is operating, this type of machine is known as variable flux permanent magnet (VFPM). Moreover, VFPM

machines are those which contain methods to adjust the PM flux level during the operation, it can be strengthen or weaken the PM flux which provides the flexibility of controlling the efficiency across the machine operation cycle as well as achieving high speed range. The PM flux adjusting can be achieved electrically by adding DC excitation winding, these machines are known as hybrid excitation machines, or mechanically by including extra mechanical components, or by other types of techniques.

This thesis investigates and compares the electromagnetic performance and torque-speed characteristics of several SFPM machine topologies. Mechanical variable flux methods are applied to these machines in order to improve the torque-speed characteristics and compromise between the mechanical complexity and performance of the machine. The following sections provide introduction and review of SFPM and VFPM machines.

1.2. Electrical Motors in Hybrid and Electric Vehicles

In the past four decades a large increase in the environment temperature has been recorded worldwide which led to an international warning regarding the global warming. Therefore, efforts are made in order to reduce the extensive emission of greenhouse gases such as carbon dioxide (CO_2). Since the conventional internal combustion engine (ICE) vehicles are one of the main sources of the CO_2 emission, hybrid electric vehicles (HEV) and electric vehicles (EV) are proposed and developed as a solution for this issue. Electrical motors are the key component of the HEV and EV, as a result motors for such applications have gained extensive research interest in the field of electrical machine design and control.

It has been defined that, HEV and EV applications require electric motor with characteristics such as: 1) high power and torque density; 2) high overload torque; 3) wide speed range; 4) high efficiency over wide torque and speed range; 5) wide constant power range; 6) reliable and robust; 7) low noise and vibration; 8) low cost. In the current marketed products, IPM motors are the dominant. Multi-layer IPM motor is employed in the BMW i-series plug-in EVs, whereas V-shaped IPM motor is used in Toyota Prius and Camry EVs. Moreover, IPM motors are used in Nissan Leaf and Ford Focus EVs without any further information published regarding their specification. On the other hand, the classical induction motor is used by Tesla Motors Inc. in all their products; they refer to their electric induction motors as copper rotor motor in order to distinguish it from the motors with PMs in the rotors.

Moreover, SFPM machines have gained extensive research interest since they combine the advantages of large torque capability due to the utilization of the flux focusing effect and low copper usage since concentrated windings are employed. Additionally, robust rotor and easy cooling can be achieved since the active parts, i.e. PMs and windings are both located on the stator as stated previously. Moreover, it has been found that the SFPM machine can achieve similar torque and power density as that in IPM and SPM machines as it will be stated later (see section 1.4.6). However, as mentioned previously, conventional SFPM machine has relatively low speed range and hence it is inadequate for such applications. Therefore, the research of this thesis is focusing on investigating different topologies of SFPM machines with high speed capabilities and introduces variable flux techniques to solve this issue.

1.3. Origin of Switched Flux Machine

The concept of SFPM machine was proposed first in the year 1955, by Rauch and Johnson [1]. The machine was first introduced as flux switching alternator. However, due to the weak magnets and the absence of reliable electronic converters at that time, the machine was very simple and academic. Another machine known as Law's relay actuator was described as an origin idea of the SFPM machine. This topology was proposed in the year 1990 by Bolton and Shakweh, but it can be dated back to 1952 [2].

However, due to the significant improvements in electronic inverters and controlling methods, as well as the invention of new high energy-product rare earth permanent magnets the flux switching method was re-investigated in the late 1990s and was the key to three new different types of permanent magnet machines, i.e. DSPM [3, 4], FRPM [5-7] and SFPM.

1.3.1. Flux switching alternator

Fig. 1.1 shows the flux switching alternator, the rotor contains a two-pole salient stack, while the stator includes two permanent magnets with a pair of iron yokes and windings around each yoke. Fig. 1.1 (a) shows the first operation case of the flux path in the machine indicating a flux linkage direction from left to right in both windings shown by the arrows. In the second case, Fig. 1.1 (b), the rotor moves 180 electrical degrees, thus the flux linkage direction is reversed but it still has the same amount as in the first case. A reversal of flux polarity occurs each half cycle of the rotation period allowing the rotor to maintain the motion and to produce the electromagnetic torque.

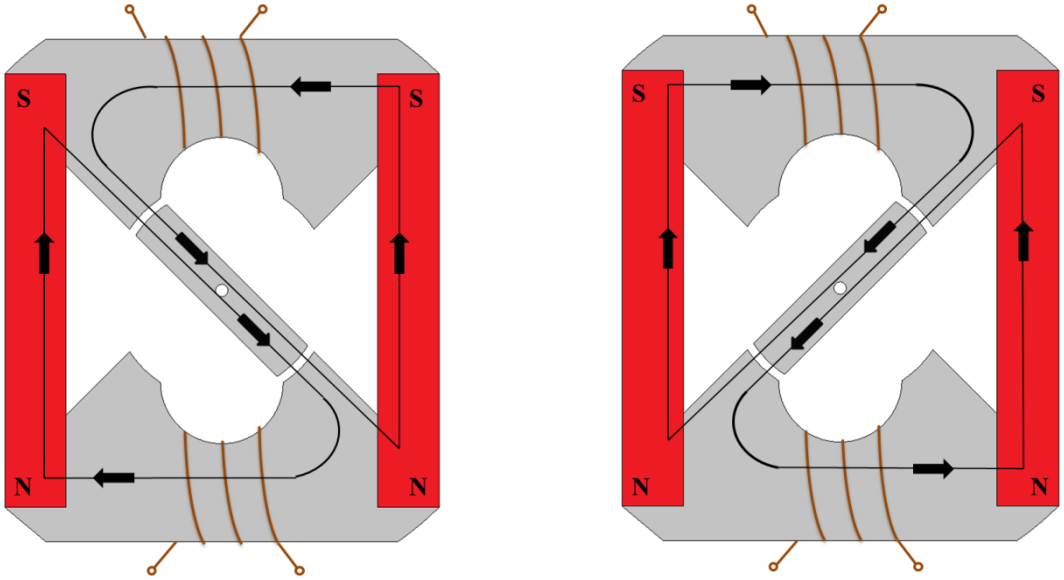

(a) Operation case 1: left to right flux path (b) Operation case 2: right to left flux path

Fig. 1.1 Flux switching alternator.

1.3.2. Law's relay actuator

The structure of this actuator is similar to the flux switching alternator, a simple robust rotor is employed with a stator containing a pair of permanent magnets and coils wound around pair of iron yokes. Figs. 1.2 (a) and (b) show the operation principle and the flux linkage circuit of the machine. The direction of the flux is from left to right in the first case, the rotation is maintained when the flux is switched as the rotor rotates 180 electrical degrees.

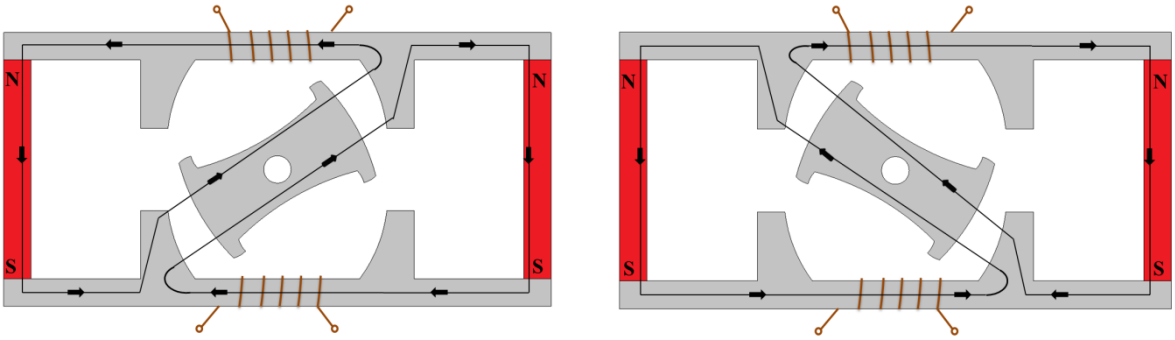

(c) Operation case 1: left to right flux path (d) Operation case 2: right to left flux path

Fig. 1.2 Law's relay actuator.

1.4. Switched Flux Permanent Magnet Machine

Switched flux permanent magnet machine is an AC brushless permanent magnet machine which has a topology mixed of doubly salient stator structure and a robust rotor similar to that of switched reluctance machine, Fig. 1.3. This machine has the advantages of high power and torque density, and high efficiency. It is recognised by the easy to control temperature and the high speed [8]. Figs. 1.3 (a) and (b) shows the cross-section of SFPM machine with all and alternate pole windings, respectively.

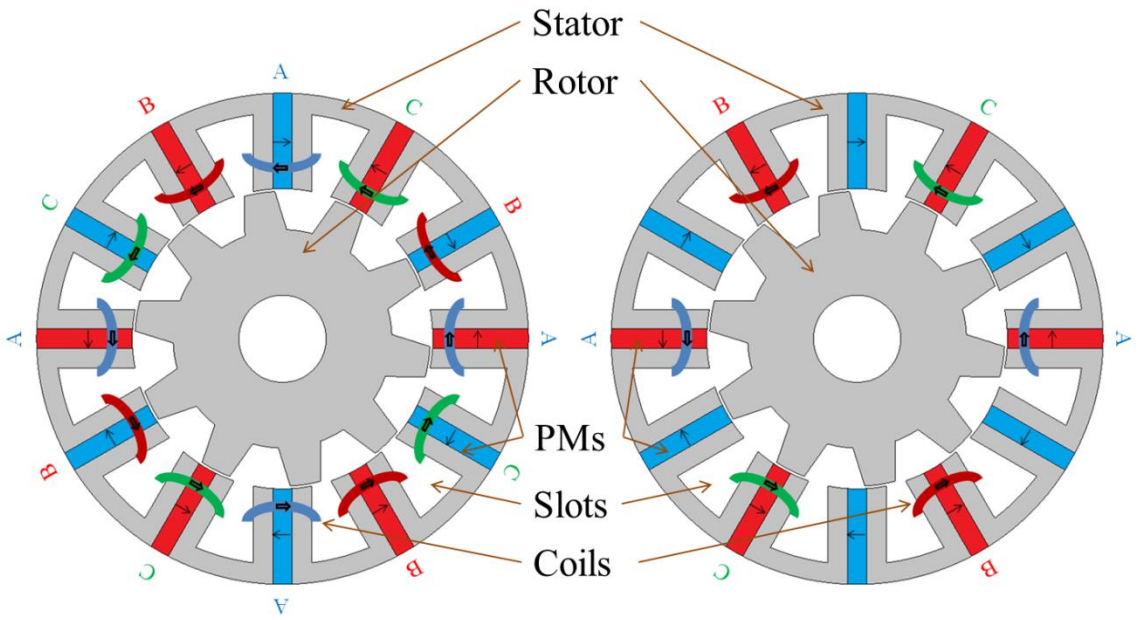

(a) All pole winding (b) Alternative pole winding

Fig. 1.3. Switched flux permanent magnet machine.

1.4.1. Structure

As mentioned previously, the rotor is simple and robust similar to that of switched reluctance motor and the stator is designed based on the doubly salient machine. Each stator pole made by two ferromagnetic laminated cores shaped like "U" with a magnet between and surrounded by the concentrated armature winding. The magnets are circumferentially magnetized in alternative opposite directions [9]. The winding configuration depends on the number of the rotor poles and the magnetization direction of each stator pole, Fig. 1.4.

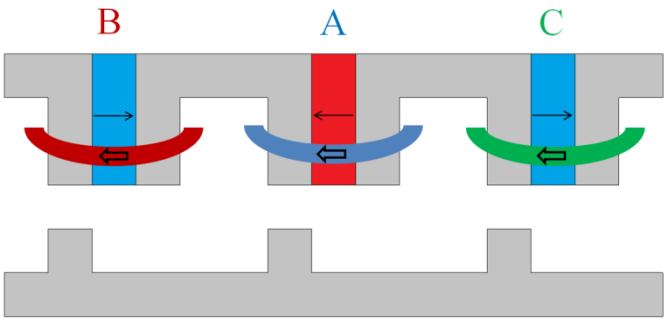

Fig. 1.4 Linear section of SFPM machine presents the permanent magnets orientation and the winding configuration.

1.4.2. Operation principle

Fig. 1.5 presents the operation principle of the SFPM machine. When the rotor pole aligns with one of the stator teeth over the wound area, the flux linkage will complete a close circuit by passing through the rotor to the stator and through the permanent magnet and back to the rotor again, Fig. 1.5 (a). While the rotor moves the rotor pole lines up with the same stator tooth which is belongs to the same coil and the flux linkage completes a close circuit again, Fig. 1.5 (b). The permanent magnet provides the same flux linkage during the operation while the polarity being switched hence it is called switched flux machine. However, since the flux linkage completes a full circuit the SFPM machine has bipolar flux linkage [3].

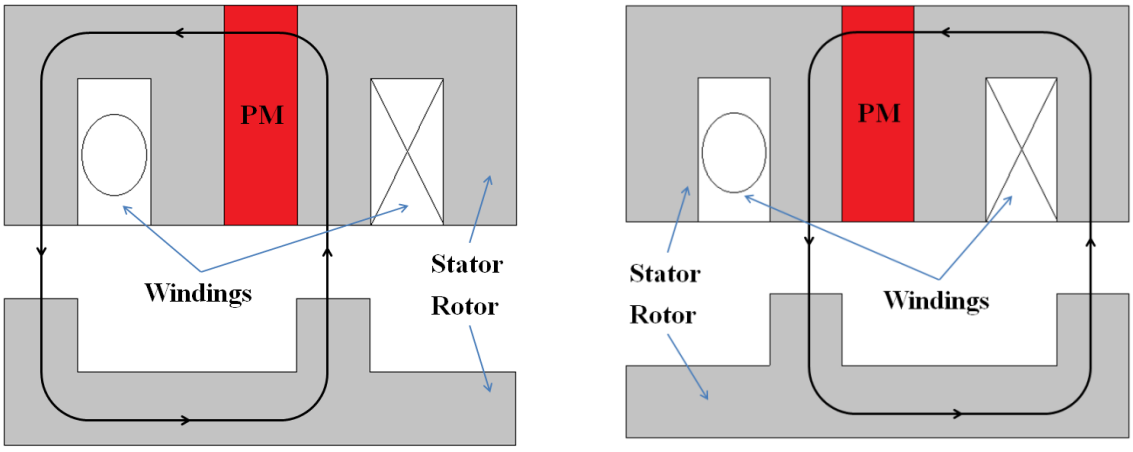

(a) (b)

Fig. 1.5 Operation principle of SFPM machine.

1.4.3. Winding configurations

1.4.3.1. Coil connections

In order to determine the combination of stator and rotor poles in SFPM machines, the following equations are used to obtain the possible combinations [10]:

$$N_s = K_1 m \tag{1-1}$$

$$N_r = N_s \pm K_2 \tag{1-2}$$

where m is the number of phases, K_1 and K_2 are integers. K_1 should be even when m is an odd number since the stator pole number must be even.

When the number of phases is even, any two opposite sectors are belonging to different phases. The phase coils defined by drawing one sector contains $2\pi/m$ radians. For other phases, the sector rotates by $2n\pi/m$ (where n is integer n=1, 2, ..., m-1). It is worth mentioning that this method works for all even numbers excluding 2.

If the number of phases is odd, the coils belonging to one phase can be obtained by drawing two opposite sectors having $2\pi/m$ radians. Other phase sectors rotate by $2n\pi/m$ (where n is integer n=1, 2, ..., m-1). This method works for 2 phases as well as any odd number of phases.

1.4.3.2. Winding factor

The winding factor can be presented as:

$$K_w = K_d K_p \tag{1-3}$$

K_d and K_p are the distribution and pitch factors, respectively. They are defined by:

$$K_d = \frac{sin\frac{Av\alpha}{2}}{A\,sin\frac{v\alpha}{2}} \tag{1-4}$$

$$K_p = cos\left(\pi v \left|\frac{N_r}{N_s} - 1\right|\right) \tag{1-5}$$

where A, v and α are the number of back-EMF vectors, the order of the harmonics and the angle between two adjacent vectors, respectively. In general, a SFPM machine has a relatively high winding factor. The distribution factor normally reduces and the pitch factor increases when the number of stator poles increases.

1.4.4. Performance analyses

Based on the general analysis the PM flux linkage is sinusoidal verses the rotor position. Therefore, the back-EMF is essentially sinusoidal which makes this machine suitable for brushless AC drive operation. SFPM machines are also characterised by high irreversible demagnetization withstand capability since the armature reaction flux in the machine does not pass through the PMs. This makes the machine suitable for flux weakening control. Since an assumption has been made that the flux-linkage and hence the back-EMF are sinusoidal, AC current is used to produce the unidirectional torque and power. The electromagnetic torque of a SFPM machine is given by [11]:

$$T_e = \frac{3}{2} N_r (\Psi_{pm} I_q + (L_d - L_q) I_d I_q) \tag{1-6}$$

where Ψ_{pm} is the PM flux linkage, I_d, I_q, L_d and L_q are the d- and q-axis currents and inductances, respectively. However, since the inductances in the SFPM machine are relatively constant and the saliency ratio is close to 1, the reluctance torque is negligible and the SFPM machine torque is a product of permanent magnet torque only [9]. Therefore, the torque can be simplified to:

$$T_e = \frac{3}{2} N_r \Psi_{pm} I_q \tag{1-7}$$

However, by using flux weakening control, the machine power is controlled by the inverter, therefore two basic equations for the current and voltage constraints, i.e. maximum current and maximum voltage, I_{max} and U_{max}, are defined as [12]:

$$I_d^2 + I_q^2 \leq I_{max}^2 \tag{1-8}$$

$$U_d^2 + U_q^2 \leq U_{max}^2 \tag{1-9}$$

The maximum phase voltage of the machine can be found by:

$$\left(\frac{U_{max}}{\omega}\right)^2 \geq (L_q I_q)^2 + (L_d I_d + \Psi_{pm})^2 \tag{1-10}$$

The machine speed ω can be found by:

$$\omega = \frac{U}{N_r \sqrt{(\Psi_{pm} + L_d I_d)^2 + (L_q I_q)^2}} \tag{1-11}$$

When $U=U_{max}$, $I_d=-I_{max}$ and $I_q=0$, the armature current is used to weaken the PM flux, then the maximum operation speed at which the machine can reach is:

$$\omega_{max} = \frac{U_{max}}{N_r(\Psi_{pm}-L_d I_{max})} \tag{1-12}$$

However, when $\Psi_{pm} \leq L_d I_{max}$ the motor speed is theoretically infinite. Thus, a factor K_{fw}, flux weakening factor, is defined in order to evaluate the flux weakening capability of the machine:

$$K_{fw} = \frac{L_d I_{max}}{\Psi_{pm}} \tag{1-13}$$

Obviously, the higher the flux weakening factor, the better the flux weakening capability of the machine. When the factor is equal to 1, the best performance can be obtained since theoretically infinite maximum speed can be expected. Nevertheless, despite the fact flux weakening factor higher than 1 can maintain high flux weakening capability, the influence of either low PM flux linkage or high inductance leads to low maximum power. Therefore, it is preferred to design the machine with the factor close to unity.

Moreover, the flux weakening factor equation can be extended since the permanent magnet flux linkage can be presented as $\Psi_{pm}= N_a B_m A_m$ where B_m is the magnetic loading, A_m is the cross-section area of the magnet and N_a is the number of turns per phase, assuming the flux leakages are neglected and the winding factor is 1. Additionally, the maximum current can be presented as:

$$I_{max} = \frac{\sqrt{2} J_s A_{slot} K_{pa}}{N_a} \tag{1-14}$$

Hence, the flux weakening factor can be presented as:

$$K_{fw} = \frac{\sqrt{2}\Psi_d J_s A_{slot} K_p}{B_m A_m I_d N_a^2} \tag{1-15}$$

where K_{pa} is the windings packing factor and A_{slot} is the area of the stator slot. This equation also can be further extended by adding the current density $J_s=I_a/A_{wire}$ where A_{wire} is the area of the copper and I_a is the phase current, and by assuming a simple geometrical design which is used the magnetic loading can be presented as $B_m=l_m B_r/l_m+\mu_o l_g$ where B_r, l_m and l_g are the airgap flux density and the length of the airgap and magnet, respectively. The extension of

the flux weakening factor equation would be complex due to the large number of parameters but it can be presented as:

$$K_{fw} \propto \frac{\Psi_d, A_{slot}, I_a, K_{pa}, l_g}{A_m, N_a, I_d, l_m, B_r, A_{wire}} \tag{1-16}$$

Each parameter presented in the above equation can be adjusted to improve the flux weakening characteristic either before or after the machine is fully designed and constructed. The flux variation methods in VFPM machines are in fact an adjustment of one of these parameters.

1.4.5. Torque-speed characteristics

Although the PM machines can be designed to produce the rated torque over the entire speed range, the requirements for a large inverter and low phase inductance could be an issue since large inverters place a higher demand on power device switching requirements and might create high short circuit current which could damage the machine winding and/or the inverter. Therefore, it is preferred to have a machine with high inductance and use flux weakening control method to drive the machine [13-15].

The torque-speed characteristics of several PM machines are investigated in [16-25]. The torque speed curve is divided into three regions: constant torque region, flux weakening or constant power region and maximum speed limit. Fig. 1.6 presents the maximum torque per amp and voltage vector trajectories of conventional SFPM machine and torque-speed curve regions.

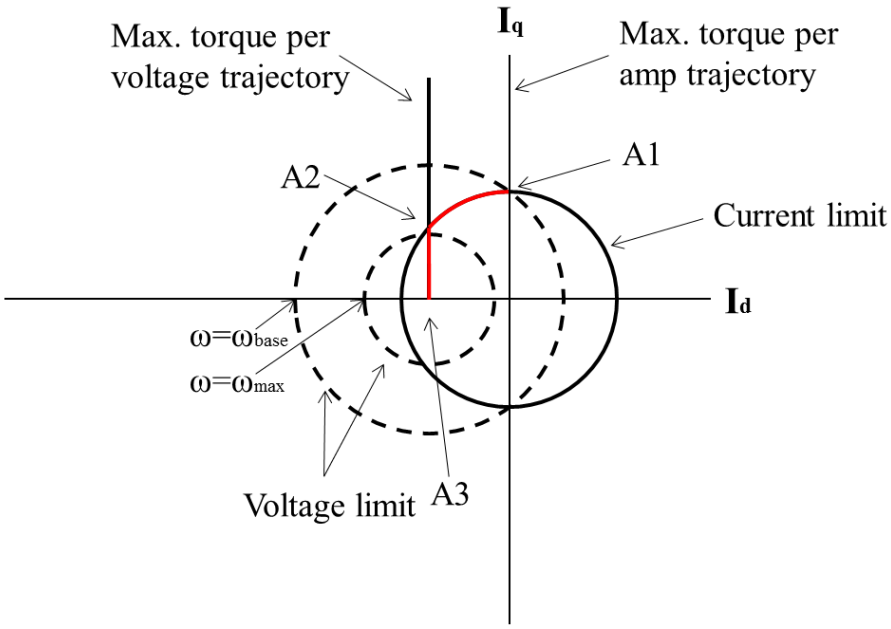

(a) Maximum torque per ampere and voltage vector trajectories of SFPM machine

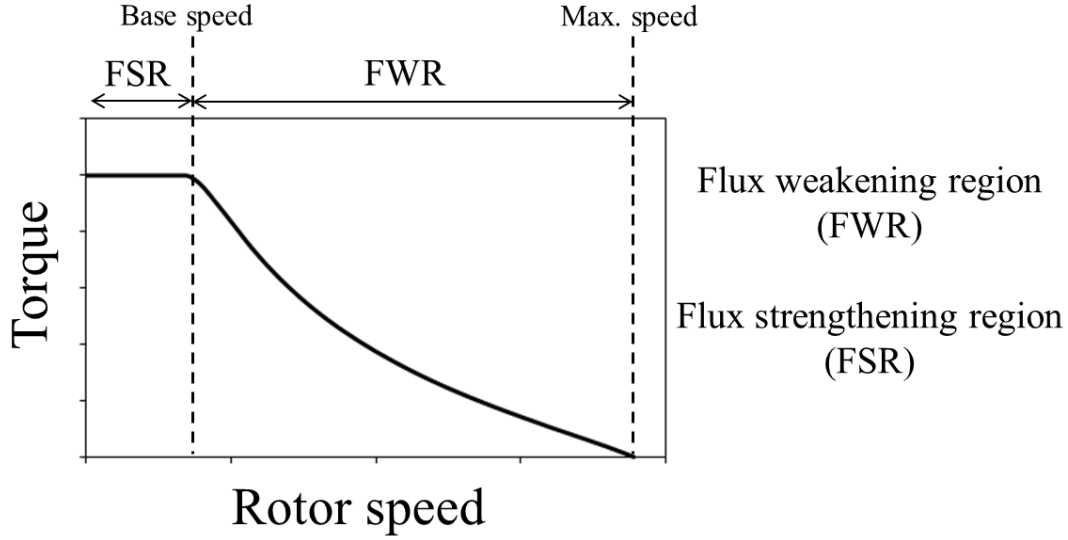

(b) Torque-speed regions in SFPM machine

Fig. 1.6 Torque-speed characteristics of SFPM machine.

1.4.5.1. Constant torque region, ($\omega \leq \omega_{base}$), ($I_{max} = I_a$) and ($U_{max} \geq U_a$)

This region starts from the start of the motor until the base speed ω_{base}. In this region the inverter supplies the motor with the rated voltage and current, the current angle equal to zero therefore the q-axis current equal to the rated current while the d-axis current is set to zero. The flux in airgap is a combination of the PM flux and the q-axis current flux. Fig. 1.7 presents the phase diagram of the constant torque region. The current is constant in this region and the current vector is fixed at A1, Fig. 1.6 (a). The current is presented as:

$$I_q = I_{max},\ I_d = 0 \ \text{ and } \ I_{max} = \sqrt{I_q^2 + I_d^2}$$

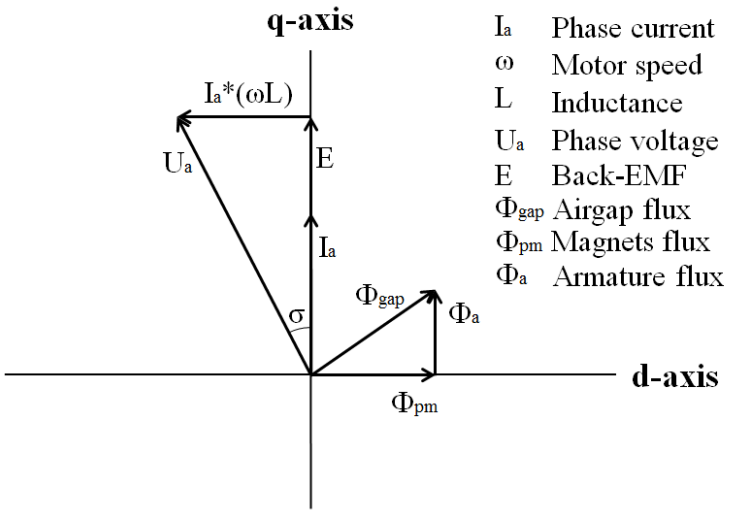

Fig. 1.7 Constant torque region.

1.4.5.2. Flux weakening region, ($\omega_{base} < \omega \leq \omega_{max}$), ($I_{max} = I_a$) and ($U_{max} = U_a$)

This region starts from the base speed ω_{base} and extends to the maximum speed ω_{max}. In this region the rated voltage is constant while the current angle varies. D-axis current starts increasing due to the requirement of d-axis flux to oppose the PM flux, the q-axis current makes the contribution of q-axis flux in the airgap which reduces so that the voltage keeps constant. With large inductance the current angle would change fast so the current keeps the voltage constant that may causes a large drop in the flux weakening region. Fig.1.8 presents the phase diagram, the current is varying in this region and the current vector moves from A1 to A2, along the current-limit circle as the speed increases, Fig. 1.6 (a). The current presented as:

$$I_q = I_{max}\, sin\, \beta,\ I_d = -I_{max}\, cos\, \beta \text{ and } I_{max} = \sqrt{I_q^2 + I_d^2}$$

where β is the angle between the d- and q-axis currents and varies from 0° to 90°.

However, when the flux weakening factor is higher than 1, i.e. $I_{max} > \Psi_{pm}/L_d$, a second flux weakening region can be achieved when $I_d = -\Psi_{pm}/L_d$ by decreasing the I_q and consequently higher speed range can be achieved. In this region, the current vector moves from A2 to A3 along the maximum-output trajectory, Fig. 1.6 (a).

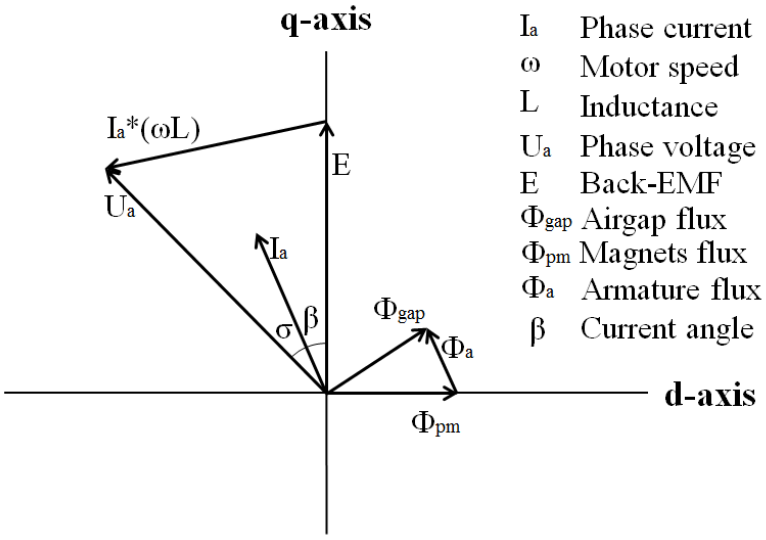

Fig. 1.8 Flux weakening region.

1.4.5.3. Maximum speed region, ($\omega = \omega_{max}$), ($I_{max} \leq I_a$) and ($U_{max} = U_a$)

While the speed increasing, the back-EMF increases from one side and the voltage drop across the inductance increases proportionally from other side. At a certain speed when the PM flux to inductance value is exceeding the rated current in the inverter both back-EMF and the voltage drop across the inductance would be in phase. Beyond this speed the machine is unable to produce torque and no longer can operate, Fig. 1.9. The current vector in this case is fixed at A3 along the maximum-output trajectory, Fig. 1.6 (a). The current in this region is presented as:

$$I_q = 0,\ I_d = -I_{max} \text{ and } I_{max} = \sqrt{I_q^2 + I_d^2}$$

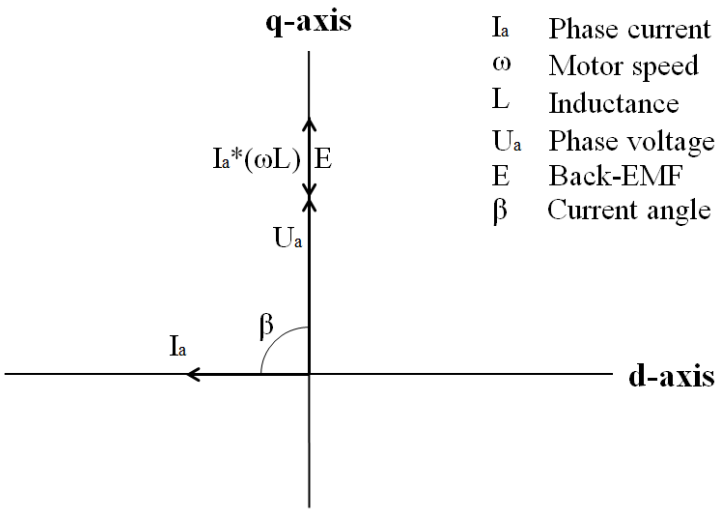

Fig. 1.9 Maximum speed limit.

It is important to mention the losses are neglected in the expressions above due to the complication. Accounting for the losses would reduce the maximum speed due to the lower induced voltage that caused by iron loss. Also the current value and angle would differ due to the copper loss, inverter losses and the faults in supplying the current feedback and rotor position. The voltage supplied by the inverter is constant but some dropping would occur due to the inverter losses.

1.4.6. Research in SFPM machines

There has been an extensive research on SFPM machines in the past 10 years including performance investigation using lumped parameter circuit [9, 26], optimization of design parameters [27, 28], comparison of different stator and rotor pole combinations [29-31], study of the cogging torque [32-34], torque ripple analyses [35, 36], investigation of the inductances [37, 38], study of the end-effect influence on the performance [39-41], calculation of the losses [42-47] and investigation of different control strategies [48-50]. Moreover, comparative studies of SFPM machine with other types of PM machines are presented in [3, 51-53]. Overall, the SFPM machine shows a significant potential as a strong candidate for several industrial applications such as aerospace, automotive and wind power. Therefore, several topologies with different features are derived from the original structure of the conventional switched flux machine. The next section of this chapter is focusing on the different topologies of SFPM machine. Generally, the advantages and drawbacks of the SFPM machines can be summarised as shown in Table 1.1.

Table 1.1 Advantages and drawbacks of SFPM machines

Advantages	**Drawbacks**
• Simple and robust rotor • Flux focusing utilization • Sinusoidal back-EMF waveform • Easy to manage the temperature rise • Suitable for applying external variable flux components • Easier to identify demagnetised magnets • Less copper usage and copper loss	• Low over load capability due to magnetic saturation • Complicated stator structure • Small slot area • Large magnet volume • Stator outside leakage • Inherently unchangeable PM flux

1.5. Different Topologies of SFPM Machine

Several topologies have been derived from the standard structure of the conventional 3-phase SFPM machine to fulfil the different requirements and cost restrictions. Cheaper SFPM topologies using less magnetic material or DC coils to replace the rare earth magnets, novel topologies with fault tolerance capability, linear and tubular SFPM topologies for linear motion applications, and external rotor topologies for direct-drive applications have been proposed and developed [54-82]. In this section the different SFPM machine topologies are categorised and reviewed.

1.5.1. Less magnet usage topologies

Several SFPM topologies are proposed to reduce the magnet usage while improving or maintaining the electromagnetic performances equivalent to the conventional SFPM machine. The indication behind these topologies is increasing the slot area by reducing the volume of the magnets therefore higher electric loading will maintain or even improve the torque performance compared to the conventional SFPM machine. Fig. 1.10 presents the multi-tooth, E-core, C-core and thin-PM SFPM machine topologies.

In order to reduce the magnet usage the alternative wound conventional SFPM machine topology is used. The stator poles without windings are replaced by stator teeth, Fig. 1.10 (a). Since the lamination core design is shaped like letter “E” thus the machine is named E-core, the magnetic orientation has to be redone alternatively for 6 permanent magnets. Comparing with the conventional SFPM machine which has the same outer diameter, E-core has higher torque density at the same rated current [54]. Moreover, the C-core machine is an alteration of the E-core SFPM machine by removing the extra iron cores between the two stator poles, i.e. replacing the E-core with C-core shaped lamination, Fig. 1.10 (b). Similar to the E-core machine, the C-core topology has better torque performance compared to that of the conventional SFPM machine having the same size [55].

Furthermore, the multi-tooth topology has an even or odd number (>1) of teeth in each stator pole, whereas the number of rotor poles in multi-tooth is usually high due to the multi stator teeth, Fig. 1.10 (c). In terms of electromagnetic performance the multi-tooth produces high torque at low electric loading but saturates quickly as the electric loading increases compared with the conventional SFPM machine which has same stator outer diameter [56-58]. On the other hand, a thin-PM SFPM machine topology is developed to reduce the magnetic material

usage [59]. This machine has same structure as the conventional SFPM machine but with thinner PMs, Fig. 1.10 (d).

Another SFPM machine topology has been proposed using ferrite magnets instead of the expensive rare earth NdFeB magnets. Although this machine has the same amount of PM material as the conventional SFPM machine, it is classified as cheap topology due to the usage of ferrite magnets. This topology consists of two PMs sandwiched in each stator pole in order to increase the flux focusing effect [60].

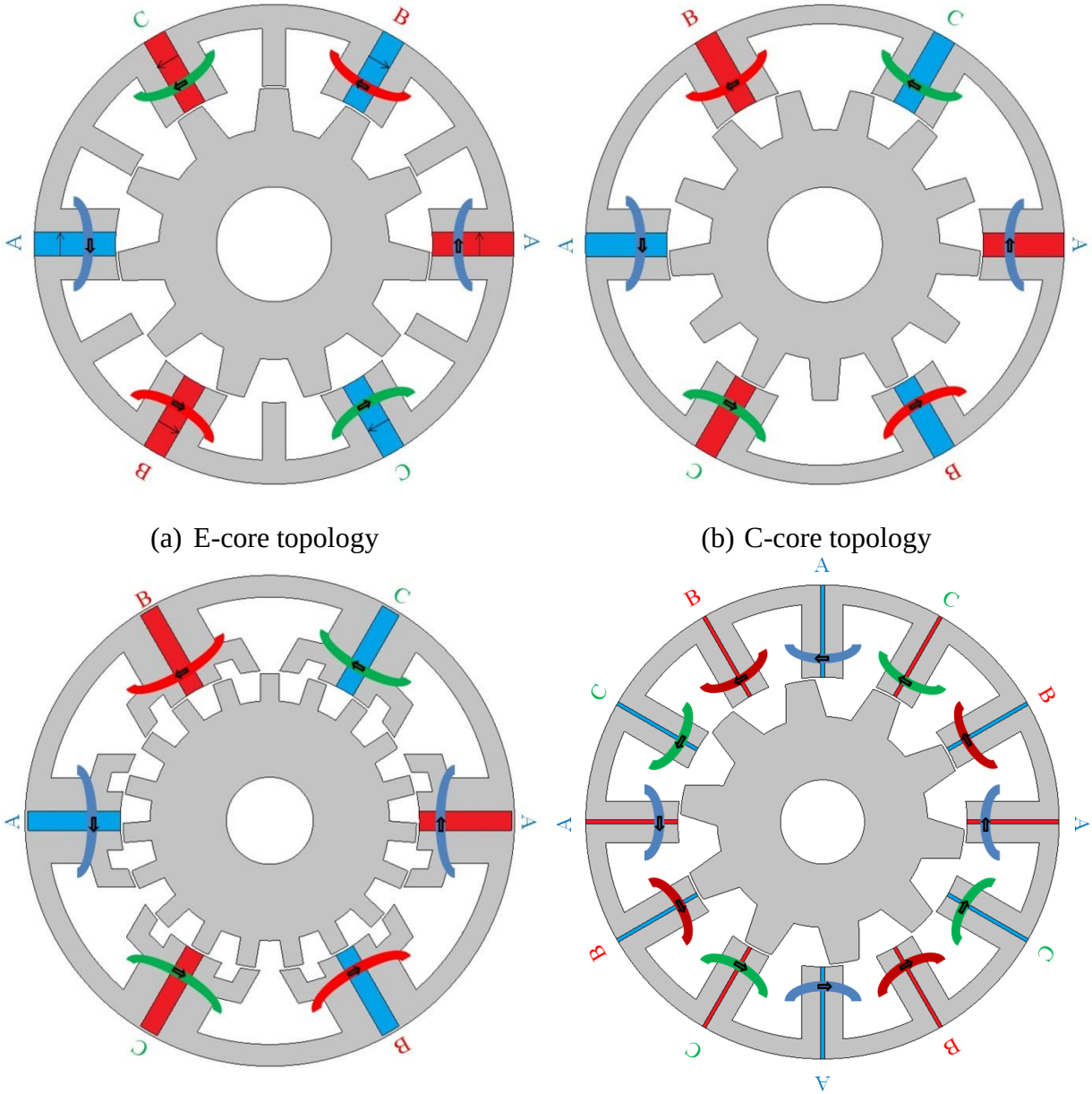

(a) E-core topology (b) C-core topology

(c) Multi-tooth topology (d) Thin-PM topology

Fig. 1.10 Different SFPM machine topologies with less PM material.

1.5.2. Magnetless topologies

The permanent magnet source can be replaced by a surface DC current model, Fig. 1.11 (a). The original conventional design of SFPM machine contains 12 stator poles; each pole has a permanent magnet and armature winding coil. The proposed topology suggests replacing the permanent magnets with DC current source components. The DC current source is situated between the "U" shaped iron cores around a small iron bridge located in the middle of the stator teeth, the iron bridge connecting the two "U" shaped cores as well as increasing the permeance for the magnetic flux sources, Fig. 1.11 (b) [61]. In order to achieve better performance this topology can be remodelled, the DC windings can be distributed around the inner slots of the machine, Fig. 1.11 (c). The proposed winding configuration increases the total slot area of the machine which permits more DC excitation winding. Moreover, the DC coils can be connected alternatively as shown in Fig. 1.11 (d). When the end-winding is ignored, the machines with all and alternative DC field windings produce similar performance as the conventional SFPM machine [62]. It is worth mentioning these topologies can be considered variable flux machines since the DC current can be regulated.

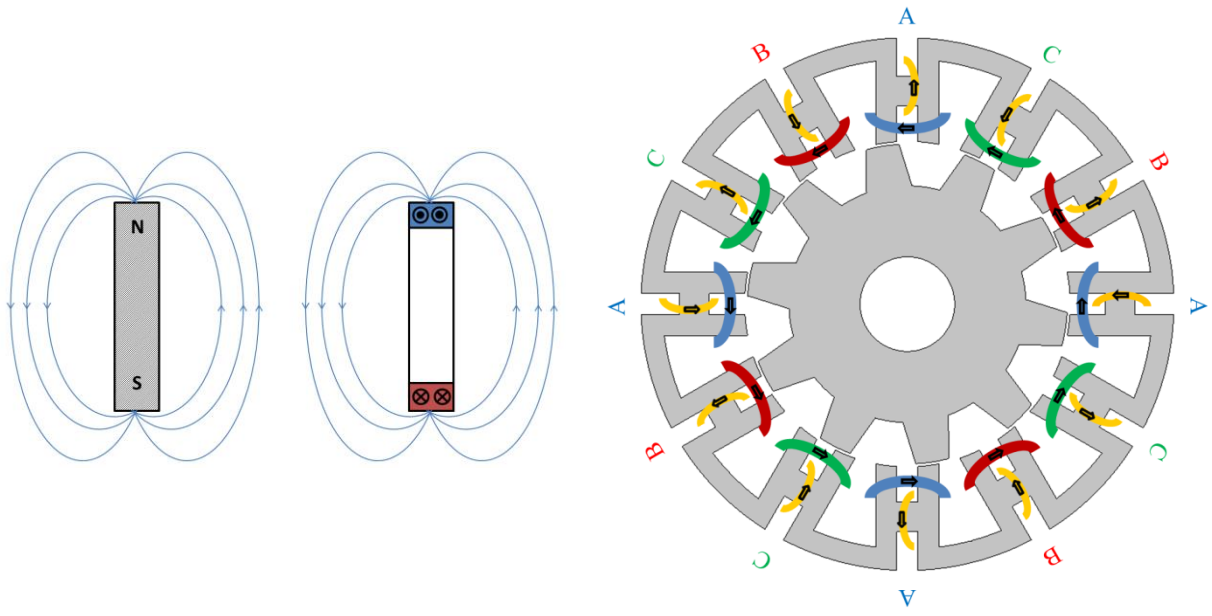

(a) Flux sources (b) DC flux source topology

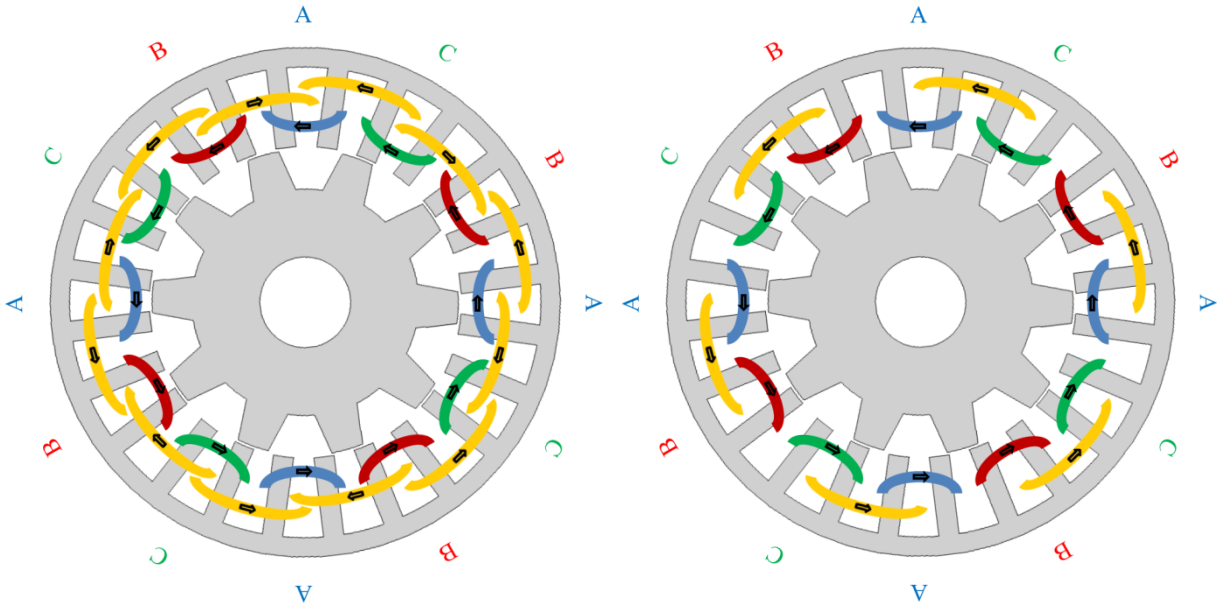

(c) All pole DC winding topology (d) Alternative pole DC winding topology

Fig. 1.11 Different SFPM machine topologies using DC flux sources.

1.5.3. Fault tolerant topologies

For critical applications such as aerospace, fault tolerance drives can help to improve the system reliability level and prevent the system from a complete shut down when a fault occurs during the system operation. However, such solutions might increase the total cost of the system and the issues with large size might occur. Therefore, fault tolerant machines are of a great interest for fault sensitive applications. In order to achieve a high level of fault tolerance, winding configurations offering full magnetic and physical isolation are needed. Using such winding configurations ensures when a fault occurs in one phase no effect on the other phases electrically and physically would follow. Thus, different topologies are proposed suggesting a full separation of the machine phases.

All pole wound SFPM machine contains two phase windings in each stator slot which increase the possibility of machine failure if one phase is faulted. Therefore, replacing all pole wound with alternative winding, i.e. each slot has a coil belonging to one phase, to prevent the machine from a total failure in case of one phase fault occurred, Fig. 1.12 (a) [10]. Further development is applied to the alternative winding machine to achieve better isolation of phases. Fig. 1.12 (b) shows the core separation machine in which the permanent magnets are removed from the unwounded stator poles. This separation creates a full magnetic and physical isolation of phase windings, though the machine performances, i.e. torque and power, might suffer from significant reduction [63].

A simple technique can be added to the conventional SFPM machine to achieve high fault tolerance. Fig. 1.12 (c) shows SFPM machine with iron separator used to separate the slot area and hence the windings of different phases, such a separator can also provide a path for the coil flux to pass through [64, 65]. Another approach to avoid complete shutdown of the machine in case of a fault is using multiphase, several SFPM machines with high number of phases are developed in [66]. Although using multiphase does not provide a full separation of the coils belonging to different phases, the high number of phases keeps the machine operating until the next maintenance is taken. It is worth mentioning the E-core topology presented in the previous section has a fault tolerance capability since the middle E-shaped core teeth provide physical separation of phases winding.

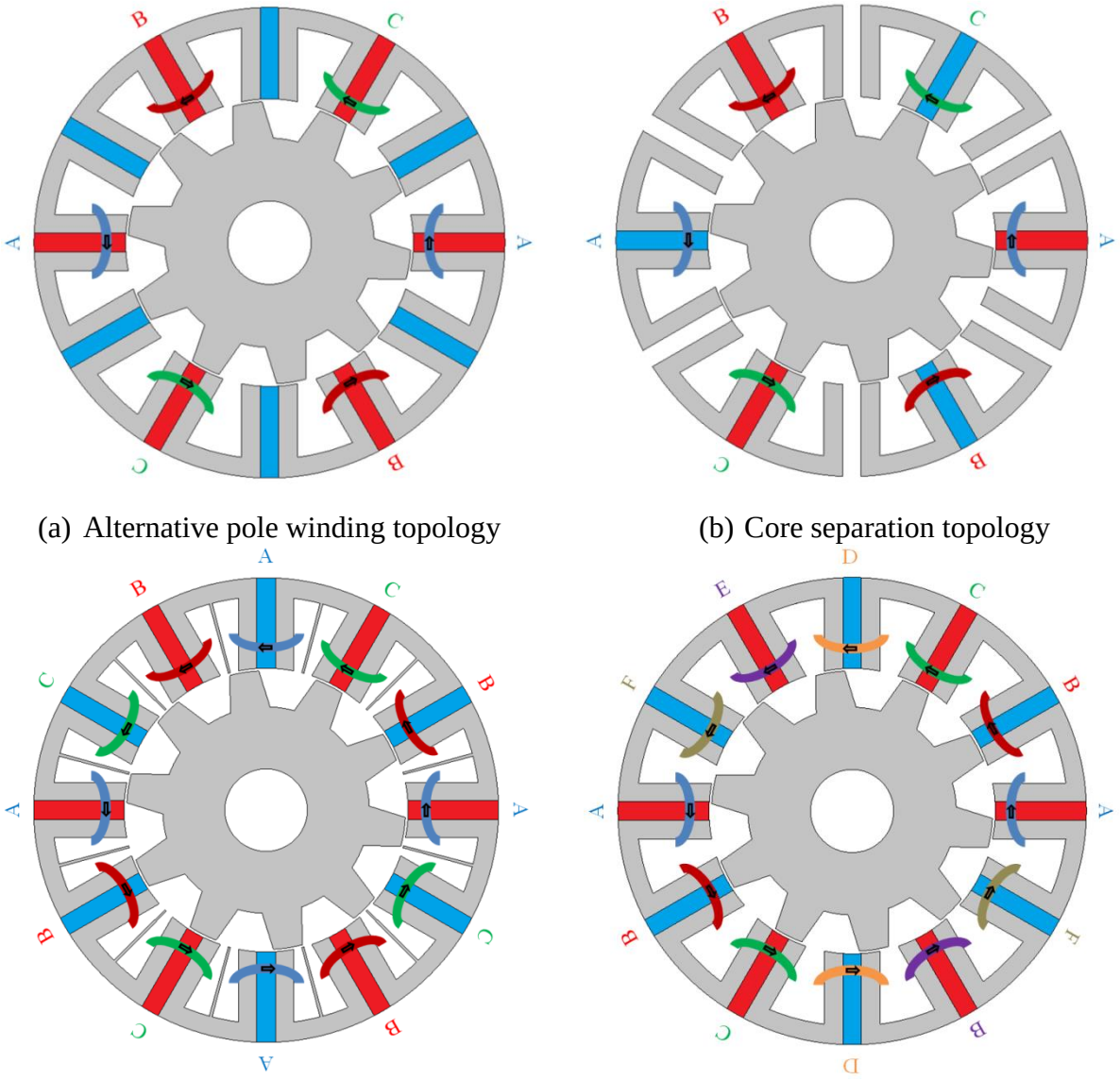

(a) Alternative pole winding topology

(b) Core separation topology

(c) Double layer separator topology

(d) Multiphase topology

Fig. 1.12 Different SFPM machine topologies employing fault tolerance methods.

1.5.4. Modular, external, linear and tubular rotor machine topologies

A modular rotor is made of non-ferromagnetic material with ferromagnetic 'C' shaped cores in the near airgap side, Fig. 1.13 (a). This technique is used to reduce the leakage of the flux in the rotor due to the operation requirement as well as reduces the iron loss. The modular rotor was first proposed and applied in switched reluctance machine [67-69], however in SFPM machine the modular rotor is described in [70].

In-wheel applications normally prefer external rotor motors over normal internal rotor motors since the mechanical transmission components such as gears and driven belts are not required. Beside the advantage of in-wheel traction, an external rotor SFPM machine has the ability of including external cooling systems and/or flux controlling component without increasing the outer diameter of the machine since the stator is internal. External rotor switched flux machines are proposed and investigated for direct-drive applications in [71-73]. Fig. 1.13 (b) shows cross-section of external rotor SFPM machine.

Linear machines are preferred over hydraulic, pneumatic or actuators in many industrial applications, such as transportation, automobile, aerospace and robotics due to their reliability, high power density and relatively small size. Linear SFPM machines have all the advantages of rotary SFPM machine which are simple and robust mover, as well as high thrust density and PMs and armature windings are located on the stator. Furthermore, linear SFPM machines can be reversed in structure, i.e. the armature windings and PMs can be mounted on short mover, which lead to significant reduction in cost since less copper and PM materials are used. Fig. 1.13 (c) shows a section of linear SFPM machine, several topologies of linear SFPM machines have been proposed and investigated in [74-78].

Tubular switched flux machines have been developed due to their high torque density, simple mover structure and inexistence of end winding and net attraction force between stator and armature. In general, tubular machines are suitable for several applications such as free piston energy converters, reciprocating compressors and healthcare devices [79]. Several tubular SFPM machines have been developed in [80-82]. A 3D model of tubular SFPM machine is presented in Fig. 1.13 (d).

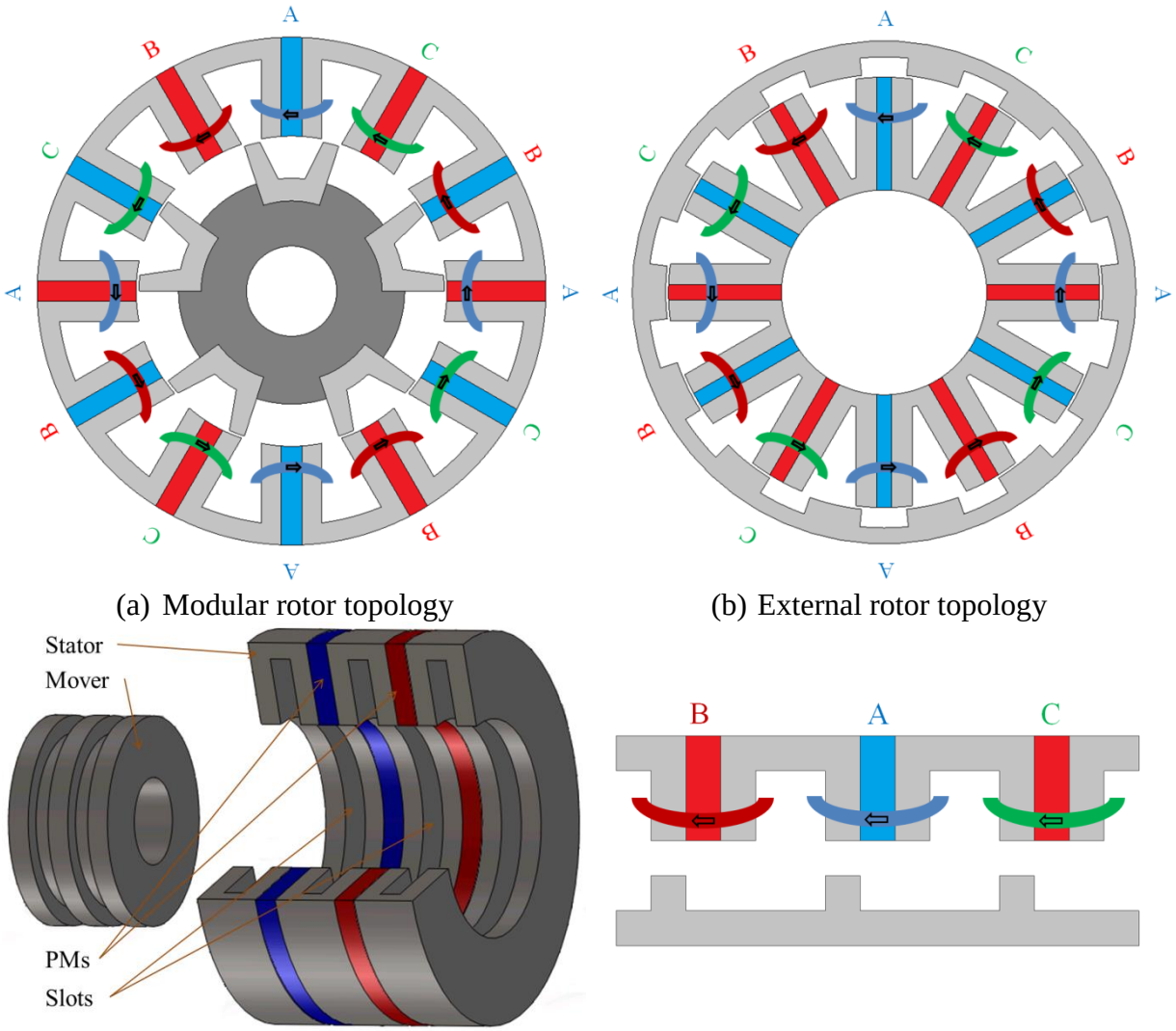

(a) Modular rotor topology (b) External rotor topology

(c) Tubular SFPM machine (d) Linear SFPM machine

Fig. 1.13 Modular rotor, external rotor, linear and tubular SFPM machine topologies.

Table 1.2 Comparison of different SFPM machines topologies

	Less magnet	**Magnetless**	**Fault tolerant**	**Others**
Manufacture cost	Medium	Low	High	High
Mechanical structure	Medium	Medium	Complex	Complex
Magnetic saturation	High	Medium	High	Low
Airgap flux density	Medium	Low	Medium	High
End winding length	Medium	High	Medium	Medium
Torque density	Medium	Low	Medium	High
Magnet usage	Medium	Non	Medium	High
Copper usage	Medium	High	Medium	Medium

1.6. Variable Flux Permanent Magnet Machines

Conventionally, flux weakening control methods are used to drive the PM machines in order to extend the operation speed range. However, due to the inverter limitations in terms of maximum current and voltage, the speed range is still limited and inadequate for some applications, such as automotive. Therefore, for further speed range extension and more flux weakening capability improvement as well as without scarifying the high torque and efficiency of the PM machines, variable flux concept has been proposed. By using electrical, mechanical or other types of techniques the PM flux level can be varied in order to introduce adjustable speed range and flux weakening capability as well as high efficiency at high speed. Table 1.3 summarises the advantages and drawbacks of VFPM machines.

Table 1.3 Advantages and drawbacks of variable flux PM machines

Advantages	Drawbacks
• Easy to achieve extended constant power region without the need for complex electronics • Enhanced torque in the constant torque region without sacrificing the high flux weakening capability • High efficiency over the entire torque-speed curve	• Complex structure • Low torque density • Extra DC source required, or • Extra mechanical component required

1.6.1. Electrical variable flux machines

By including DC excitation winding in the PM machines, i.e. hybrid excitation machines [83, 84], the airgap flux level can be controlled. Normally, in a flux weakening region the DC excitation produces d-axis flux to oppose the flux produced by the PM similar to that of flux weakening control [85]. These machines are characterised by their potential to extend the flux weakening capability and improve the efficiency at high speed as well as enhance the constant torque region, which is known as flux strengthening [86]. In the past 10 years many hybrid excitation topologies have been proposed and developed, however they can be grouped due to the correspondence of their DC excitation flux path to the PM flux path, i.e. parallel or series flux path.

1.6.1.1. Parallel flux path hybrid excitation permanent magnet machines

In these machines the excitation flux and the flux created by the permanent magnets are in different paths, i.e. parallel paths. Since the DC excitation flux linkage circuit is in parallel with PM flux linkage circuit and does not pass through the PM, those machines characterised by their ability to avoid demagnetization risk. According to the location of the magnets there are two main types of parallel flux machines, PM on the stator and PM on the rotor.

1.6.1.1.1. Hybrid excitation machines with PMs on the stator

Generally, these types of machines have the same structure as the conventional SFPM machine with a modification on the stator to include the DC excitation windings. In [87] half magnets are used leaving space for DC excitation windings to go around the stator teeth and slot area, Fig. 1.14 (a), while shorter magnets are used to introduce space for DC excitation to wound around the PM in [88], Fig. 1.14 (b). Another approach proposed in [89], same structure as the conventional SFPM machine, is used with the DC coils and armature windings are wound the same way and share the same slot area.

Moreover, the DC coils can be located behind the magnets and back iron and surrounded by ferromagnetic yoke as shown in Fig. 1.14 (c). This machine structure uses the principles of both switching flux and flux concentration. When the DC coils are excited with positive current, the DC excitation winding creates short circuit flux around the top of magnets in which the stator yoke back-iron saturates. Therefore, the magnet flux will be pushed toward the rotor in order to strengthen the airgap flux density. Moreover, when negative DC current is used, the flux produced by the DC excitation shorts circuit the PMs leading to lower flux linkage [90, 91].

A hybrid excitation machine was proposed based on E-core SFPM machine topology. DC excitation coils are employed on the middle teeth of the E-shaped core which contains no permanent magnets, Fig. 1.14 (d). This machine has the same non-overlapping winding as the conventional E-core SFPM machine and the slot area is divided between the DC excitation winding and the armature winding [92].

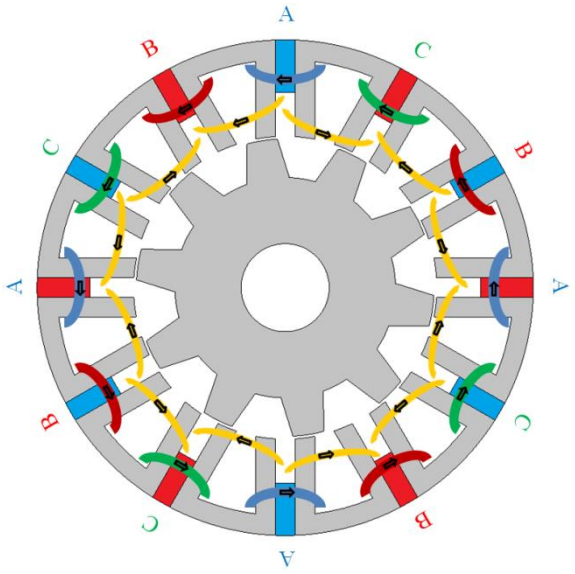

(a) Hybrid SFPM (distributed winding)

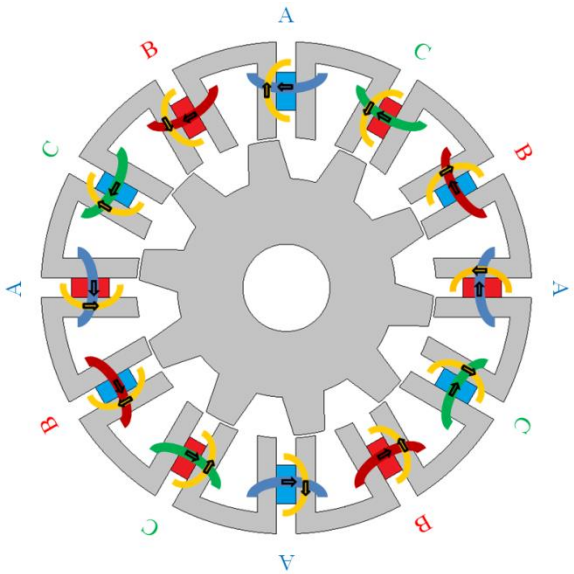

(b) Hybrid SFPM (toroidal winding)

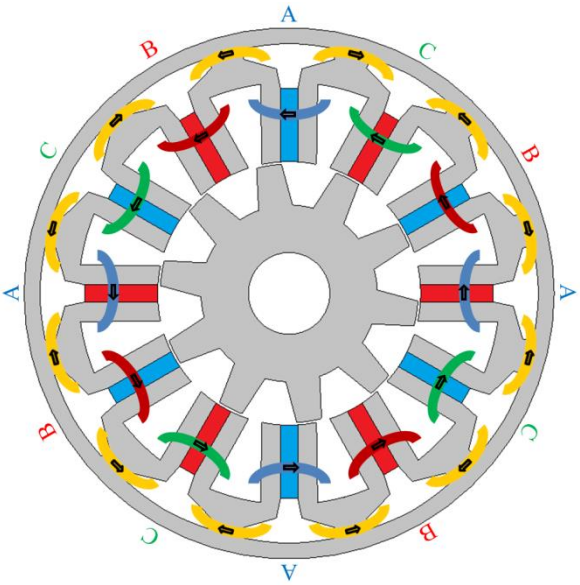

(c) Back-DC SFPM topology

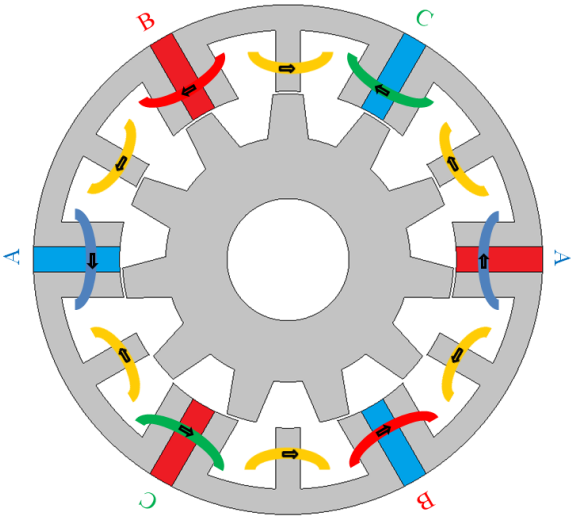

(d) Hybrid E-core topology

Fig. 1.14 Hybrid excitation SFPM machine topologies with magnets on the stator.

Table 1.4 Parallel flux path hybrid excitation switched flux machines with PMs on the stator

	Hybrid SFPM	**Back-DC SFPM**	**Hybrid E-core**
Manufacture cost	Medium	High	Low
Mechanical structure	Complex	Complex	Medium
Magnetic saturation	High	Low	Medium
Airgap flux density	Low	Medium	High
End winding length	Medium	Medium	Low
Torque density	Low	Medium	High
Magnet usage	Low	High	Low
Copper usage	High	High	Medium
Flux strengthening	High	Medium	Medium
Flux weakening	High	High	Medium

1.6.1.1.2. Hybrid excitation machines with PMs on the rotor

This category contains the machines with PMs on the rotor and both armature and DC excitations on the stator. The homopolar and bipolar hybrid excitation machines generally consist of a new rotor which contains the permanent magnets, solid cores and other laminated cores, while the stator includes the armature windings wound around laminated core and the DC excitation wound toroid around the laminated core and armature winding, Figs. 1.15 (a) and (c). The stator includes teeth made of lamination in which the armature windings are located. The solid part is used as external shield and yoke for the DC excitation winding, Figs 1.15 (b) and (d). The airgap flux can be either strengthened or weakened due to the DC excitation winding, which gives a good range of flux variation and flexibility in terms of efficiency and speed control. In the bipolar machines the magnets could be axially or circumferentially magnetised while in the homopolar only circumferential magnetisation applied. The difference between the structure of homopolar and bipolar rotors are the solid core connection with laminated cores, Figs. 1.15 (a) and (c) [93-97]. On the other hand, the claw pole structure contains a rotor and two stators, external and internal. The surface of the rotor is divided into permanent magnet poles and solid iron poles. The inner stator is located inside the rotor and contains the DC excitation winding, while the outer stator has the armature winding and is located around the rotor. In this machine a fixed excitation of magnets comes together with variable flux supplied by circumferential DC excitation windings located in the inner stator. The airgap flux is divided into two sections, magnets and iron poles. When the DC excitation winding is not excited, permanent magnets are the only sources of flux in the machine, and the direction of the flux in the stator core is toward the airgap with respect to the shaft. In the airgap, the flux crosses mostly by the poles with magnets, only a few portion crosses in front of the iron poles which forms leakage. The DC excitation flux is either added or subtracted from the magnet flux according to the current direction [98-101]. Figs. 1.15 (e) and (f) show the cross-section and 3D model of the claw and consequent pole machine.

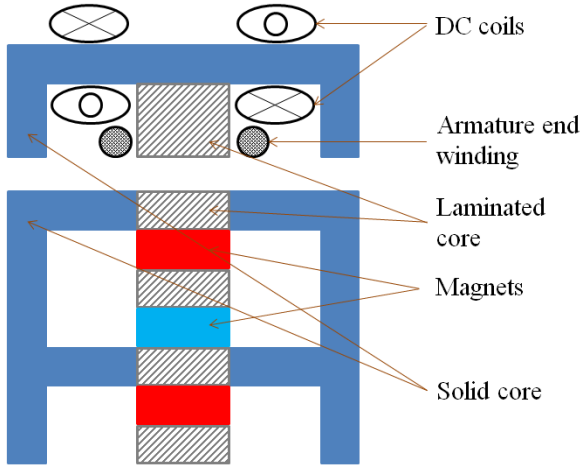

(a) Homopolar cross-section

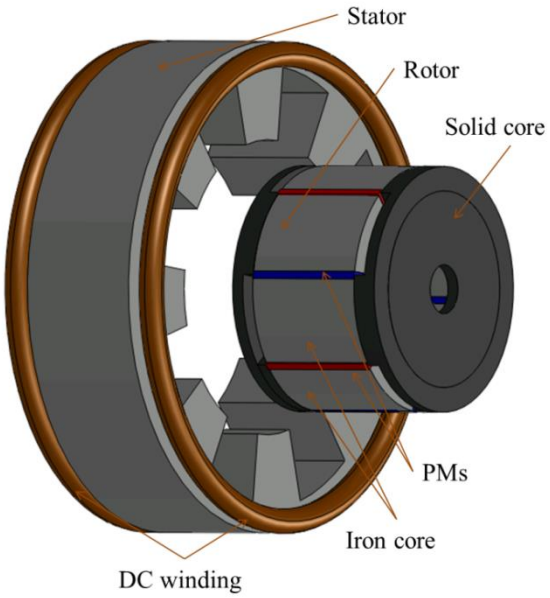

(b) Homopolar 3D model

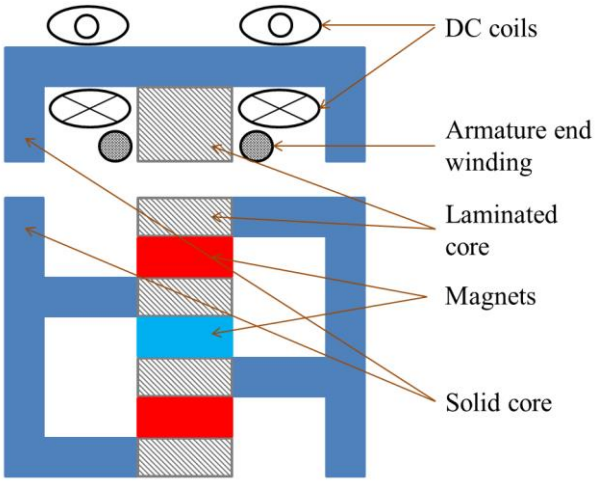

(c) Bipolar cross-section

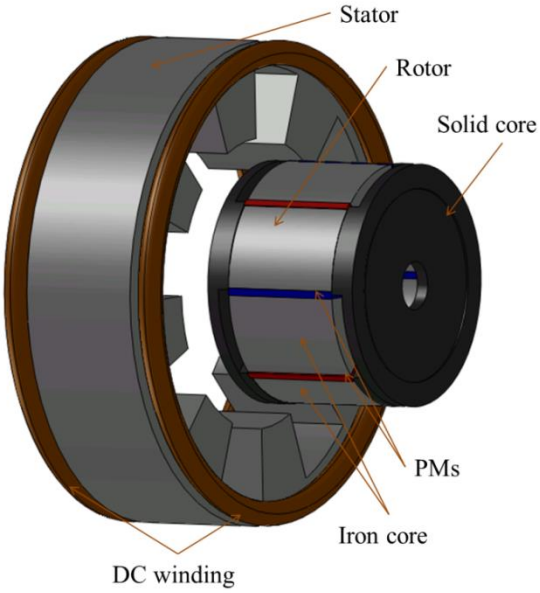

(d) Bipolar 3D model

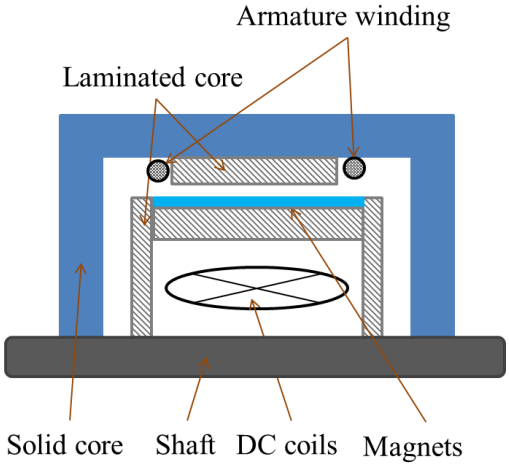

(e) Claw pole cross-section

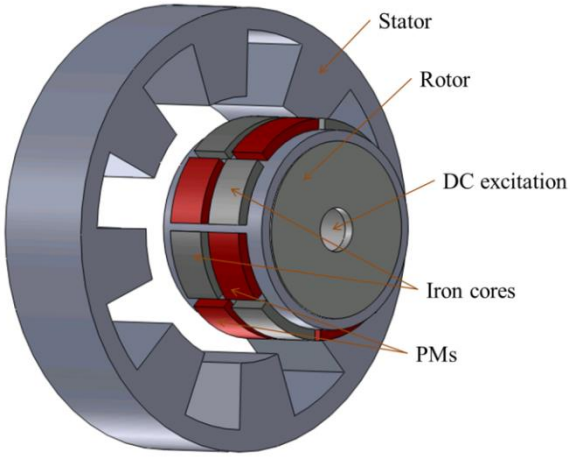

(f) Consequent pole 3D model

Fig. 1.15 Hybrid excitation PM machines with magnets on the rotor.

Table 1.5 Comparison of parallel flux path hybrid excitation machines with PMs on the rotor

	Homopolar	**Bipolar**	**Claw pole**
Manufacture cost	High	High	Medium
Mechanical structure	Complex	Complex	Medium
Magnetic saturation	-	-	-
Airgap flux density	-	-	-
End winding length	Medium	Medium	Low
Torque density	-	-	-
Magnet usage	Medium	Medium	High
Copper usage	High	High	Medium
Flux strengthening	Medium	High	Low
Flux weakening	High	High	Low

1.6.1.2. Series flux path hybrid excitation permanent magnet machines

Although the parallel flux path machines are preferred since they minimize the PM demagnetization risk, series flux path DC excitation machines have also been developed. In these types of machines the flux linkage of the permanent magnets and the DC excitation windings are in series. Therefore, the DC excitation flux passes through the PMs which increase the risk of irreversible PMs demagnetization.

1.6.1.2.1. Hybrid excitation surface-mounted machine

This machine consists of a stator with conventional teeth and armature winding, whereas the rotor has surface permanent magnets on the outside and DC coils on the inside, Fig. 1.16. In order to strengthen the PM flux, the DC excitation flux has same direction as the PM to push the magnet flux toward the airgap. However, the flux with opposite direction supplied by the DC excitation passes through the PM in order to weaken the airgap flux. However, due to the position of the DC excitation winding in the rotor this machine may require brushes/slip rings to supply the DC current [102, 103].

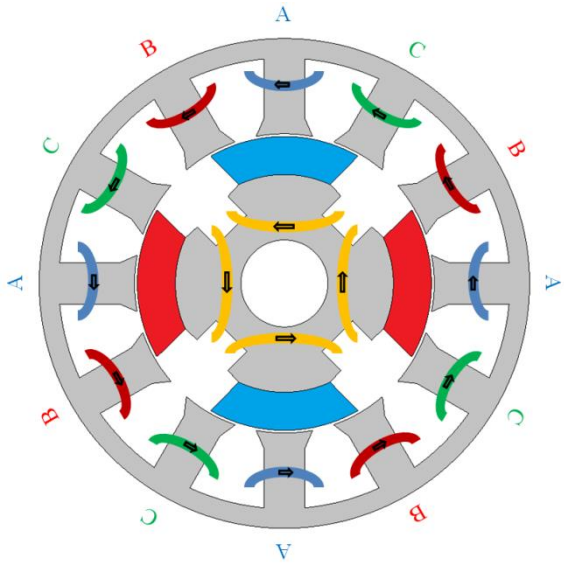

Fig. 1.16 Hybrid excitation surface mounted machine.

1.6.1.2.2. Hybrid excitation doubly salient

The hybrid excitation doubly salient machine has a normal doubly salient structure and additional DC excitation winding placed in series with the permanent magnets. In this machine the two permanent magnets have a unique location between the stator teeth and the back iron. This location allows the magnetic flux to be concentrated in one tooth at time, which leads to high flux focusing. This magnetic configuration allows for some extra space between the two magnets for the DC excitation winding, Fig. 1.17. This machine is noted by the improved performance, high power density, low cost due to ferrite magnet usage and robust structure [104-107].

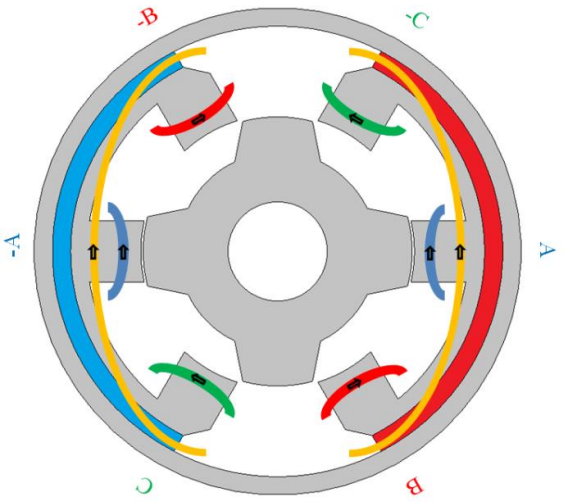

Fig. 1.17 Hybrid excitation doubly salient machine.

Table 1.6 Comparison of hybrid excitation surface mounted and doubly salient machines

	Hybrid excitation surface mounted	**Hybrid excitation doubly salient**
Manufacture cost	High	Medium
Mechanical structure	Complex	Medium
Magnetic saturation	Medium	Medium
Airgap flux density	High	Medium
End winding length	Short	Long
Torque density	High	Medium
Magnet usage	High	Medium
Copper usage	Medium	High
Flux strengthening	Medium	Medium
Flux weakening	Medium	Low

1.6.2. Mechanical variable flux machines

The mechanical variable flux machines are PM machines with mechanically adjustable PM flux. The structure of PM machines is upgraded to control the permanent magnet flux by either adding extra mechanical component or by altering the original structure of the machine. The majority of the mechanical flux variation methods can only achieve flux weakening due to the possibility to weaken the permanent magnet flux by providing flux leakage path. There are two main types of mechanical adjustment methods, i.e. rotational and linear.

1.6.2.1. Rotational adjustment machines

These machines consist of a rotatable part with mechanical components, i.e. core poles, PMs or windings, by rotating this part the mechanical component either boosts or weakens the flux in the airgap. The flux weakening capability of these machines is controlled by the relative position of this part and the rotation angle determines the level of flux weakening.

1.6.2.1.1. Axial field rotational adjustment machine

This machine consists of stator with the armature winding sandwiched between two rotor disks each one containing permanent magnet poles, Figs. 1.18 (a) and (b). In order to achieve flux weakening the rotor poles are skewed so that the different magnet poles from each rotor face each other which leads to magnetic short circuit and therefore lower airgap flux [108, 109]. In [110], hybrid excitation axial field surface mounted machine is proposed, a DC excitation winding added inside the stator for better flux control.

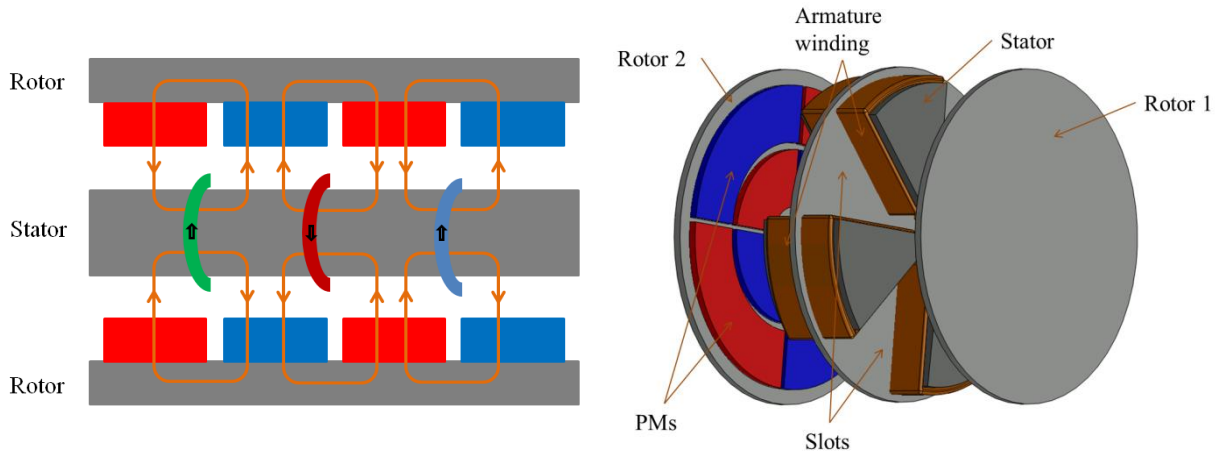

(a) Modular cross-section (b) 3D model

Fig. 1.18 Variable flux axial field surface-mounted PM machine.

1.6.2.1.2. Radial field rotational adjustment machine

Fig. 1.19 shows cross-section and 3D model of the radial field surface-mounted machine. This machine includes a stator with conventional teeth and two rotors and each rotor has a set of permanent magnets and can be adjusted mechanically. In this machine, two operational modes can be applied, in the first one the maximum effective flux when the same magnetic poles in the two rotors align with each other. The second mode is the no flux mode or the braking mode the machine can be stopped by making the different magnetic poles align. In terms of flux weakening capability the rotors can be displaced from each other therefore a reduction in the PM flux in the airgap can be achieved, however axial magnetic force might cause difficulties in displacing the rotors [111].

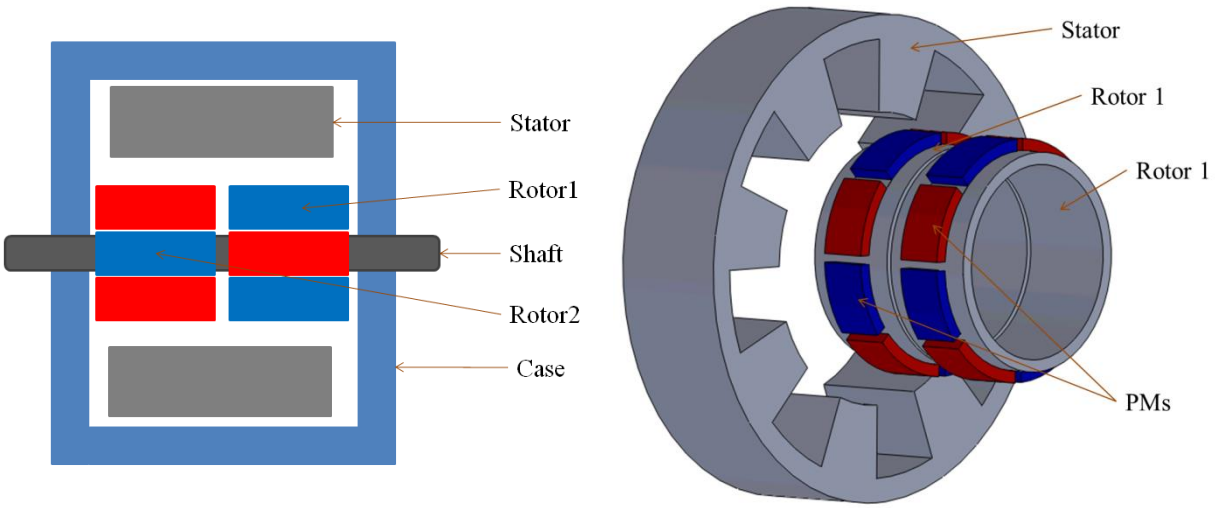

(a) Modular cross-section (b) 3D model

Fig. 1.19 Variable flux radial field surface-mounted PM machine.

1.6.2.1.3. Radial field-surface rotational adjustment machine (double layer rotor)

This machine contains two layers of rotor and each one has surface permanent magnet poles, Fig. 1.20. In order to control the flux weakening capability of the machine the rotors can be skewed. The different magnet poles can be aligned to create PM short circuit flux and consequently flux weakening state, while same magnet poles alignment leads to adding the flux of each magnet and therefore strengthening the airgap flux [112].

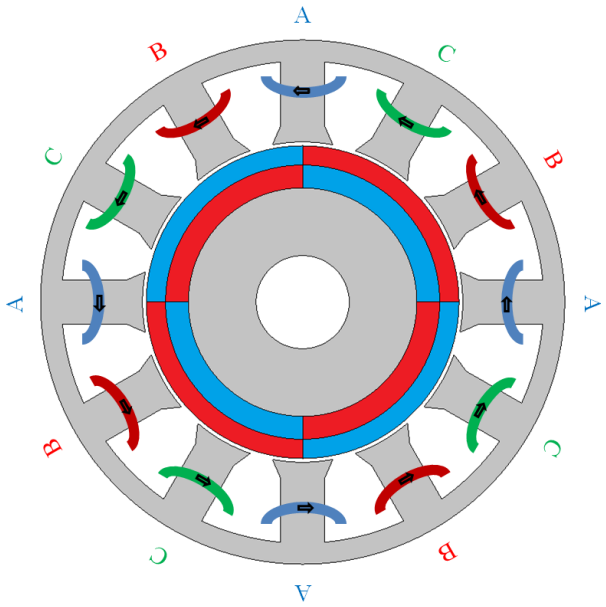

Fig. 1.20 Variable flux radial field surface-mounted PM machine with double layer rotor.

Table 1.7 Comparison of axial, radial and double layer radial SPM machines with mechanical flux adjustment

	Axial field	**Radial field**	**Radial field-surface**
Manufacture cost	High	High	Medium
Mechanical structure	Complex	Complex	Medium
Magnetic saturation	-	-	-
Airgap flux density	High	Medium	High
End winding length	Non	Medium	Medium
Torque density	-	-	-
Magnet usage	High	Medium	Medium
Copper usage	Medium	Medium	Medium
Flux strengthening	None	None	None
Flux weakening	Medium	Medium	Medium

1.6.2.2. Linear adjustment machines

These machines include movable linear components. By adjusting these components linearly, the flux in the airgap can be varied.

1.6.2.2.1. Linear adjustment in rotor

Two mechanical methods are used in IPM machines to achieve flux weakening. Fig. 1.21 (a) shows the first method, which consists of inserting iron pieces axially into the flux barriers in the rotor in order to create a short circuit path for the PMs flux [113, 114]. Moreover, a similar method but with the iron bars are located inside the rotor and displaced from the PMs by tension springs is presented in Fig. 1.21 (b). When the machine crosses the base speed the centrifugal force works to overcome the tension spring force and therefore those iron bars move to create a short circuit path for the PMs flux [115].

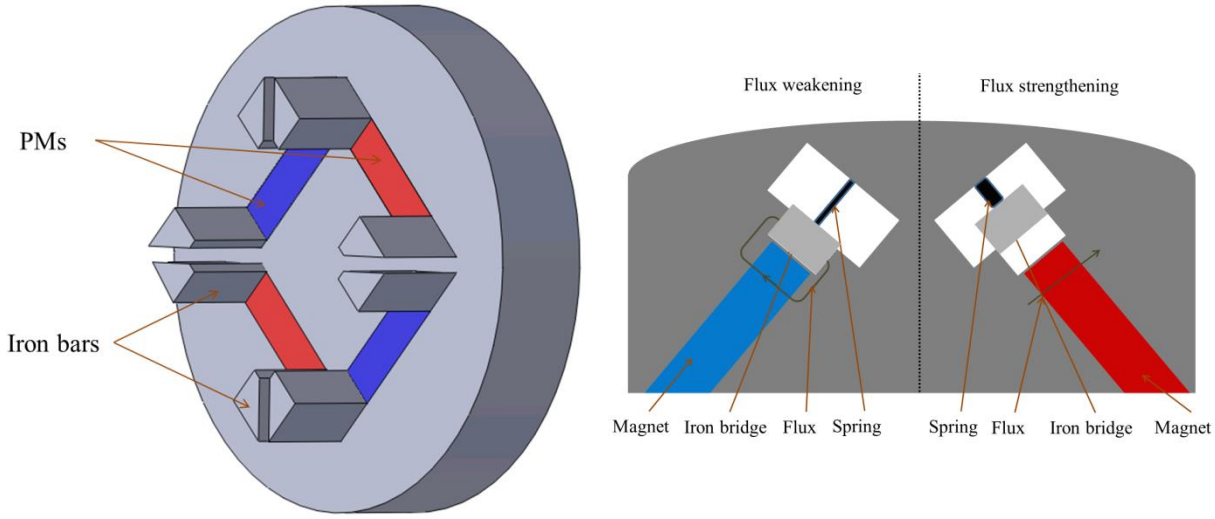

(a) Inserted iron bar topology (b) Built-in iron bar topology

Fig. 1.21 IPM machine with mechanical flux adjusting bars.

1.6.2.2.2. Linear adjustment in stator

This technique uses mechanically movable pieces (made of ferromagnetic material) located outside the stator, as shown in Fig. 1.22. The PM flux is controlled by the position of those iron pieces. At open position, i.e. when these pieces located away from the magnets, the PM flux linkage flows through the stator tooth, stator back-iron, airgap, rotor pole and rotor back-iron and therefore the flux distribution is same with that of the conventional SFPM machine without these pieces. By moving the pieces to the closed position, i.e. located at the top of the magnets, a part of the PM flux will be short circuited through these pieces [116, 117].

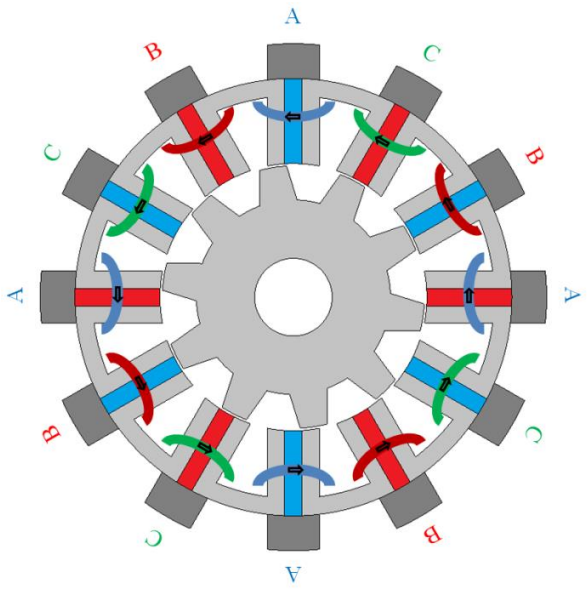

Fig. 1.22 SFPM machine with mechanically movable pieces.

1.6.2.2.3. Airgap mechanical adjustment

The airgap length can be adjusted to strengthen or weaken the airgap flux level. In axial-field permanent magnet machines the distance between the stator and the rotor can be adjusted to control the flux passing through by displacing the rotor away from the stator. The distance between the rotor and stator determines the flux weakening level. However, Fig. 1.23 shows SFPM machine with segmented stator poles, by moving those stator poles away from the rotor the airgap length decreases and therefore lower flux density and consequently high flux weakening capability can be achieved [118].

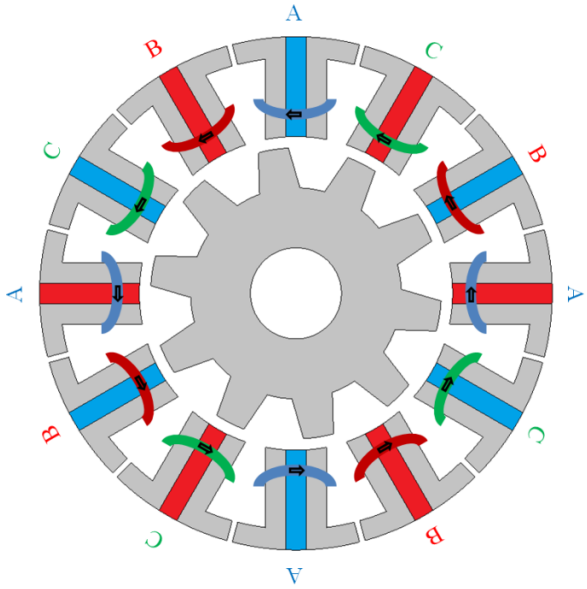

Fig. 1.23 SFPM machine with adjustable airgap.

Table 1.8 Comparison of linear mechanical flux adjustment machines

	Rotor linear	**Stator linear**	**Airgap adjustment**
Manufacture cost	High	Medium	High
Mechanical structure	Complex	Medium	Complex
Magnetic saturation	-	Medium	Medium
Airgap flux density	-	-	-
End winding length	Low	Medium	Medium
Torque density	High	High	Medium
Magnet usage	Medium	High	High
Copper usage	Medium	Medium	Medium
Flux strengthening	Non	Non	-
Flux weakening	Medium	High	-

1.6.3. Other types of variable flux machines

There are machines which contain flux adjusting techniques but do not qualify as electrical or mechanical. This category contains two main types, memory motors and winding adjustment machines.

1.6.3.1. Memory motor

The memory motor is proposed as new variable flux machine, using AlNiCo magnets which they can easily be demagnetized and re-magnetized by using short pulse d-axis current. the variation of PM remanence provides flux weakening and strengthening during the machine operation [119]. The memory motor is divided into four major types.

1.6.3.1.1. Pole changing memory motor

The concept of this machine is to change the number of rotor poles by magnetizing or demagnetizing the PMs. The rotor contains radially inserted tangentially magnetized permanent magnets sandwiched between the iron cores, each pole has more than one magnet, Fig. 1.24. Normally, a pole changing memory machine has a stator/rotor pole combination of non-integer number. Therefore, by applying a short pulse of stator current the number of rotor pole changes, the higher the number of rotor pole, the better the flux level in the airgap. Additionally, demagnetization and re-magnetization of the magnets provide flux weakening and strengthening [120, 121].

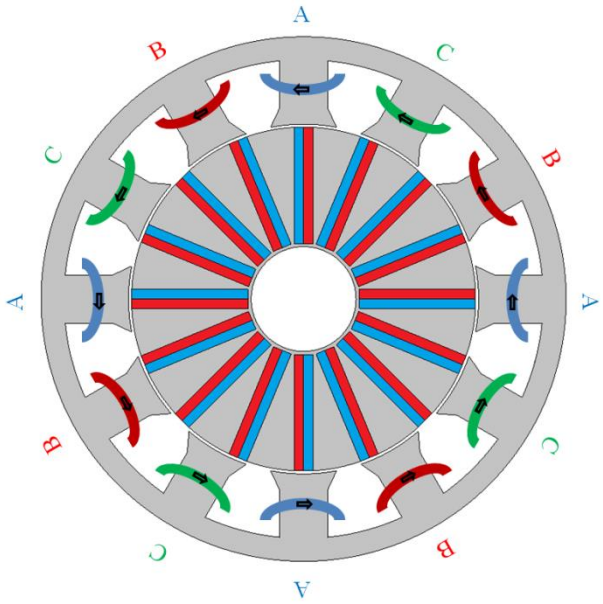

Fig. 1.24 Pole changing memory motor.

1.6.3.1.2. Flux controlled memory motor

The rotor has tangentially magnetized permanent magnets sandwiched between iron cores and triangles made of nonmagnetic material between the iron cores to direct the flux toward the airgap, Fig. 1.25. However, by applying opposite stator current, i.e. d-axis current, the magnets partially demagnetized which leads to lower airgap flux density and consequently higher flux weakening capability. When the current is applied in different direction the magnets are re-magnetized and the airgap flux level increases [122].

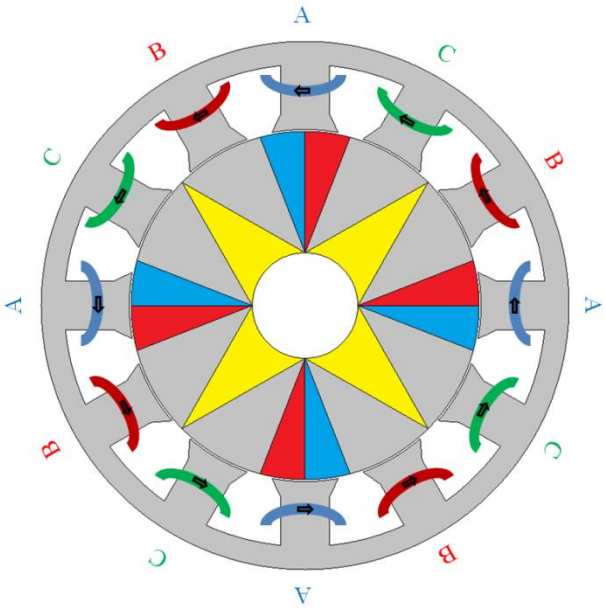

Fig. 1.25 Flux controlled memory motor.

1.6.3.1.3. Composite memory motor

This machine has a stator with conventional teeth and two sets of magnets are used in the rotor, the first set is NdFeB circumferentially magnetized and the second is AlNiCo radially magnetized. The rotor magnets magnetisation directions and dimensions are designed to keep countering the magneto-motive force (MMF) of the armature to be below the coercive force. Between the shaft and the rotor iron core there is a bush made of nonmagnetic material as well as slots filled with nonmagnetic material to fix the magnets in the d-axis position, the slots are shaped as semicircle at two ends and rectangles in the middle. The reason of these slots is to increase the q-axis magnetic resistance and prevent armature reaction created by load current from affecting the d-axis airgap flux when it is weakened. Therefore, the main purpose of the slot is to prevent the AlNiCo from demagnetizing. Additionally, there are joints between NdFeB and each two adjacent AlNiCo magnets, their shape is trapezoidal and they are filled by either nonmagnetic material or air. All these additions in the rotor are to reduce the magnetic leakage and narrow the magnetic circuit as much as possible. Therefore, this machine is designed to prevent demagnetization of NdFeB magnets even under extreme operation conditions. The length of these magnets has to be chosen carefully to avoid being demagnetized by the NdFeB magnet flux. The demagnetization and re-magnetization of AlNiCo magnets provide flux weakening and strengthening capability [123, 124]. Fig. 1.26 shows the interior composite rotor machine.

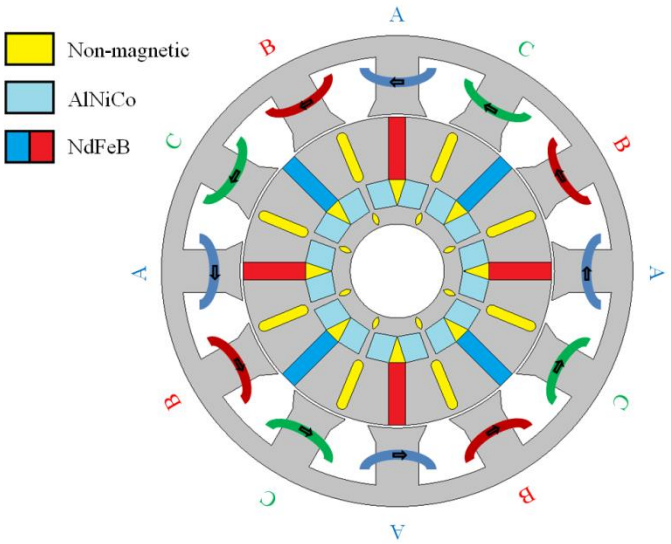

Fig. 1.26 Memory machine with interior composite rotor.

1.6.3.1.4. Flux mnemonic machine

The structure of this machine is based on the doubly salient machine, it consists of external salient rotor and internal stator contains the armature winding on the surface side and both permanent magnets and the DC excitation winding on the inner part, Fig. 1.27. The advantages of this machine are the simple rotor structure with no windings or magnets and the stator inner part is used by the magnets and the DC excitation windings. Unlike other memory motors the exceptional feature in this machine is using DC excitation pulses to magnetize and demagnetize the PMs instead of d-axis flux [125, 126].

This machine works in three different modes. First mode is the doubly salient operation in which the magnets are fully magnetized when the armature current applied, the electromagnetic torque produced by the permanent magnets only. Secondly the mixed mode between doubly salient and switched reluctance mode, the magnets are partially demagnetized hence the magnet torque reduces while the reluctance torque becomes significant. The torque of the machine in the second mode is a product of PM and reluctance torque combination. Finally, the switched reluctance operation mode, the magnets are fully demagnetized therefore no PM flux in the motor and the machine works as reluctance machine [127].

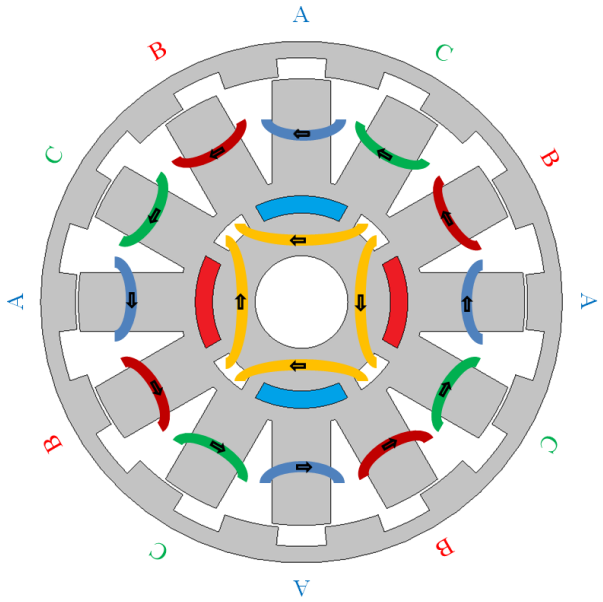

Fig. 1.27 Mnemonic machine.

Table 1.9 Comparison of memory motors

	Pole changing	**Flux control**	**Composite**	**Mnemonic**
Manufacture cost	Medium	Medium	High	High
Mechanical structure	Medium	Complex	Complex	Complex
Magnetic saturation	-	-	-	-
Airgap flux density	-	-	High	High
End winding length	Low	Low	Low	Medium
Torque density	Medium	-	-	High
Magnet usage	High	Medium	High	Medium
Copper usage	Medium	Medium	Medium	High
Flux Strengthening	High	-	High	High
Flux weakening	High	-	Medium	Medium

1.6.3.2. Winding adjustment machines

A new method using simple electronic switching circuit for high speed operation is proposed. Fig. 1.28 (a) presents the double winding set machine in which two sets of armature winding both are 3 phases, i.e. dual 3-phase, are used. In order to achieve high torque when the machine is operating under constant torque region, both phase sets are utilized. Moreover, to achieve flux weakening capability one winding set is shut down, therefore the number of turns per coil reduces which leads to lower PM flux linkage and therefore higher flux weakening capability [128, 129].

Another winding adjustment topology proposed in [130, 131] is the mixed pole machine. This machine consists of two different stator winding sets hence two different stator pole pairs can be used, Fig. 1.28 (b). Therefore, by switching between the winding sets during the operation the stator/rotor pole combinations change and consequently the PM flux linkage. On the other hand, in both winding adjustment machines the flux weakening mode can also be achieved by supplying one winding set with variable voltage and/or frequency.

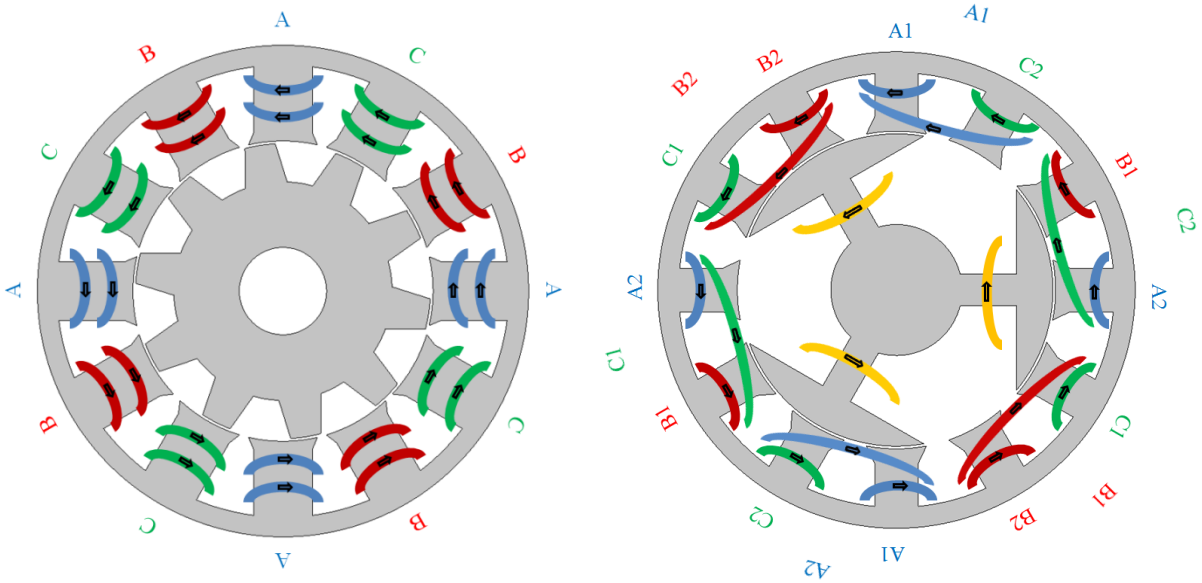

(a) Double winding set machine (b) Mixed pole machine

Fig. 1.28 Winding adjustment machine topologies.

Table 1.10 Comparison of different winding adjustment machines

	Double winding set	**Mixed pole**
Manufacture cost	Medium	High
Mechanical structure	Medium	Medium
Magnetic saturation	Medium	High
Airgap flux density	-	-
End winding length	Low	High
Torque density	-	-
Magnet usage	None	None
Copper usage	Medium	High
Flux strengthening	None	None
Flux weakening	High	Medium

1.7. Research Scope and Contributions of Thesis

1.7.1. Scope of research

The review presented in the previous sections of this chapter has mainly covered different topologies of SFPM and VFPM machines. However, this thesis explores and compares different types of SFPM and VF methods. For easy understanding, Fig. 1.29 illustrates the reviewed structure and the selected SFPM machines and variable flux methods to be investigated further in this thesis as well as the research methodologies. Less magnet machines, i.e. multi-tooth, E-core and C-core as well as the conventional SFPM machine with different stator/rotor poles combinations, i.e. 12/10, 12/13 and 12/14, are selected due to the different number of PMs and rotor poles. Whereas, the variable flux method consists of using

iron bars described in section 1.5.2 is selected since no alternation to the original machine is required and it is easy to be applied to any SFPM machine. The selection criteria are shown in Table 1.10. A summary of each chapter is shown here.

Table 1.11 Selection criteria of SFPM and VFPM machines

Less Magnet Usage SFPM Machines	Conventional SFPM Machines	Linear Bars Mechanical Adjustment
• Less PM usage • High torque and torque density • Flexible for applying external components	• Different rotor pole numbers • High torque and torque density • Flexible for applying external components	• Applicable for any fully designed SFPM machine • It can be adjusted radially, axially or circumferentially • Able to weaken the machines flux at different levels

Chapter 2

Using 2D-finite element analysis (FEA), the electromagnetic performances with emphasis on the torque-speed characteristics of the six selected SFPM machines are analysed and compared. Particular comparison is made regarding the torque per magnet ratio and the influence of high electric loading on the output torque performance. Experimental validation of the FEA results is provided.

Chapter 3

The influence of the end-effect on the torque-speed characteristics of the six analysed SFPM machines is investigated. The full model of each SFPM machine including the third dimension and full coil windings is designed and analysed using 3D-FEA. However, to obtain the influence of the end-effect on the torque-speed characteristics, the 2D- and 3D-FEA predicted PM flux-linkage and the d- and q-axis inductances are investigated and compared. Moreover, the predicted results are experimentally validated.

Chapter 4

Mechanical variable flux method consists of using ferromagnetic pieces, i.e. flux adjusters, is introduced and applied to the six SFPM machines. The influence of such method on the open circuit results, electromagnetic performance and torque-speed characteristics is investigated and compared with that of the original machines, i.e. without flux adjusters. Prototypes of the machines with flux adjusters are tested to validate the FEA results.

Chapter 5

In chapter 5, a modification of the mechanical variable flux method presented in chapter 4 is proposed by employing alternate pole flux adjusters. A comparison study of the electromagnetic performance of the three SFPM machines with different stator/rotor pole combinations, i.e. 12/10, 12/13 and 12/14, equipped with the modified variable flux method is presented and a prototype machine is tested.

Chapter 6

A novel SFPM machine topology with high magnetic utilization due to the use radial and circumferential PM sets is proposed. External and internal rotor configurations are designed and optimized. A comparison between the proposed topology and conventional SFPM machine with the same overall size and stator/rotor pole combination is presented, including electromagnetic performance, torque-speed characteristics, losses and efficiency. Moreover, this topology can be introduced as mechanical variable flux machine.

Chapter 7

A comparative study of the SFPM machine with mechanical adjuster, backside DC excitation hybrid excitation SFPM machine (reviewed in section 1.5.1.1) and the proposed topology in chapter 6 is presented. In addition to the electromagnetic performance and torque-speed characteristics, the flux weakening capability, the required power for switching between flux strengthening and weakening states and demagnetization withstand capability are compared.

1.7.2. Contribution of thesis

The contributions of this thesis can be summarised as:

- Comparative study of six different SFPM machines has illustrated the differences in their torque/power speed characteristics and defined the suitable applications in which they may be used.
- A mechanical variable flux technique is proposed by employing all pole flux adjusters.
- A modified mechanical variable flux technique by employing alternate pole flux adjusters is proposed in which the mechanical components can be reduced to half.
- A novel SFPM machine topology with radial and circumferential permanent magnet sets is proposed offering high PM utilization and variable flux ability.

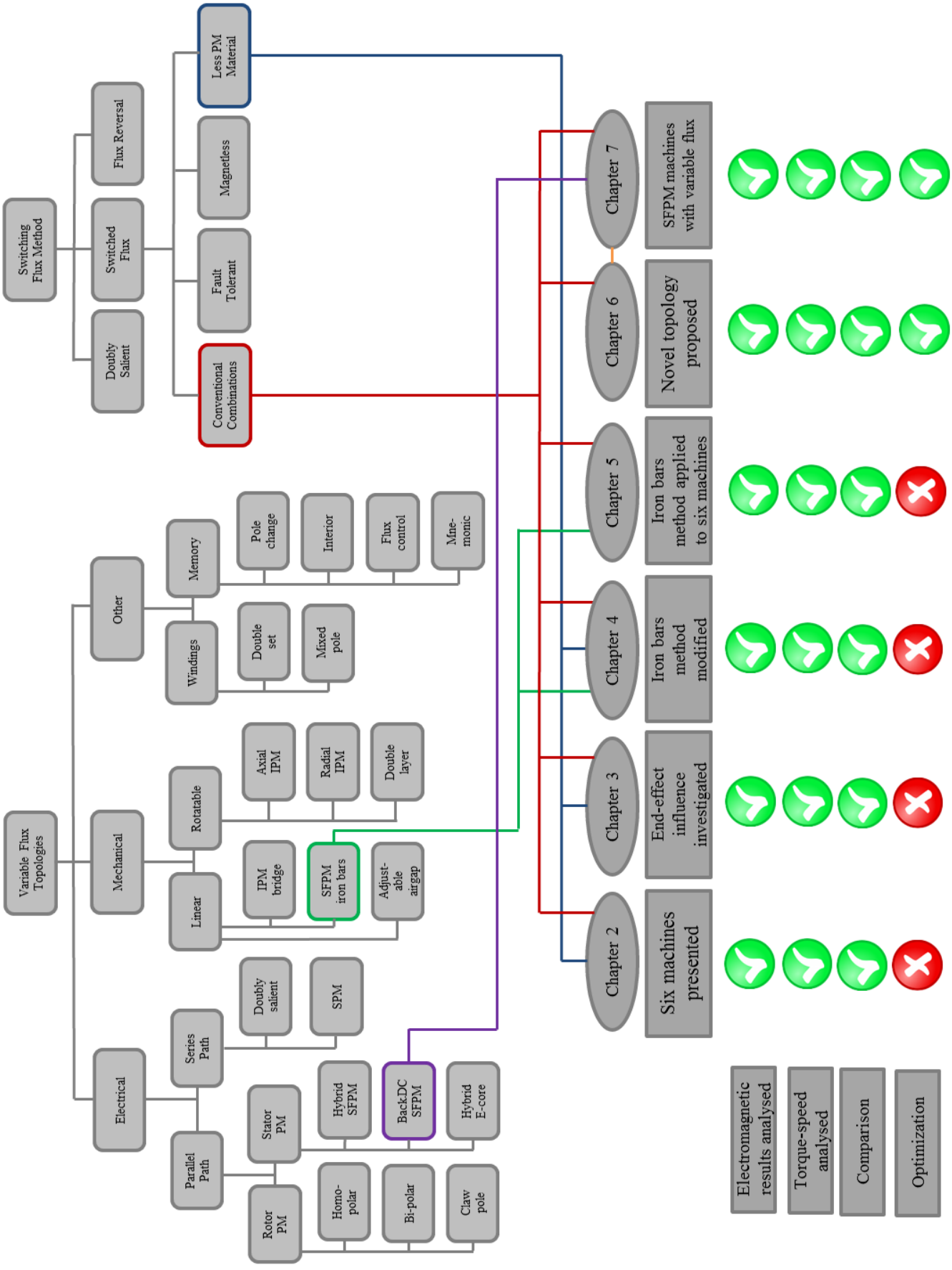

Fig. 1.29 Research methods and arrangement of chapters.

2. Comparative Study of the Electromagnetic Performance of Different SFPM Machines

2.1. Introduction

Several stator/rotor pole combinations for SFPM machine are proposed in [10, 132]. In [10], it is shown that the optimal stator/rotor pole combination for maximum torque is 12/13. However, an odd number of rotor poles resulting in significant unbalanced magnetic force, which causes high acoustic noise and vibration. Therefore, even number of rotor poles is preferred since they compromise between high torque and low unbalanced magnetic force.

Furthermore, as mentioned previously, due to high cost of rare earth magnet material, ferrite magnets may be employed [60], while part or all of the PMs can be replaced by DC excitation as proposed in [61, 133]. However, such options cause reduction in the machine performance, i.e. torque density and efficiency. Alternatively, multi-tooth, C-core, and E-core SFPM machine topologies are designed using half of the PMs employed by the conventional SFPM machine but without sacrificing the torque density [54, 56, 134].

In this chapter, the open circuit results, electromagnetic torque performance and torque-speed characteristics of different SFPM machines are investigated, compared and validated both theoretically and experimentally. The comparison includes the influence of the rotor pole number by comparing three conventional machines with different stator/rotor pole combinations, i.e. 12/10, 12/13 and 12/14, as well as three novel machine topologies with low PM material usage, i.e. multi-tooth, E-core and C-core SFPM machines. The results are predicated and investigated using 2D-finite element analysis (FEA) and analytical methods. Finally, prototypes are constructed and measurements of open circuit, electromagnetic torque and torque-speed curves are performed in order to verify the analyses.

2.2. Topologies of SFPM Machines

In Fig. 2.1 (a)-(c), the conventional SFPM machines are shown, in which the same stator is employed but with different rotor pole numbers, i.e. 12/10, 12/13 and 12/14. The cross-sections of multi-tooth, E-core and C-core SFPM machines are shown in Fig. 2.1 (d)-(f), respectively. The six machines have the same outer diameter, airgap and active length, their

design parameters are illustrated in Table 2.1. The number of turns per phase is 72 with a packing factor of 0.4 in all the machines except for the C-core machine, which has 84 turns per phase since all these machines are optimized at the same copper loss and phase current [27, 54, 55, 58]. The winding configuration of SFPM machines depends on the number of rotor poles and the orientation of the PMs. Therefore, in conventional machines with different stator/rotor pole combinations, the winding configuration of the 12/13 is considerably different from the 12/10 and 12/14 SFPM machines due to the odd rotor pole number (see appendix A1). It should be mentioned that the optimum number of rotor poles is used in multi-tooth, E-core and C-core machines [54, 55, 57].

Table 2.1 Major design parameters of analysed SFPM machines.

Topologies	**Multi-tooth**	**E-core**	**C-core**
Number of rotor poles	19	11	13
Number of stator poles	6	6	6
Rotor outer radius(mm)	27	29.25	29.25
Rotor pole width(mm)	3.5	5.3	4.7
Rotor pole height(mm)	5	7.6	7.6
Stator outer radius(mm)	45	45	45
Stator tooth thickness(mm)	6	4.4	4.4
Stator back iron thickness(mm)	4.4	4.5	3.5
Magnet height(mm)	17	15.2	15.2
Magnet width(mm)	3.6	4.4	4.4
Total slot area(mm^2)	212	103	280
Rotor pole width(mm)	3.5	5.3	4.7
Axial length(mm)	25	25	25
Airgap length (mm)	0.5	0.5	0.5
Number of turns per phase	72	72	84
Magnets remanence (T)	1.2	1.2	1.2
Conventional combinations	**12/10**	**12/13**	**12/14**
Number of rotor poles	10	13	14
Number of stator poles	12	12	12
Rotor outer radius(mm)	27	27	27
Rotor pole width(mm)	5.6	4.2	3.8
Rotor pole height(mm)	7	7	7
Stator outer radius(mm)	45	45	45
Stator tooth thickness(mm)	3.6	3.6	3.6
Stator back iron thickness(mm)	3.6	3.6	3.6
Magnet height(mm)	17.5	17.5	17.5
Magnet width(mm)	3.6	3.6	3.6
Total slot area(mm^2)	100	100	100
Rotor pole width(mm)	5.6	4.2	3.8

Axial length(mm)	25	25	25
Airgap length (mm)	0.5	0.5	0.5
Number of turns per phase	72	72	72
Magnets remanence (T)	1.2	1.2	1.2

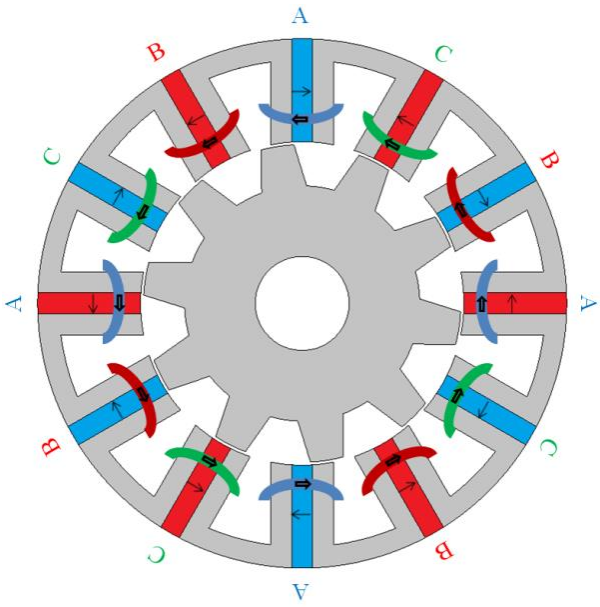

(a) 12/10 stator/rotor combination machine

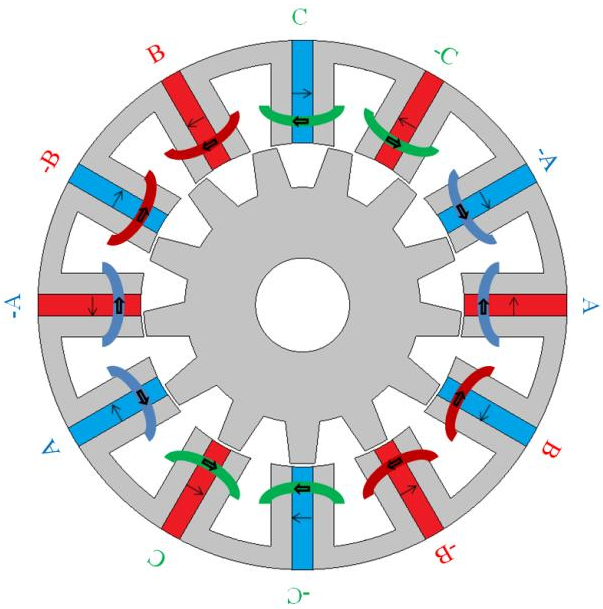

(b) 12/13 stator/rotor combination machine

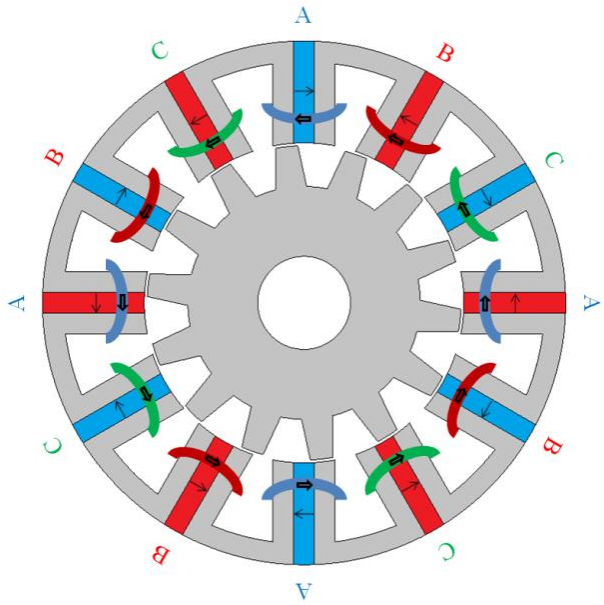

(c) 12/14 stator/rotor combination machine

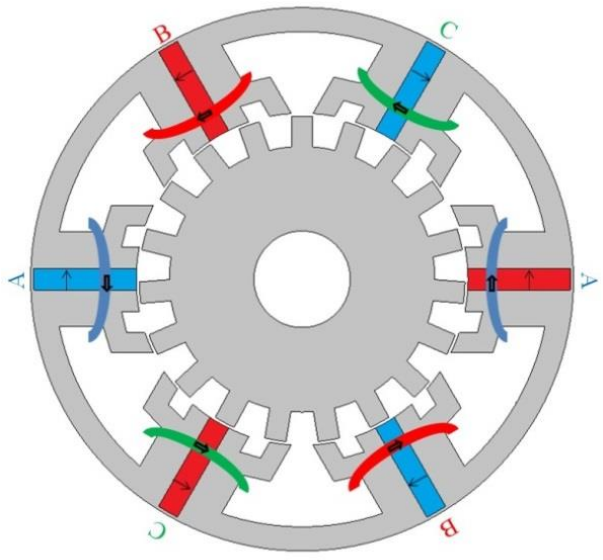

(d) Multi-tooth topology

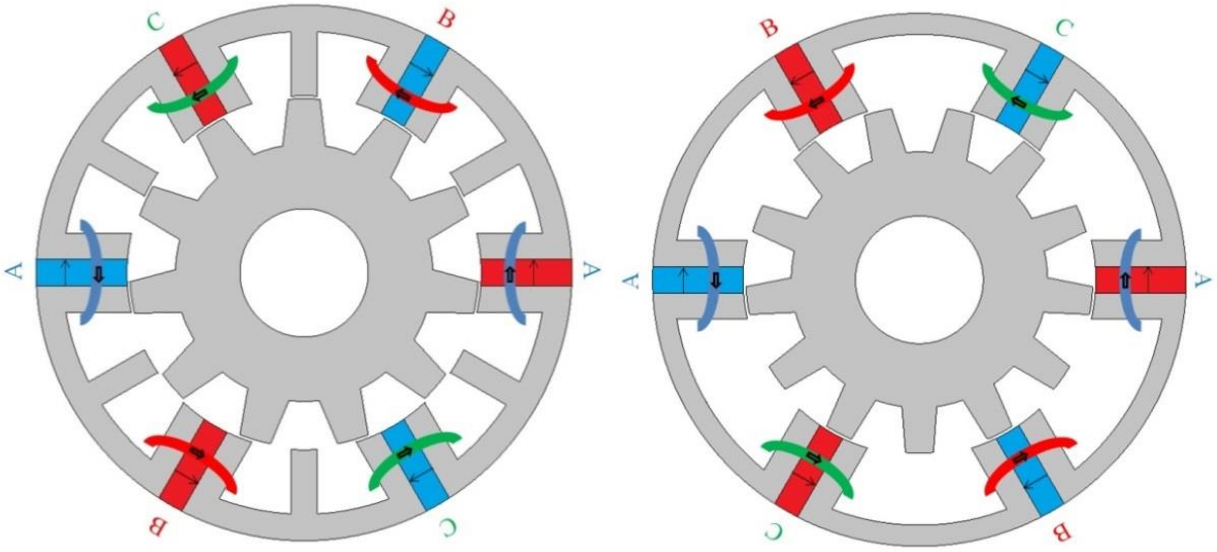

(e) E-core topology (f) C-core topology

Fig. 2.1 Different SFPM machine topologies.

2.3. Comparison of SFPM Machine Performance

2.3.1. Open circuit

Fig. 2.2 presents the equipotential and flux density distributions of the six studied SFPM machines, predicted under open circuit condition with rotor locked at d-axis position.

The airgap flux density distribution waveforms of the conventional SFPM machines with different stator/rotor pole combinations, i.e. 12/10, 12/13 and 12/14, and multi-tooth, E-core, and C-core SFPM machines, are shown in Fig. 2.3 (a). It demonstrates that a similar peak value of airgap flux density of around 2T is observed in the six machines due to the flux focusing effect.

The PM flux linkage waveforms of the conventional machines and multi-tooth, E-core and C-core machines are presented in Fig. 2.3 (b). It can be seen that the 12/10 machine has the highest peak flux linkage among the conventional SFPM machines followed by 12/13 and 12/14, respectively. Since the three machines have the same stator and number of turns per phase, the flux-linkage is inversely proportional to the rotor pole number, due to flux-leakage. On the other hand, the E-core and C-core machines have similar peak value of flux-linkage, which is higher than that produced by the multi-tooth machine, due to the higher number of

turns per phase in the C-core machine and the presence of the middle tooth in the E-core machine.

Since the winding factor of the 12/13 machine is higher than those in 12/10 and 12/14 machines due to the odd number of rotor poles [10], the back-EMF of 12/13 machine is the largest among the conventional combinations, Fig. 2.3 (c). Compared with the multi-tooth and the E-core machines, the C-core machine produces the highest back-EMF. Although the PM flux linkage of the multi-tooth is the lowest, higher back-EMF than the E-core machine is observed in the multi-tooth machine due to the high electrical frequency, Fig. 2.3 (c). Furthermore, it can be seen that the harmonics are relatively small in the three conventional SFPM machines except 12/13 machine, which has a significant 3rd harmonic due to the angular difference between the adjacent slot conductors [10], Fig. 2.3 (d). Since the 5th and 7th harmonics in the three conventional SFPM machines are small, the torque ripples at low current levels are mainly produced by the cogging torque. E-core and C-core machines produce significant 7th harmonic, this causes distortion in the back-EMF waveform and therefore ripples in the electromagnetic torque, Fig. 2.3 (d).

The cogging torque waveforms of the six SFPM machines are shown in Fig. 2.3 (e). It shows that the E-core and 12/10 machines exhibit the largest cogging torque, which is about 0.2Nm, followed by the C-core and 12/14 machines. However, the lowest cogging torque is observed in the multi-tooth and the 12/13 machines. The cogging torque frequency is determined by the least common multiple (LCM) of the stator and rotor poles number. In the conventional combinations, the 12/13 machine has the lowest cogging torque due to the odd number of rotor poles. Moreover, the largest cogging torque is observed in 12/10 followed by 12/14, since the higher number of stator/rotor pole combination reduces the net distribution of the flux density and causes lower cogging torque. On the other hand, the multi-tooth machine has significantly low cogging torque due to the large number of rotor poles. Although the E-core and C-core machines have odd number of rotor pole, significant cogging torque is observed in those machines due to their large slot opening.

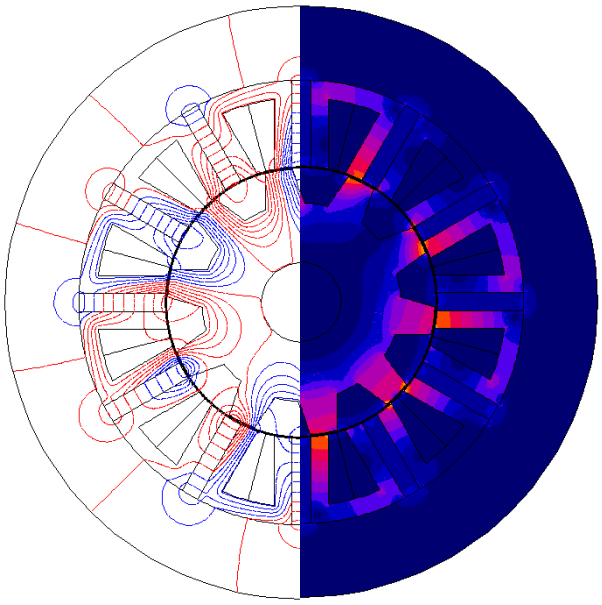

(a) 12/10 stator/rotor combination machine

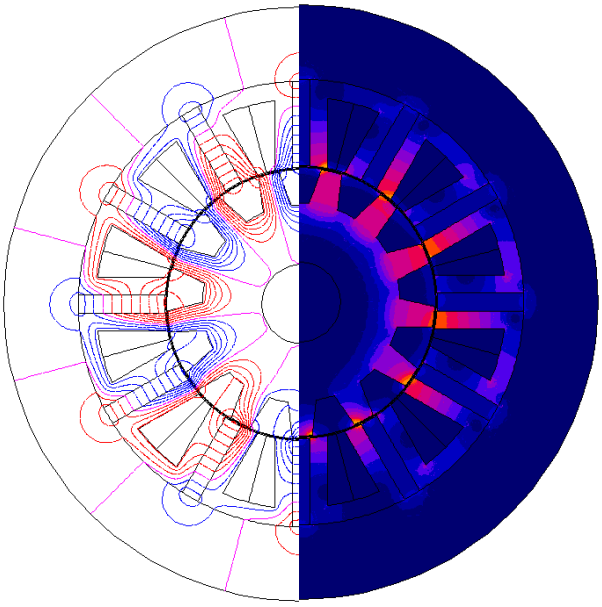

(b) 12/13 stator/rotor combination machine

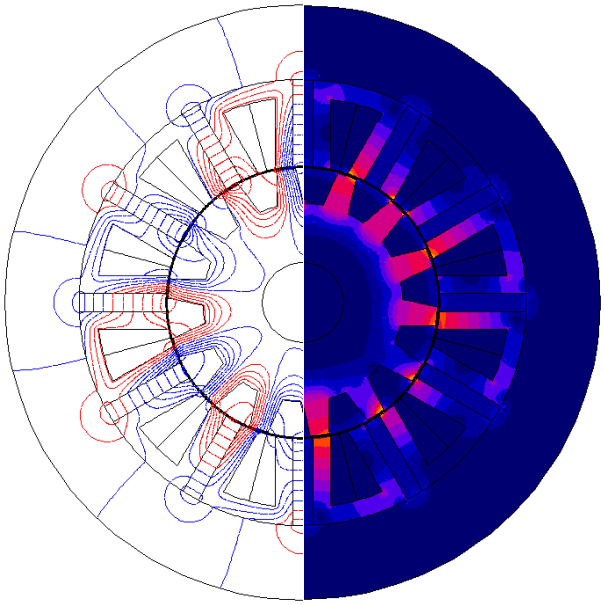

(c) 12/14 stator/rotor combination machine

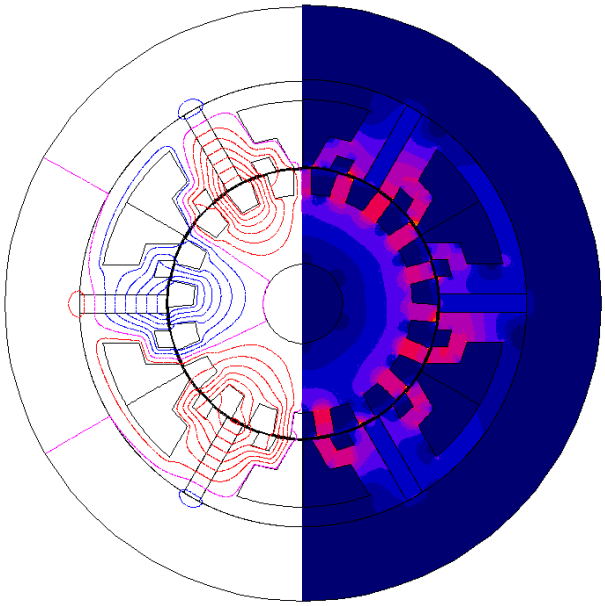

(d) Multi-tooth topology

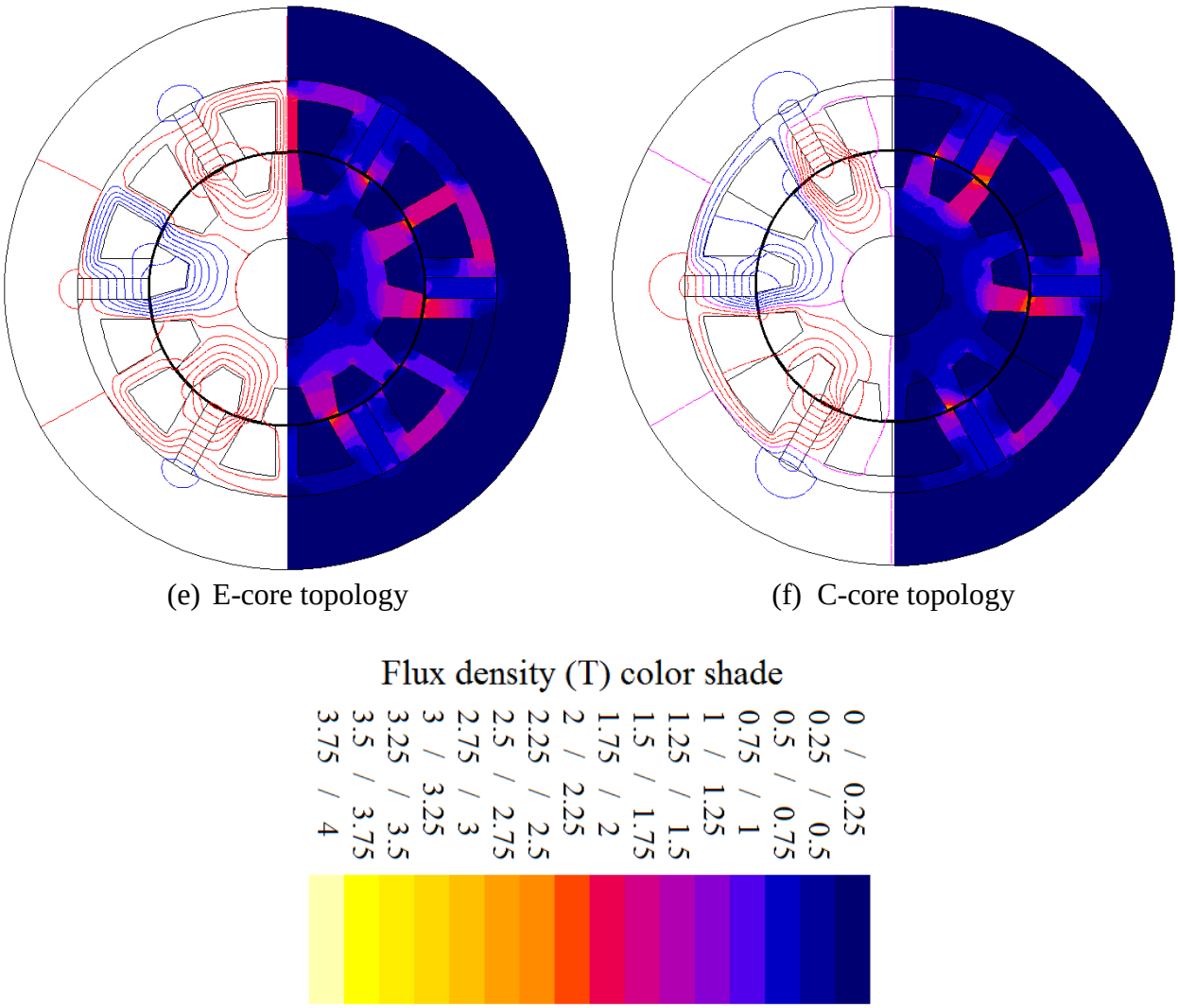

(e) E-core topology (f) C-core topology

Fig. 2.2 Open circuit equipotential and flux density distributions of SFPM machines.

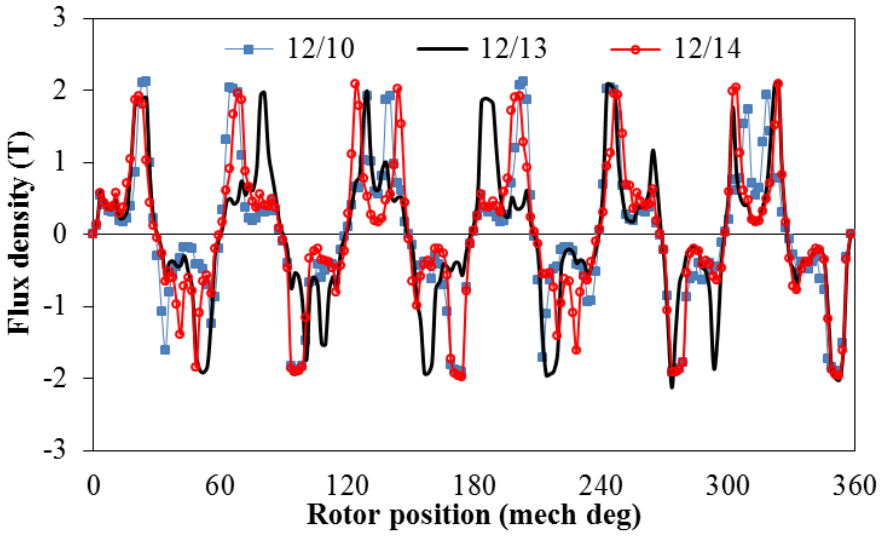

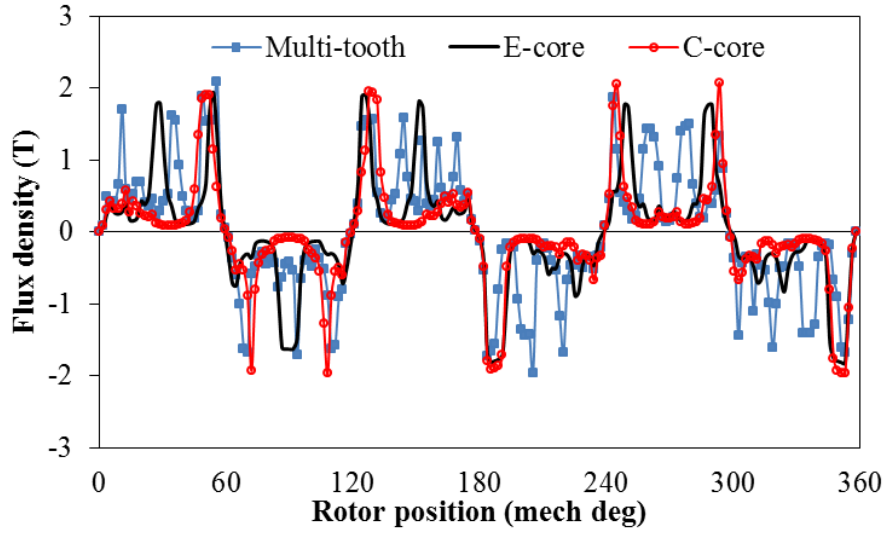

(a) Airgap flux density

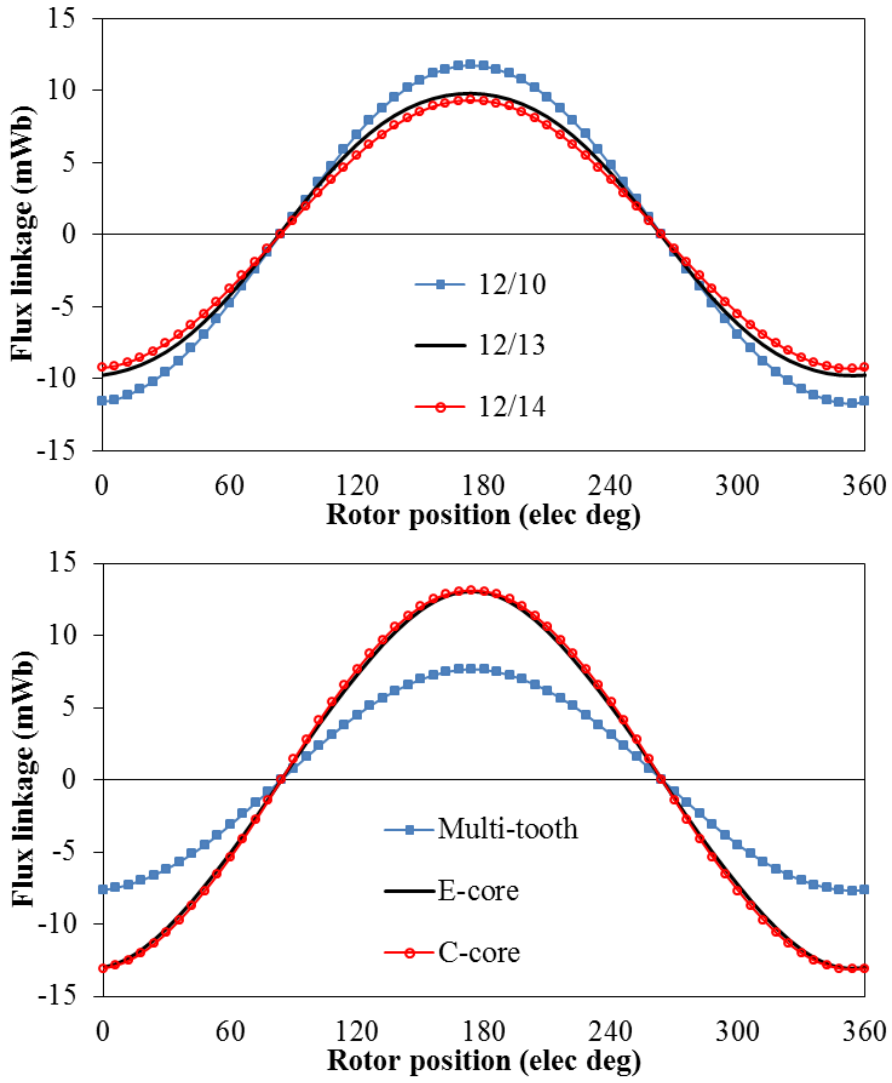

(b) Flux linkage waveforms

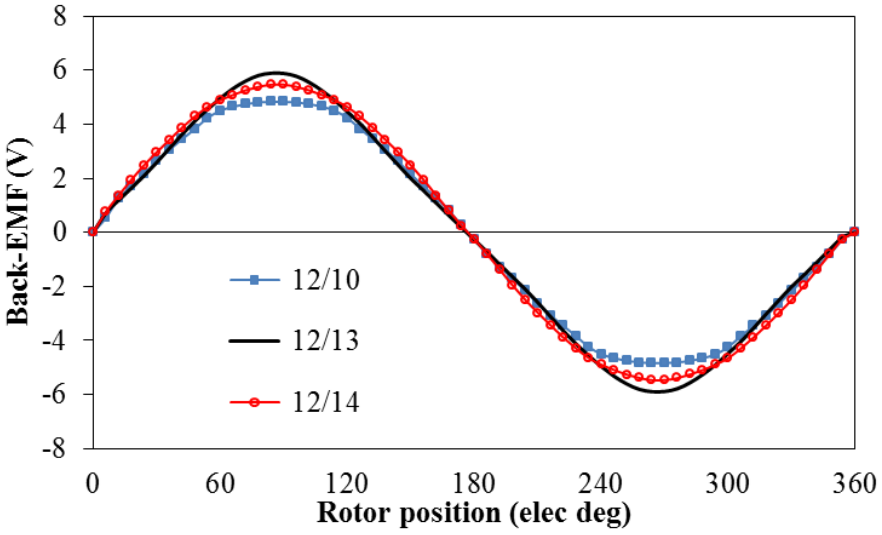

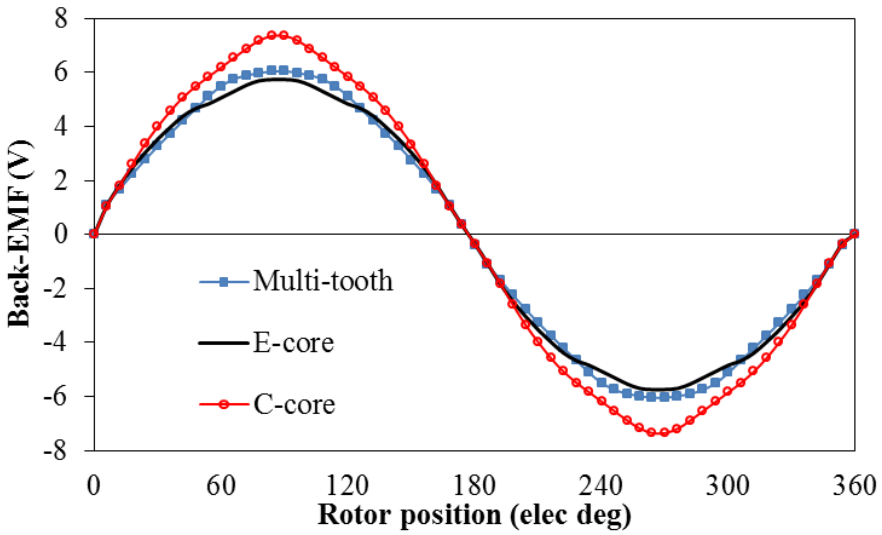

(c) Back-EMF waveforms at rotor speed (400rpm)

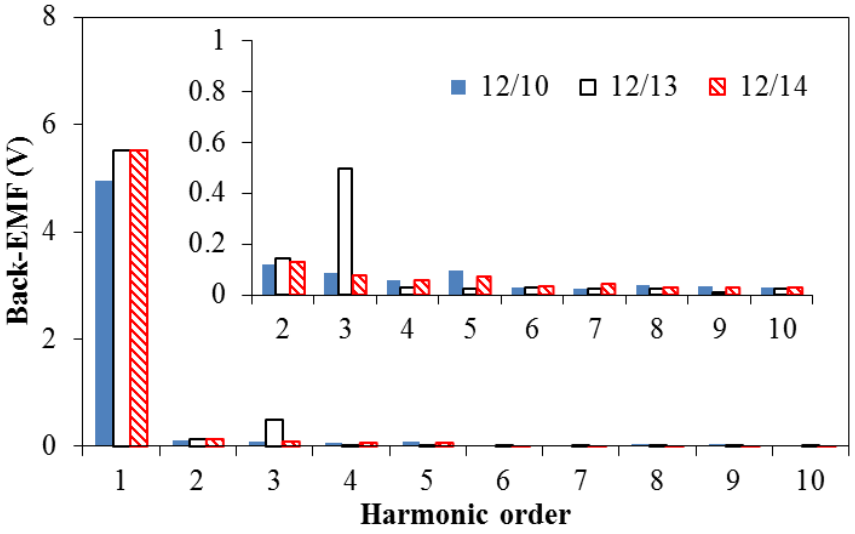

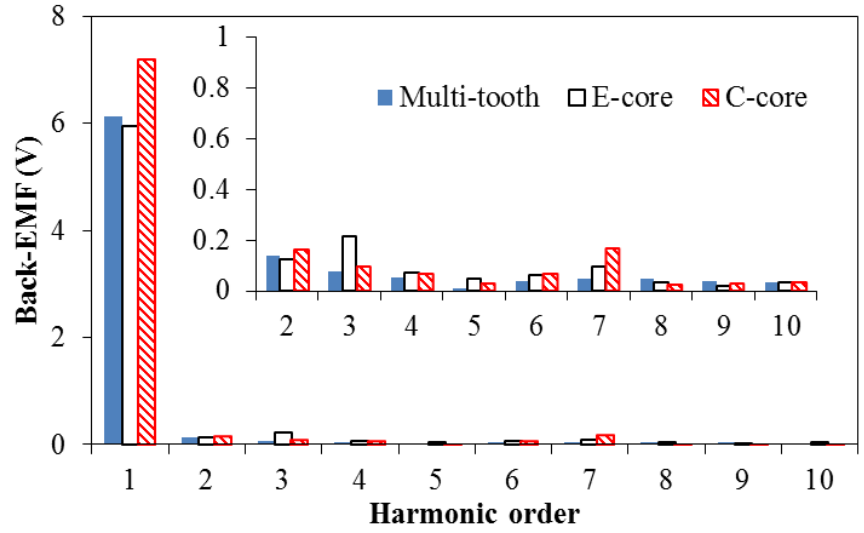

(d) Back-EMF harmonics

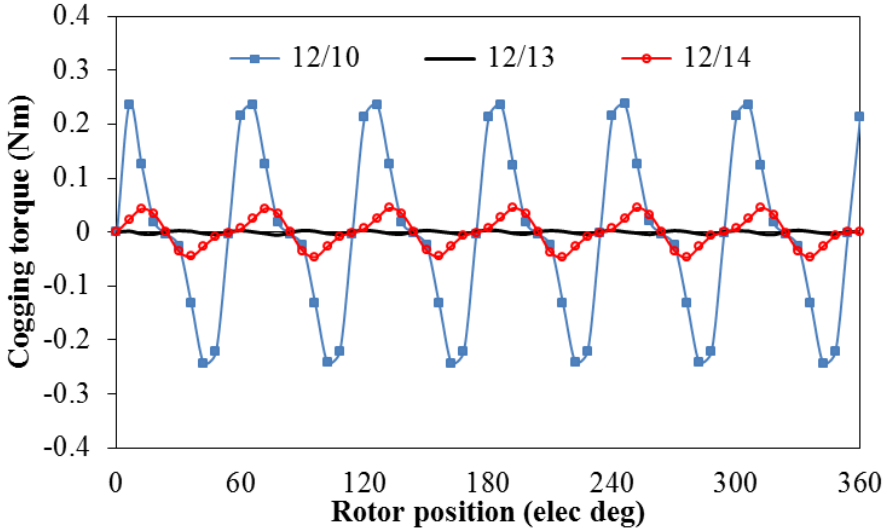

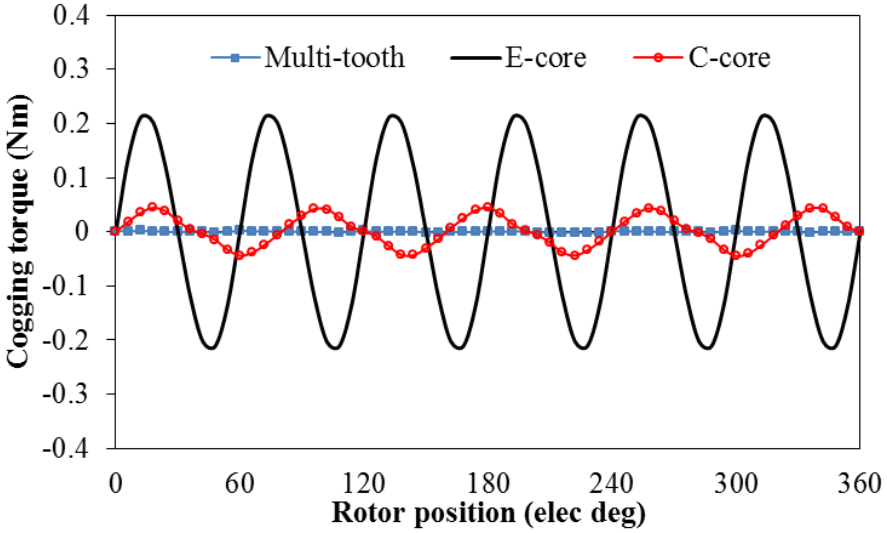

(e) Cogging torque waveforms

Fig. 2.3 Comparison of open circuit results of analysed SFPM machines.

2.3.2. Electromagnetic torque

The torque waveforms of the three conventional combinations and the multi-tooth, E-core, and C-core machines under load condition of I_d=0, I_q=15A, calculated by 2D-FEA are shown in Fig. 2.4 (a). It shows that the C-core machine produces the largest torque among the six machines, followed by the E-core machine, which has relatively large torque ripple. However, the multi-tooth and the 12/14 machines exhibit relatively large torque with small torque ripple, while 12/13 machine has small torque ripple compared with other machines. Table 2.2 summarizes the torque ripple and average torque of the six machines. Since the load condition with zero current angles, the torque equation of the SFPM machine can be presented in (1-7). Therefore, at same q-axis current the torque is proportional to the number of rotor poles and PM flux-linkage. However, although the rotor pole number of 12/13 machine is lower than that of 12/14 SFPM machine, similar torque is observed in 12/13 machine due to its relatively higher PM flux-linkage. On the other hand, the high number of rotor poles in the multi-tooth machine leads to high torque although it has the lowest PM flux-linkage.

Unlike conventional machines, the influence of magnetic saturation on the multi-tooth, E-core and C-core machines is relatively large due to the high electric loading per coil in those machines (Fig. 7 (c)). Due to its small stator teeth and small rotor pole width, the multi-tooth machine saturates at a relatively low current level compared to the other machines. Moreover, the C-core machine exhibits the highest torque at low current levels since a higher number of turns per phase is used. However, the magnetic circuit will be saturated at lower current level compared to the E-core machine due to thinner back-iron and absence of stator middle teeth.

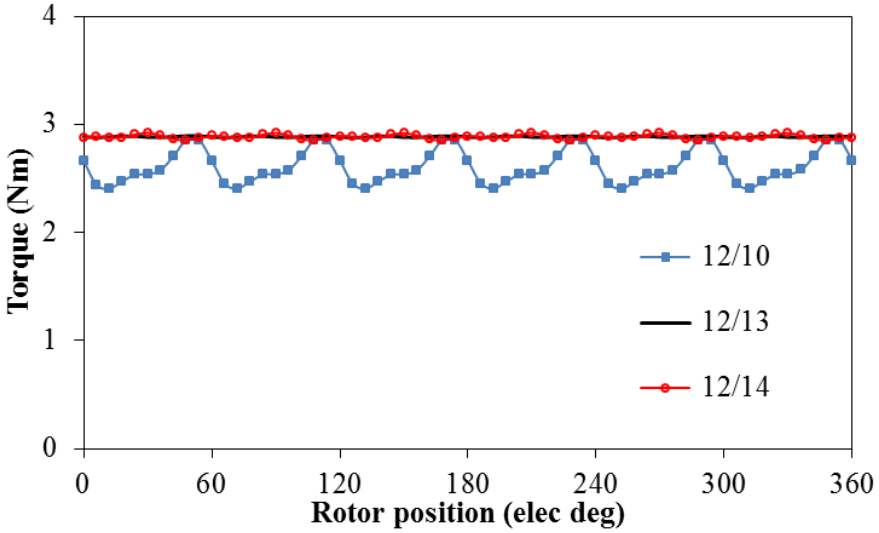

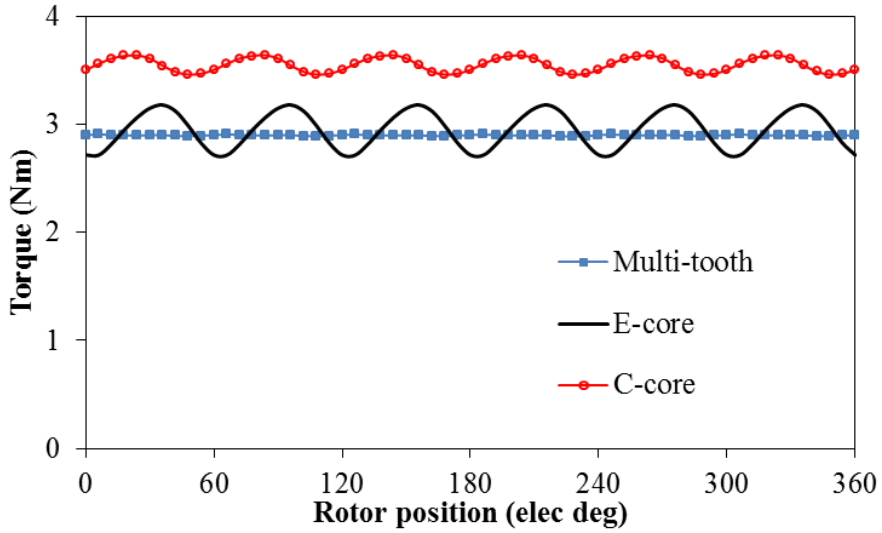

(a) Electromagnetic torque waveforms at load condition of 15A phase current (I_d=0, I_q=15A)

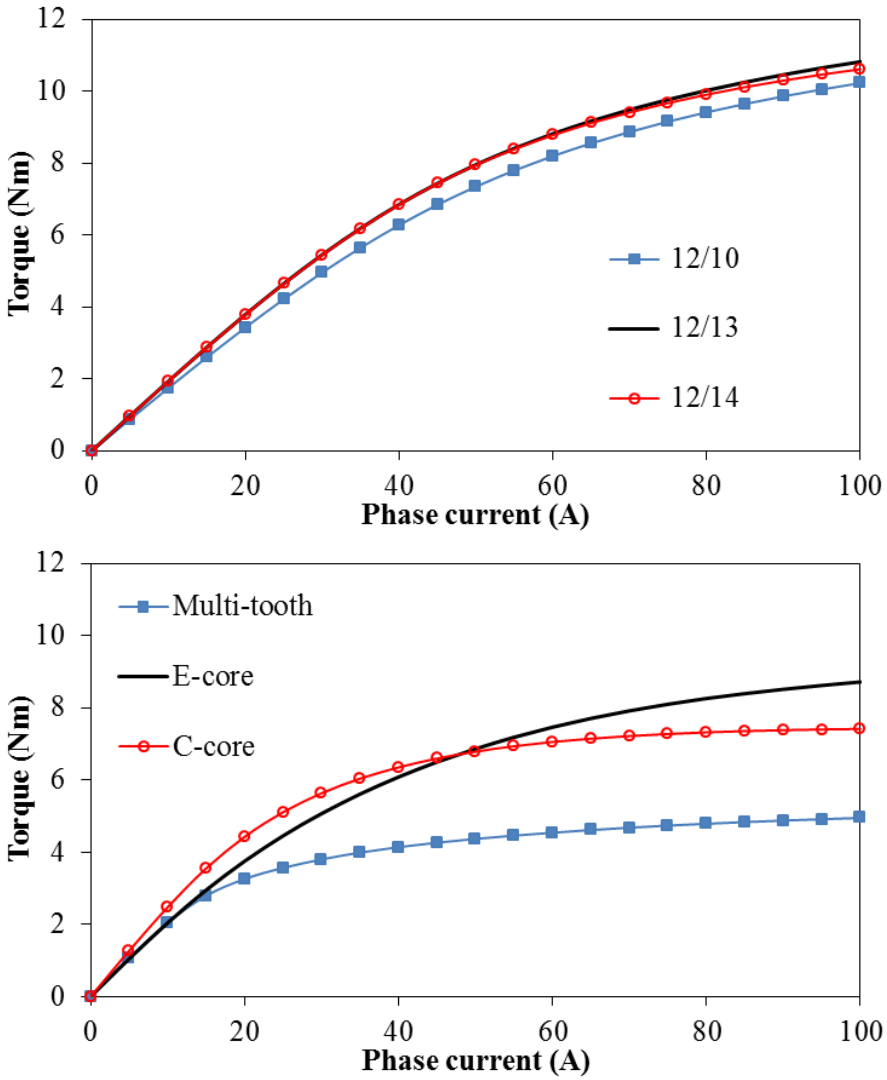

(b) Torque-current curves of six analysed SFPM machines

Fig. 2.4 Electromagnetic torque performance of alternate analysed SFPM machines.

Table 2.2 Torque ripple comparison of the six analysed SFPM machines (at rated current)

	12/10	**12/13**	**12/14**	**M-tooth**	**E-core**	**C-core**
Lower torque peak (Nm)	2.4	2.83	2.85	2.76	2.71	3.46
Higher torque peak (Nm)	2.85	3	2.92	2.8	3.17	3.63
Torque ripple %	15.67	5.61	2.26	1.46	14.6	4.89
Peak-peak torque (Nm)	5.26	5.83	5.77	5.57	5.89	7.09
Average torque (Nm)	2.6	2.92	2.88	2.79	2.94	3.54

2.3.3. Torque-speed characteristic

In general, the torque-speed characteristic of SFPM machines can be analytically predicted by (1-6) and (1-10). To predict the torque-speed characteristic of SFPM machines accounting for the magnetic saturation and cross-coupling, the method presented in [135] is used. Full accounting for magnetic saturation and cross-coupling can be obtained when d- and q- axis inductances are calculated at different d- and q-axis currents (see appendix A2).

Figs. 2.5 and 2.6 show the PM flux-linkage at different q-axis currents and the d- and q-axis inductances against d- and q-axis currents. It can be seen that in 12/10, 12/13 and 12/14 SFPM machines the influence of magnetic saturation and cross-coupling is relatively small. However, such effects are more visible in the multi-tooth machine, due to the multi-tooth structure and the high number of rotor poles, leading to higher flux density in the small stator teeth and rotor poles, as well as the largest inductance of the 6 machines. The influence of cross-coupling also occurs in all six of the analysed SFPM machines, being extremely high in the multi-tooth machine and relatively high in the E-core and C-core machines compared to the conventional machines, since higher magnetic saturation is observed in those machines. Moreover, the multi-tooth, E-core and C-core machines have much larger inductance values than the 12/10, 12/13 and 12/14 machines due to the larger number of turns per coil. On the other hand, the 12/13 machine exhibits the largest inductance among the conventional machines due to the winding connection, followed by the 12/14 machine. The d-axis inductance is slightly smaller than the q-axis inductance in the conventional, E-core and C-core machines, while similar values of d- and q-axis inductance are observed in the multi-tooth machine. Moreover, the influence of electric loading on the PM flux linkages of the multi-tooth, E-core and C-core machines are more significant.

The torque-speed characteristic of each machine is analytically calculated by employing the obtained inductances and PM flux linkage in equations (1-6) and (1-10). Figs. 2.7 and 2.8 present the torque and power-speed curves of the six analysed machines, respectively. The

flux weakening capability in the multi-tooth, E-core and C-core machines are much wider than those of the conventional combination SFPM machines. In general, the flux weakening factor K_{fw}, defined by (1-13), is employed in order to determine the flux weakening capability of SFPM machines.

Table 2.3 shows the flux weakening factor for all machines. In addition, the maximum values of the torque and power, and the base and maximum speeds are compared. A larger K_{fw} value indicates better flux weakening capability and if K_{fw} is equal to or larger than one, i.e. L_d multiplied by I_{max} is larger than Ψ_{pm}, then the operating speed of the machine is theoretically infinite, as in the multi-tooth and C-core SFPM machines. On the other hand, the conventional SFPM machines have relatively small inductances and low flux weakening capability. Furthermore, it can be seen that the higher the rotor pole numbers, the higher the flux weakening capability and the higher the maximum speed in the conventional machines, i.e. Ψ_{pm} is lower in the machine with higher rotor pole number.

As mentioned earlier, it is known that the higher the flux weakening factor, the better the flux weakening capability of the machines. As K_{fw} approaches unity, the best performance can be obtained from the machine. However, as K_{fw} increases above 1, two effects can be seen. Either the extremely large inductance leads to the maximum voltage being reached at lower speed or the low PM flux-linkage leads to low torque and power. Despite the fact that infinite maximum speed can be achieved, the small base speed leads to low power at extended constant power region. Therefore, both multi-tooth and C-core machines produce lower peak power compared to the other machines. It is also worth mentioning that the torque-speed curves are obtained at maximum phase current of 15A and DC-link voltage of 36V.

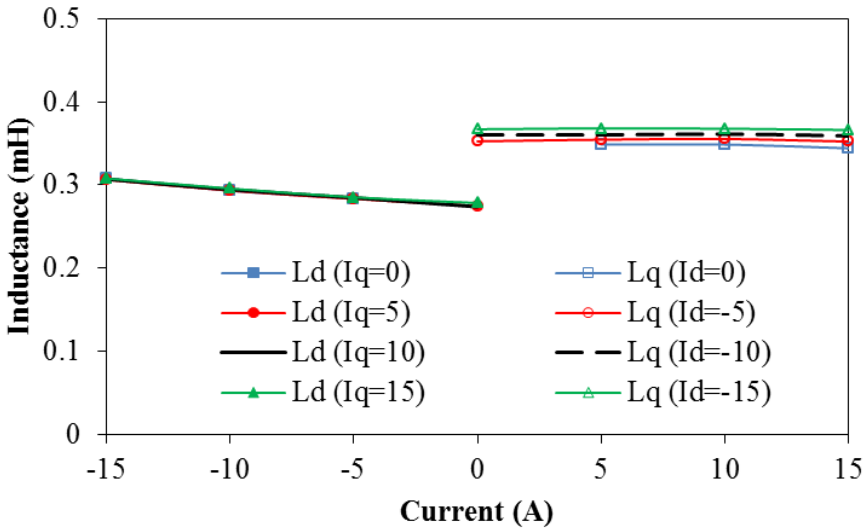

(a) 12/10 stator/rotor combination machine

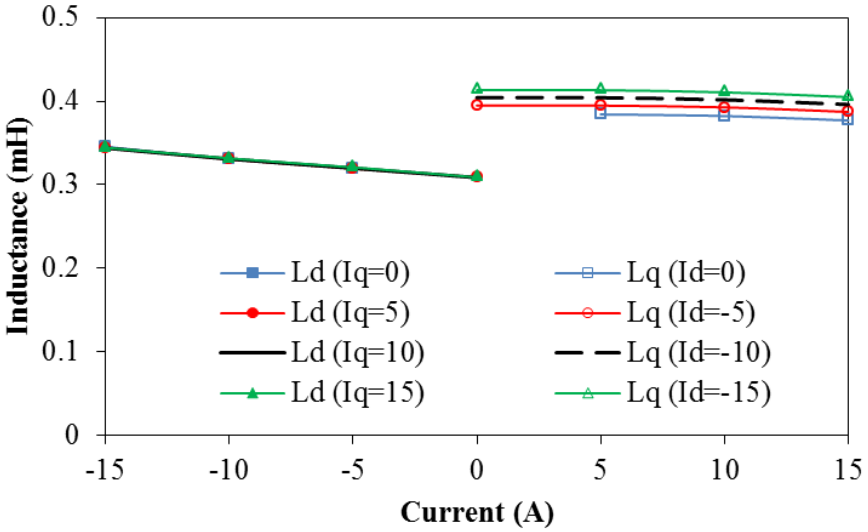

(b) 12/13 stator/rotor combination machine

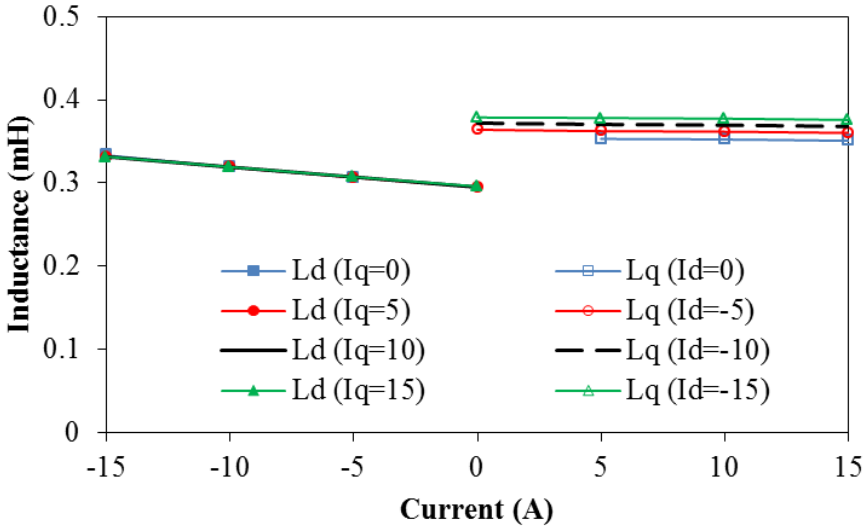

(c) 12/14 stator/rotor combination machine

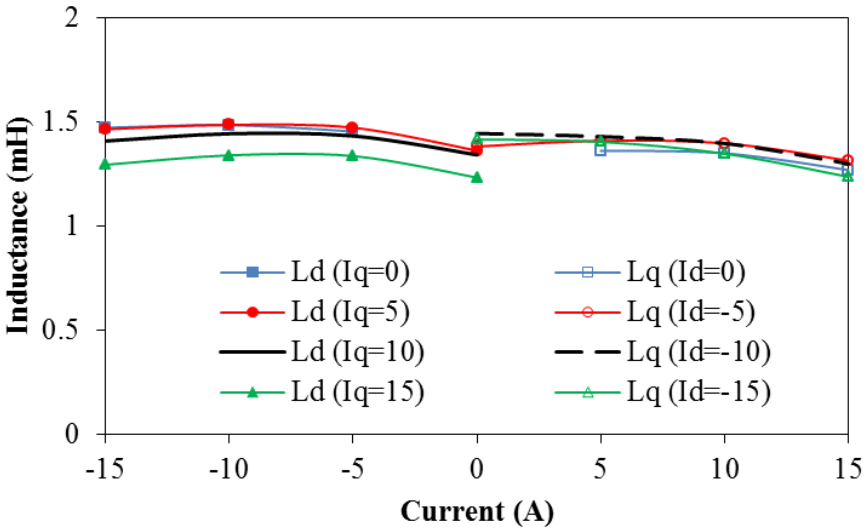

(d) Multi-tooth machine

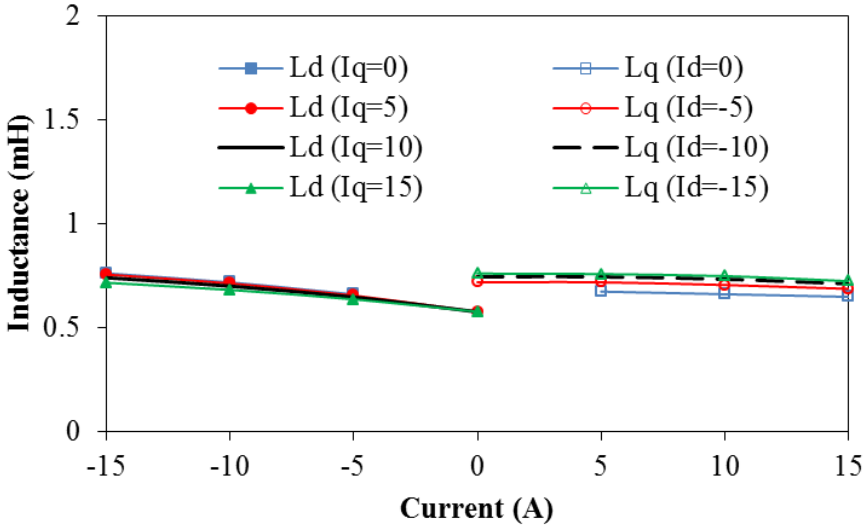

(e) E-core machine

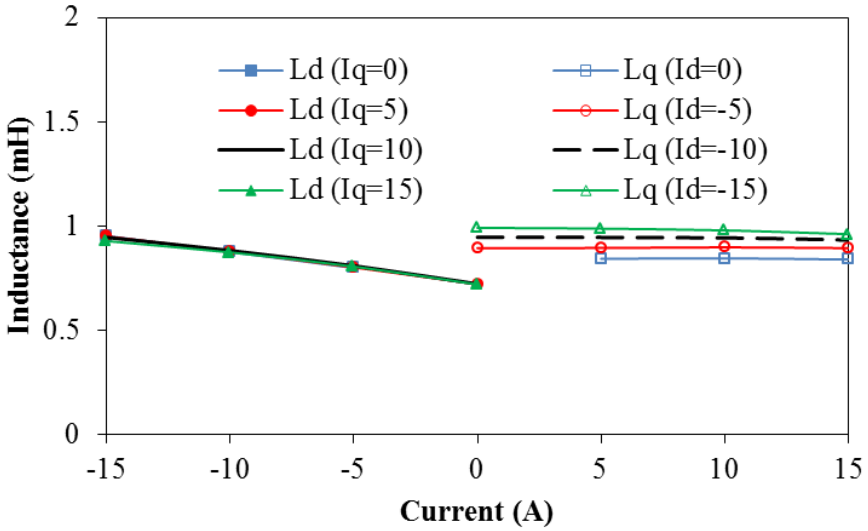

(f) C-core machine

Fig. 2.5 D- and q- axes inductances at different currents.

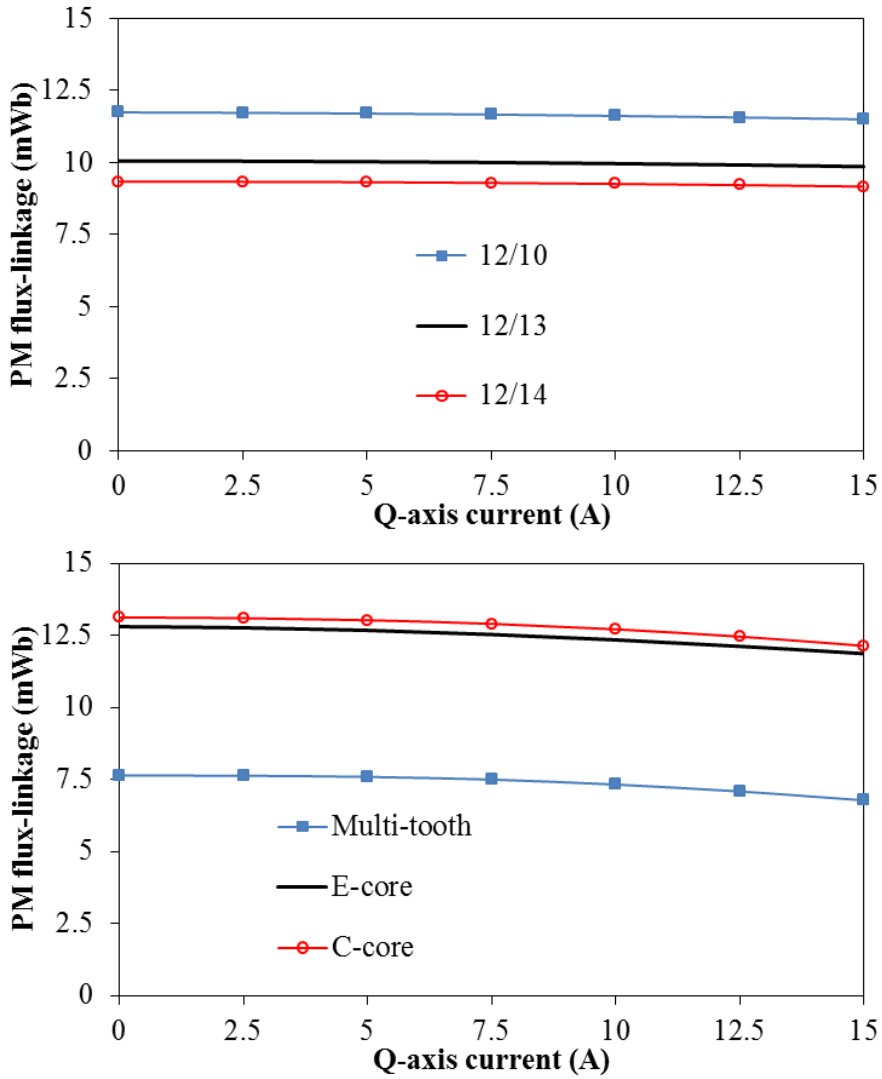

Fig. 2.6 PM flux linkage at different q-axis current.

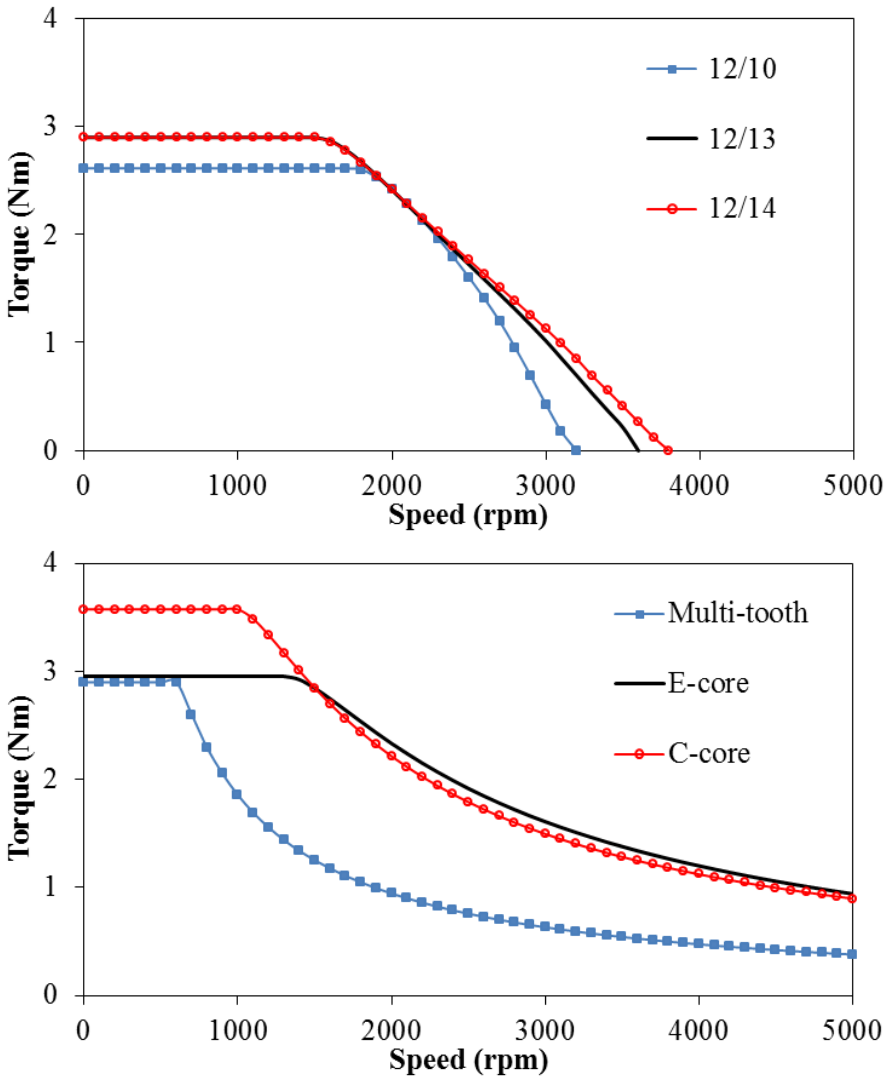

Fig. 2.7 Torque-speed curve of six analysed SFPM machines at load condition of (15A phase current, 36V DC-link voltage).

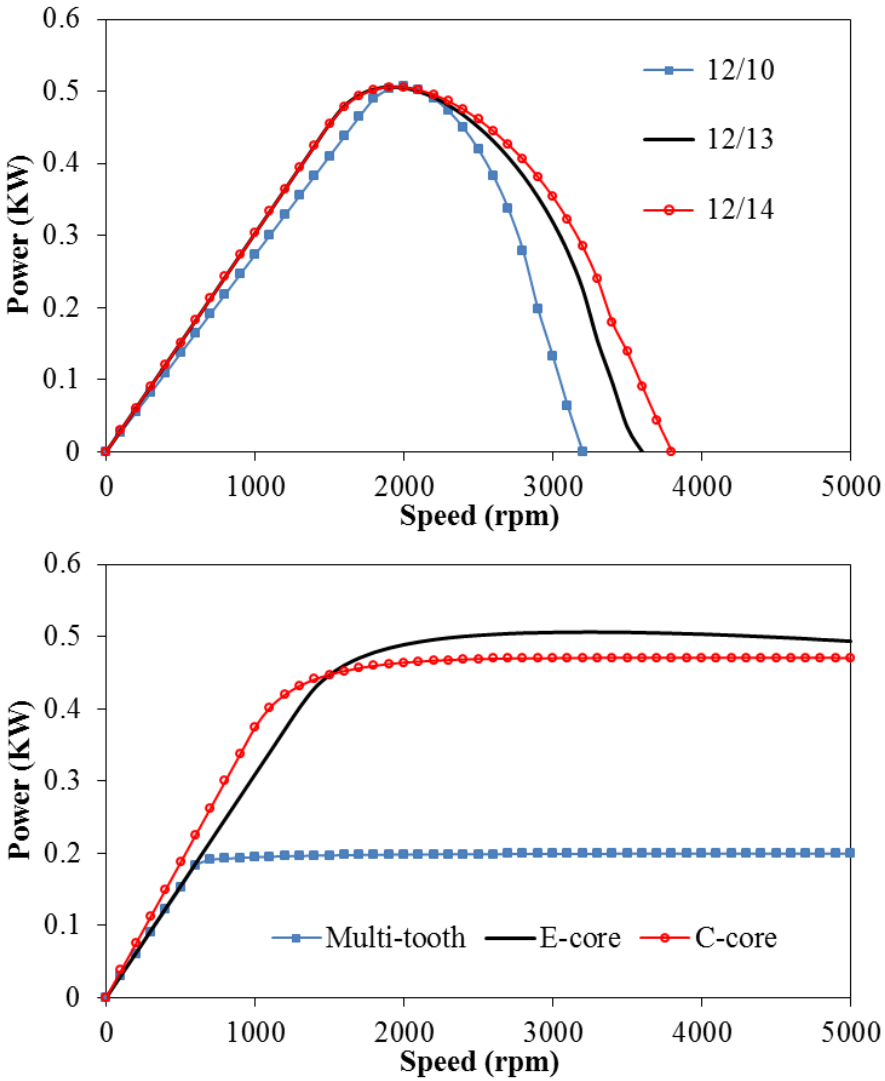

Fig. 2.8 Power-speed curves of different SFPM machines at load condition of (15A phase current, 36V DC-link voltage).

Table 2.3 Comparison of speed range, maximum torque and power, d-axis inductance, PM flux linkage and flux weakening factor of SFPM machines

Machines	Base speed (rpm)	Max. speed (rpm)	Max. torque (Nm)	Max. power (W)	L_d(mH)	Ψ_m(Wb)	K_{fw}
12/10	2,000	3,600	2.60	506	0.308	0.011751	0.39
12/13	1,500	4,900	2.98	506	0.346	0.010041	0.51
12/14	1,500	3,000	2.89	405	0.333	0.009332	0.53
Multi-tooth	700	∞	2.84	174	1.471	0.007593	2.90
E-core	1,500	16,000	2.95	506	0.761	0.012816	0.90
C-core	1,000	∞	3.55	385	0.953	0.013126	1.08

2.4. Comparison of Permanent Magnet Volume

Since the usage of PMs in the analysed SFPM machines is different, the average torque per magnet volume (T/M) ratio is compared. Table 3.4 shows the PM volume, average torque and T/M ratio of each machine at the rated phase current of 15A. The highest T/M is obtained in the C-core machine followed by the multi-tooth and the E-core machines. In the conventional SFPM machines, both 12/13 and 12/14 SFPM machines produce high T/M followed by the 12/10 SFPM machine. Fig. 2.9 presents the T/M against different current levels of the six machines. Compared to the conventional machines the multi-tooth has much higher T/M ratio at low current level, and similar ratio at high currents since a low volume of magnet material is used. Overall, the multi-tooth, E-core and C-core machines have larger T/M compared to the conventional machines.

Table 2.4 Torque per magnet volume ratio in SFPM machine (I_{ph}=15A)

Machines	12/10	12/13	12/14	M-tooth	E-core	C-core
Magnet volume (mm^3)	18900	18900	18900	9450	10200	10200
Average torque (Nm)	2.6	2.92	2.89	2.89	2.95	3.55
T/M volume (Nm/mm^3)	1.38	1.54	1.52	3.06	2.89	3.47
Torque density (Nm/mm^3)	1.63	1.83	1.81	1.81	1.85	2.22

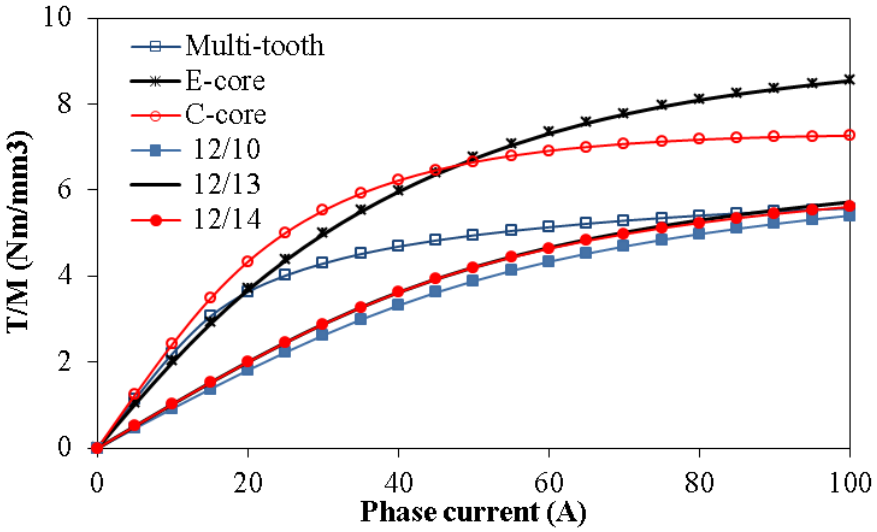

(a) Convetional SFPM machines

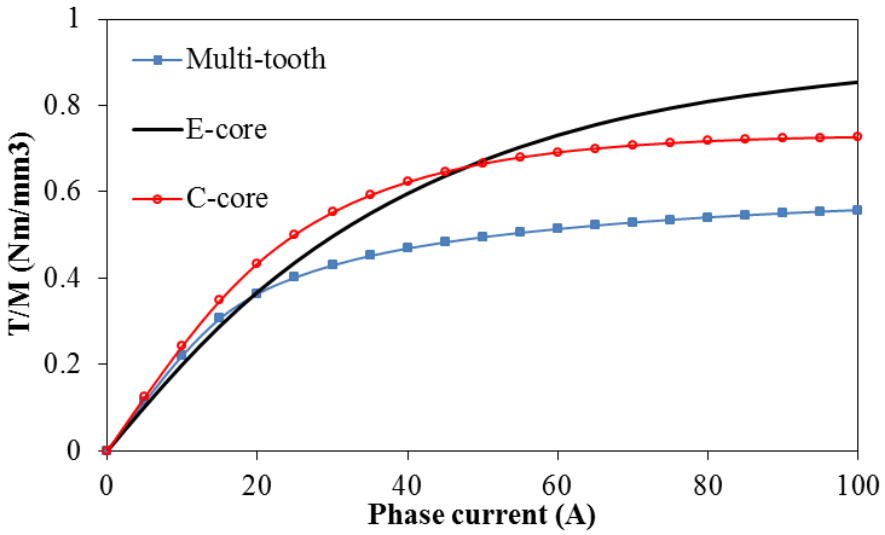

(b) Multi-tooth, E-core and C-core SFPM machines

Fig. 2.9 Torque per magnet volume ratio at different current levels of analysed SFPM machines.

2.5. Experimental Validation

Prototypes of the multi-tooth, E-core, C-core and conventional SFPM machines are constructed with the specification illustrated in Table 2.1. Fig 2.10 presents the prototypes of the SFPM machines and the dynamic testing rig.

Using an external DC motor, the back-EMF of the six machines is tested at rotor speed of 400rpm. Measured and predicted back-EMF waveforms are presented in Fig. 2.11. It can be seen that the measured back-EMF is lower than the predicted due to the large end-effect in the SFPM machines.

Moreover, the torque-current curves of the six machines are tested and presented together with their predicted counterpart in Fig. 2.12. Similar to the back-EMF due to the end-effect the measured results are lower than the predicted. However, by increasing the current level, the difference between the measured and predicted results increases. The reason is due to the manufacturing tolerance of the material and the influence of the temperature rise which is not accounted in the FEA calculations.

The torque-speed characteristics of the six SFPM machines are tested using flux weakening control under maximum current and DC-link voltage of I_{max}=7.5A (reduced due to the limitations of testing rig) and 36V, respectively, as shown in Fig. 2.11. During the

measurements, phase resistance, voltage drop, and dead time in the inverter are considered in the control algorithm [136].

Furthermore, it can be also seen that for all the machines the measured constant torque region is lower than the predicted due to the influence of end-effect. However, better flux weakening capability than that of the 2D-FEA in all machines except for the multi-tooth machine is observed. Therefore, the influence of end-effect on the torque-speed characteristics is investigated in the next chapter. It is worth mentioning the torque-speed curve measurements are carried on up to rotor speed of 1500rpm in all the analysed machines except multi-tooth machine where the maximum measured speed is 1000rpm limited by the high mechanical vibration due to the high frequency of this machine, Fig. 2.12.

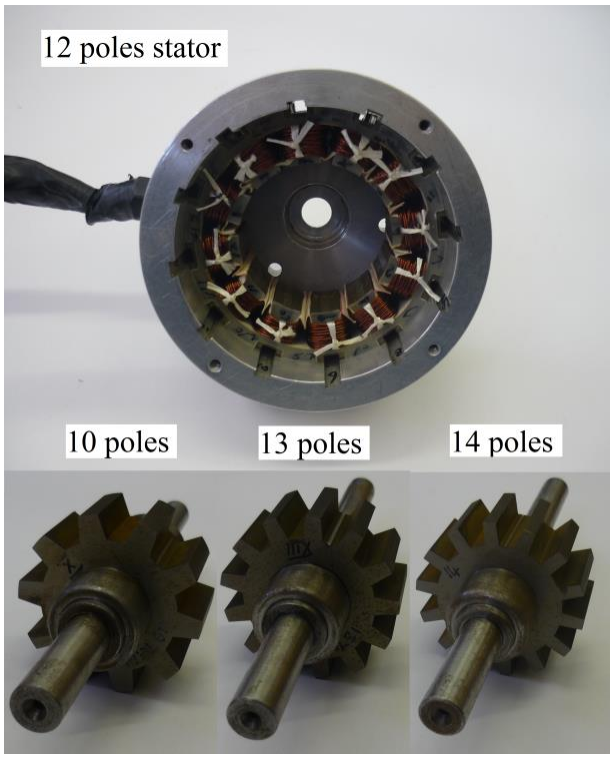

(a) Conventional 12 pole stator and 10, 13, and 14 poles rotors

(b) Multi-tooth stator and 19 pole rotor

(c) E-core stator and 11 pole rotor

(d) C-core stator and 13 pole rotor

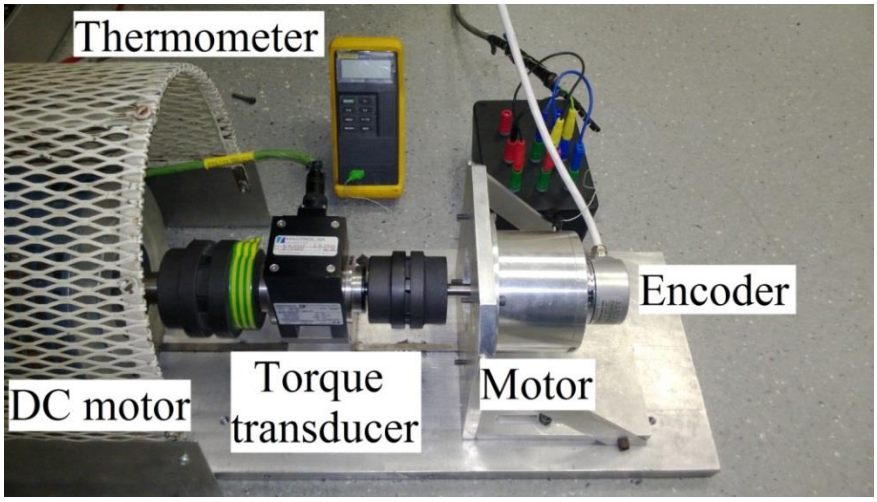

(e) Complete test bench

Fig. 2.10 Prototypes of conventional, multi-tooth, E-core and C-core SFPM machines and dynamic testing bench.

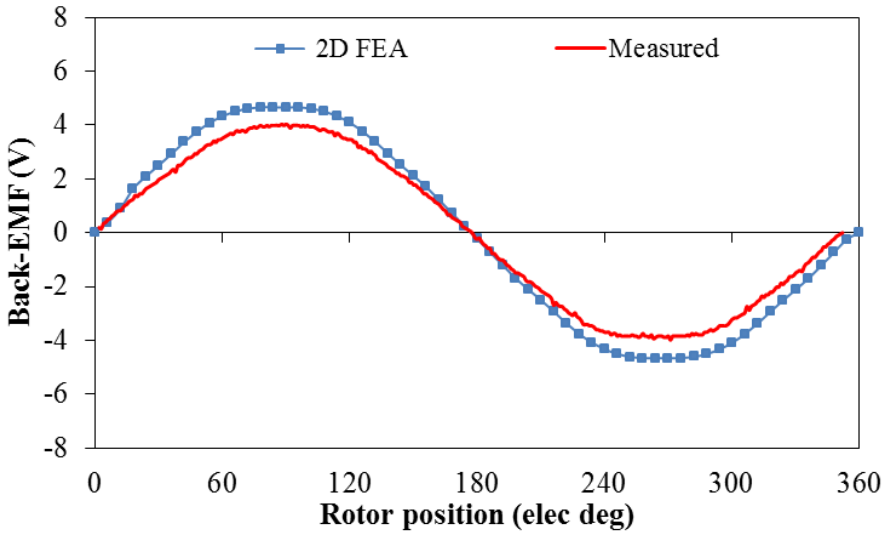

(a) 12/10 stator/rotor combination machine

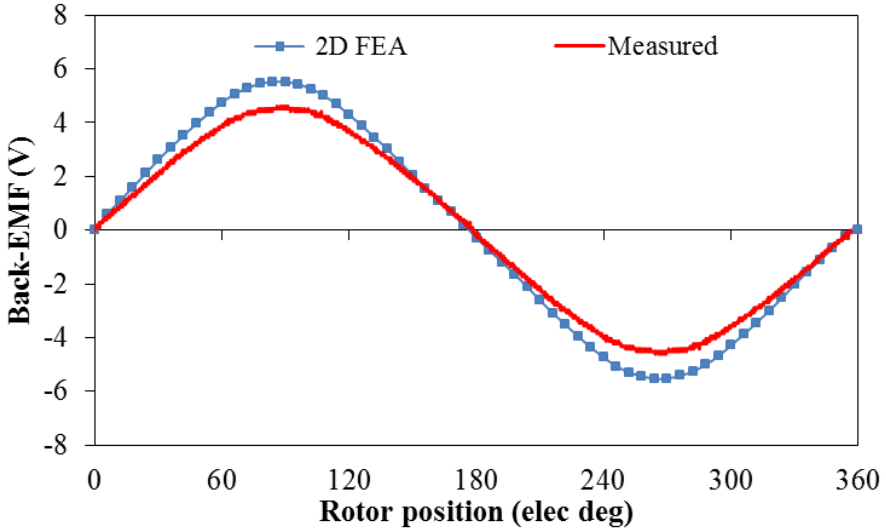

(b) 12/13 stator/rotor combination machine

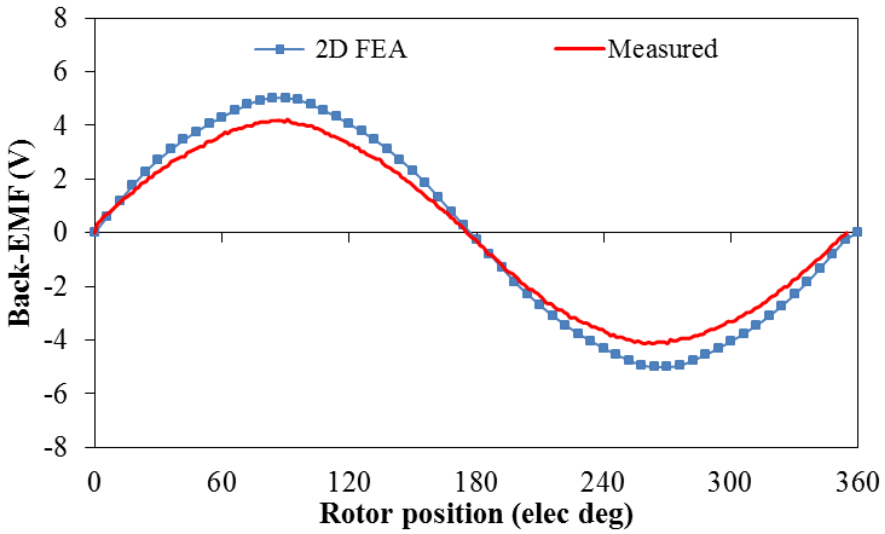

(c) 12/14 stator/rotor combination machine

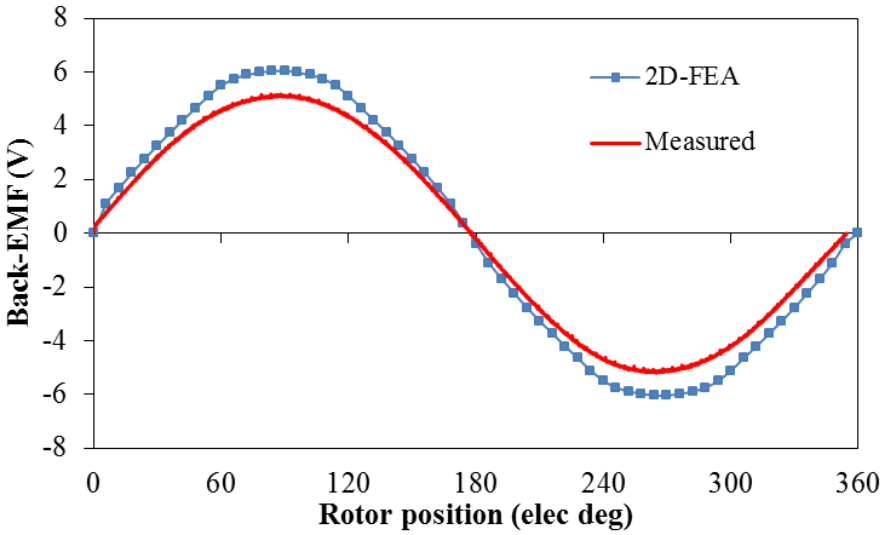

(d) Multi-tooth machine

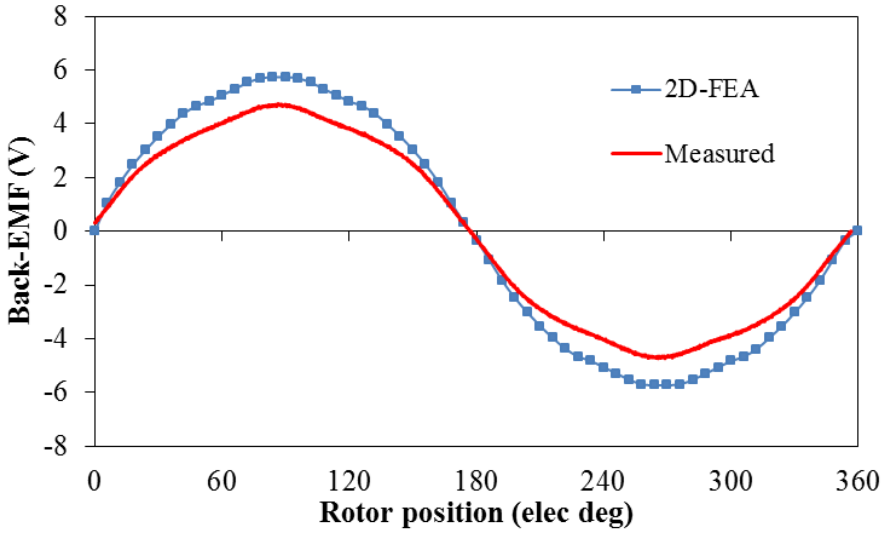

(e) E-core machine

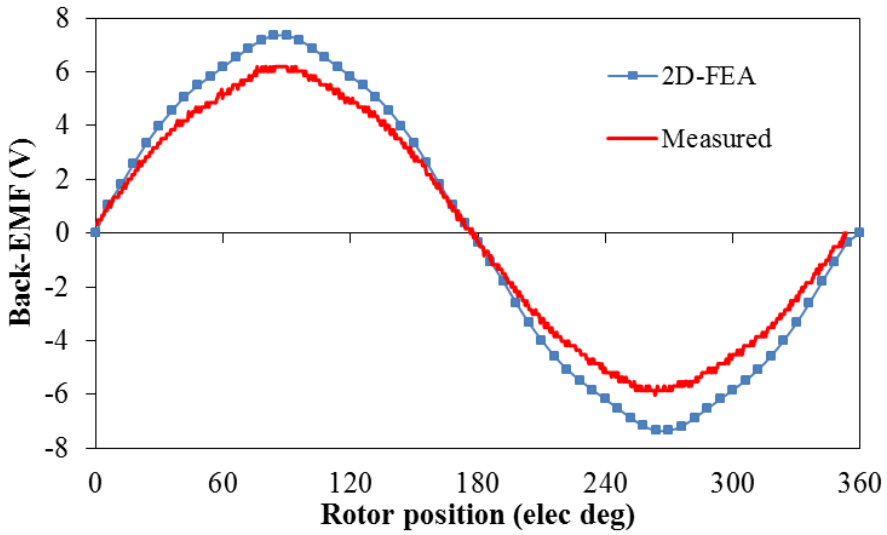

(f) C-core machine

Fig. 2.11 Measured, 2D, and 3D-FEA predicted back-EMF waveforms of SFPM machines (rotor speed 400rpm).

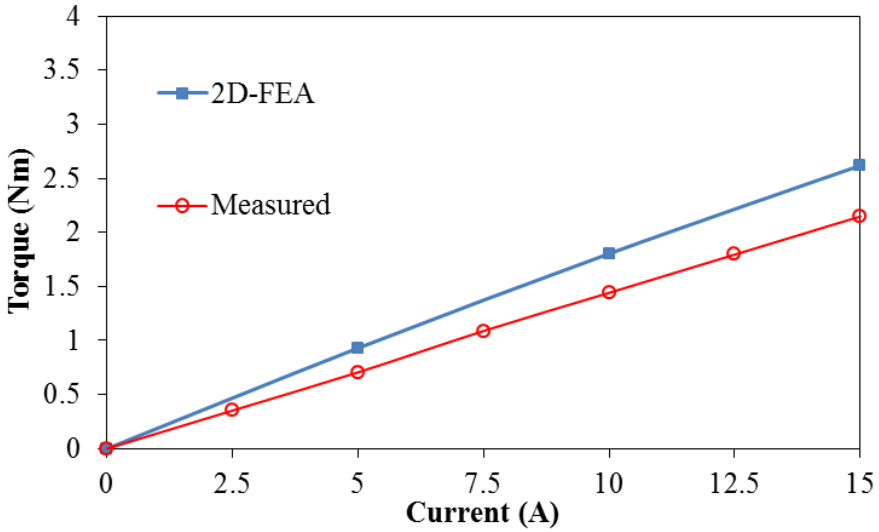

(a) 12/10 machine

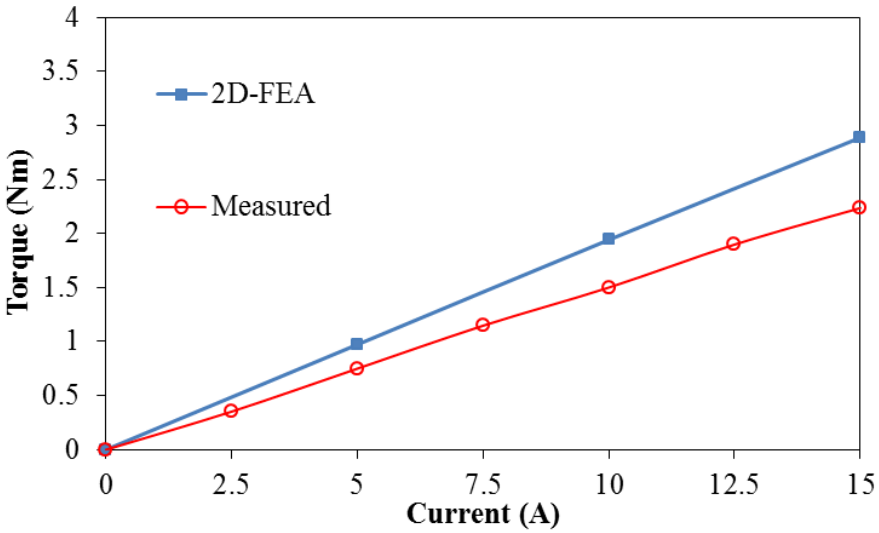

(b) 12/13 machine

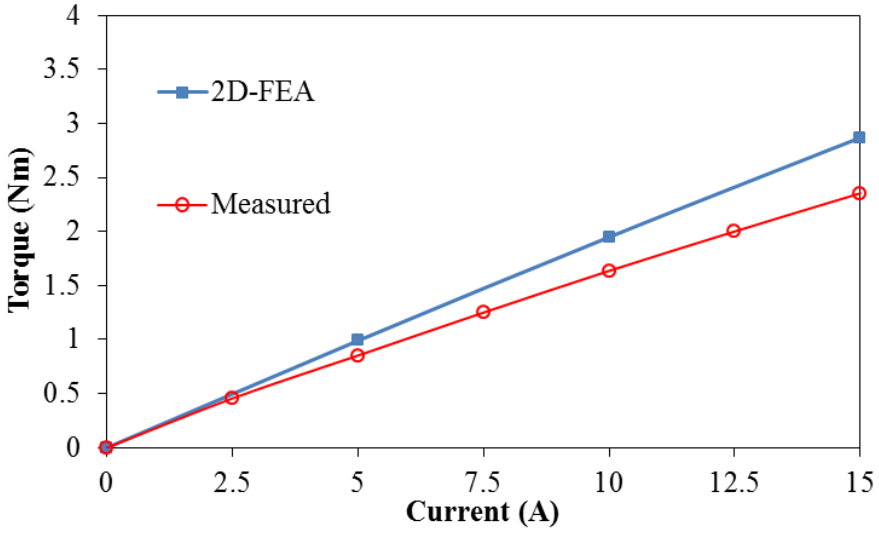

(c) 12/14 machine

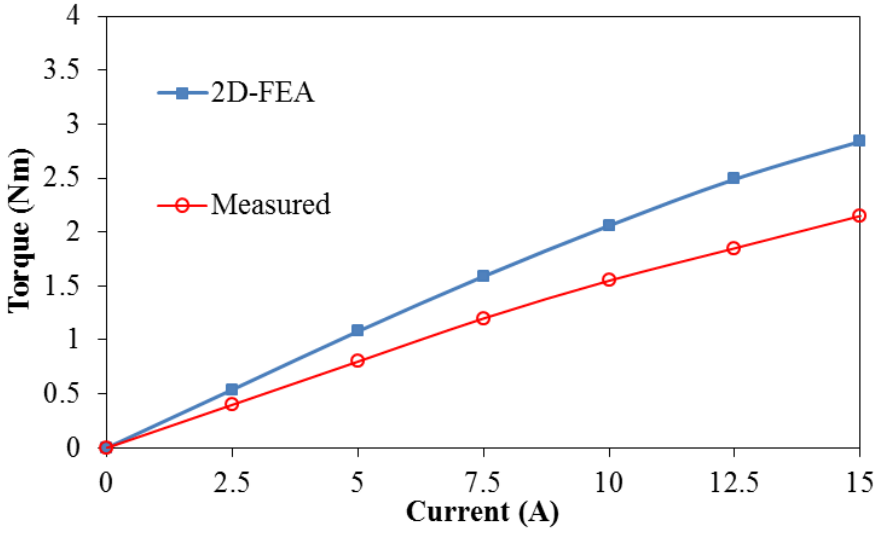

(d) Multi-tooth machine

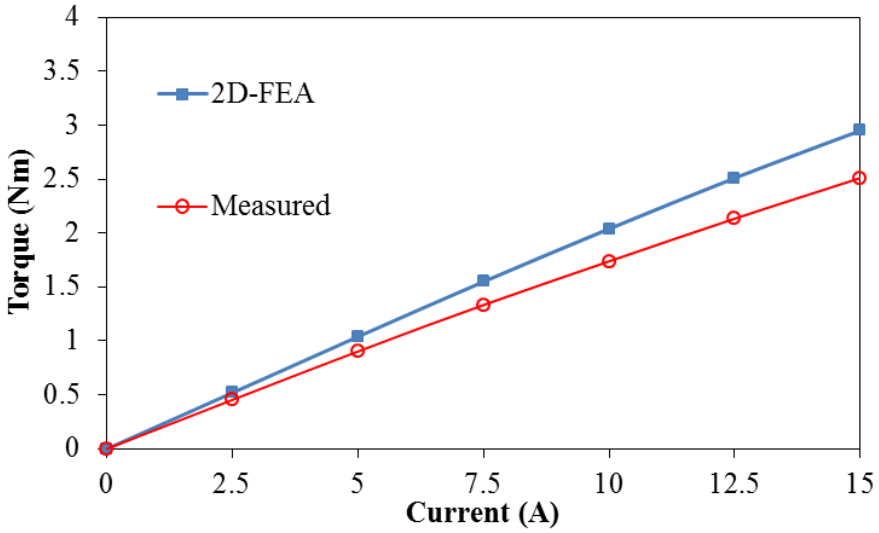

(e) E-core machine

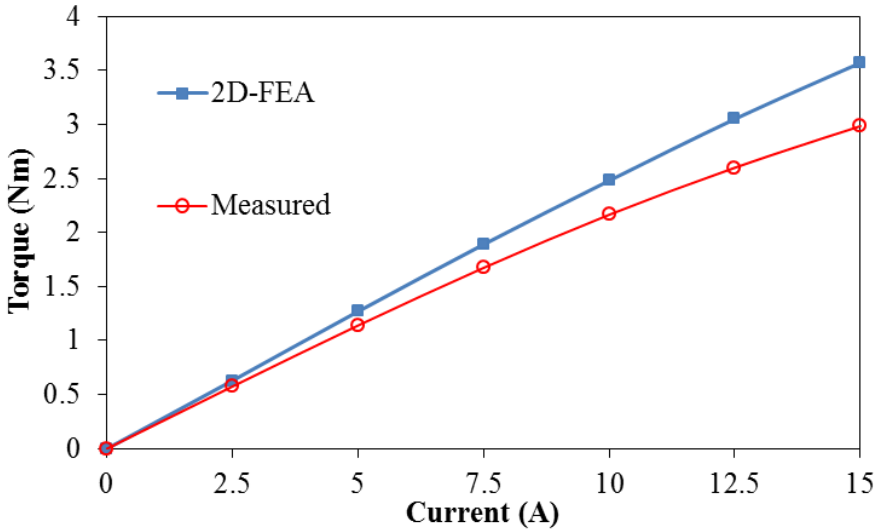

(f) C-core machine

Fig. 2.12 Measured and predicted torque-current curve of SFPM machines.

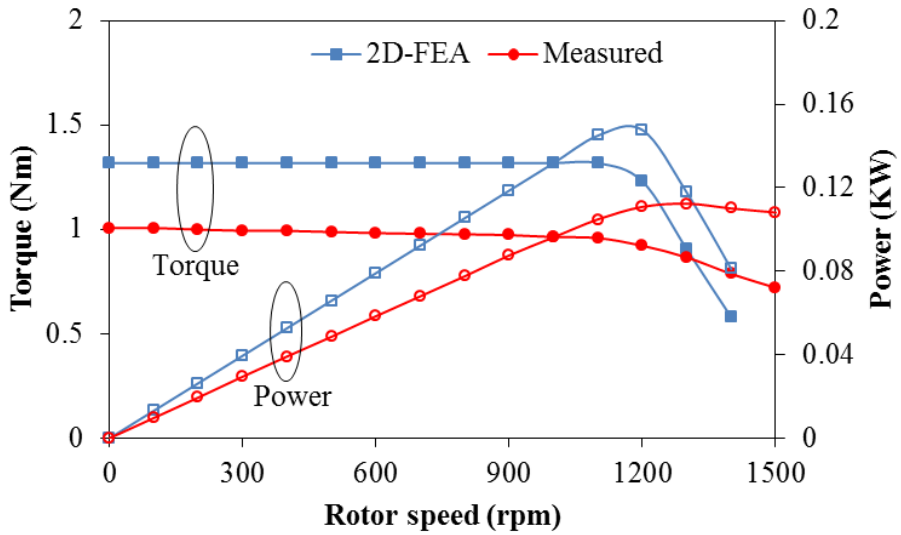

(a) 12/10 stator/rotor combination machine

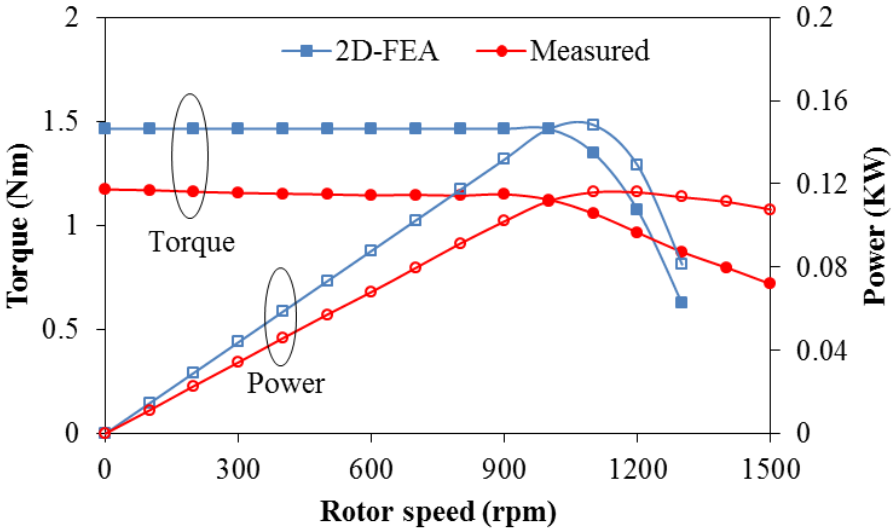

(b) 12/13 stator/rotor combination machine

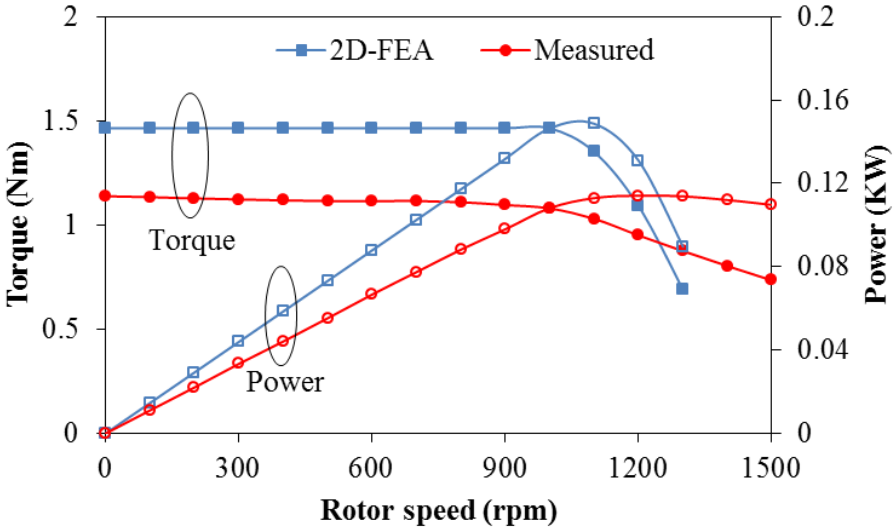

(c) 12/14 stator/rotor combination machine

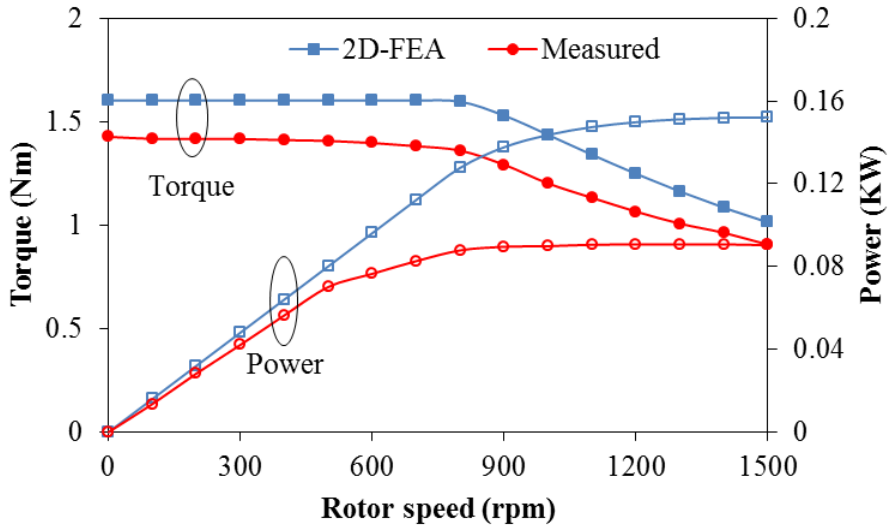

(d) Multi-tooth machine

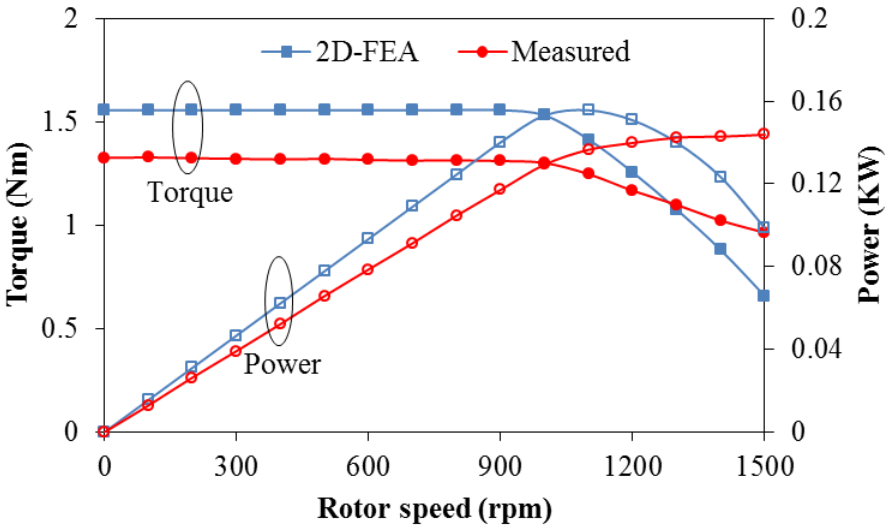

(e) E-core machine

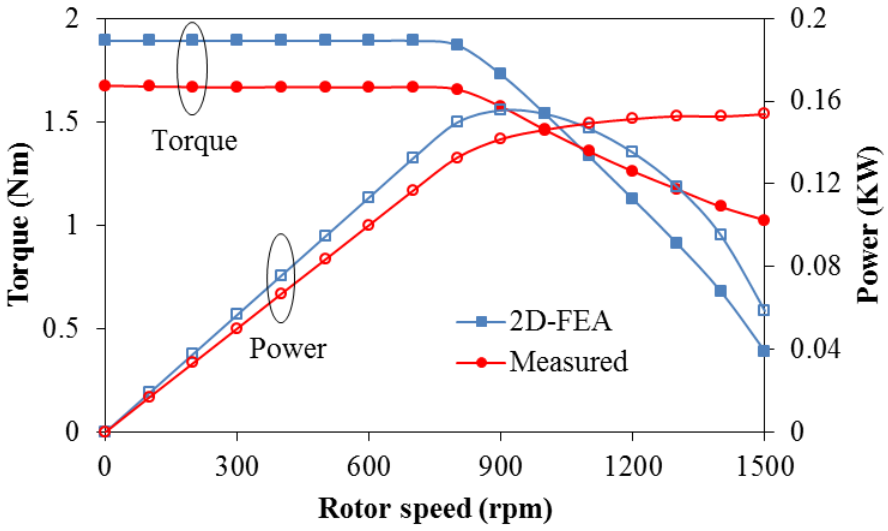

(f) C-core machine

Fig. 2.13 Torque- and power-speed curves of analysed SFPM machines at load condition (phase current 7.5A, DC-link voltage 36V).

2.6. Conclusion

In this chapter, a comparative study of electromagnetic performance including the torque-speed characteristics of six SFPM machines, i.e. conventional SFPM machines with stator/rotor pole combinations of 12/10, 12/13 and 12/14 and multi-tooth, E-core and C-core SFPM machines, is presented. A significantly wider speed range is observed for the multi-tooth, E-core and C-core SFPM machines compared with the conventional SFPM machines, which exhibit limited speed range. It is found that the limited flux weakening region in the conventional SFPM machines is caused by their low d-axis inductance. However, the flux weakening region can be increased by increasing the rotor pole number. Moreover, the

number of turns per coil and the machine structure of the multi-tooth, E-core and C-core machines cause magnetic saturation at lower current level compared to the conventional machines. In terms of the torque per magnet volumes ratio, the multi-tooth, E-core and C-core SFPM machines have overall better results than the conventional SFPM machines.

3. Influence of End-Effect on Torque-Speed Characteristics of Different SFPM Machines

3.1. Introduction

Generally, in many PM machines the spoke location of the PMs may cause large flux leakages in the end-region, known as end-effect, in addition to the flux leakage outside the stator. However, such effect leads to a significant reduction in the electromagnetic performance and therefore need to be considered in the prediction methods. Analytical method including the end-effect can be used as shown in [137, 138]. Moreover, in [139] the flux leakage in the end-region is modelled using a lumped parameter circuit. Although the analytical and lumped parameter circuit methods can predict the results relatively fast, the result accuracy might be an issue. Therefore, by using 3D-FEA, the end-effect can be considered accurately, though this method is not preferred time wise [140].

Furthermore, the influence of the end-effect on the electromagnetic performance has been investigated in several PM machines [41, 141-146]. In [141], the influence of the end-effect in IPM machine is highlighted. The analytical model of SPM machine including the magnetic saturation and end-effect is presented in [142], whereas in [143] the end-effect influence on the torque-speed curve is studied. Moreover, 3D-FEA and 2D-FEA results are compared for doubly salient machine in order to examine the end-effect influence with the increase of the axial length [41, 144]. A 3D-model of SFPM machine is developed and analysed using lumped parameter circuit and 3D-FEA, and validated by experiments in [40, 145, 146].

However, in order to analyse and compare the influence of the end-effect on the torque-speed characteristics, the conventional SFPM machines with different stator/rotor pole combinations, i.e. 12/10, 12/13 and 12/14, as well as the novel topologies with less PMs, i.e. multi-tooth, E-core and C-core SFPM machines, are studied in this chapter. Moreover, the influence of the end-effect on the PM flux-linkage and inductances is obtained by comparing 2D- and 3D-FEA predicted results. Furthermore, the torque- and power-speed curves are calculated analytically using the FEA predicted PM flux-linkages and inductances. Finally, experiments are performed in order to validate the results. Fig. 3.1 shows the 3D-models of the six analysed machines.

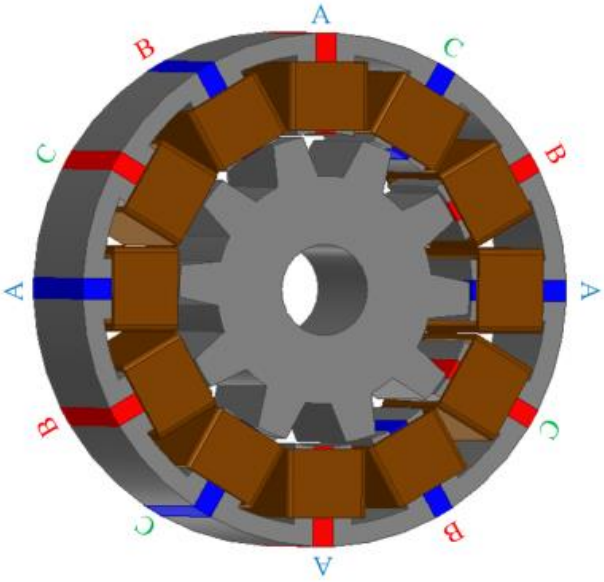

(a) 12/10 stator/rotor pole

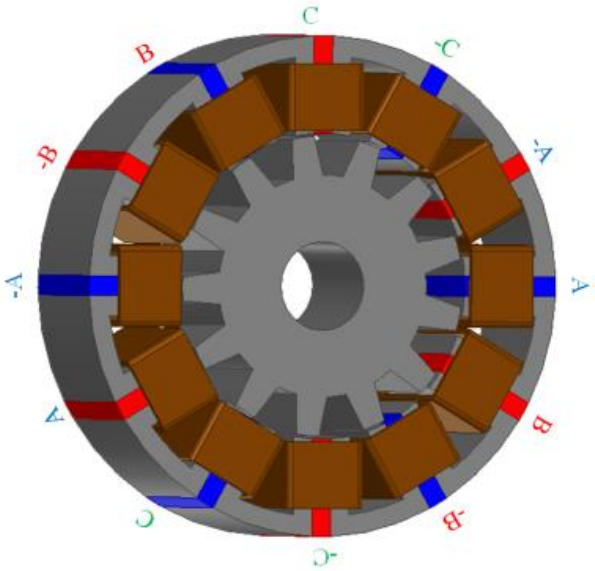

(b) 12/13 stator/rotor pole

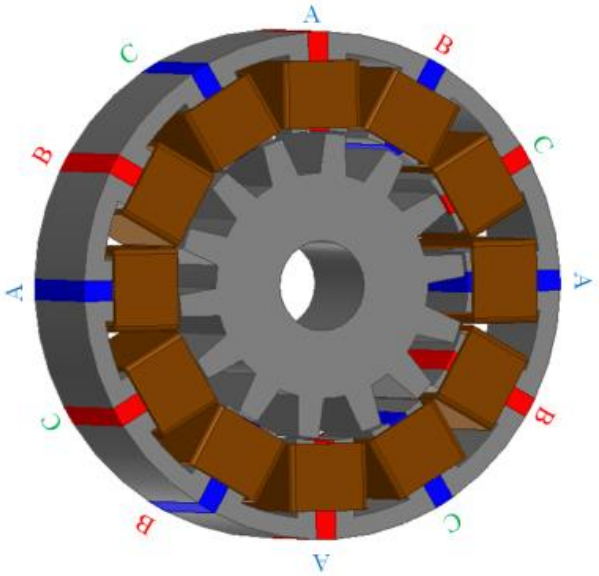

(c) 12/14 stator/rotor pole

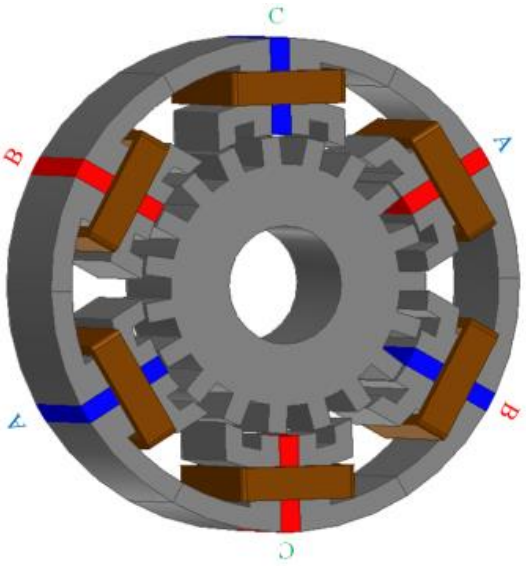

(d) Multi-tooth

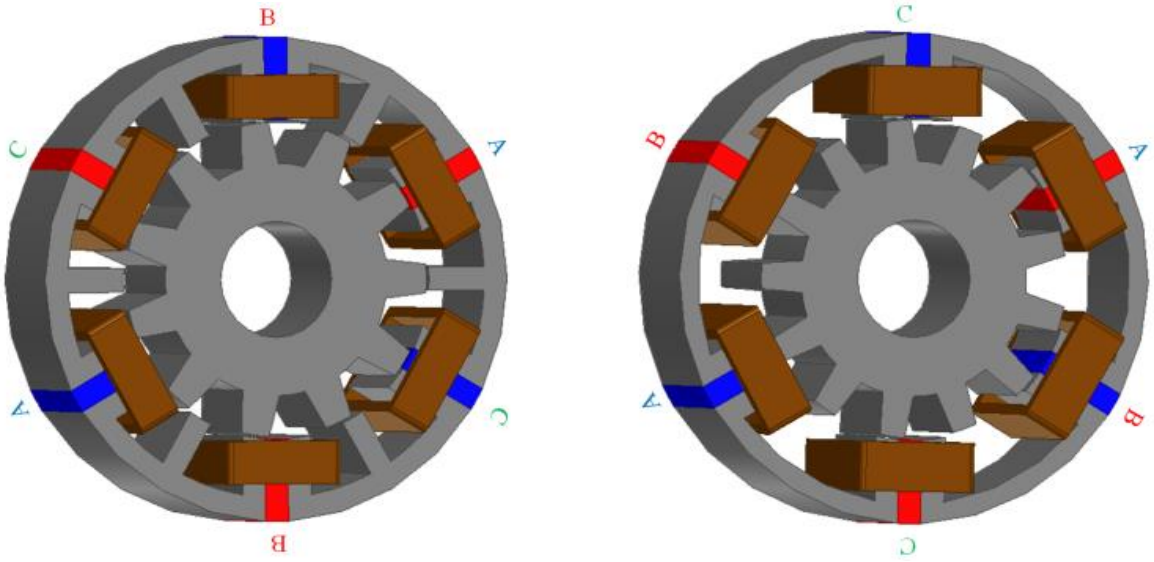

(e) E-core (f) C-core

Fig. 3.1 3D models and winding layouts of different SFPM machine topologies.

3.2. End-Effect Influence on Torque-Speed Characteristic

In order to increase the prediction accuracy of the torque-speed characteristics, the end-effect influence needs to be considered. The torque-speed characteristics calculated analytically using the predicted PM flux linkage and inductances as shown in (1-6) and (1-10). However, to investigate and highlight the end-effect on the torque-speed characteristics, the PM flux-linkages and inductances are predicted using 2D- and 3D-FEA.

3.2.1. PM flux linkage

Fig. 3.1 presents the PM flux linkage of the six analysed SFPM machines at different current levels predicted by 2D and 3D-FEA. It can be seen that the PM flux-linkage predicted by 2D-FEA is higher than that of 3D-FEA due to the PM end-leakage flux, i.e. end-effect. Furthermore, higher armature reaction on the PM flux-linkage is observed in the 3D-FEA results compared to its counterpart of 2D-FEA, since the high current level leads to higher magnetic saturation in the stator and therefore higher stator end leakage. Overall, a small reduction in the conventional machines is observed, i.e. about 6.5% and 7.5% at open circuit and 15A current, respectively. However, due to lower PM number and higher turns per coil as well as wider PM and stator tooth, the influence of end-effect on the PM flux-linkage is relatively higher in the multi-tooth, E-core and C-core machines, i.e. 9.5%, 13% and 9% under open circuit condition. Nevertheless, since the C-core has larger number of turns per coil, higher flux-linkage can be exhibited and therefore lower influence of end-effect is observed compared to that of the E-core machine. Moreover, since the influence of magnetic

saturation is higher compared to the conventional machines, 22%, 14.5% and 16% are the reductions in the PM flux-linkage at 15A in multi-tooth, E-core and C-core machines, respectively. Furthermore, since thinner back-iron is used in the C-core machine the influence of magnetic saturation is higher than that of the E-core machine.

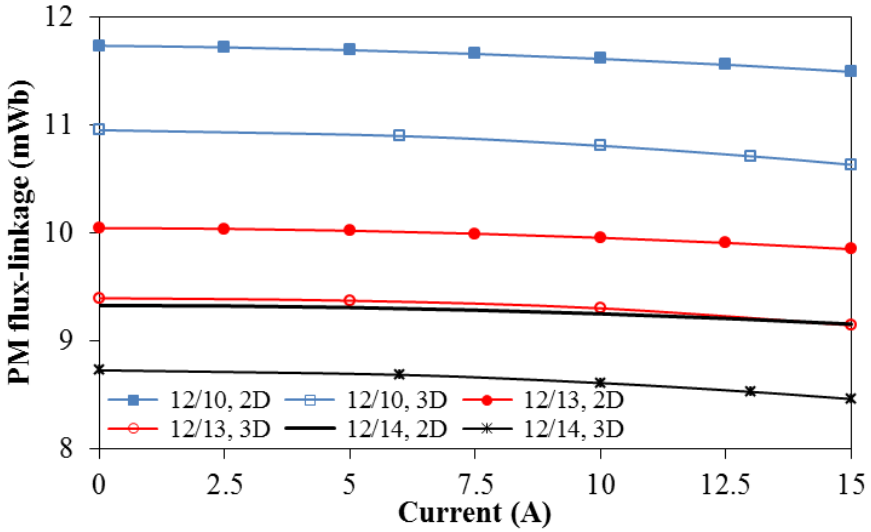

(a) 12/10, 12/13 and 12/14 machines

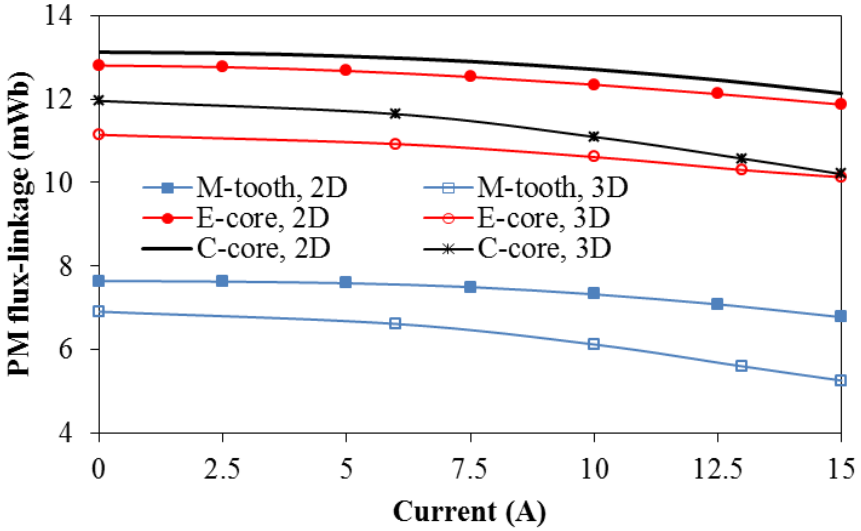

(b) Multi-tooth, E-core and C-core machines

Fig. 3.2 2D- and 3D-FEA predicted PM flux linkage against q-axis current in SFPM machines.

3.2.2. Inductances

In Chapter 1, the inductances are calculated using full-coupling method in which full accounting for magnetic saturation and cross-coupling is considered. However, in order to minimize the required time for the calculation, partial-coupling method is used (see appendix A2). Moreover, using both 2D- and 3D-FEA the d- and q-axis inductances of the six machines are calculated and presented in Fig. 3.2.

Generally, including the end-effect in the calculation of the inductances leads to higher values compared to the 2D-FEA predicted results. This is due to the end leakage inductance. On the other hand, higher d- to q-axis inductance ratio is exhibited when the end-effect is accounted due to lower magnetic saturation along the d-axis path due to end effect.

Moreover, it can be seen that in the conventional machines the 3D-FEA predicted d- and q-axis inductances increase with their respective currents at relatively higher rate compared to that of the 2D-FEA due to the end region PM flux leakage which provide more space for the armature flux therefore d-axis inductances increase at higher rate compared to the q-axis. However, in the multi-tooth, E-core and C-core machines, the magnetic saturation is higher. Therefore, at high current levels lower inductance values are observed due to the higher stator leakage, i.e. similar to the PM flux-linkage.

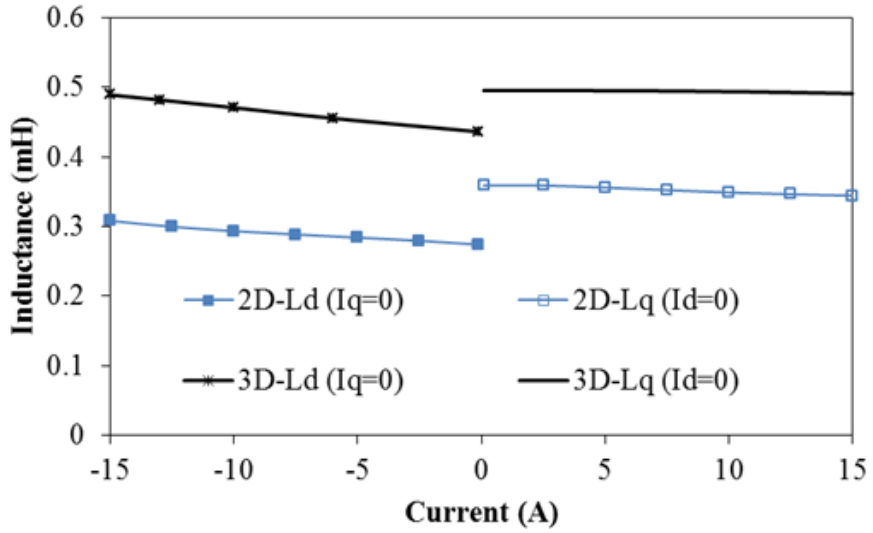

(a) 12/10 machine

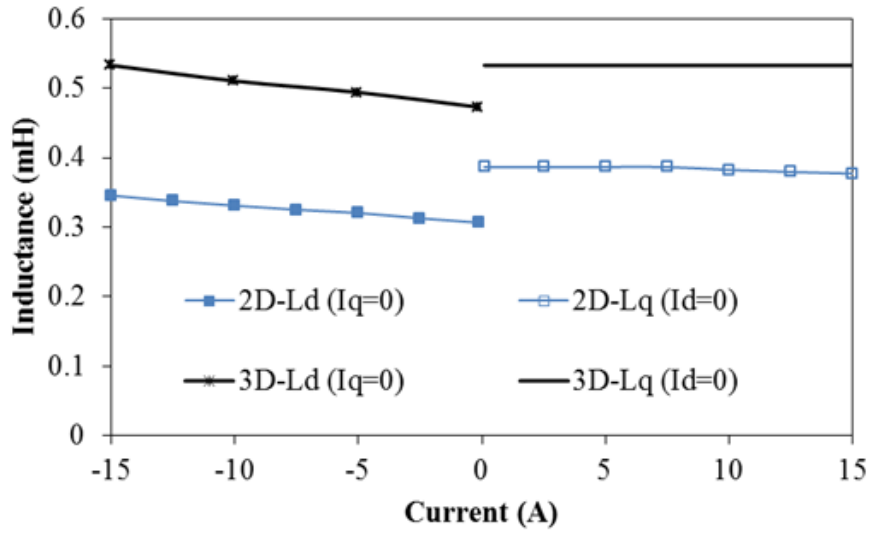

(b) 12/13 machine

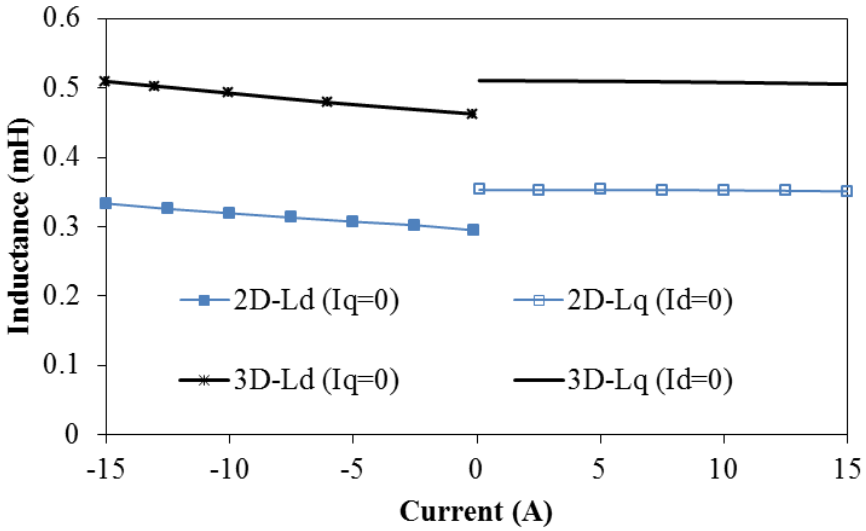

(c) 12/14 machine

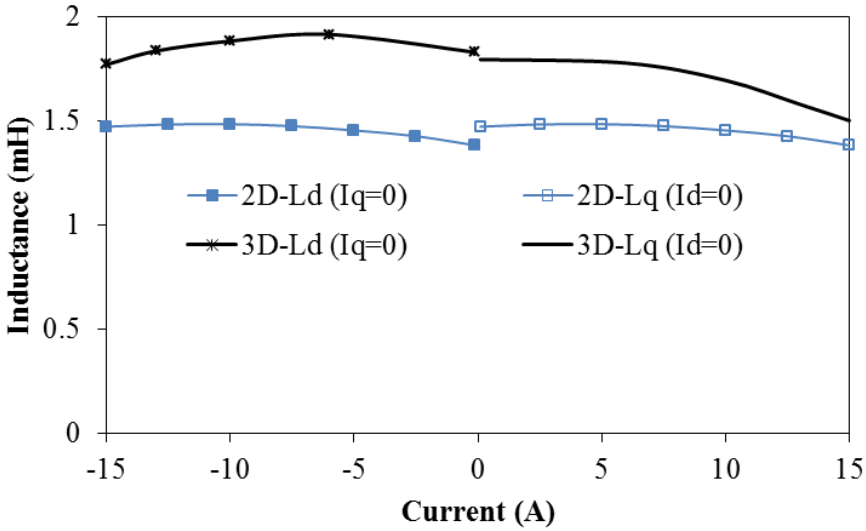

(d) Multi-tooth machine

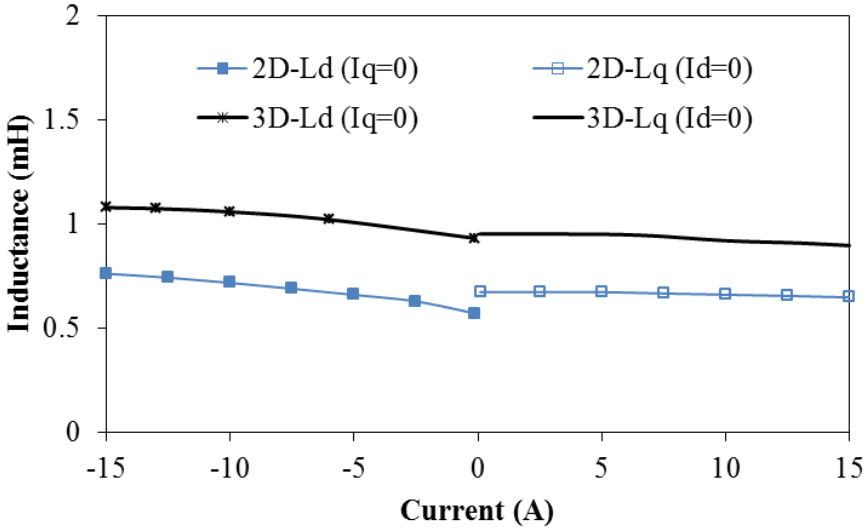

(e) E-core machine

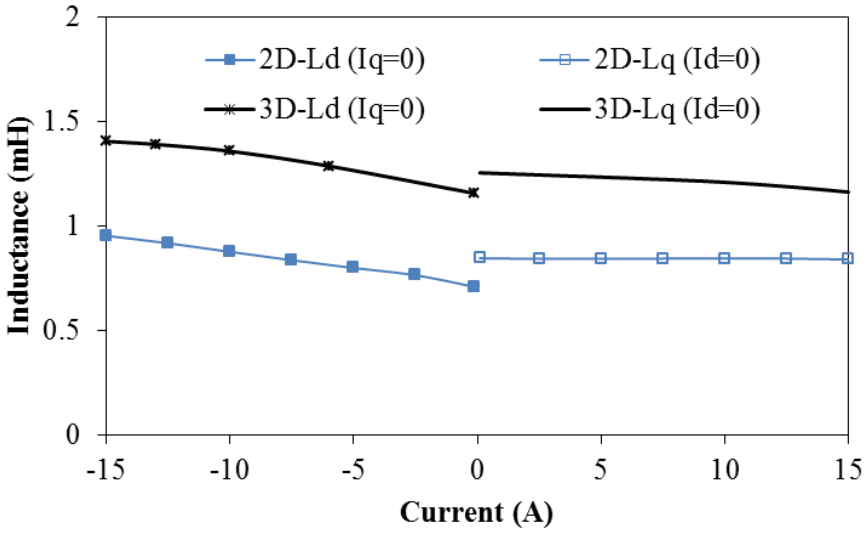

(f) C-core machine

Fig. 3.3 D- and q-axis inductances of SFPM machines predicted by 2D- and 3D-FEA.

3.2.3. Torque-speed curves

Fig. 3.3 presents the torque- and power-speed curves of the six machines calculated by both 2D- and 3D-FEA PM flux linkage and inductances which are presented in Figs. 5.1 and 5.2, respectively. Table 3.1 presents the d-axis inductance, PM flux linkage, flux weakening factor, maximum torque, and speed range of the conventional, multi-tooth, E-core and C-core machines. However, when the end-effect is not considered, large torque but limited maximum speed and small flux weakening capability are exhibited by the conventional SFPM machines. On the other hand, slightly lower torque while much higher maximum speed and flux weakening capability can be observed in the 3D-FEA results due to the large increase in the d-axis inductance and the reduction in PM flux linkage. Moreover, it is found that the higher the rotor pole number, the better the flux weakening factor due to the lower PM flux linkage whether the end-effect is accounted or ignored. In terms of maximum power, limited constant power region is observed in the 2D-FEA calculations. However, by including the end-effect, the maximum power value maintained and the constant power region significantly extended.

Furthermore, when the end-effect is ignored, the multi-tooth, and C-core SFPM machines exhibit infinite speed range and the flux weakening factor is higher than 1, whereas significantly large maximum speed is observed in the E-core machine. The relatively large d-axis inductance leads to faster reach the maximum phase voltage and consequently low base speed and maximum power. However, including the end-effect in the torque-speed calculation leads to lower PM flux linkage and therefore lower constant torque, as well as

higher inductance values cause faster maximum phase voltage reach and consequently lower base speed and maximum power. Therefore, in the multi-tooth, E-core and C-core machines, the maximum power reduces when the end-effect is accounted.

Overall, when the end-effect is considered, the flux weakening factors in the conventional machines increase to values close to 1, therefore significant flux weakening and high power capabilities are observed. However, the flux weakening factors increase further to be higher than 1 in the multi-tooth, E-core and C-core machines. Therefore, the wide flux weakening capability is maintained, whilst low power capability is produced.

Table 3.1 Comparison of end-effect influence on flux weakening factor, speed range, and maximum torque and power

Machines		Ψ_{pm} (Wb)	L_d (mH)	K_{fw}	Base speed (rpm)	Max. speed (rpm)	Max. torque (Nm)	Max. power (KW)
12/10	2D	0.01175	0.308	0.39	1800	3100	2.6	0.5
	3D	0.01063	0.489	0.69	1800	6000	2.4	0.5
12/13	2D	0.01004	0.346	0.51	1600	3400	2.9	0.5
	3D	0.00934	0.533	0.85	1600	9700	2.68	0.5
12/14	2D	0.00933	0.333	0.53	1500	3600	2.89	0.5
	3D	0.00846	0.509	0.91	1500	13800	2.67	0.5
Multi-tooth	2D	0.00764	1.471	2.88	600	∞	2.89	0.17
	3D	0.00691	1.769	3.84	500	∞	2.8	0.12
E-core	2D	0.01281	0.761	0.90	1400	13000	2.95	0.5
	3D	0.01114	1.078	1.45	1200	∞	2.51	0.35
C-core	2D	0.01312	0.953	1.08	1000	∞	3.57	0.47
	3D	0.01195	1.404	1.76	900	∞	2.98	0.3

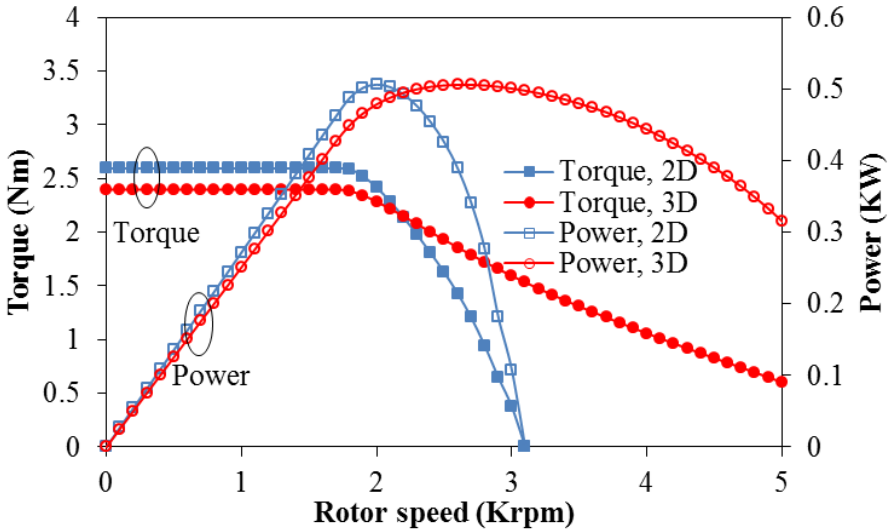

(a) 12/10 machine

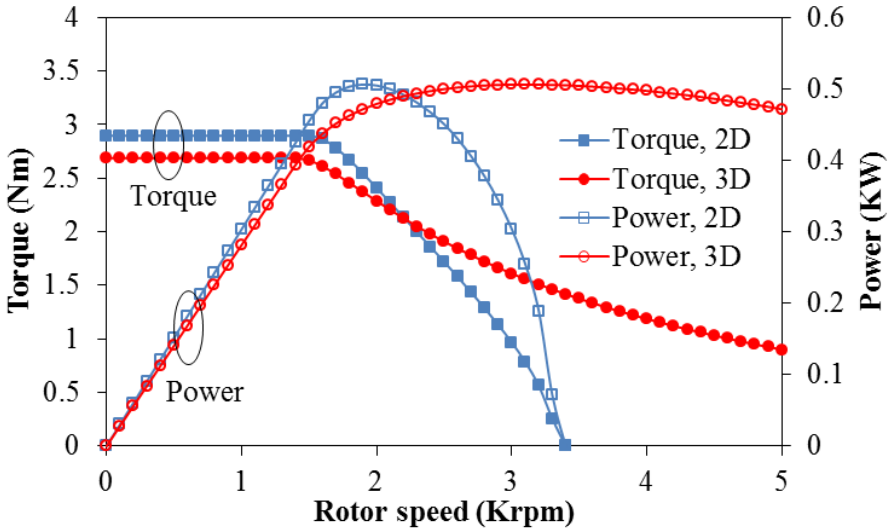

(b) 12/13 machine

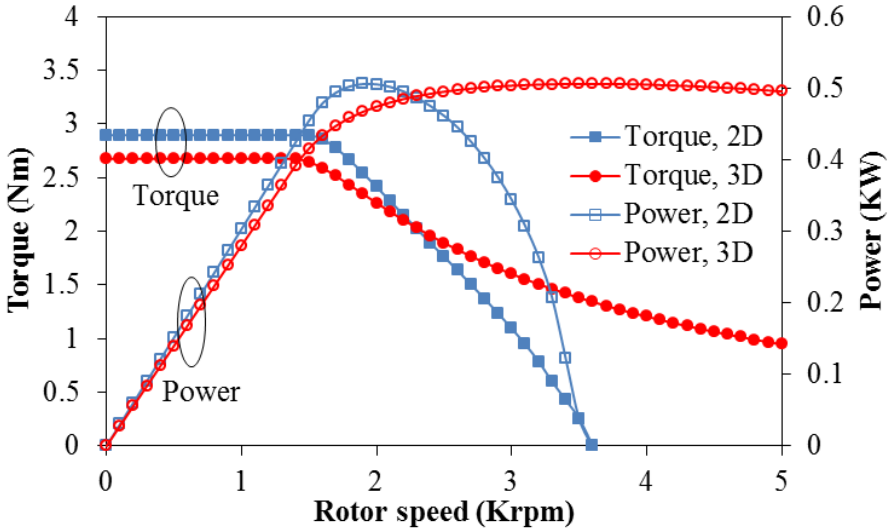

(c) 12/14 machine

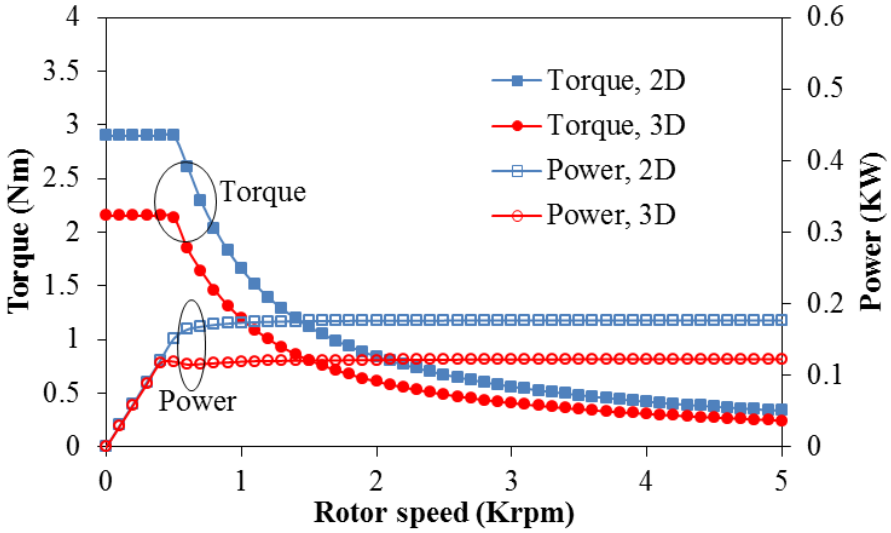

(d) Multi-tooth machine

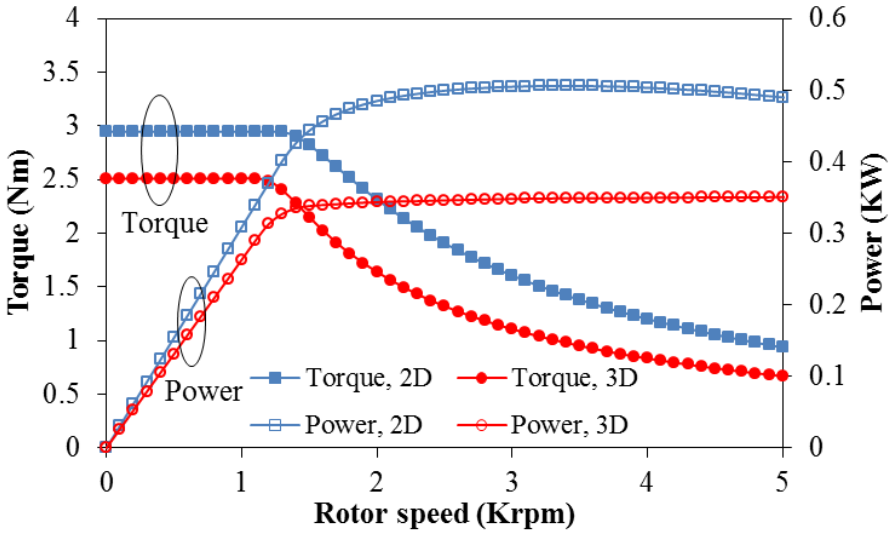

(e) E-core machine

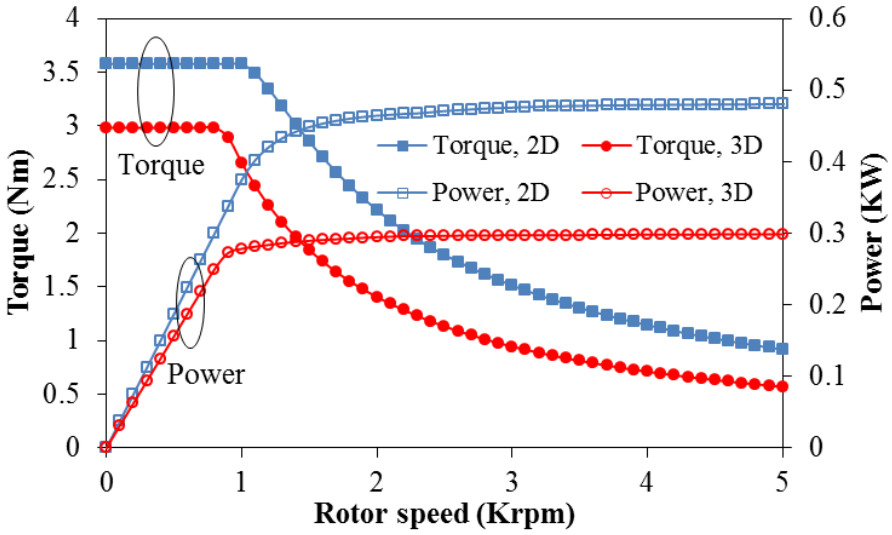

(f) C-core machine

Fig. 3.4 Torque- and power-speed curves of SFPM machines predicted by 2D- and 3D-FEA under (I_{ph}=15A, $V_{link\text{-}DC}$=36V).

3.3. Experimental Validation

In order to validate the obtained results the prototypes of conventional SFPM, multi-tooth, E-core and C-core machines presented in Fig. 2.10 are used. Three tests are carried on to evaluate the predicted results, i.e. PM flux linkage, inductances and torque-speed curves.

3.3.1. PM flux linkage

In order to obtain the measured PM flux linkage at different current levels, the static torque is measured first. By applying DC current of $I_a=I_{test}$, $I_b=I_c=-0.5I_{test}$, the rotor moves to the q-axis position, i.e. 0 degree current angle. Once the rotor is on the q-axis, the machine can be fixed on a chunk and a balanced beam set on the rotor shaft as shown in Fig. 3.4 (a), the weight

gage can be used to measure the force produced by the motor. Moreover, by setting the current to ($-I_a/2=I_b=I_c$) the static torque can be obtained by converting the force in which the gauge is recording. Additionally, the PM flux linkage can be found by:

$$\Psi_{pm} = \frac{2T_e}{3N_r I_q} \tag{5-1}$$

A comparison between measured and predicted by both 2D- and 3D-FEA PM flux linkage is presented in Figs. 3.4 (b) and (c). A difference between the measured and 3D-FEA results at high current is observed. Overall, a good agreement between the measured and 3D-FEA results at low current is observed.

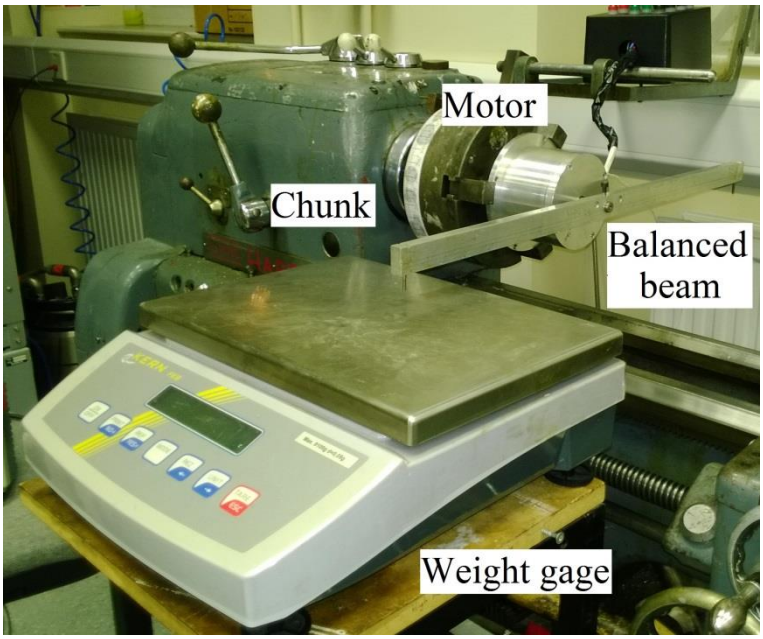

(a)

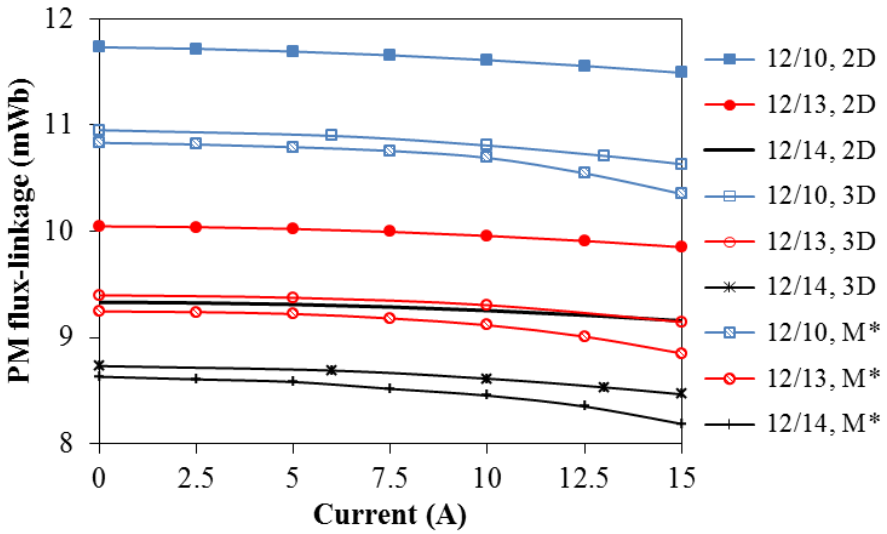

(b) 12/10, 12/13 and 12/14 machines

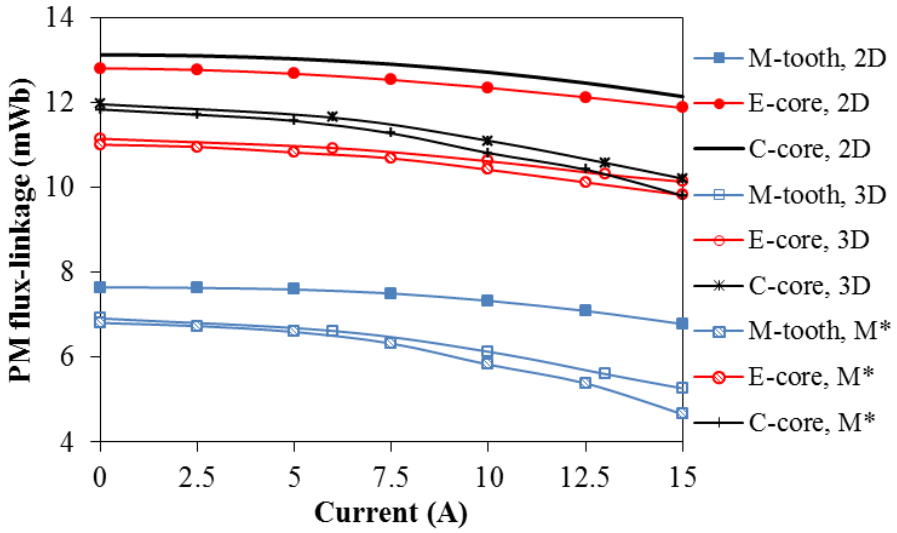

(c) Multi-tooth, E-core and C-core machines

Fig. 3.5 Comparison of measured (M*) and predicted PM flux linkage at different q-axis current levels in SFPM machines.

3.3.2. Inductance

Using RLC meter the phase inductance is measured and compared with its counterpart predicted by 2D- and 3D-FEA, Table VI. Good agreement is shown between the 3D-FEA and measured values.

Table 3.2 Measured and predicted phase inductance of SFPM machines (1 kHz)

	12/10	**12/13**	**12/14**	**M-tooth**	**E-core**	**C-core**
2D-FEA	0.209	0.316	0.221	1.205	0.552	0.609
3D-FEA	0.261	0.382	0.291	1.401	0.662	0.721
Measured	0.253	0.336	0.275	1.391	0.641	0.695

3.3.3. Torque-speed curves

The torque- and power-speed characteristics of the six SFPM machines are tested using flux weakening control under maximum current and DC-link voltage of I_{max}=7.5A (reduced due to the limitations of testing rig) and 36V, respectively. Overall, good agreement is exhibited between the measured and 3D-FEA results. Furthermore, it can be also seen that for all the machines the measured and predicted 3D-FEA results have better flux weakening capability than the 2D-FEA results. However, due to the influence of magnetic saturation which is highlighted in Fig. 3.1, the E-core and C-core machines produce better flux weakening capability at low current level, i.e. 7.5A, when the end-effect is accounted. The multi-tooth has significantly large inductance therefore similar conclusion to that of the 15A is observed.

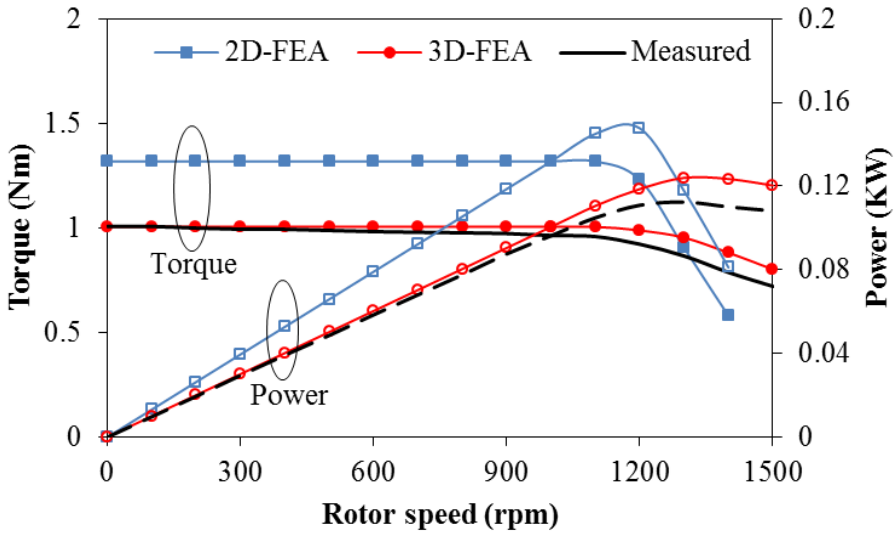

(a) 12/10 machine

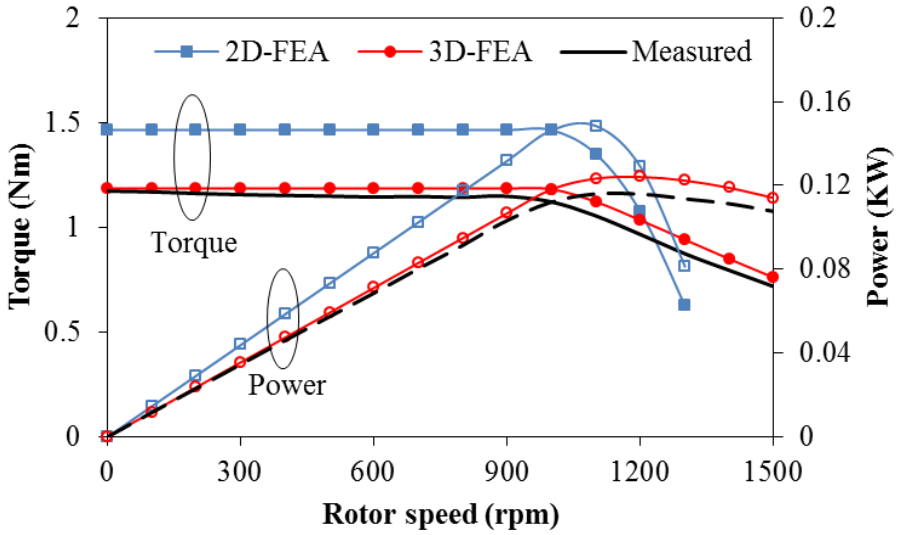

(b) 12/13 machine

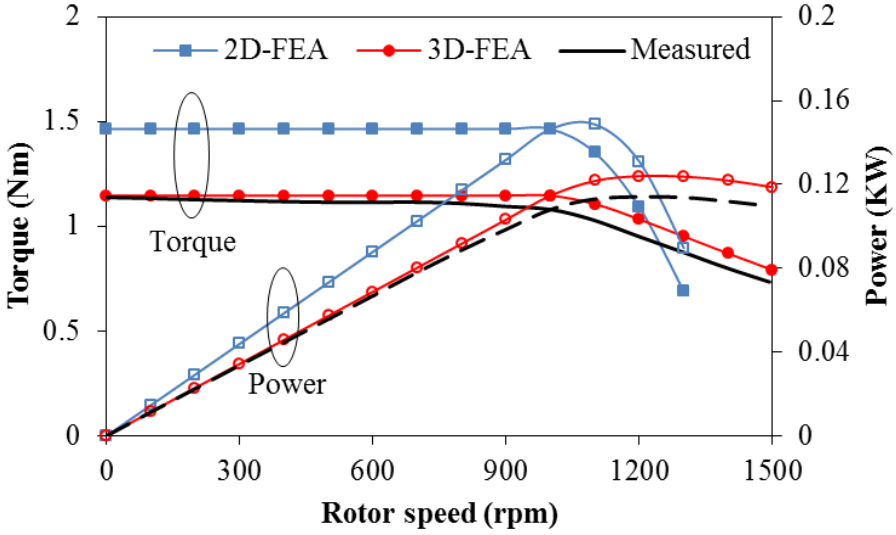

(c) 12/14 machine

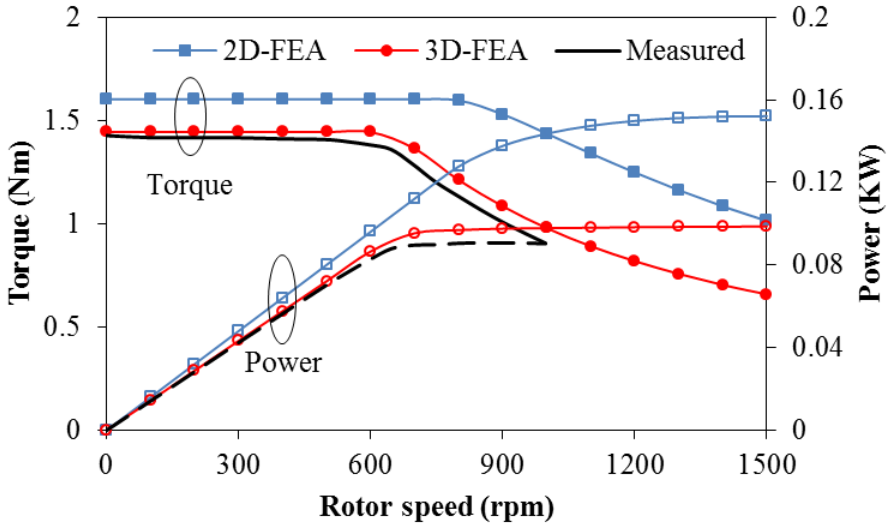

(d) Multi-tooth machine

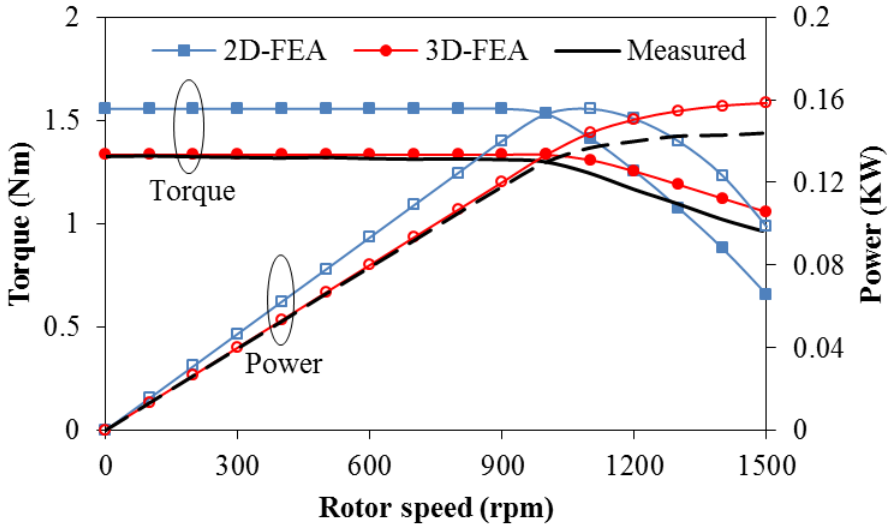

(e) E-core machine

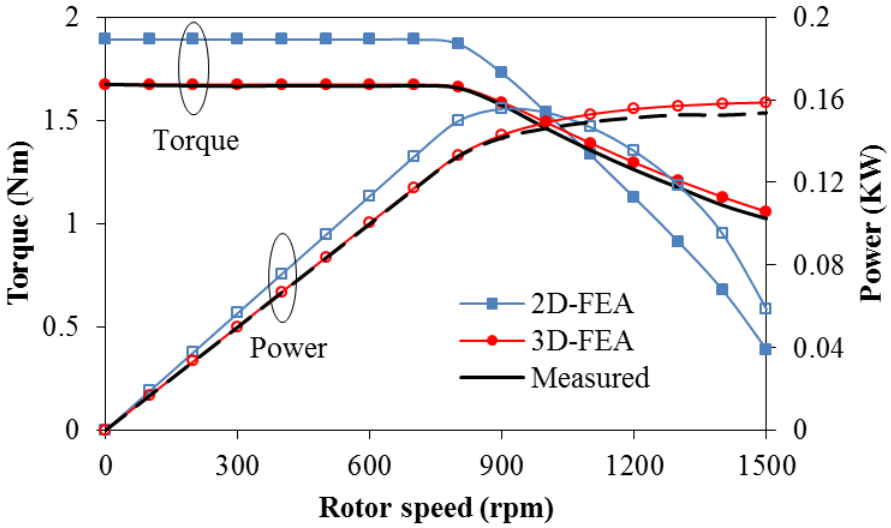

(f) C-core machine

Fig. 3.6 Measured and 2D- and 3D-FEA predicted torque- and power-speed curves of SFPM machines.

3.4. Conclusion

In this chapter, the three conventional SFPM machines having different stator/rotor pole combinations, i.e. 12/10, 12/13 and 12/14, as well as the three novel topologies with less PMs, i.e. multi-tooth, E-core and C-core SFPM machines, have been studied to investigate the influence of the end-effect on their torque-speed characteristics. It has been found that, smaller torque in the constant torque region while wider flux weakening capability is observed in the conventional machines when the end-effect is accounted. Moreover, the higher the rotor poles, the better the flux weakening capability due to the lower PM flux-linkage no matter whether the end-effect is considered or not. On the other hand, since higher inductances are obtained in the multi-tooth, E-core and C-core machines undesirable influence on the results by the end-effect is observed. Smaller constant torque region, and lower base speed and less maximum power are exhibited when the end-effect is considered. It is worth highlighting that including the end-effect in the optimizing of SFPM machine, i.e. using 3D-FEA optimization, might results in different optimum values with its counterpart 2D-FEA.

4. Comparison of Electromagnetic Performance of SFPM Machines with Mechanical Flux Adjusters

4.1. Introduction

As mentioned in Chapter 1, due to constant flux of permanent magnets, limited operation speed range and relatively low efficiency at high speed are observed in PM machines. In some applications such as automotive, high operation speed range and high efficiency over a wide operation region are essential requirements. Therefore, the PM machines are normally operated using flux weakening control. However, due to the inverter voltage and current limitations, the speed range is still inadequate for such requirements. As a result, some electrical and mechanical approaches have been developed to adjust the PM flux level in order to achieve wider speed range and improve the flux-weakening capability in PM machines.

However, by including DC field winding to the PM machines, i.e. hybrid excitation machines [83], [84], the airgap flux density can be controlled. Normally, in the flux weakening region the DC excitation produces d-axis flux to oppose the flux produced by the PM similar to that of flux weakening control [85]. These machines are characterised by their potential to extend the flux weakening capability and improve the efficiency at high speeds as well as to enhance the constant torque region, which is known as flux strengthening [86].

In the past ten years many hybrid excitation switched flux permanent magnet (SFPM) machine topologies are proposed and developed [61, 87, 88, 90-92, 147, 148]. In [90] and [91], the DC coils are located behind the PMs and back iron, and surrounded by ferromagnetic yoke, while shorter PMs are used to provide space for the DC coils in [61, 87, 88]. Another approach is illustrated in [147]; the same structure as the conventional SFPM machine is used with the DC coils and the armature windings share the same slot. Moreover, a hybrid E-core SFPM machine topology is developed and presented in [92].

On the other hand, several mechanical methods have been proposed offering flux control in PM machines. In [149] and [150], mechanical flux adjusting method consists of two rotor plates are used for an axial flux surface mounted PM machine. The PM flux-linkage can be

adjusted by the relative movement of the two rotor plates. A similar concept is also applied to radial flux surface mounted PM machine, which divides the rotor into two separated parts [111]. Moreover, by filling the axial or radial flux barriers with movable pieces made of ferromagnetic material in the interior permanent magnet (IPM) machine, the PM flux-linkage can also be adjusted during the operation [113, 114, 151]. However, since the PMs in these machines are located inside the rotor, the reliability and manufacture, i.e. assembling, become challenging issues.

However, with the PMs located on the stator, the SFPM machines can overcome such problems. In addition to their high torque and power density, SFPM machines have the merits of high reliability and easy assembling as well as easy heat dissipation [9]. The principle of mechanically movable flux adjusters (FAs) has been proposed in [116] for a 12/14 stator/rotor pole combination SFPM machine, which is similar to method for the doubly salient PM machine, which has been proposed in [117]. However, the influence of the FAs on the torque-speed characteristics and flux weakening capability has not been investigated.

In this chapter, the influence of the FAs on the torque-speed characteristics and electromagnetic performance of the different SFPM machines investigated and compared in Chapter 1, i.e. the conventional SFPM machines with different stator/rotor pole combinations and the novel topologies using less PM material, are investigated and compared, to highlight the influence of the rotor pole number in conventional SFPM machines as well as to determine the most suitable machine topologies to be provided with FAs.

4.2. Concept of Mechanical Flux Adjusters in SFPM Machines

This technique uses mechanically movable pieces (made of ferromagnetic material) located outside the stator, as shown in Fig. 4.1. The PM flux is controlled by the position of FAs. At open position, Fig. 4.1 (a), the PM flux-linkage flows through the stator teeth, stator back-iron, airgap, rotor poles and rotor back-iron, and therefore the flux distribution is same with that of the conventional SFPM machine without FAs. By moving the FAs to the closed position, Fig. 4.1 (b), a part of the PM flux will be short-circuited through the FAs.

In PM machines, the maximum speed that can be theoretically calculated is presented in (1-12) and from the maximum speed a flux weakening factor is derived and presented in (1-13). Therefore, by short-circuiting the PMs flux by FAs, the flux-linkage Ψ_{pm} decreases, leading to larger flux weakening factor and wider operation speed range at the same phase current

and DC-link voltage limits. Additionally, since the PMs short-circuited flux is stationary, the iron loss in the stator reduce significantly leading to improve the efficiency of the machine, especially at high speeds.

The FA size is normally optimized according to the application, i.e. the required level of flux weakening capability. However, in this study the width of FA is optimized and selected to be the sum of two stator teeth and one magnet width, and the optimum height is twice of the stator back-iron thickness. Therefore, the optimized FA provides significant PM short-circuiting flux but no effect on the performance of machines operated in constant torque region, i.e. when FAs at the open position the machine performance is the same as that of the machines without FAs.

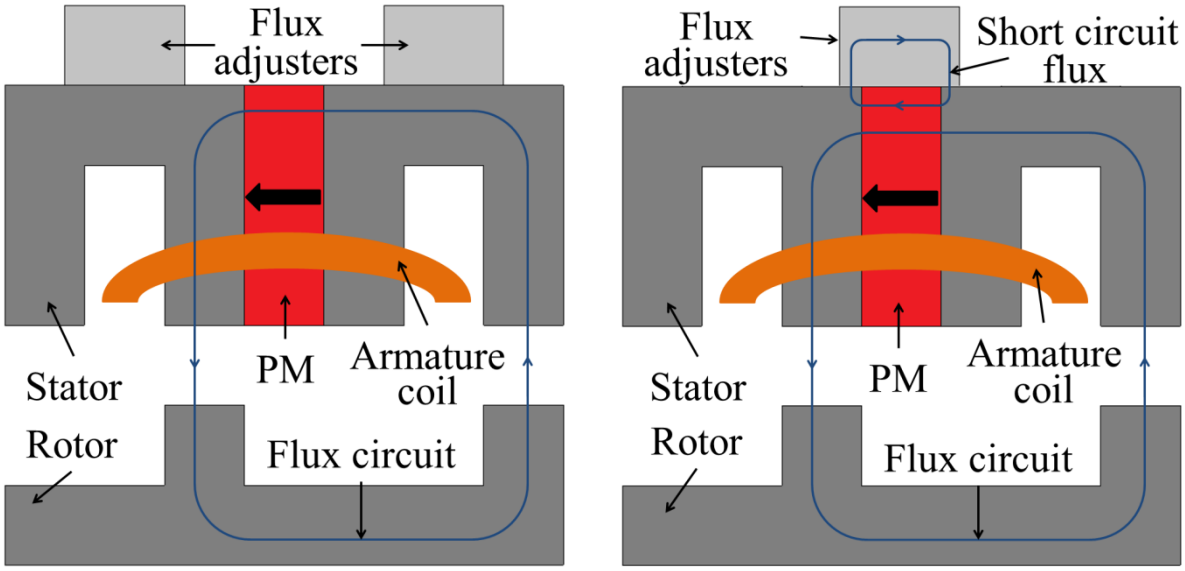

(a) Open position (b) Closed position

Fig. 4.1 Concept of flux adjusters in SFPM machines.

4.3. Different SFPM Machine Topologies

The studied SFPM machines are the same six machines investigated in the two previous chapters; they have the same outer diameter, axial length and airgap length, i.e. 90mm, 25mm and 0.5mm, respectively. Their major design parameters are listed in Table 2.1. Fig. 2.1 presents the cross-section of the six machines. Compared with the conventional SFPM machines, only half of FAs are required for the multi-tooth, E-core, and C-core SFPM machines, which can be considered as an advantage.

4.4. Influence of Flux Adjusters on Open Circuit Performance

4.4.1. Flux distribution

Fig. 4.2 illustrates the equipotential and flux density distributions of the six analysed SFPM machines with FAs at open and closed positions. By moving the FAs to the closed position, the short-circuited PM flux leads to lower airgap flux density as shown in Fig. 4.3. However, more reduction in the airgap flux density can be achieved in the multi-tooth, E-core, and C-core machines, i.e. 68%, 61% and 57%, when the FAs are located at the closed position, since the FA size of these machines are relatively larger than that of the conventional machines in which the reduction in the airgap flux density is about half of the original value.

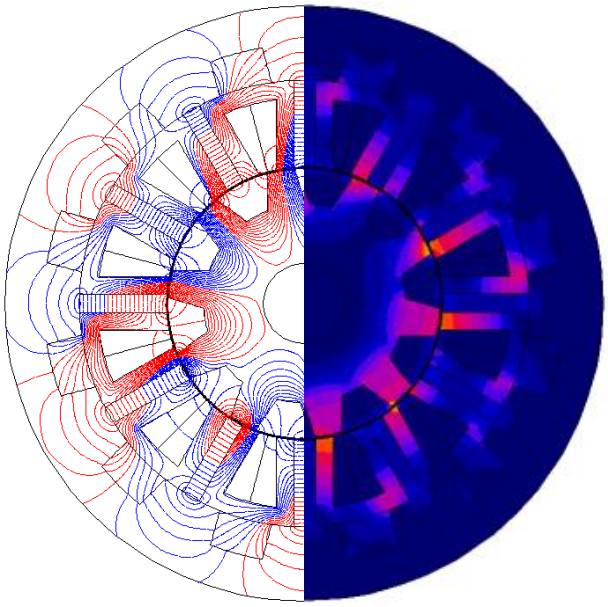

(a) 12/10 machine, FAs at open position

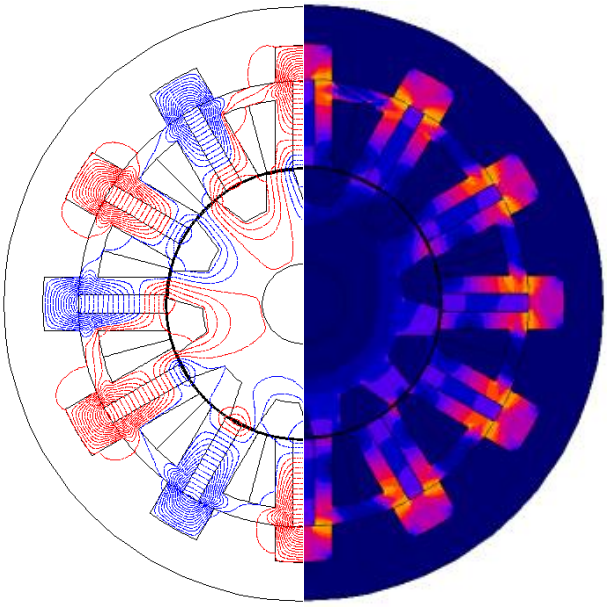

(b) 12/10 machine, FAs at closed position

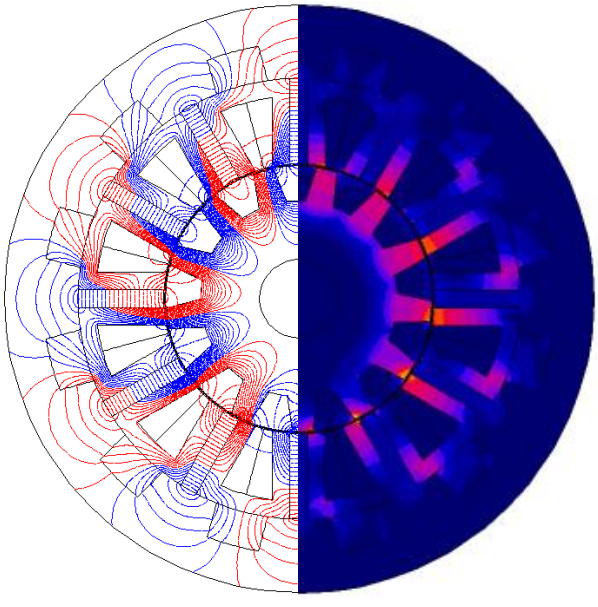

(c) 12/13 machine, FAs at open position

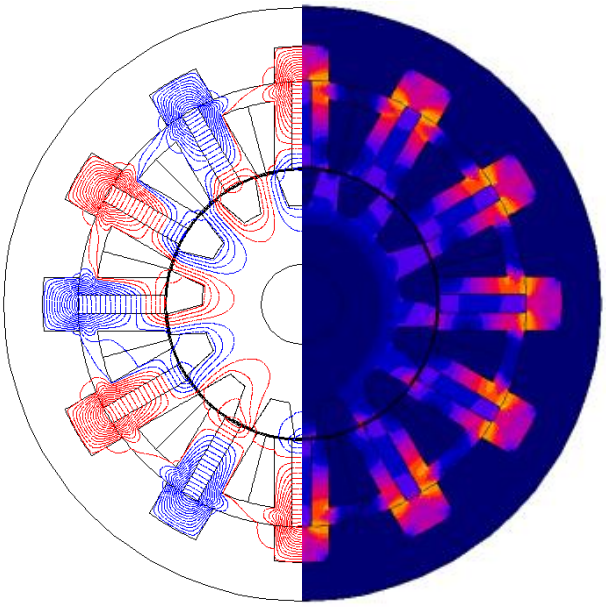

(d) 12/13 machine, FAs at closed position

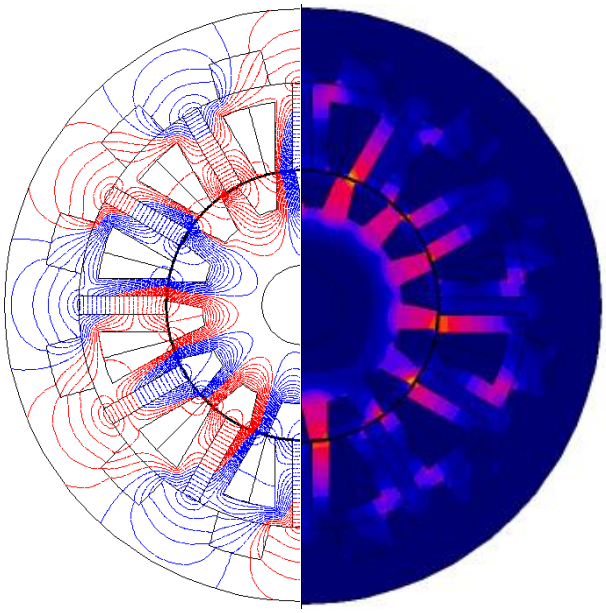

(e) 12/14 machine, FAs at open position

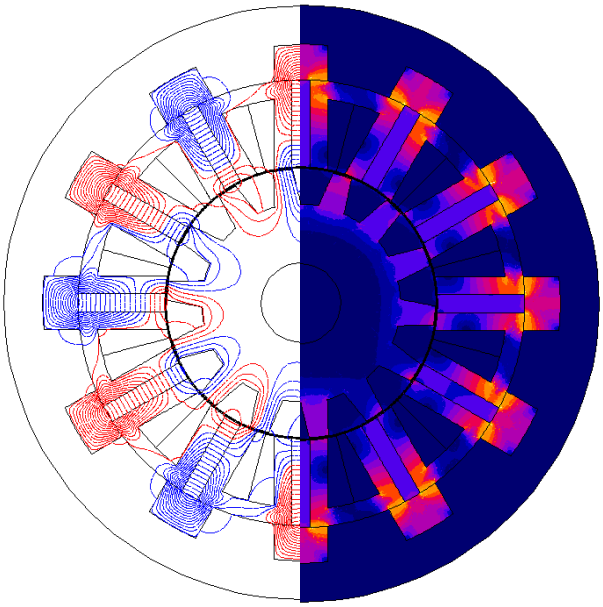

(f) 12/14 machine, FAs at closed position

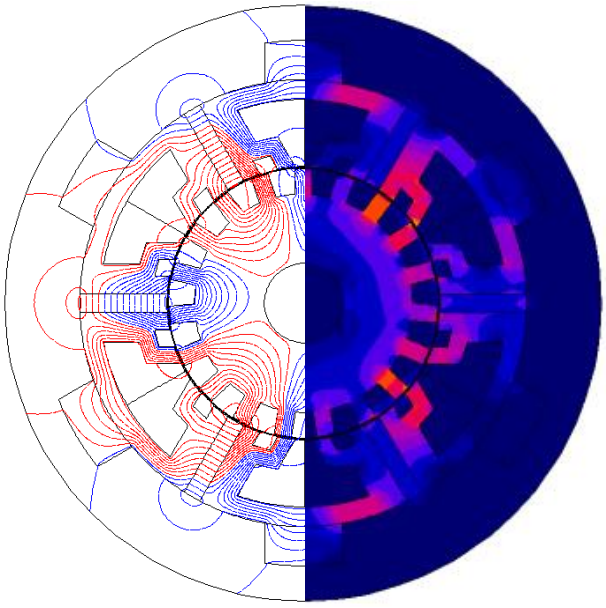

(g) M-tooth machine, FAs at open position

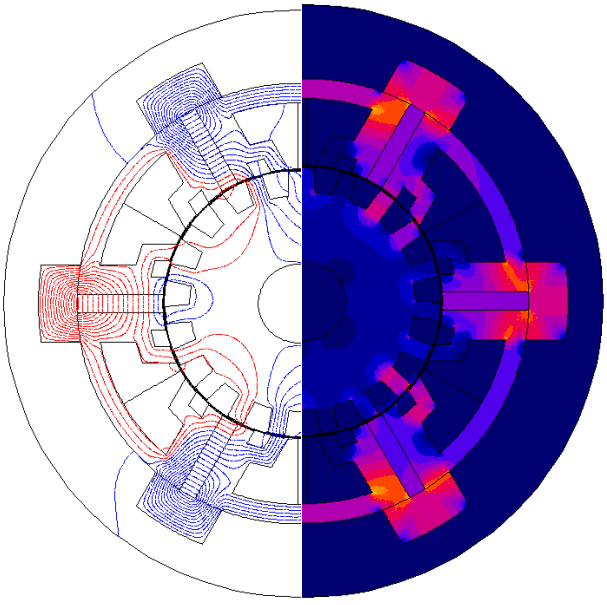

(h) M-tooth machine, FAs at closed position

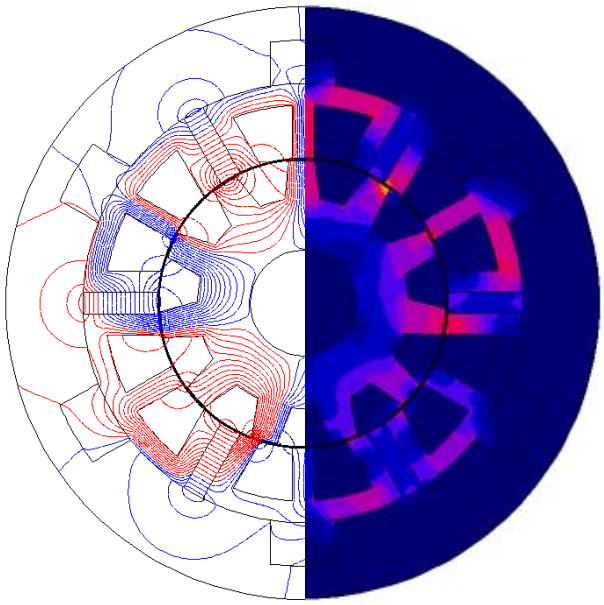

(i) E-core machine, FAs at open position

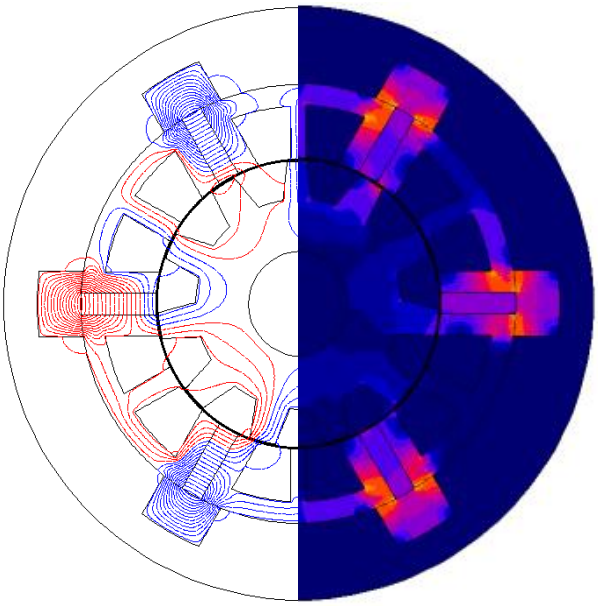

(j) E-core machine, FAs at closed position

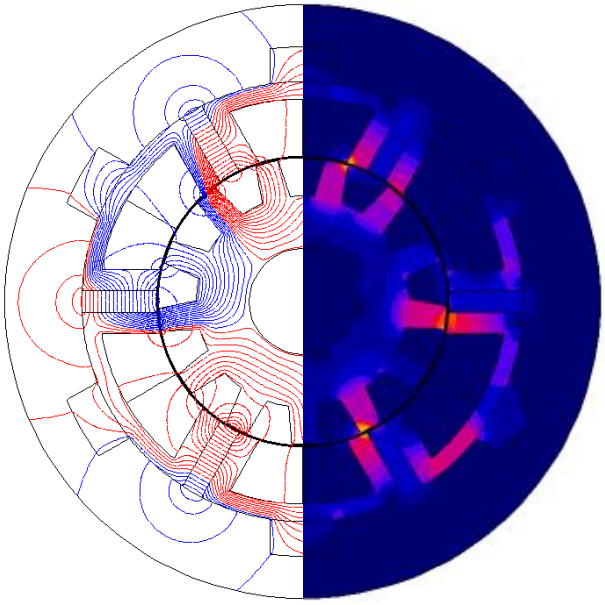

(k) C-core machine, FAs at open position

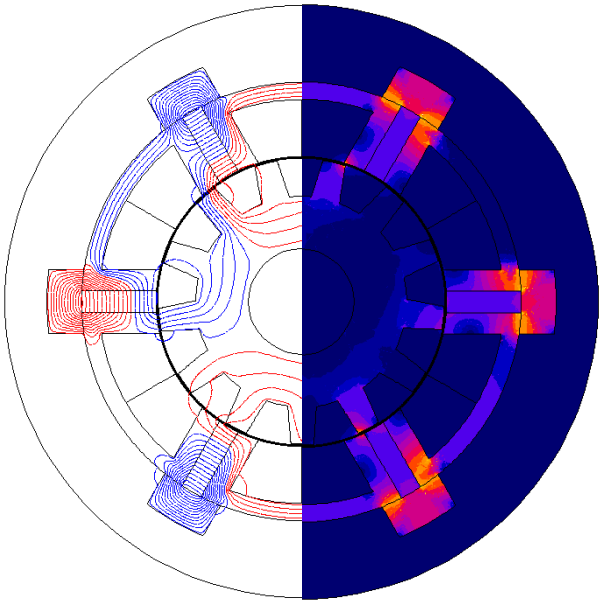

(l) C-core machine, FAs at closed position

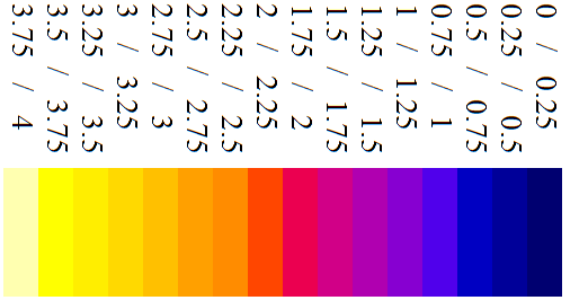

(m)Flux density (T) colour shade

Fig. 4.2 Comparison of equipotential and flux density distributions of SFPM machines with flux adjusters at open and closed positions.

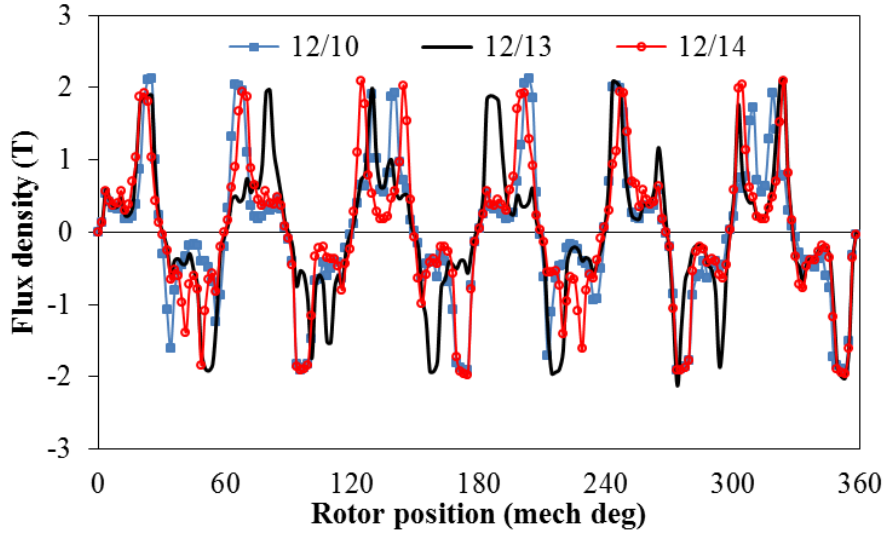

(a) 12/10, 12/13 and 12/14 conventional SFPM machines with FAs at open position

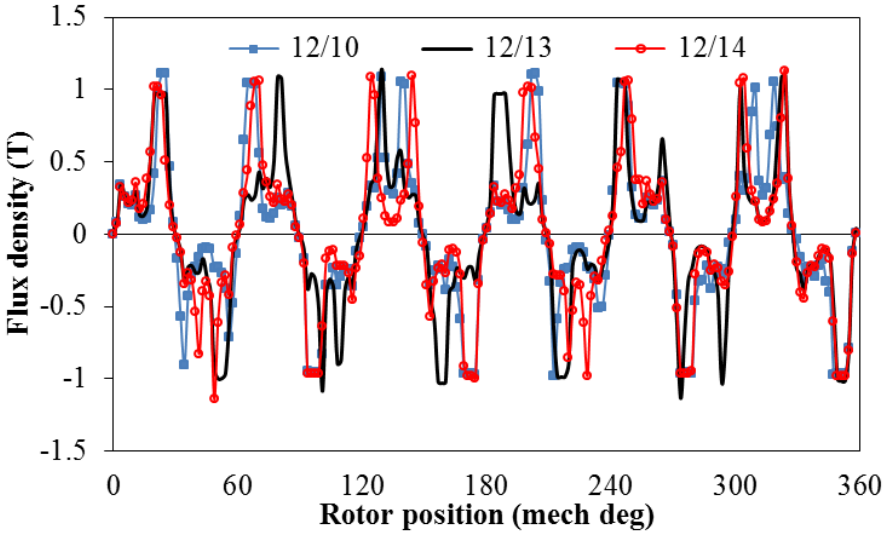

(b) 12/10, 12/13 and 12/14 conventional SFPM machines with FAs at closed position

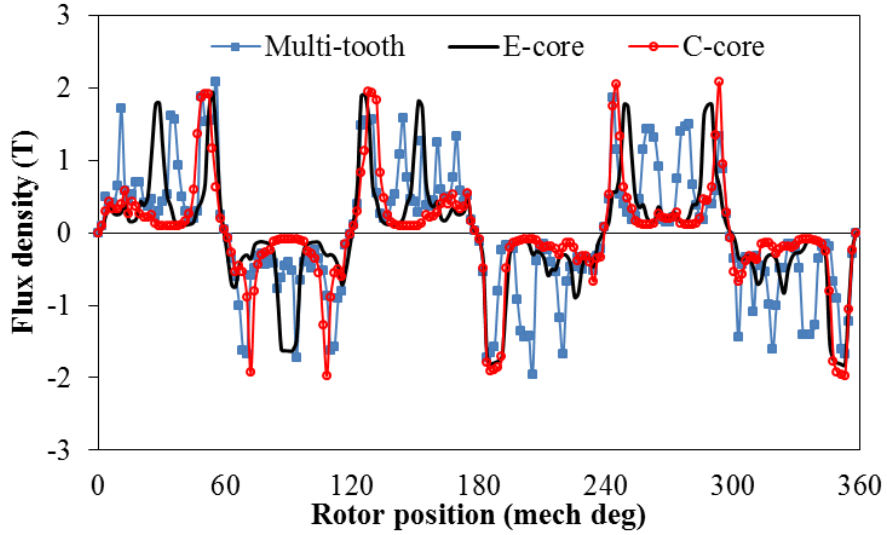

(c) Multi-tooth, E-core and C-core SFPM machine topologies with FAs at open position

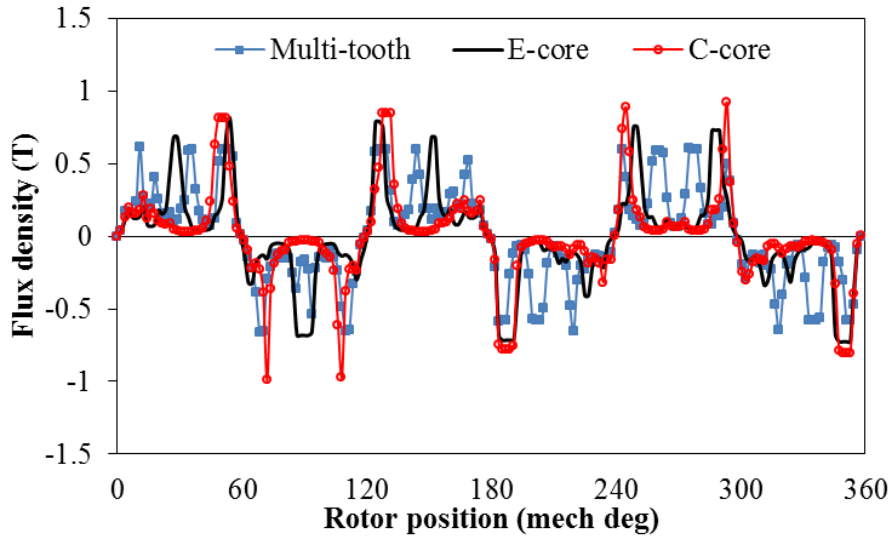

(d) Multi-tooth, E-core and C-core SFPM machine topologies with FAs at closed position

Fig. 4.3 Airgap flux density distributions of SFPM machines.

4.4.2. Back-EMF

Since the FAs at open position has no influence on the SFPM machine results, the back-EMF of the six analysed SFPM machines with FAs at open position is same as that without FAs presented in Chapter 1. When FAs are located at closed position the peak value of the back-EMF waveform in conventional machines is reduced at the same rate since same stator and FAs size is used. Therefore, the number of rotor pole has no influence on the level of flux when same FAs are used, Fig. 4.4. Moreover, the back-EMF of the multi-tooth, E-core and C-core machines reduces at different rates since different stators and FA sizes are used.

Fig. 4.5 presents the back-EMF harmonic order when FAs at open and closed positions. Since lower PM flux flowing through the machine when the FAs are in closed position, the magnetic saturation level reduces. Therefore, by placing the FAs in closed position the reduction in the high saturation level leads to higher harmonic effect as it can be seen in E-core and C-core machines, Fig. 4.5 (f). However, the 3rd harmonic in the 12/13 machine reduces when the FAs included due to the same reason, since the 3rd harmonic in this machine is generated due to the coils connection (see appendix A3).

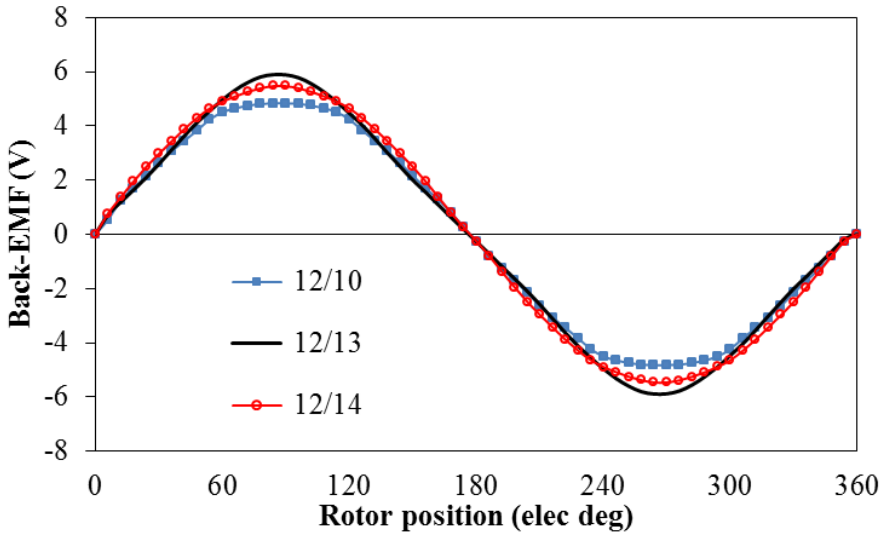

(a) 12/10, 12/13 and 12/14 conventional SFPM machines with FAs at open position

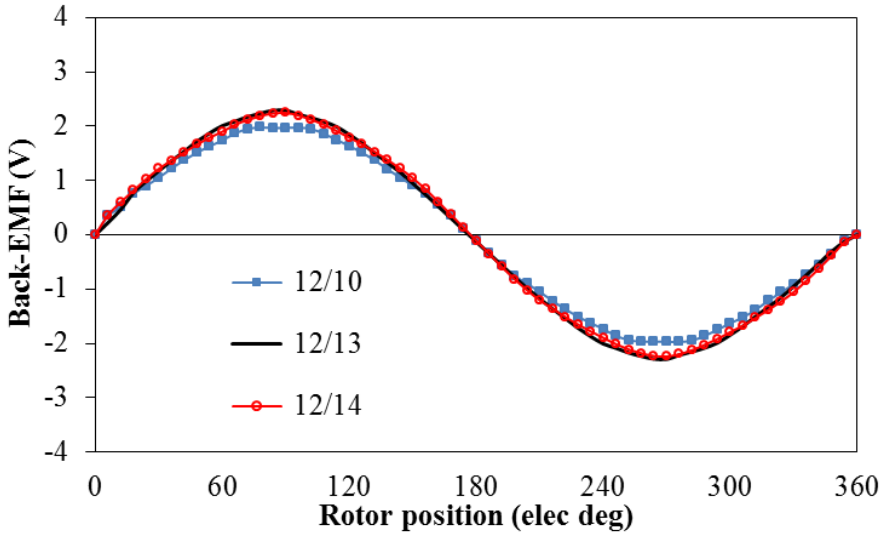

(b) 12/10, 12/13 and 12/14 conventional SFPM machines with FAs at closed position

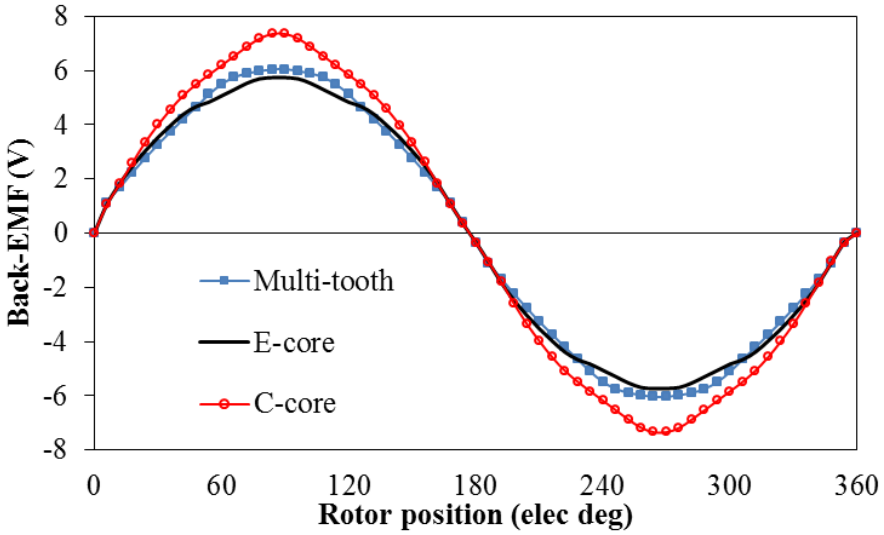

(c) Multi-tooth, E-core and C-core SFPM machine topologies with FAs at open position

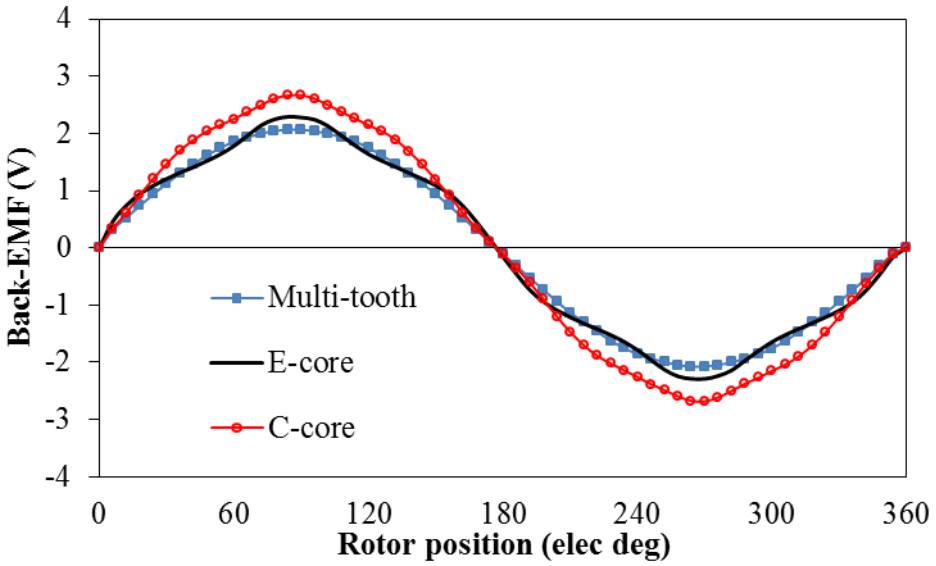

(d) Multi-tooth, E-core and C-core SFPM machine topologies with FAs at closed position

Fig. 4.4 Back-EMF waveforms of SFPM machine with FAs at open and closed positions (rotor speed=400rpm).

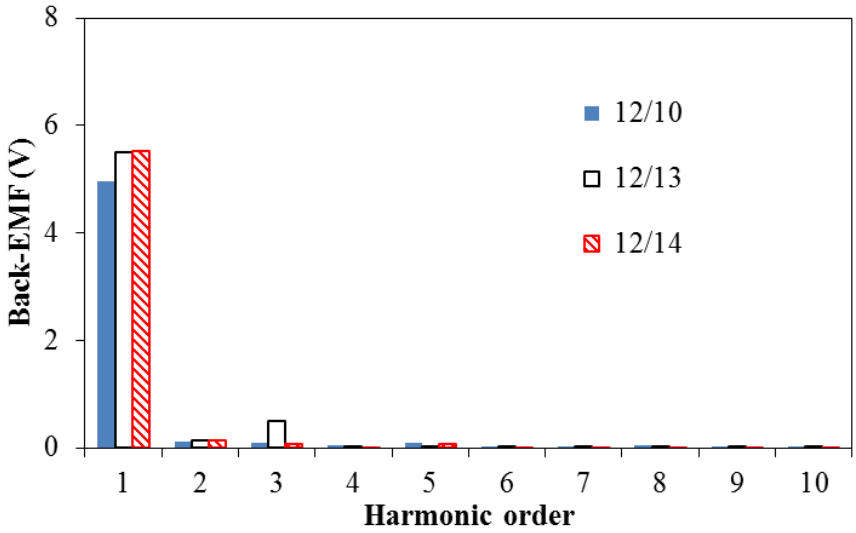

(a) 12/10, 12/13 and 12/14 conventional SFPM machines with FAs at open position

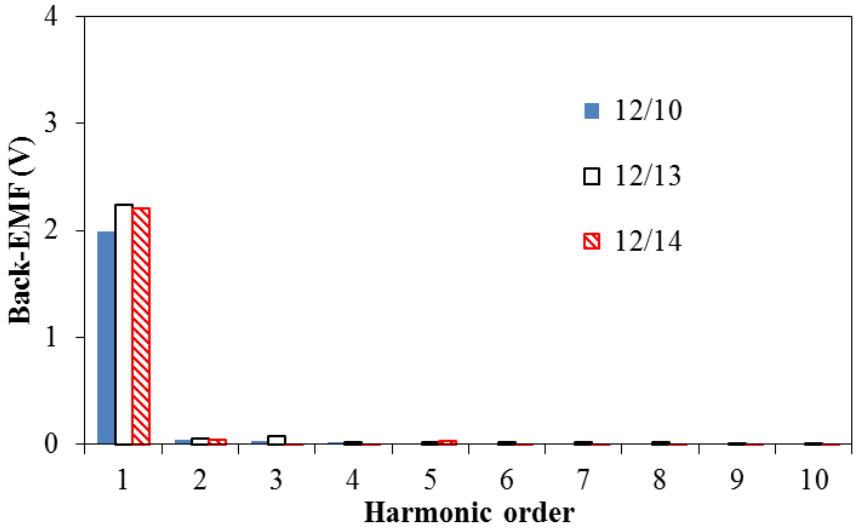

(b) 12/10, 12/13 and 12/14 conventional SFPM machines with FAs at closed position

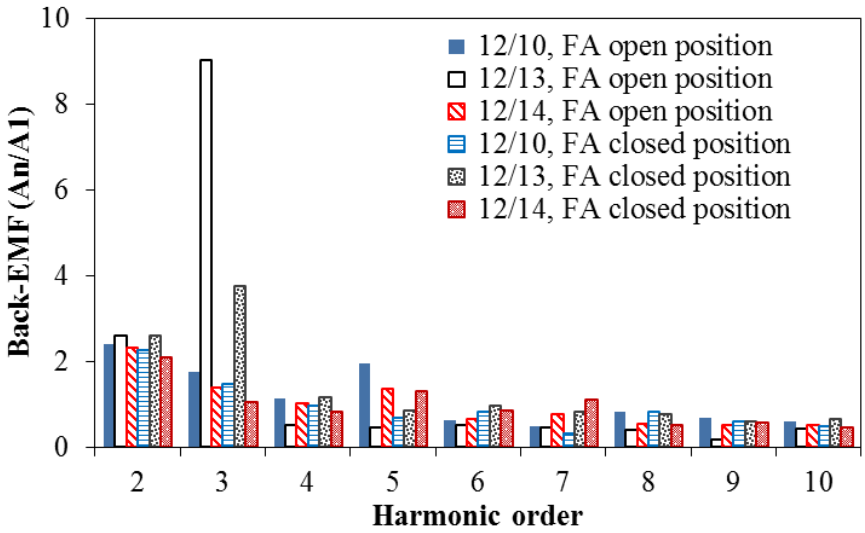

(c) Back-EMF harmonics (A1/An) of 12/10, 12/13 and 12/14 conventional SFPM machines

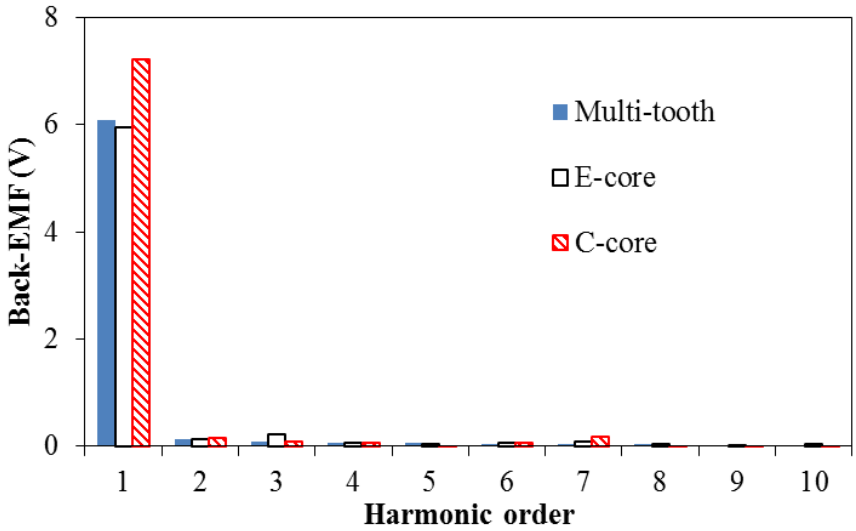

(d) Multi-tooth, E-core and C-core SFPM machine topologies with FAs at open position

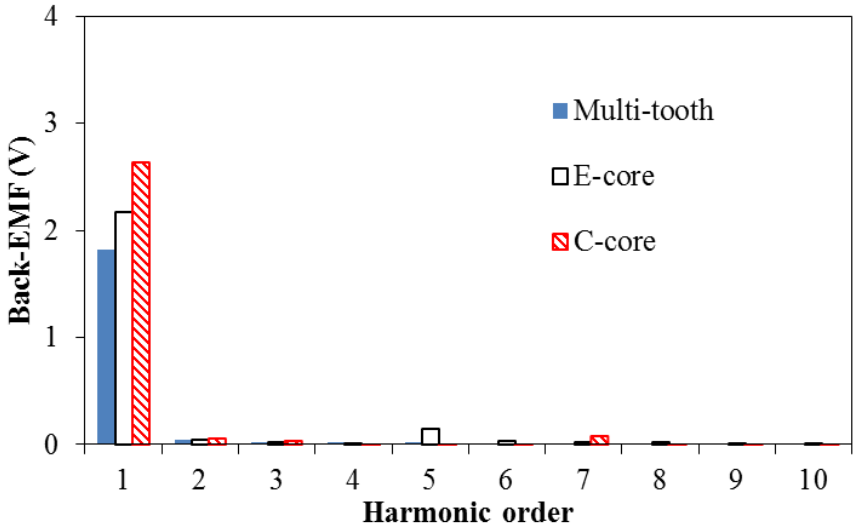

(e) Multi-tooth, E-core and C-core SFPM machine topologies with FAs at closed position

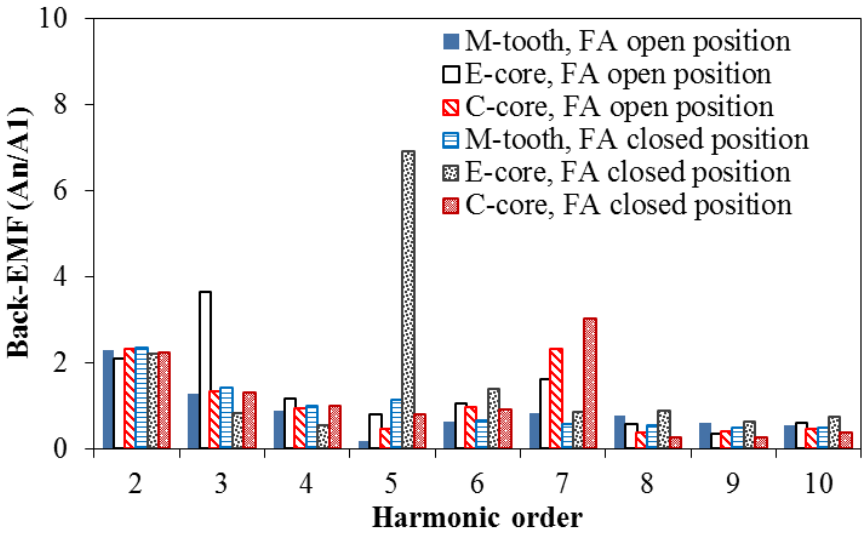

(f) Back-EMF harmonics (An/A1) of Multi-tooth, E-core and C-core SFPM machines

Fig. 4.5 Back-EMF harmonics in SFPM machine with FAs at open and closed positions.

4.4.3. Cogging torque

In PM machines the electromagnetic torque ripple is mainly due to cogging torque, back-EMF harmonics, and variation of d- and q-axis inductances, i.e. reluctance torque ripple [23]. However, the d- and q-axis inductances are nearly equal in the SFPM machine. Therefore, negligible reluctance torque is produced and no contribution to the electromagnetic torque is exhibited [24]. On the other hand, the conventional SFPM machines are characterised by their essentially sinusoidal back-EMF waveform with relatively small harmonics. Therefore, the cogging torque is the main source of the torque ripple in conventional SFPM machines. Fig. 4.6 highlights the influence of the FAs on the cogging torque. As illustrated in Chapter 2, when FAs located at open position, the 12/13 machine has the lowest cogging torque among

the conventional machines due to the odd number of rotor poles. However, compared with the 12/14 machine, the 12/10 machine has the highest cogging torque, since a high number of stator/rotor pole combinations reduces the net distribution of the flux density leading to lower cogging torque. Moreover, the lowest cogging torque is observed in the multi-tooth machine due to the large number of rotor poles. Although the E-core and C-core machines have odd rotor pole number, they still generate relatively large cogging torque due to the wide slot opening which creates large reluctance variation along the airgap.

In general, adding the FAs results in cogging torque reduction, since the airgap flux density is reduced. The largest reduction is observed in the E-core and C-core machines, i.e. 80% and 77%, respectively. Whereas, the cogging torque in multi-tooth machine reduces about 45%. On the other hand, the cogging torque reduces about 54% in the 12/10 machine while only 8% and 23% reductions are exhibited in the 12/13 and 12/14 machines, respectively. Since the cogging torque is almost proportional to the square of airgap flux density and due to the influence of salient rotor on stator flux density [25], the cogging torque reductions are different when FAs at closed position, although the airgap flux density reduced at the same rate.

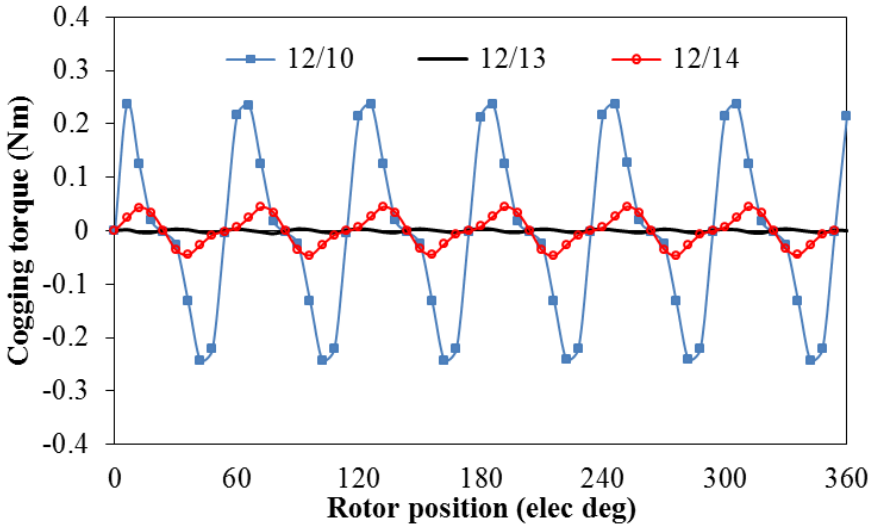

(a) 12/10, 12/13 and 12/14 conventional SFPM machines with FAs at open positions

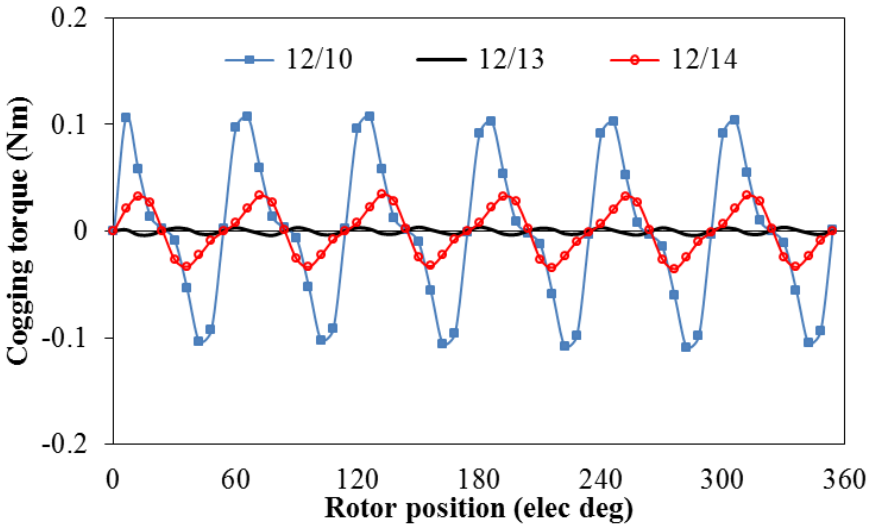

(b) 12/10, 12/13 and 12/14 conventional SFPM machines with FAs at closed positions

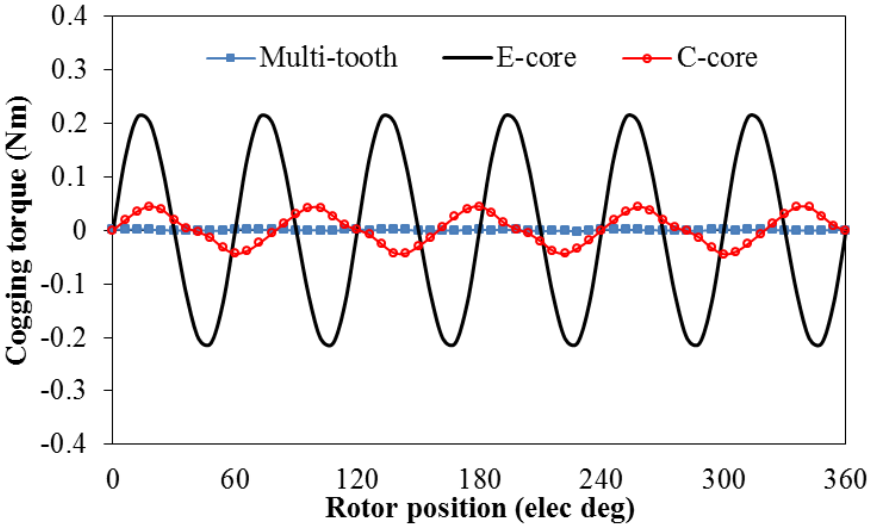

(c) Multi-tooth, E-core and C-core machines with FAs at open position

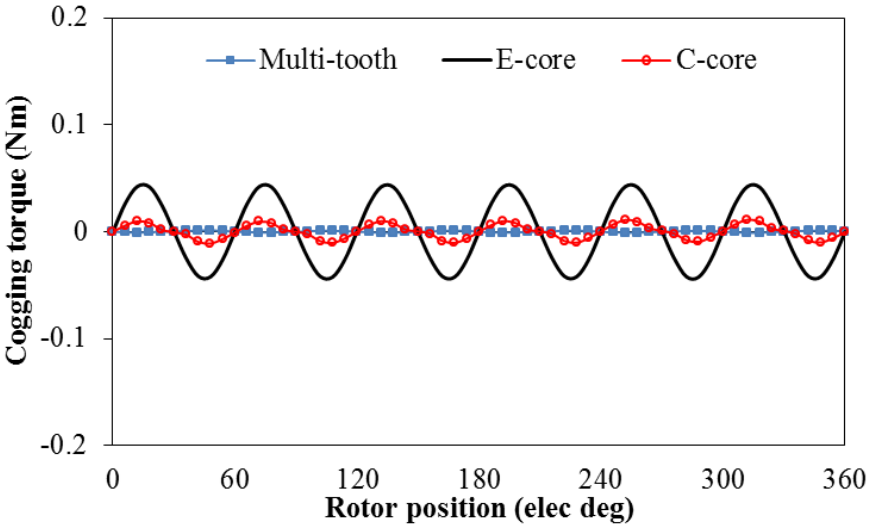

(d) Multi-tooth, E-core and C-core machines with FAs at open position

Fig. 4.6 Influence of flux adjusters on cogging torque of SFPM machines.

4.5. Influence of Flux Adjusters on On-Load Performance

4.5.1. PM flux linkage

When the FAs are located at open position, the PM flux-linkage of the multi-tooth, E-core and C-core machines reduces at relatively low current level due to the magnetic cross-coupling and saturation, which is higher than that of the conventional machines, Fig. 4.7. The reason is that the multi-tooth, E-core and C-core machines have higher electric loading and lower permeances in the magnetic circuit compared to that of the conventional machines. Moreover, the multi-tooth machine saturates at relatively low current compared to the E-core and C-core machines due to the small rotor and stator teeth. The E-core machine produces higher PM flux linkage at higher current compared to that of the C-core machine due to its thicker back-iron, Fig. 4.7 (b). However, the magnetic saturation effect appears at higher current levels when the FAs are located at closed position since the majority of PM flux is short-circuited thus less flux flows through the active magnetic circuit of the machine.

However, the reduction in the open circuit PM flux linkage of the three conventional machines is about 60%. On the other hand, 65% reduction is observed in the multi-tooth machine, whereas similar reduction of 63% is exhibited in both E-core and C-core machines. It shows that when the FAs are used, the PM flux-linkage reductions are different from those of the airgap flux density, which is mainly due to the different flux-leakages in these machines, as shown in Fig. 4.2.

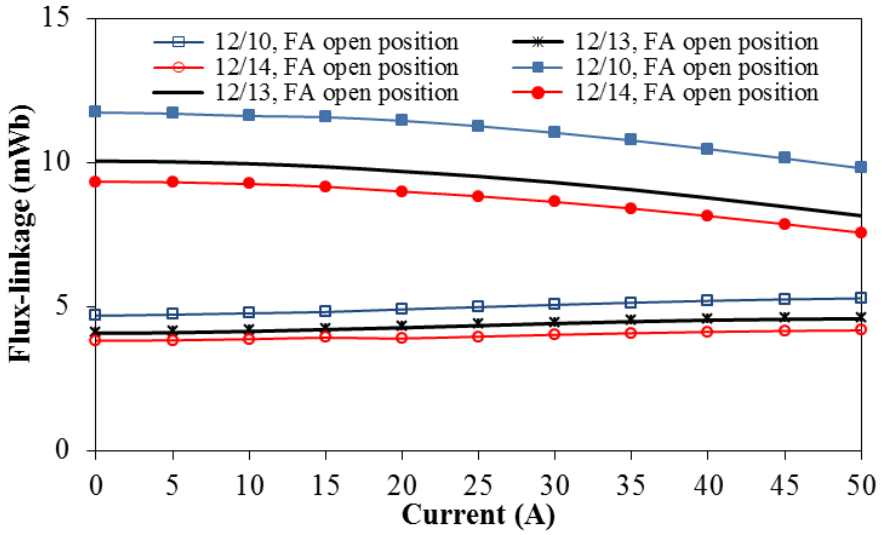

(a) 12/10, 12/13 and 12/14 conventional SFPM machines

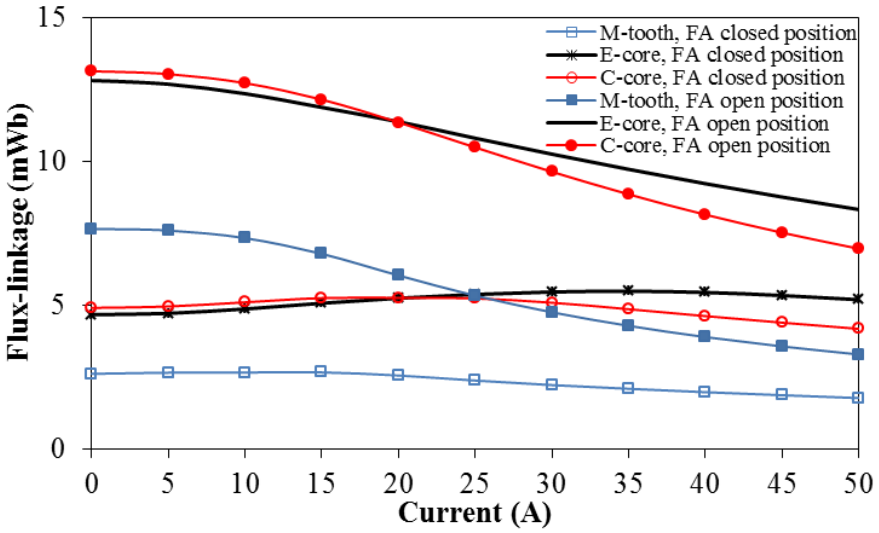

(b) Multi-tooth, E-core and C-core SFPM machine topologies

Fig. 4.7 PM flux-linkage of SFPM machines with FAs at open and closed positions.

4.5.2. Electromagnetic torque

Comparison between the electromagnetic torque waveforms of the conventional, multi-tooth, E-core, and C-core SFPM machines with the FAs at open and closed positions under load condition of (I_q=15, I_d=0) is presented in Fig. 4.8. According to (1-7), the average torque reduction percentage due to placing FAs at the closed position is the same as its counterparts of the PM flux linkage. From the comparison, the lowest torque ripple is observed in the multi-tooth SFPM machine regardless of the position of FAs. However, the highest average torque can be achieved in the C-core SFPM machine.

Table 4.1 presents a comparison between the torque ripple percentage in the six SFPM machines with FAs at open and closed positions. When the FAs are added in open position, the back-EMF waveforms of the E-core and C-core machines have significant 5^{th} and 7th harmonic, respectively. Therefore, with FAs in closed position, the torque ripple is higher although the cogging torque reduces at lower rate compared to the average torque. Moreover, the torque ripple percentage in the multi-tooth and conventional machines increases when FAs at closed position, since the reduction rate in the cogging torque is lower than that of the average torque.

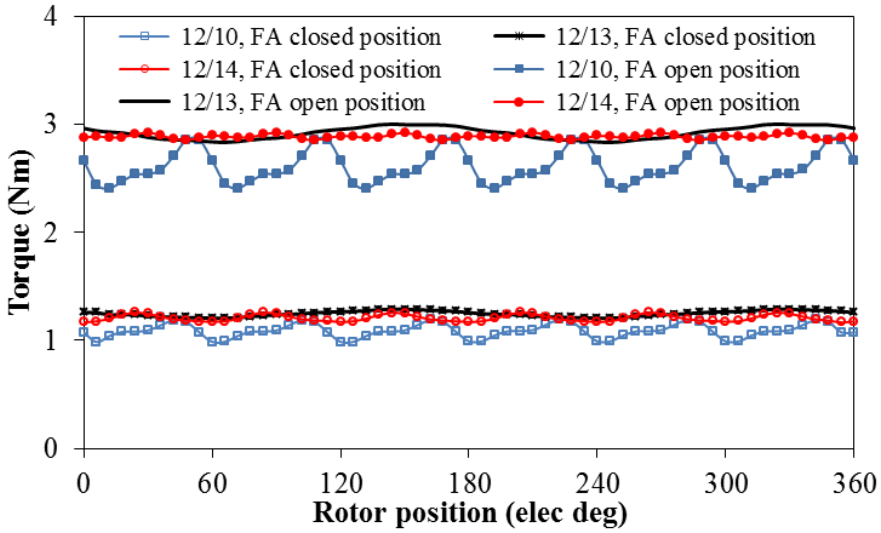

(a) 12/10, 12/13 and 12/14 conventional SFPM machines

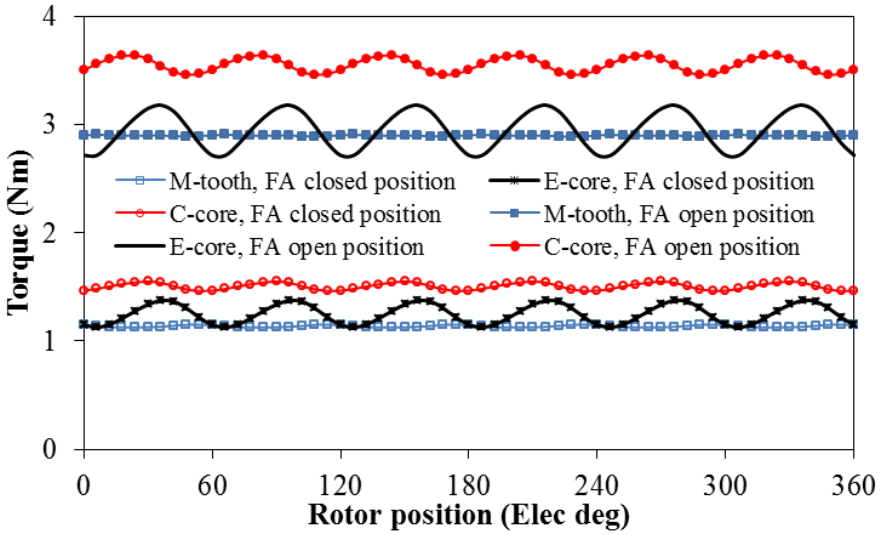

(b) Multi-tooth, E-core and C-core SFPM machine topologies

Fig. 4.8 Comparison of electromagnetic torque of SFPM machines with FAs at open and closed positions under load condition of (I_q=15A, I_d=0).

Table 4.1 Comparison of cogging torque and torque ripple of SFPM machines with FAs at open position (OP) and closed position (CP)

Machine		Higher torque peak	Lower torque peak	Peak to peak torque	Torque ripple %	Average torque	Cogging torque peak
12/10	OP	2.85	2.4	5.26	15.67	2.6	0.23
	CP	1.19	0.98	2.17	17.02	1.08	0.1
12/13	OP	3	2.83	5.83	5.61	2.92	0.004
	CP	1.3	1.2	2.49	6.49	1.24	0.003
12/14	OP	2.92	2.85	5.77	2.26	2.88	0.042
	CP	1.25	1.17	2.43	6.6	1.2	0.034
M-tooth	OP	2.8	2.76	5.57	1.46	2.79	0.005
	CP	1.06	1.03	2.09	2.27	1.04	0.0006
E-core	OP	3.17	2.71	5.89	14.6	2.94	0.21
	CP	1.37	1.12	2.5	17.9	1.25	0.04
C-core	OP	3.63	3.46	7.09	4.89	3.54	0.04
	CP	1.55	1.46	3	5.59	1.5	0.01

4.6. Inductances

4.6.1. Influence of flux adjusters on the inductance

In order to improve the accuracy of the performance prediction, the influence of the magnetic saturation and cross-coupling effect on the d- and q-axis inductances is accounted for. Therefore, the same method used in Chapter 2 to calculate the inductance is used in this section.

Moreover, the PM short-circuited flux creates high magnetic saturation in the near PM side back iron and stator tooth, as highlighted in Fig. 4.9 (a). This saturation will reduce the inductance of armature winding. Therefore, in the conventional machines, the inductance reduces when the FAs are at closed position. The d-axis inductance values are lower than the q-axis inductances when FAs are at open position. However, the d-axis inductances exceeds the q-axis inductance when FAs are moved to closed position, since the PM flux-linkage is reduced significantly leading to less magnetic saturation along the d-axis path as well as the FAs create new path for the d-axis flux as illustrated in Fig. 4.9 (b). However, it can be seen that at high d-axis current both d- and q- axis inductances reduce significantly, since the d-axis flux pushes the PM flux toward the FA which leads to the increase of magnetic saturation in the near PM side back iron and stator pole.

On the other hand, due to the wider stator tooth in the E-core and C-core, the q-axis flux reduces at lower rate compared to that of the conventional machines when FAs are at closed position. Moreover, the d-axis inductance at low d-axis current levels when FAs are at closed position is higher than the original values when FAs are at open position. At higher d-axis currents the influence of the magnetic saturation reduces the inductance leading to lower values compared to that of when FAs are at open position. In the multi-tooth machine, at low d-axis current both d- and q-axis inductances increase when FAs are added to closed position. Since the multi-tooth machine has the widest stator tooth and lowest PM flux-linkage, less saturation in the near PM side back iron occur when FAs are at closed position. However, the reduction in the inductances at high currents is due to the magnetic saturation level in the back-iron and the small stator teeth and rotor poles, Fig. 4.2. Nevertheless, when larger FA size is used in the E-core and C-core machines similar inductance reduction phenomenon as the conventional machines is observed, since wider FA leads to higher magnetic saturation in the near PM side back iron and therefore lower armature flux-linkage (see next section).

Since the three conventional machines using the same stator and FA size, same magnetic saturation level in the near PM side back iron is created leading to similar inductance levels in the three machines when FAs at closed position, Fig. 4.10. On the other hand, although the same reduction in PM flux-linkage in E-core and C-core machines is exhibited at low current levels and the C-core machine has higher inductances compared to the E-core when FAs at open position, the inductance reduction in the E-core machine is higher than that of the C-core machine since the later has higher number of turns per phase. Furthermore, the reduction in the inductance is larger in conventional machines compared to multi-tooth, E-core and C-core machines due to the higher number of turns per coil and wider stator tooth.

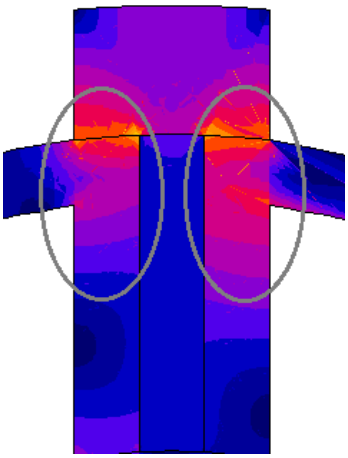

(a) Magnetic saturation in near PM side back-iron

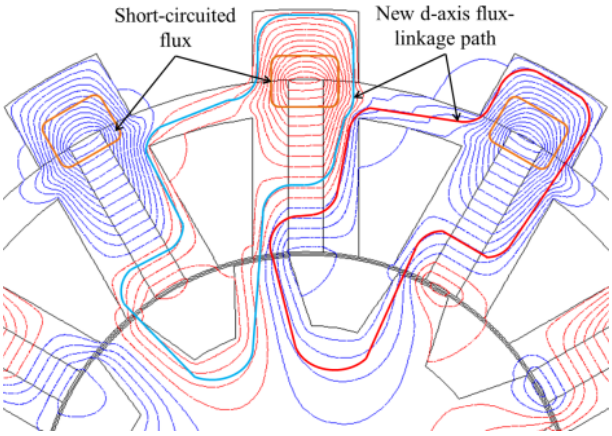

(b) D-axis flux linkage paths

Fig. 4.9 Saturation phenomenon in SFPM machine with flux adjusters.

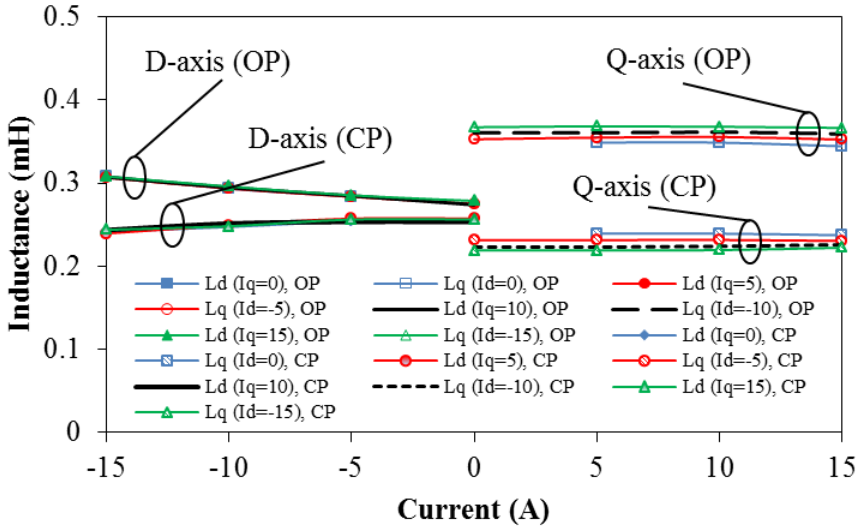

(a) 12/10 conventional machine

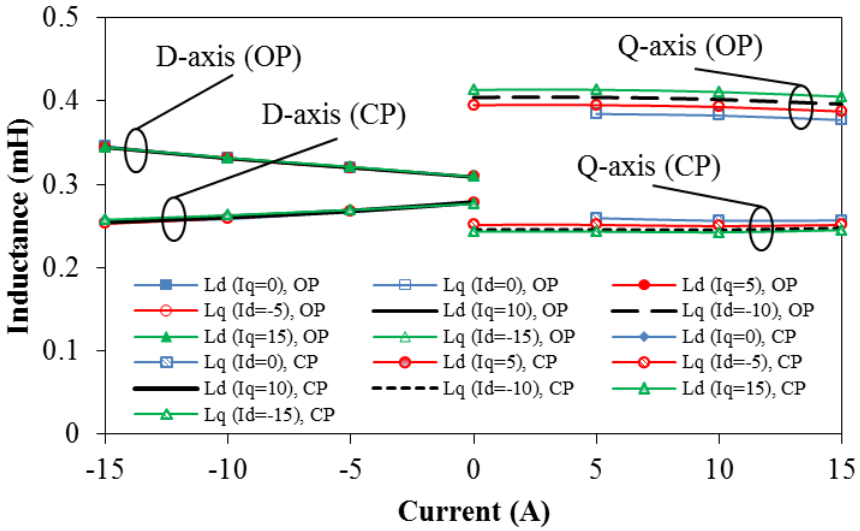

(b) 12/13 conventional machine

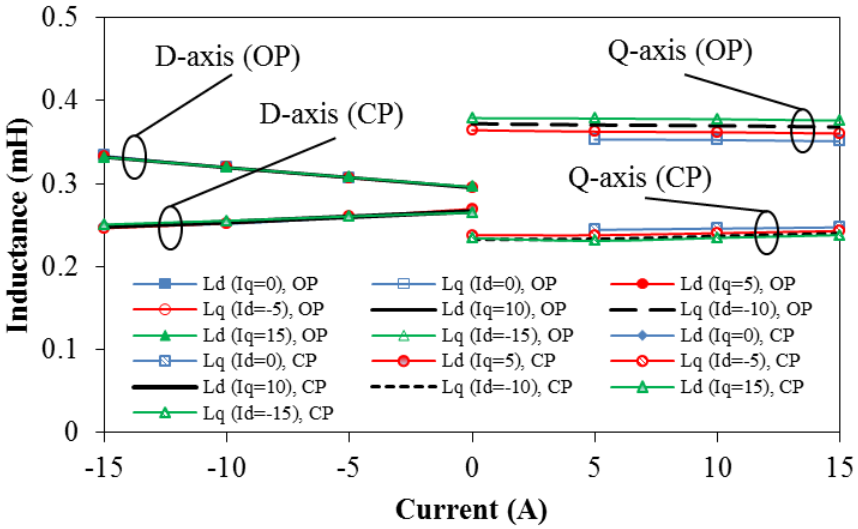

(c) 12/14 conventional machine

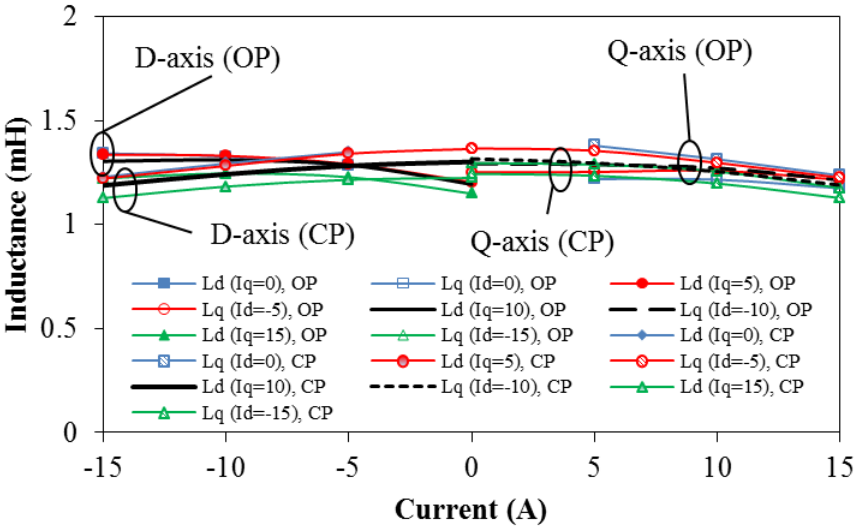

(d) Multi-tooth machine

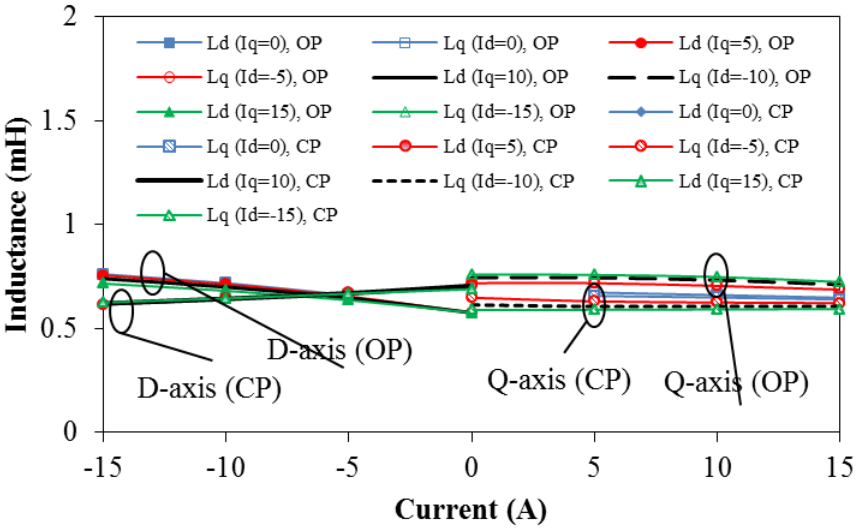

(e) E-core machine

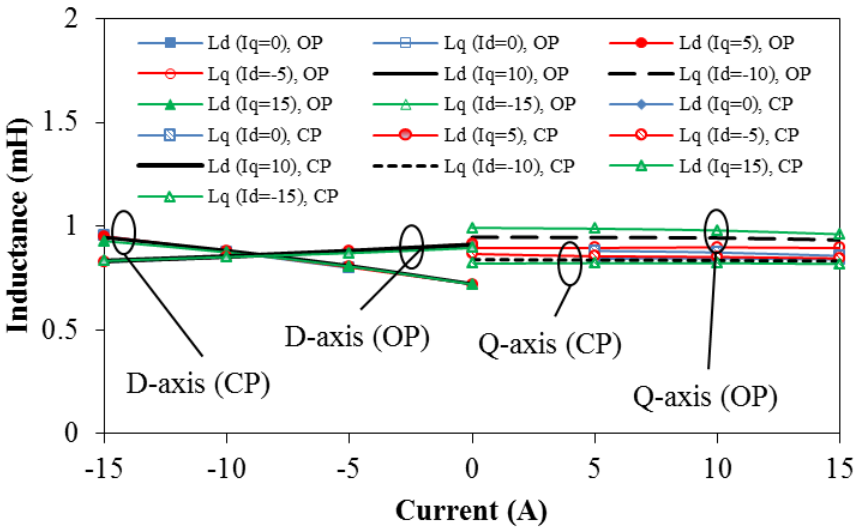

(f) C-core machine

Fig. 4.10 D- and q-axis inductances of SFPM machines with flux adjusters at open position (OP) and closed positions (CP).

4.6.2. Influence of flux adjuster size on the inductance

By using different sizes of FAs as shown in Fig. 4.11, the inductance values vary significantly. When small size of FA is used, i.e. size 1 (S1), the d-axis inductance increases to larger values at low current levels compared to the original d-axis inductance, i.e. without FAs, whereas lower q-axis inductance is observed. The reason is the lower PM flux linkage reduces the saturation along the d-axis path, i.e. flux weakening, and consequently larger d-axis inductance is observed at low currents, where the saturation in the near PM side back-iron reduces the q-axis flux. However, when high d-axis current is used, the saturation level in the stator teeth and near PM side back-iron increases leading to lower d- and q-axis inductances. On the other hand, when larger FAs are used, i.e. size 2 and 3 (S2 and S3), the saturation level in the stator teeth and near PM side back-iron increases significantly leading to lower inductance values compared with the conventional state without FAs. Overall, the ratio of the d- to q-axis inductances increases when FAs added to the machine due to the reduction in the saturation along the d-axis, reduction in the PM flux flowing in the d-axis path.

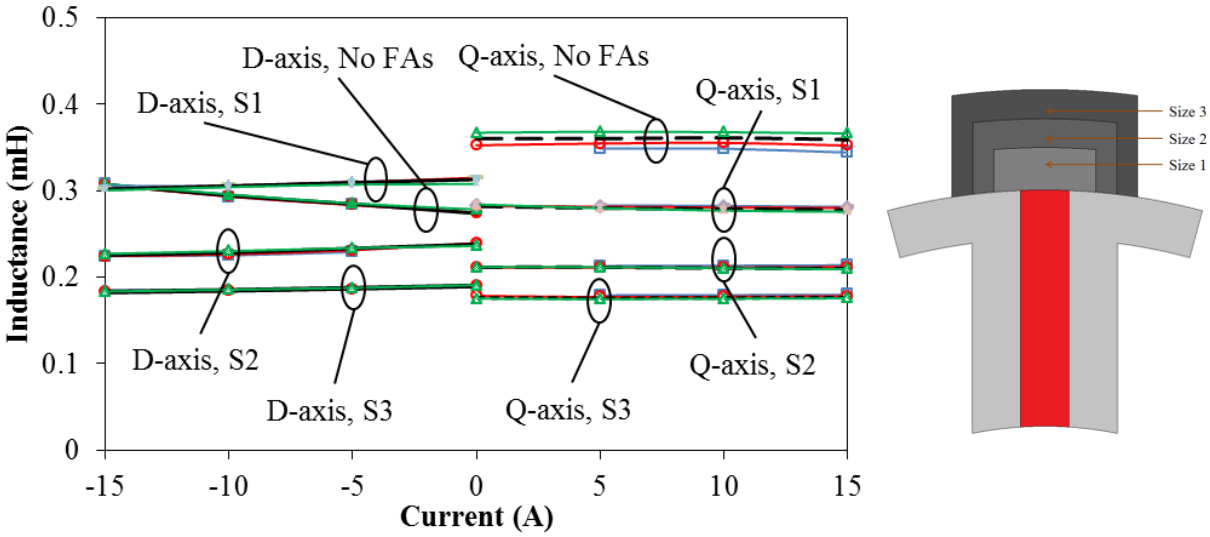

(a) Inductances (b) Flux adjuster sizes

Fig. 4.11 D- and q-axis Inductances of SFPM machine with different flux adjuster sizes.

4.7. Torque-Speed Characteristics in SFPM Machines with Flux Adjusters

Since high speed and efficiency are required in many industrial applications, such as automotive. The torque-speed characteristic is considered as a key character of PM machines. Therefore, the FAs are used to improve the operation speed range and flux weakening capability in the SFPM machines. The influence of the FAs on the torque-speed characteristic of the six SFPM machines is investigated. Using the 2D-FEA predicted inductances and PM flux-linkage as well as (1-6) and (1-10), the torque-speed curves are calculated and shown in Fig. 4.12.

Tables 4.2 and 4.3 show the comparison of d-axis inductance, PM flux-linkage, flux-weakening factor, maximum torque, speed and power of the conventional, multi-tooth, E-core and C-core machines. Although in the conventional machines the d-axis inductances reduce when FAs are added at closed position, the flux weakening factor of those machines still improves due to the large reduction in PM flux-linkage. Therefore, when the FAs are at open position, larger torque but limited maximum speed and small flux weakening capability are exhibited by the conventional SFPM machines. On the other hand, lower torque while much higher maximum speed and flux weakening capability can be obtained if the FAs are at closed position. It shows that when the FAs at closed position, the flux-weakening factor in 12/13 and 12/14 SFPM machines approach 1, which indicates the infinite speed range. In 12/10 SFPM machine, due to higher PM flux-linkage the flux-weakening factor cannot reach

to 1, although the speed range has been increased significantly. Therefore, the higher the rotor pole number, the better the flux weakening factor improvement due to lower PM flux-linkage.

Moreover, in the multi-tooth, E-core and C-core SFPM machines, the base speed slightly increases since the PM flux-linkage is reduced when FAs are at closed position. Due to the relatively large d-axis inductance the FAs do not provide the improvement which is achieved in the conventional SFPM machines. Without the FAs, the multi-tooth, and C-core SFPM machines already have the infinite speed range and the flux-weakening factor is higher than 1. Thus, the equipment of FAs will mainly improve the efficiency at high speeds. Furthermore, the flux-weakening factor of the E-core machine increases from 0.9 to 1.97. Therefore, when the FAs are used at closed position, the flux weakening capability improves at high speed.

In terms of maximum power, a very narrow constant power region is observed in the conventional machines when FAs are at open position. However, by moving the FAs to closed position, the maximum peak power maintained and the constant power region significantly extended. On the other hand, in multi-tooth, E-core and C-core machines the flux weakening factor increases further than 1 due to the reduction of the PM flux-linkage leading to lower torque and therefore lower power.

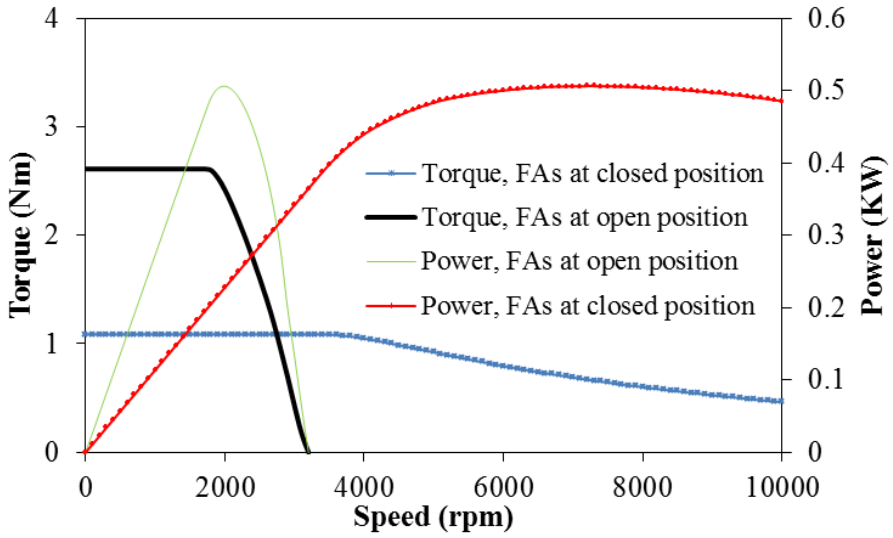

(a) 12/10 conventional machine

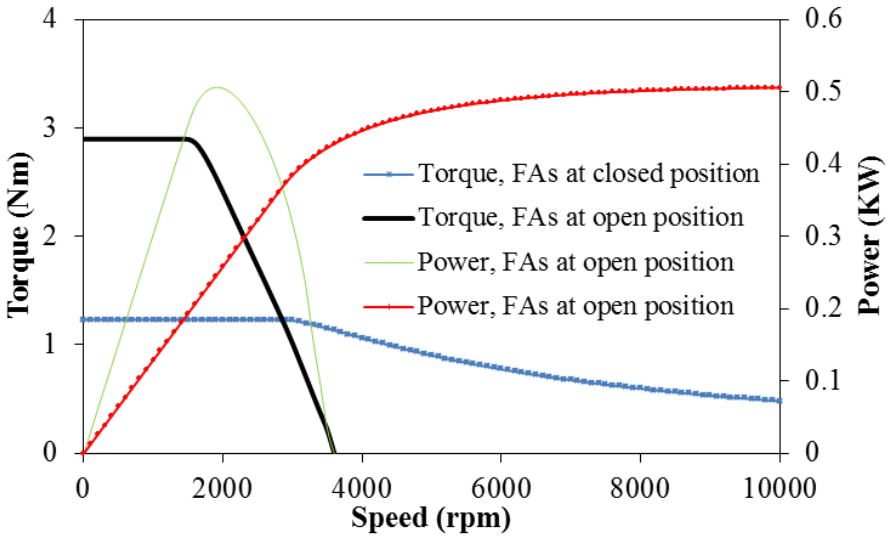

(b) 12/13 conventional machine

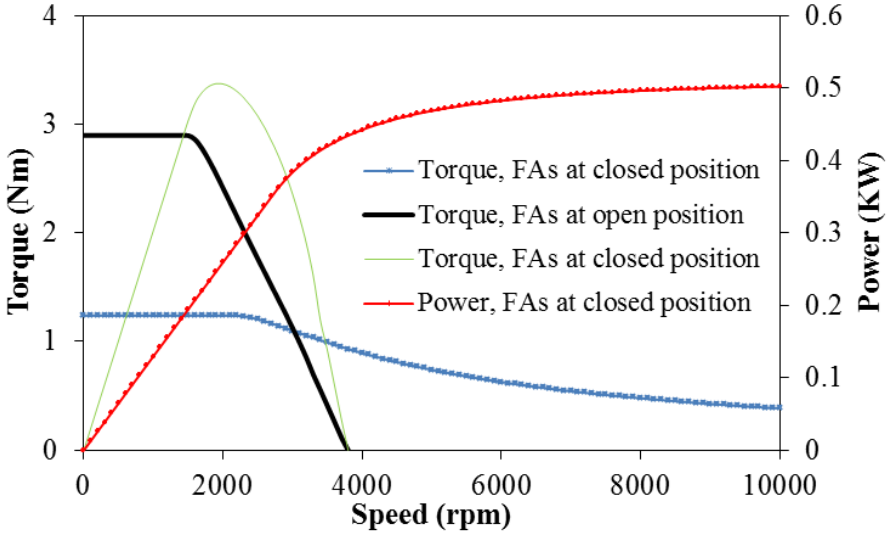

(c) 12/14 conventional machine

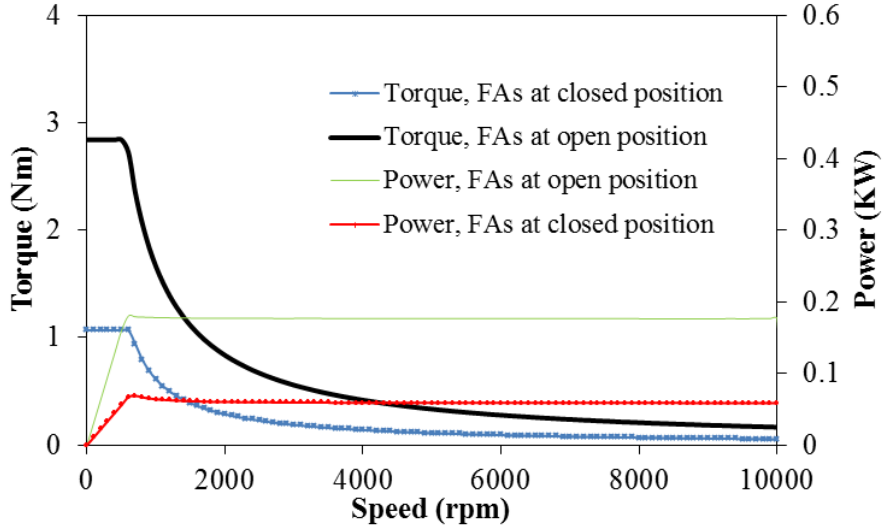

(d) Multi-tooth machine

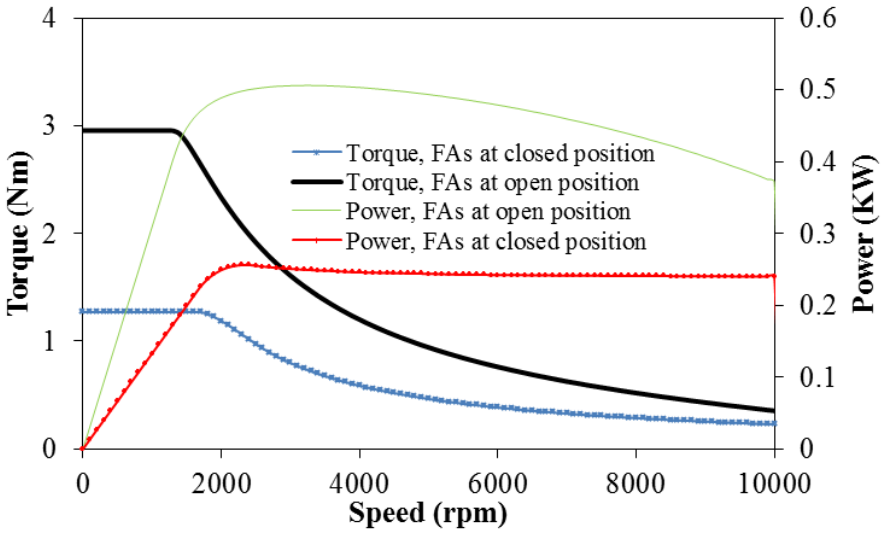

(e) E-core machine

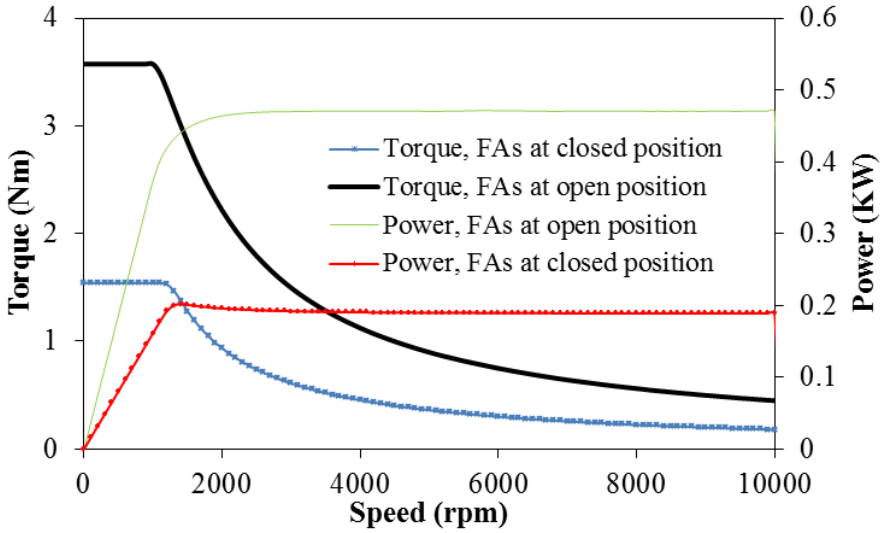

(f) C-core machine

Fig. 4.12 Torque- and power-speed curves of SFPM machines with FAs at open and closed positions under load condition of (I_{max}=15A, $V_{DC\text{-}link}$=36V).

Table 4.2 Comparison of d-axis inductance, PM flux linkage and flux weakening factor of SFPM machines with FAs at open position (OP) and closed position (CP)

Machine		L_d (mH)	Ψ_{pm} (Wb)	K_{fw}
12/10	OP	0.308	0.0117	0.39
	CP	0.242	0.0046	0.77
12/13	OP	0. 346	0.0101	0.51
	CP	0.255	0.0041	0.93
12/14	OP	0.333	0.0093	0.53
	CP	0.249	0.0038	0.99
M-tooth	OP	1.471	0.0076	2.90
	CP	1.165	0.0022	7.90
E-core	OP	0.761	0.0128	0.90
	CP	0.615	0.0047	1.97
C-core	OP	0.953	0.0131	1.08
	CP	0.827	0.0049	2.53

Table 4.3 Comparison of, maximum torque, power and speed of SFPM machines with FAs at open position (OP) and closed position (CP)

Machines		Base speed (rpm)	Max. speed (rpm)	Max. torque (Nm)	Max. power (KW)
12/10	OP	1,800	3,200	2.60	0.5
	CP	3,500	20,000	1.08	0.5
12/13	OP	1,600	3,600	2.89	0.5
	CP	2,900	∞	1.23	0.5
12/14	OP	1,500	3,800	2.89	0.5
	CP	2,200	∞	1.24	0.5
M-tooth	OP	500	∞	2.84	0.17
	CP	700	∞	1.06	0.06
E-core	OP	1,400	16,000	2.95	0.5
	CP	1,700	∞	1.27	0.25
C-core	OP	1,000	∞	3.55	0.47
	CP	1,200	∞	1.59	0.2

4.8. Experimental Validation

4.8.1. Prototype machines with flux adjusters

SFPM stator with 12 pole and three rotors having 10, 13, and 14 poles, are prototyped and shown in Fig. 4.13 (a) and (c), respectively. In order to reduce the effort and ease the movement of the FAs, they are made smaller and designed to be inserted axially to the machine, as shown in Fig. 4.13 (b). Furthermore, in order to account for the end-effect, 3D-FEA analysis are also performed and compared with the measured results.

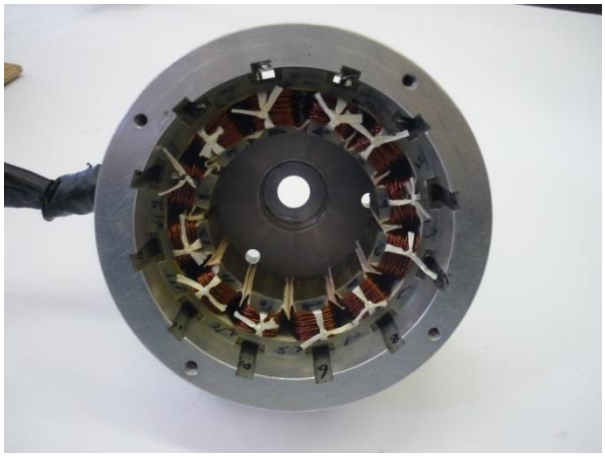

(a) Prototype of 12 pole stator SFPM

(b) SFPM stator with FAs

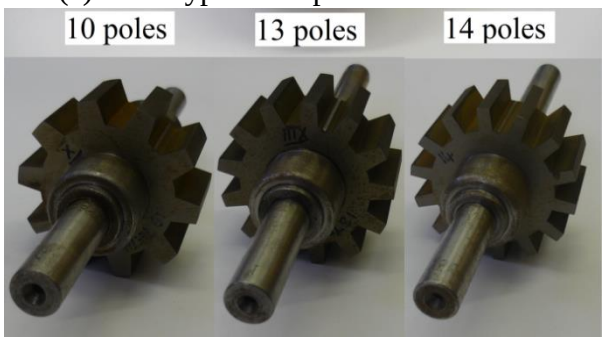

(c) 10, 13, and 14 rotor pole

(d) Flux adjusters

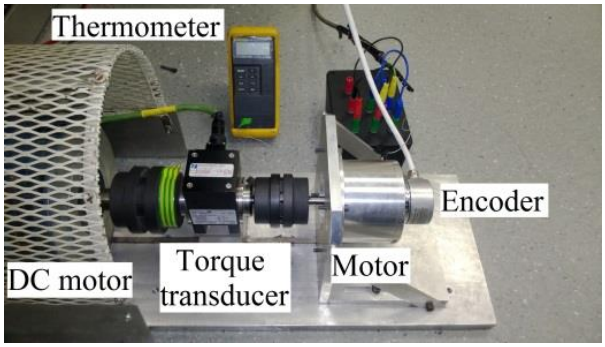

(e) Motor test bench

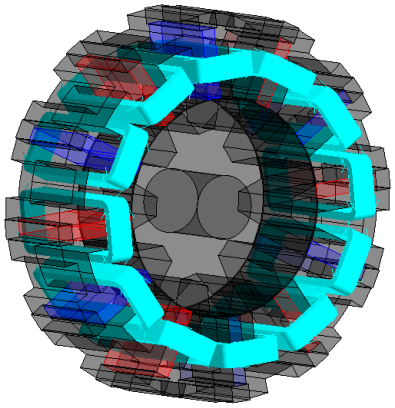

(f) 3D model of SFPM machine

Fig. 4.13 Prototype and 3D model of conventional SFPM machine.

4.8.2. Open circuit test

In order to measure the back-EMF waveforms, the machines are driven by an external DC motor that is operated at constant speed of 400rpm. Fig. 4.14 compares the measured and predicted 2D and 3D-FEA back-EMF waveforms of the 12/10, 12/13 and 12/14 machines with FAs at open and closed positions. A good agreement between the measured and 3D-FEA results is shown. It is worth highlighting that the difference between the 2D and 3D-FEA results is due to the end-effect.

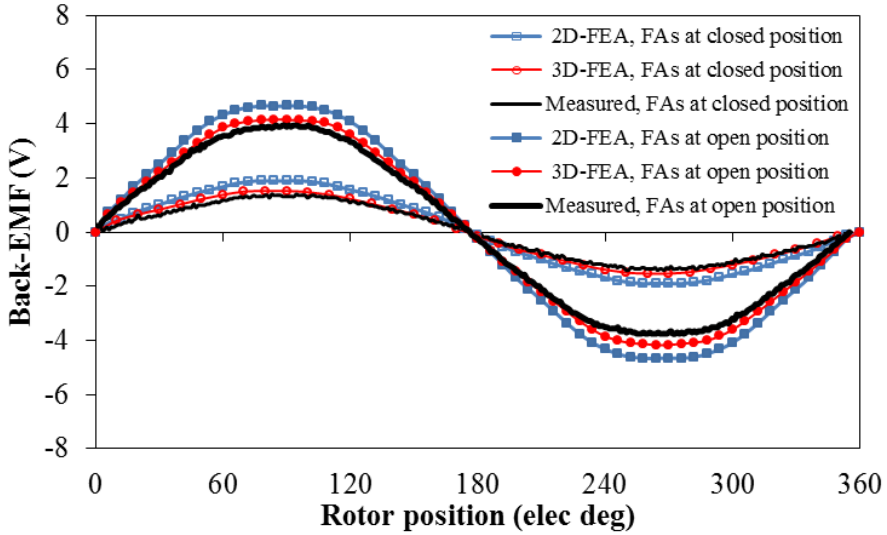

(a) 12/10 conventional SFPM machine with FAs in open and closed positions

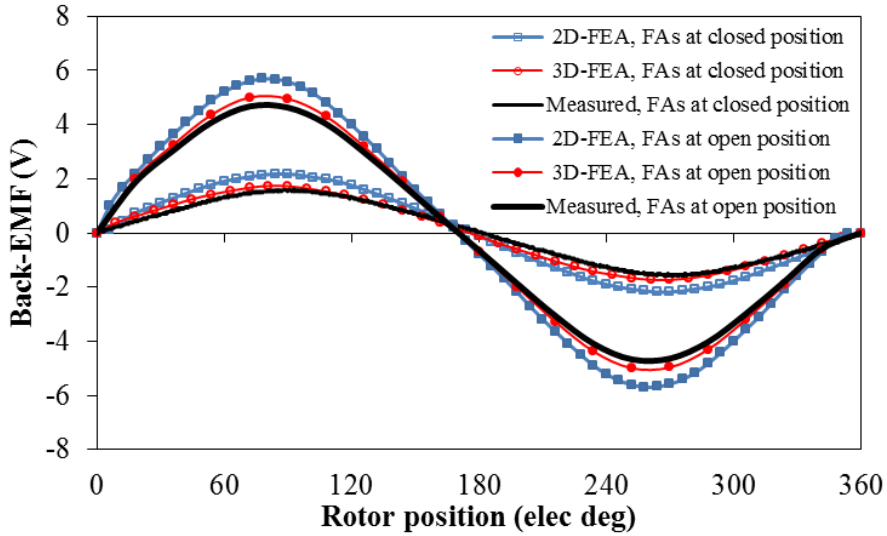

(b) 12/13 conventional SFPM machine with FAs in open and closed positions

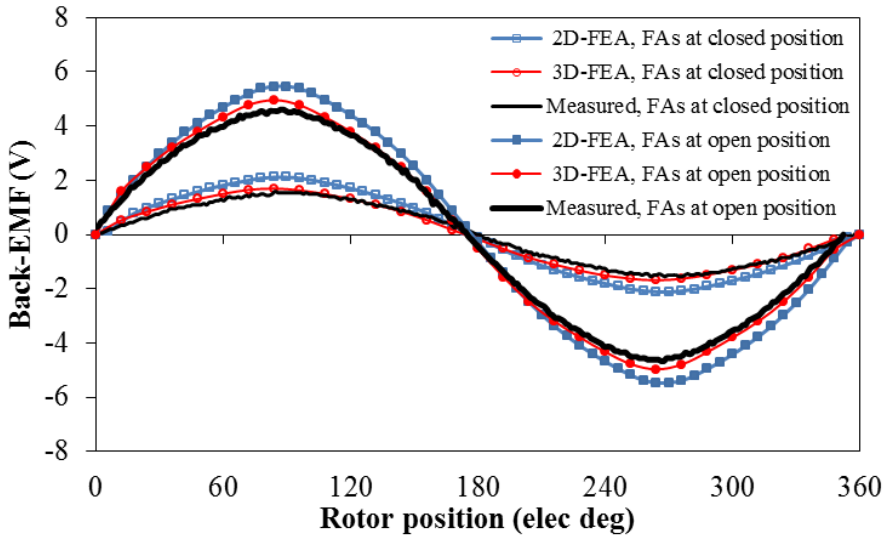

(c) 12/14 conventional SFPM machine with FAs in open and closed positions

Fig. 4.14 Comparison of 2D and 3D-FEA predicted and measured back-EMF waveforms of SFPM machines with FAs at open and closed positions (rotor speed=400rpm).

4.8.3. Electromagnetic torque

The torque-current angle curves of the three conventional machines are presented in Fig. 4.15. Both the measurement and predicted results are obtained using DC current excitation, i.e. phase A is directly connected to one of the DC source terminal while the phases B and C are parallel connected to the other DC source terminal. When the current is set to I_a=10, I_b= I_c=-5A, the rotor is moved to the d-axis position, i.e. 0 degree, then the rotor is locked. The stator will then be rotated corresponding to the current angle, from 0 to 90 degrees. Torque-current waveform of the 12/10 machine is distorted significantly since it exhibits the largest cogging torque, Fig. 4.6. A good agreement exists between the measured and 3D-FEA predicted results.

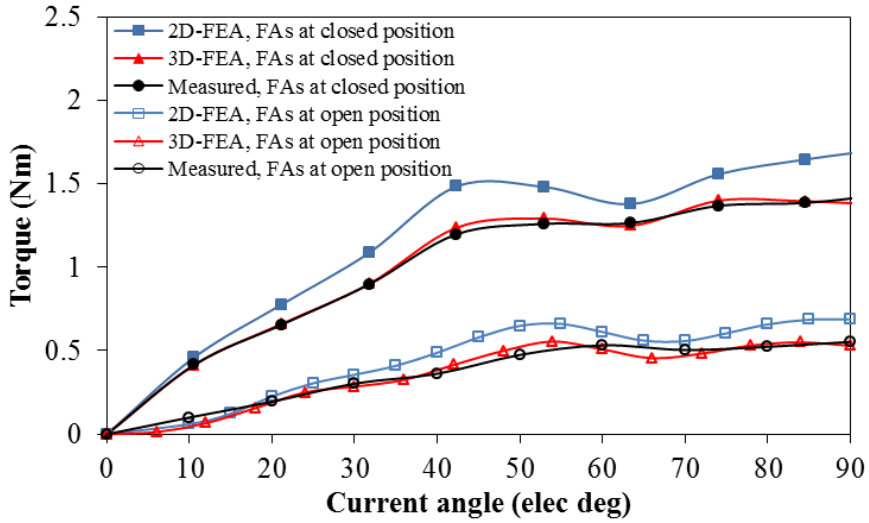

(a) 12/10 conventional machine

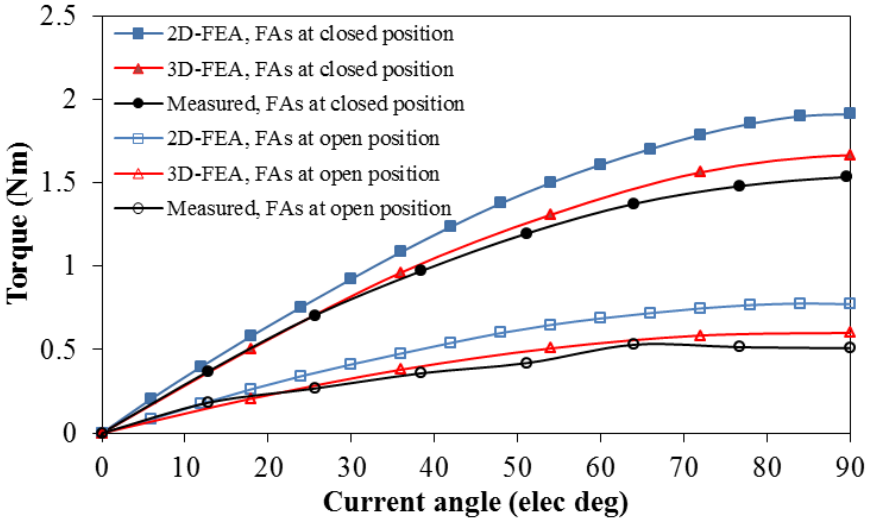

(b) 12/13 conventional machine

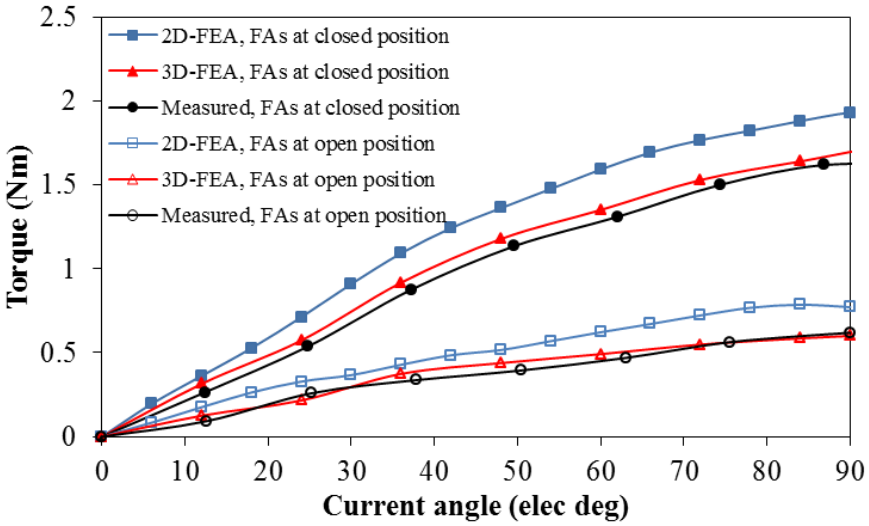

(c) 12/14 conventional machine

Fig. 4.15 2D and 3D-FEA predicted and measured torque-current angle curves of SFPM machines with FAs at open and closed position at load condition of (I_a=10A, I_b= I_c=-5A).

4.8.4. Torque-speed characteristic

The torque- and power-speed curves of the three prototype machines are measured and compared with the predicted results in Figs 4.16 and 4.17. It is worth mentioning that the control algorithm accounts for phase resistance, voltage drop, and dead time on the inverter and it is tested by using 3D-FEA predicted inductance values.

It can be seen that the measured and 3D-FEA predicted results show good agreement. Overall, the measured torque-speed curves of the three machines validate the previous results, since as can be noticed in Fig. 4.16 the base speed and flux weakening capability increase when FAs are utilized, i.e. they are at closed position.

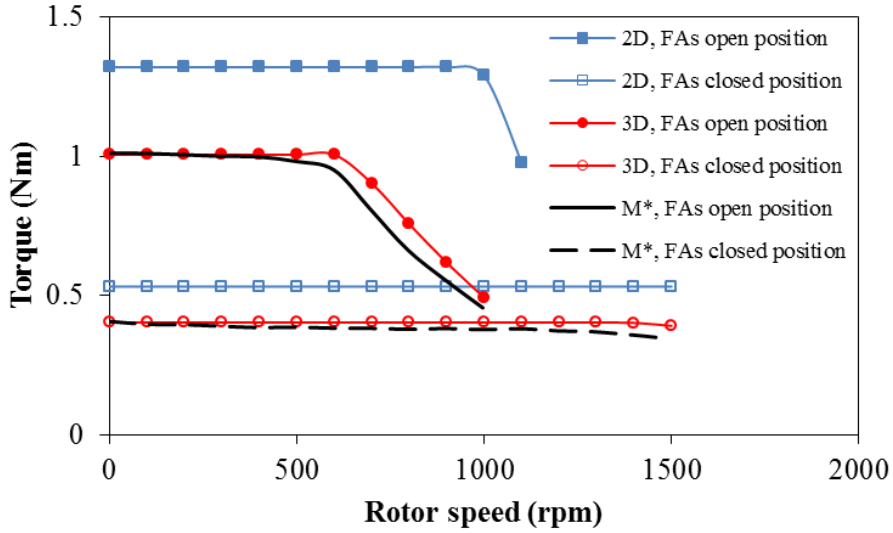

(a) 12/10 conventional machine with FAs at open and closed position

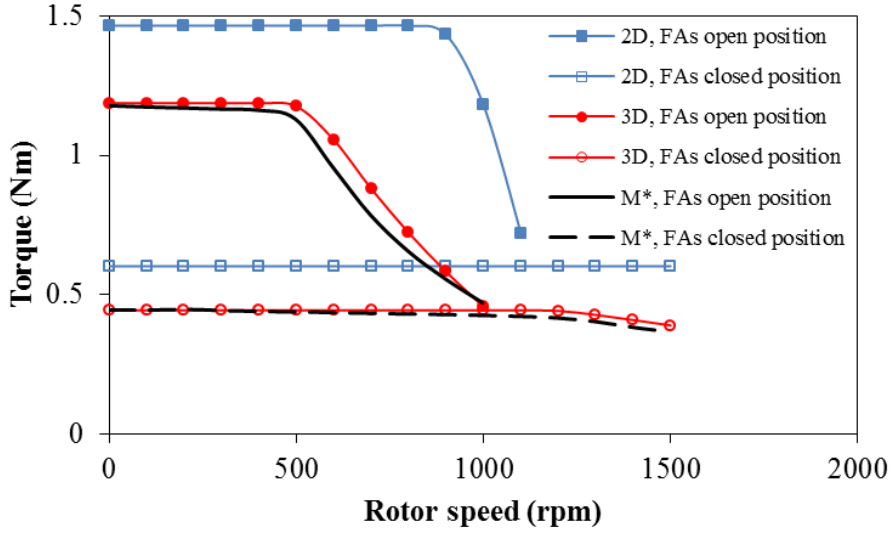

(b) 12/13 conventional machine with FAs at open and closed position

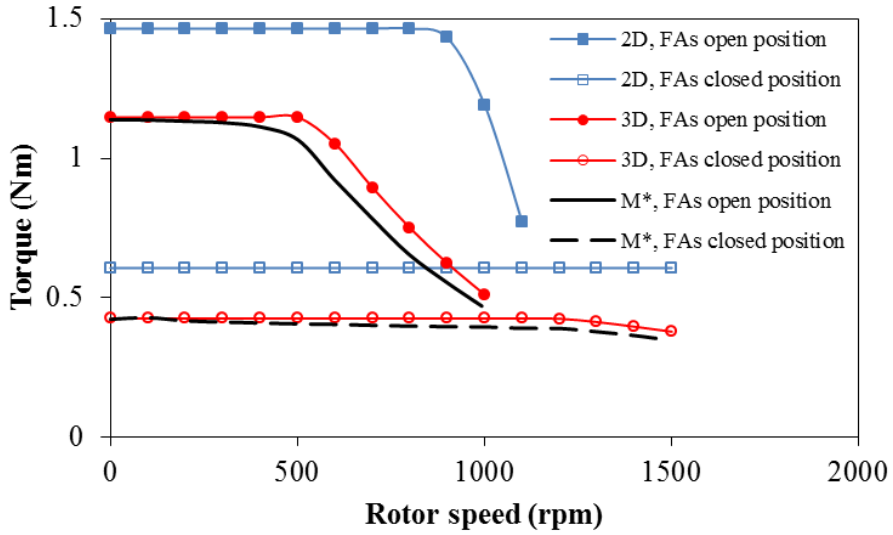

(c) 12/14 conventional machine with FAs at open and closed position

Fig. 4.16 Measured (M*), and 2D and 3D-FEA predicted torque-speed curves of SFPM machines with FAs at open and closed positions under load of (I_{ph}=7.5A and $V_{link\text{-}DC}$=26V).

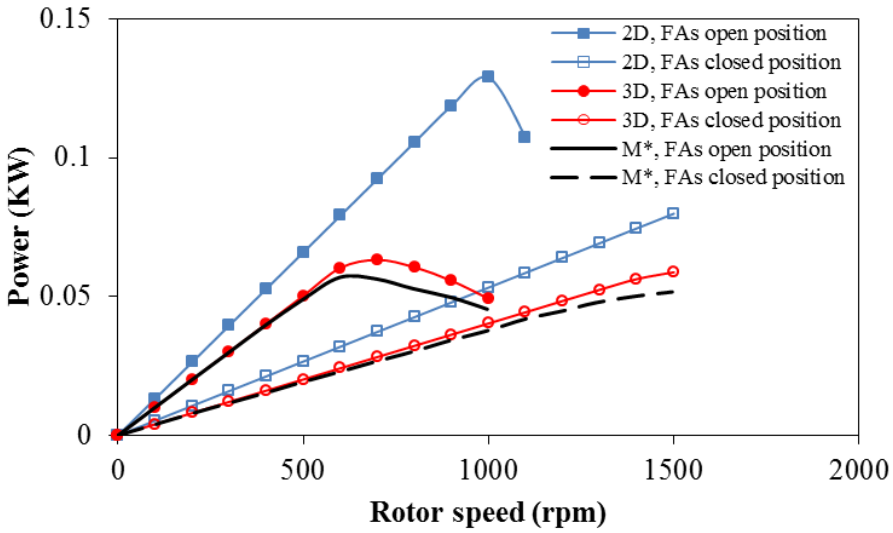

(d) 12/10 conventional machine with FAs in open and closed position

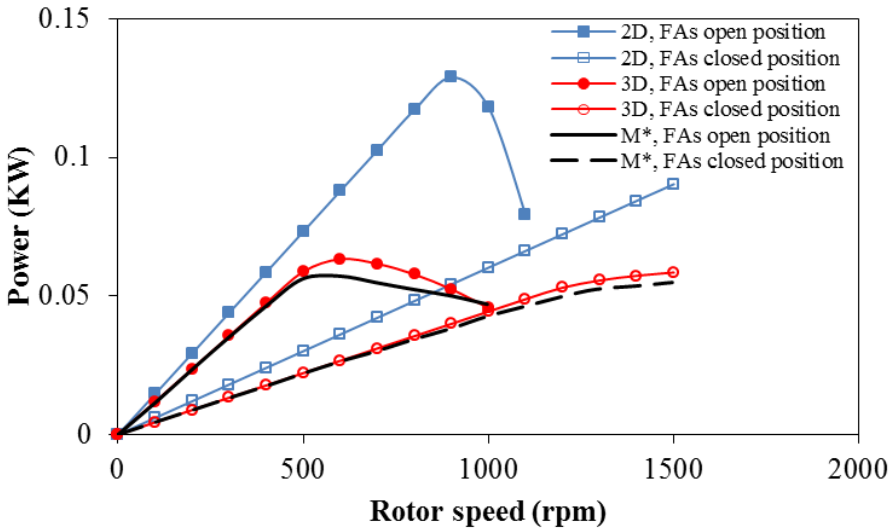

(e) 12/13 conventional machine with FAs in open and closed position

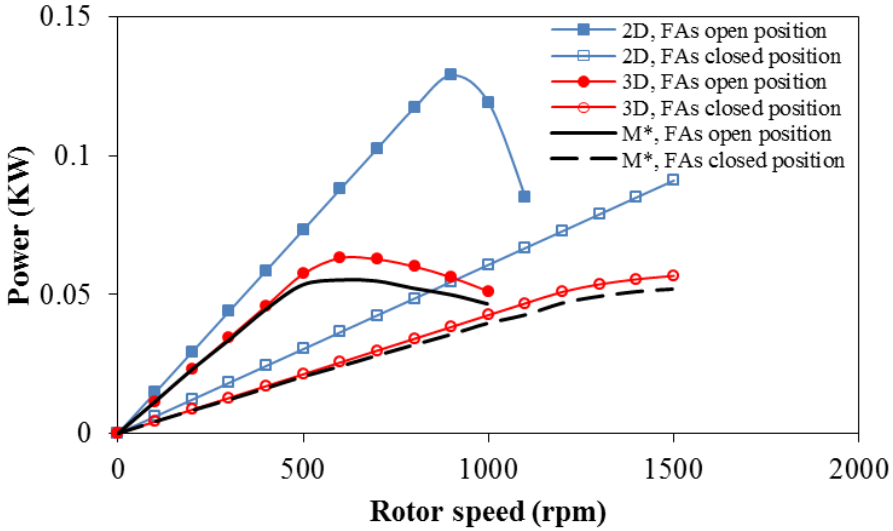

(f) 12/14 conventional machine with FAs in open and closed position

Fig. 4.17 Measured (M*), and 2D and 3D-FEA predicted power-speed curves of SFPM machines with FAs at open and closed positions under load of (I_{ph}=7.5A and $V_{link\text{-}DC}$=26V).

4.9. Conclusion

In this chapter, the mechanically movable flux adjusters are utilized to extend the operation speed range and improve the flux weakening capability of SFPM machines, different topologies such as the conventional with different stator/rotor pole combinations, multi-tooth, E-core and C-core, have been considered. Compared with the multi-tooth, E-core and C-core SFPM machines, in which infinite speed range is already achievable, significant improvement in terms of speed range is obtained in the conventional machines when they are equipped with FAs. Moreover, for the conventional machines, the larger the rotor poles, the better the flux weakening capability improvement. On the other hand, the maximum power of

the conventional combinations is maintained when FAs added, but it is achieved at higher speeds, while in the multi-tooth, E-core and C-core SFPM machines significant reduction in the maximum power is observed due to the torque reduction, which in turns caused by the lower PM flux-linkage. Moreover, it has been found that for the selected FA size in this study, lower inductance are observed in the conventional SFPM machines when FAs located at closed position compared to that without FAs. Whereas higher inductances at lower current levels and vice versa are observed in the multi-tooth, E-core and C-core machines compared with the original inductances of the machines without FAs.

5. A Novel Mechanical Flux Weakening Method for SFPM Machines

5.1. Introduction

Conventionally, flux weakening control methods are used to drive permanent magnet (PM) machines in order to extend the operation speed range. However, due to the inverter limitations in terms of maximum current and voltage, the speed range may be still limited and inadequate for some applications, such as automotive. Therefore, for further speed range extension and more flux weakening capability improvement without sacrificing the high efficiency of the PM machines, variable flux concepts have been proposed. By using electrical, mechanical or other types of techniques the PM flux level can be regulated in order to extend the speed range and improve the flux weakening capability of PM machines.

As illustrated in Chapter 1, many PM machines with electrical variable flux techniques, i.e. hybrid excitation machines, have been developed in the past 10 years [93, 94, 102, 104, 152-155]. Similar flux control concept is applied to all hybrid excitation machines. At low speed, i.e. constant torque region, the DC windings are excited with positive current in order to enhance the airgap flux density and consequently the torque. However, in order to increase the maximum speed when the machine is operating at high speed, i.e. in the constant power region, negative current is used to produce d-axis flux opposing the flux produced by the PMs, similar to that of the flux weakening control. Interior PM, consequent pole PM, homopolar embedded PM, bipolar embedded PM, claw pole and synchronous PM hybrid excitation machines are reported in [93, 94, 152-154], where the DC excitation flux path is in parallel with that of the PMs. Moreover, although the DC flux path is corresponding in path to that of the PMs which might risk demagnetizing the PMs, several doubly excited synchronous, hybrid doubly salient and hybrid stepper machines are designed and developed [102, 104, 155].

Furthermore, in the axial flux surface-mounted PM machines proposed in [149, 150], the PM flux-linkage is adjusted by the relative movement of two rotor plates or windings. Using the same concept, the radial flux surface-mounted PM machines can also be modified to be capable of adjusting the PM flux linkage by dividing the rotor into two separated parts [111]. Moreover, by inserting movable pieces made of ferromagnetic material in the flux barriers of

the interior PM machine, the PM flux-linkage can also be adjusted during the operation [113, 114, 151]. Furthermore, in the doubly salient machine whose PMs are located in the stator, movable ferromagnetic pieces located outside the stator are used to provide short-circuit path for the PM flux [117].

Other variable flux machines using different types of flux weakening techniques have been proposed, e.g. the memory motors [119]. Using Al-Ni-Co magnets, which can easily be magnetized and demagnetized by using a short current pulse in d-axis direction, the variation of PMs remanence provides flux weakening and strengthening during the machine operation [120, 125, 156, 157]. Furthermore, the pole changing and double winding set machines offer variable flux capability by changing the winding connection or the number of turns per phase and consequently change the PM flux-linkage [128].

Moreover, as mentioned previously, beside the high torque and power density, switched flux permanent magnet (SFPM) machines are characterized by their simple and robust rotor and easy heat control, since the PMs and armature windings are located in the stator. Additionally, using concentrated windings in SFPM machines leads to low copper usage and consequently low copper loss. Therefore, several hybrid excitation SFPM machines have been proposed and developed. In [91] and [87], the DC coils are located behind the PMs and back iron, and surrounded by ferromagnetic yoke. In [61], the PMs are made shorter to provide space for the DC coils, while the same structure as the conventional SFPM machine is used with the DC coils sharing the slot area with the armature windings [92]. Likewise, a hybrid E-core SFPM machine topology is presented in [116]. On the other hand, as presented in Chapter 4, a mechanical flux adjusting technique similar to that applied to doubly salient machine in [117] is applied to conventional SFPM machines with different stator/rotor pole combinations and multi-tooth, E-core and C-core machines. That method is consisted of using ferromagnetic pieces known as flux adjusters (FAs), located outside the stator to adjust the PM flux level by partially short circuiting the PM flux. Nevertheless, in this mechanical variable flux machine topology the number of FAs is the same as the number of stator poles. Therefore, to reduce the number of FAs, a new mechanical variable flux machine topology, which uses only half of FAs outside the stator with an interval of two stator pole pitches, i.e. alterative stator poles, is proposed and developed in this chapter.

In this chapter, the principle of using all and alternative FAs in the SFPM machines is proposed. The electromagnetic performance and torque-speed characteristics of different

SFPM machines with all and alternative FAs per stator pole are investigated and compared. Moreover, in order to investigate the influence of all and alternative FAs on the performance of SFPM machine, the different rotor poles and winding configurations, i.e. 12/10, 12/13 and 12/14 stator/rotor pole combinations, are considered and compared. Finally, experimental results are obtained and compared with the investigation results predicted by 2D- and 3D-fininte element analyses (FEA).

5.2. Flux Adjusters in All and Alternative Stator Poles

In conventional SFPM machines, the constant PM flux-linkage limits the speed range as well as the flux weakening capability. Therefore, by either increasing the d-axis inductance or reducing the PM flux-linkage the maximum speed can be increased since in most PM machines the PM flux-linkage is higher than the product of d-axis inductance and maximum current. The design methods that permanently reduce the PM flux-linkage is often not preferred since lower PM flux-linkage will lead to low torque capability. Thus, the adjustable PM flux-linkage can increase the maximum speed without sacrificing the torque capability. Therefore, by creating a short-circuit path for the PM flux with the FAs located outside all the stator poles, as shown in Fig. 5.1 (b), less PM flux will flow through the airgap and link the with stator windings compared to that of the original machine without FAs, Fig. 5.1 (a). However, different from the SFPM machine with FAs for all stator poles, in the topology with alternative FAs two short circuit paths can be observed, as illustrated in Fig. 5.1 (c). In addition to the flux short-circuiting path provided by the FA for the respective PM similar to that of all stator poles, the alternative FAs provide a second short-circuit path for the two adjacent PMs.

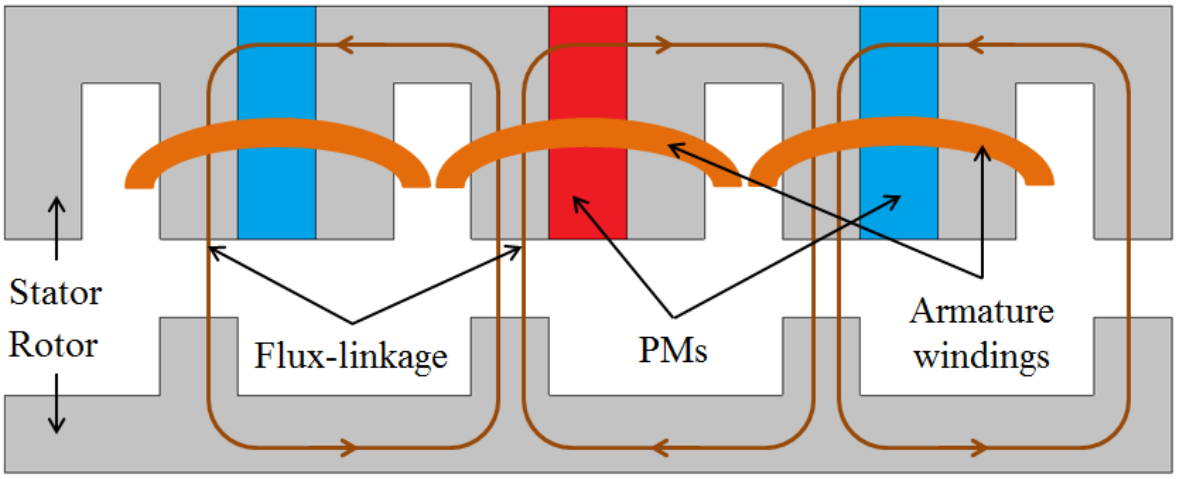

(a) Convectional SFPM machine without flux adjusters

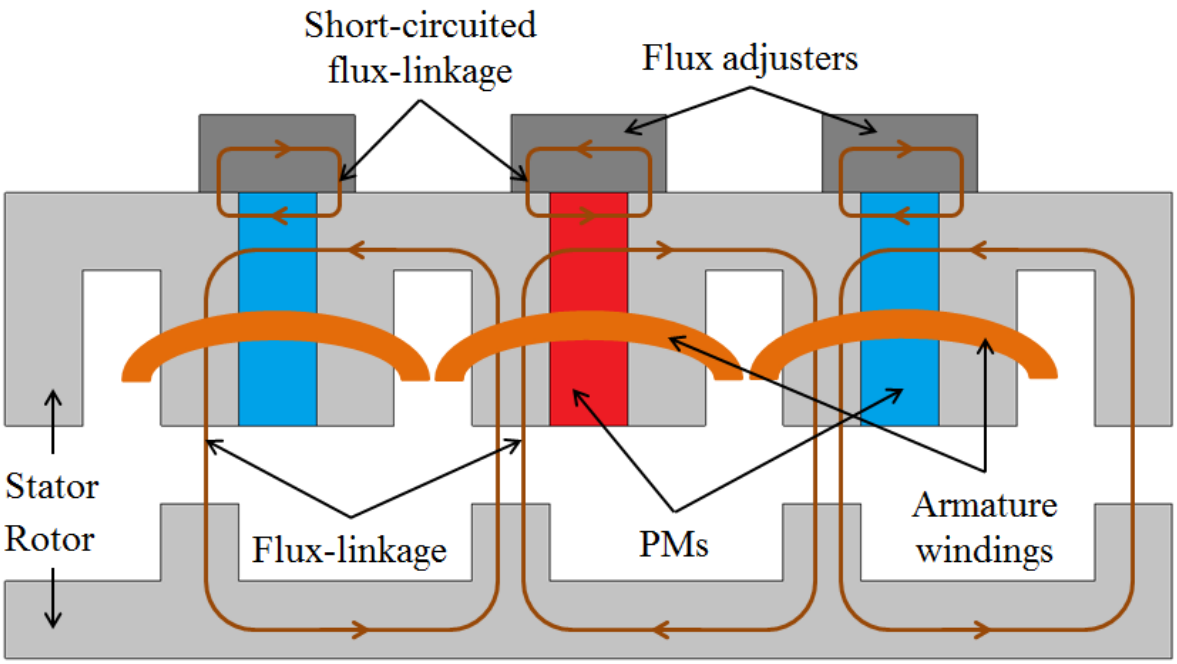

(b) SFPM machine with flux adjusters in all stator poles

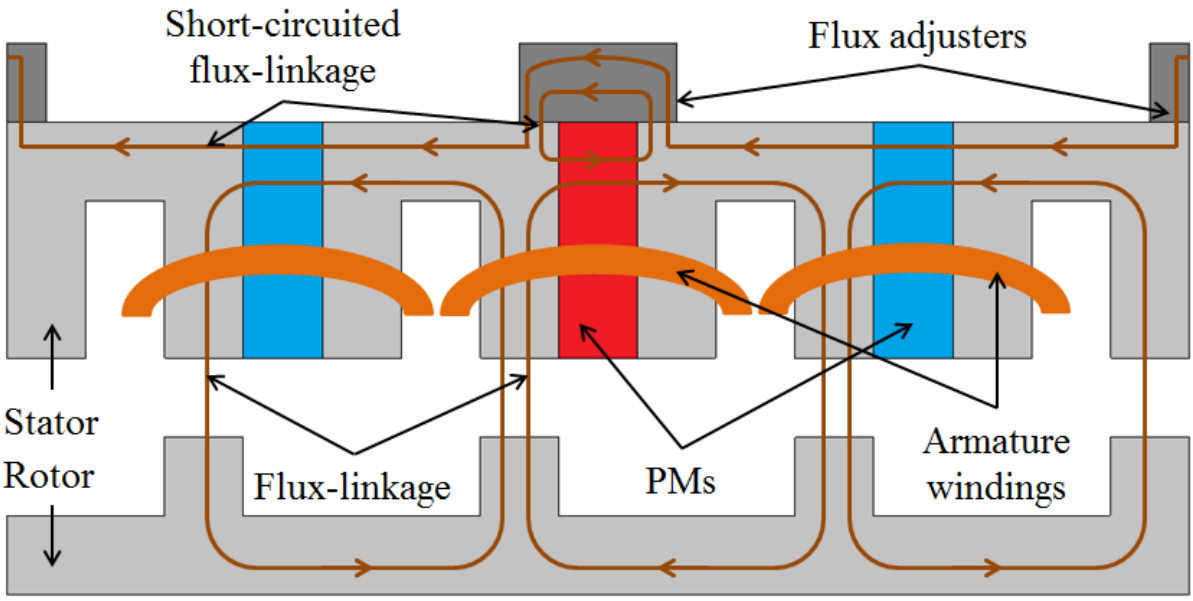

(c) SFPM machine with flux adjusters in alternative stator poles

Fig. 5.18 Concept of SFPM machine with mechanical flux adjusters.

5.3. Influence of All and Alternative Flux Adjusters on Performance of SFPM Machines

5.3.1. Open circuit results

Fig. 3 shows the open circuit field distributions of the three SFPM machines without/with FAs equipped for all and alternative stator poles. As illustrated before when the FAs are used

in all stator poles, less PM flux in the rotor is observed due to short-circuit of the PM flux. On the other hand, the alternative FAs provide short circuit path for the flux of its respective PM and the two adjacent PMs, Fig. 5.2 (c). Therefore, relatively low flux in the rotor is exhibited when alterative FAs are used.

Moreover, the back-EMF waveforms with their harmonics in the three machines without and with all and alternative FAs are compared in Fig. 4. It shows that the reduction in the back-EMF in the three machines is around 73% when all FAs are used, while with alternative FAs it is 55%. Furthermore, the use of alternative FAs results in an uneven flux distribution in the machine, thus the flux-linkage of each coil is different because of the existing of the FA on its corresponding tooth. Therefore, it can be seen in Fig. 5.3 (a), the back-EMF waveforms of the 12/10 and 12/14 machines are not uniform when alternative FAs are used. Moreover, the 2nd order harmonic of back-EMF in the 12/10 and 12/14 machines increases significantly when alternative FAs are used as shown in Fig. 5.3 (b). However, this phenomenon does not appear in the 12/13 machine due to its different the winding connection. In 12/10 and 12/14 machines, the flux-linkage waveform of each coil belong to the same phase are in phase, i.e. zero phase shift. Therefore, the distortion which occurs in one coil also appears on the phase flux-linkage and consequently back-EMF. However, there is a shift of 30° electrical between the two adjacent coils of one phase in 12/13 machine. Thus, the distortion caused by the alternative FAs on the flux-linkage of the coils is cancelled out in the phase flux-linkage and therefore no distortion appears in the phase back-EMF waveform.

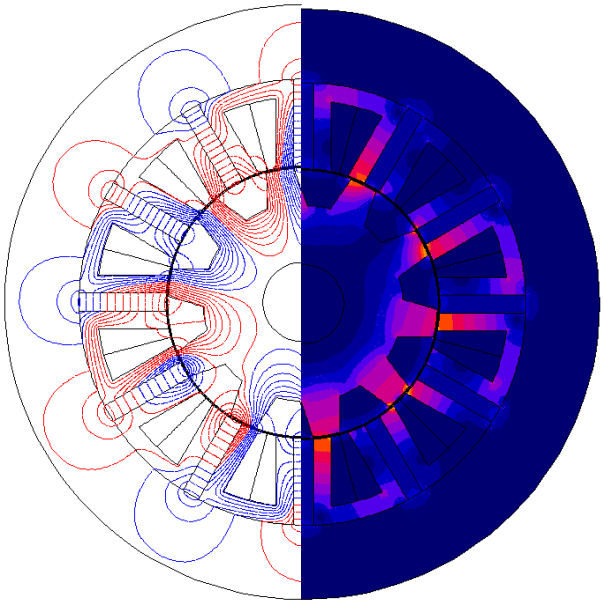

(a) 12/10 machine, without FAs

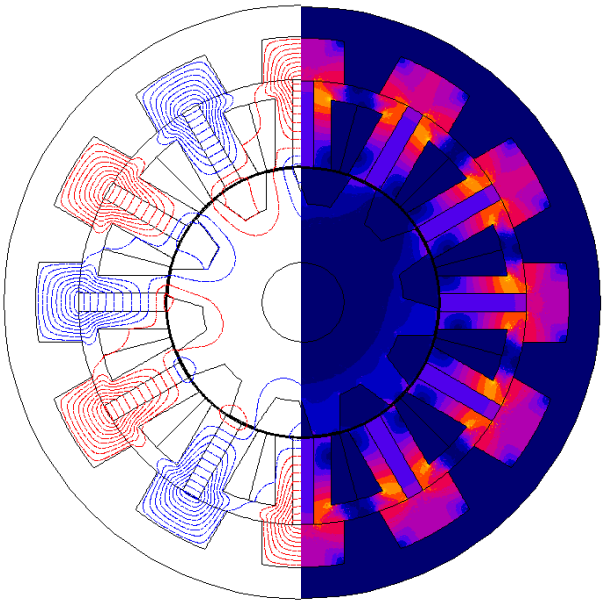

(b) 12/10 machine, with FAs at all stator poles

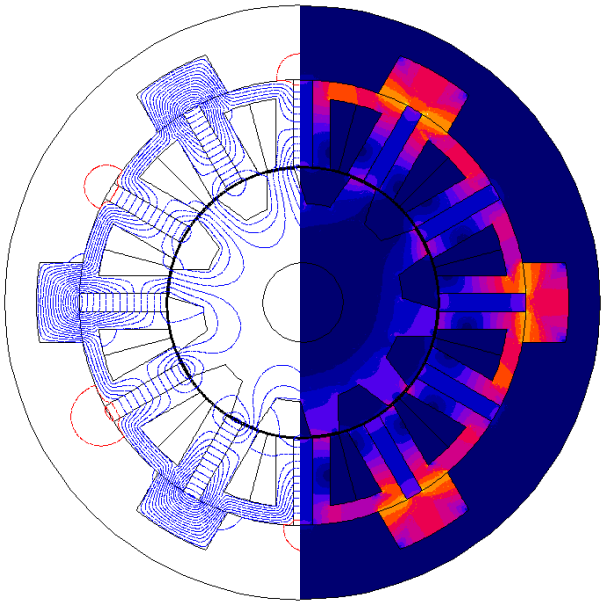

(c) 12/10 machine, with FAs at alternative stator poles

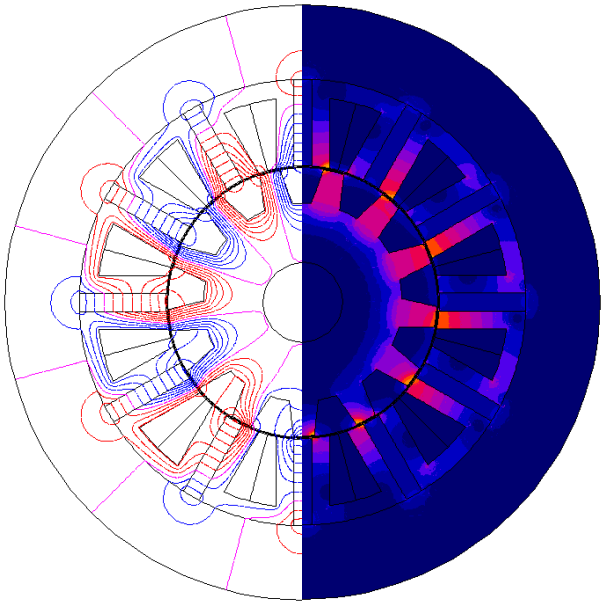

(d) 12/13 machine, without FAs

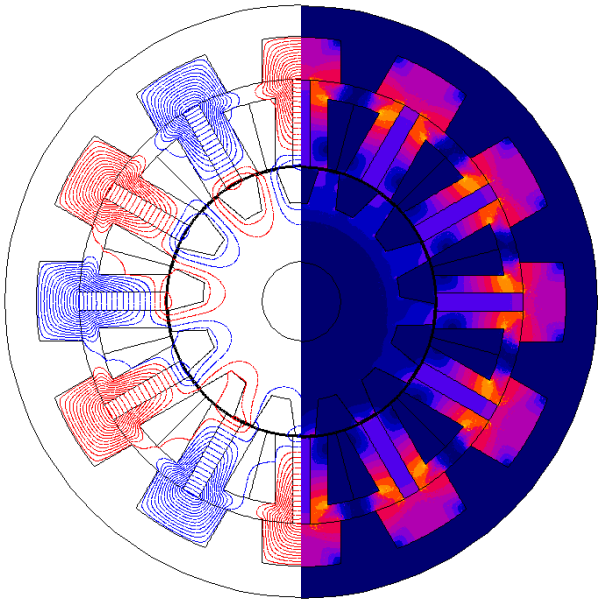

(e) 12/13 machine, with FAs at all stator poles

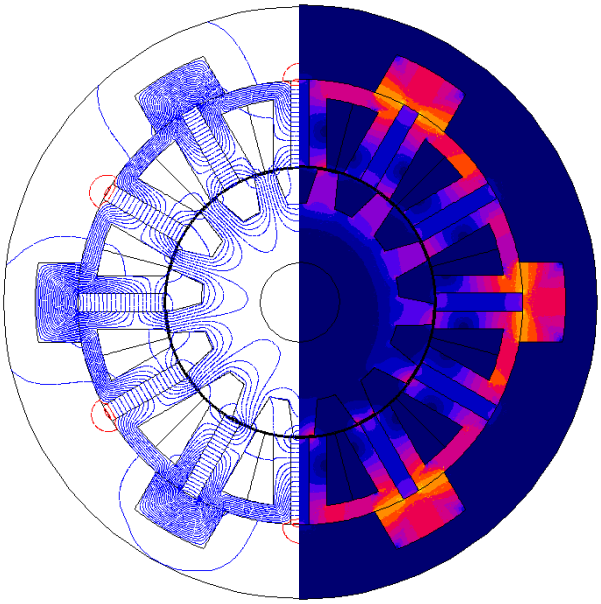

(f) 12/13 machine, with FAs at alternative stator poles

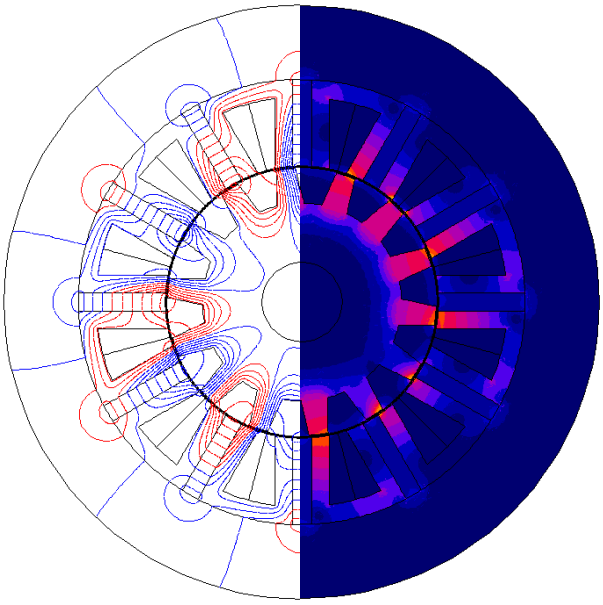

(g) 12/14 machine, without FAs

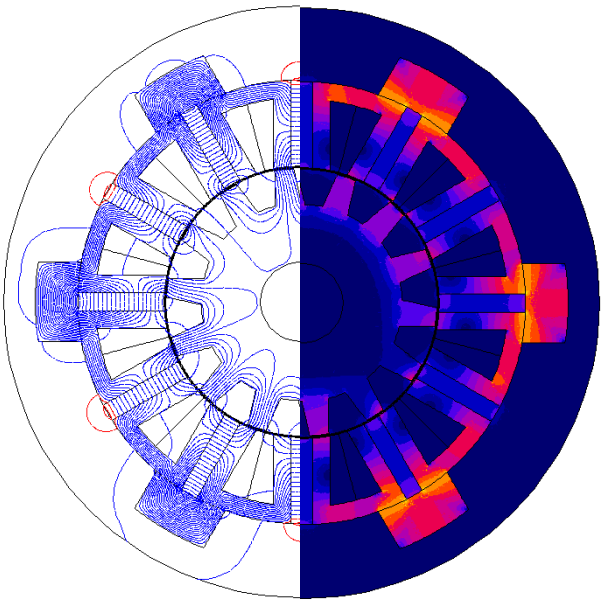

(h) 12/14 machine, with FAs at all stator poles

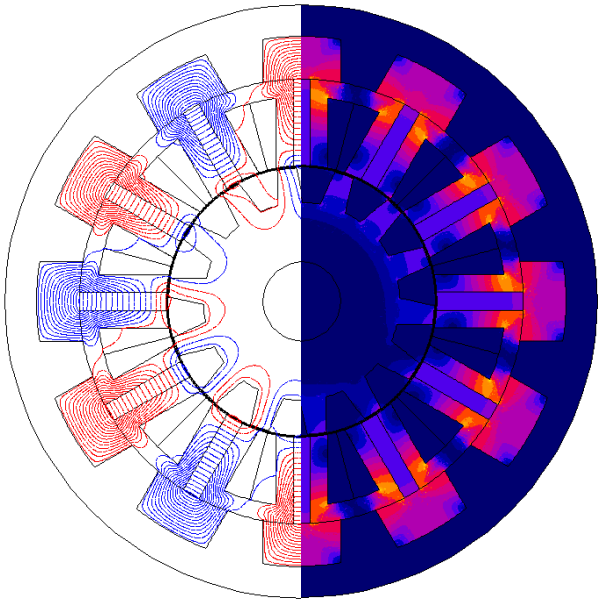

(i) 12/14 machine, with FAs at alternative stator poles

Fig. 5.2 Flux distributions in SFPM machines without and with flux adjusters at all and alternative stator poles.

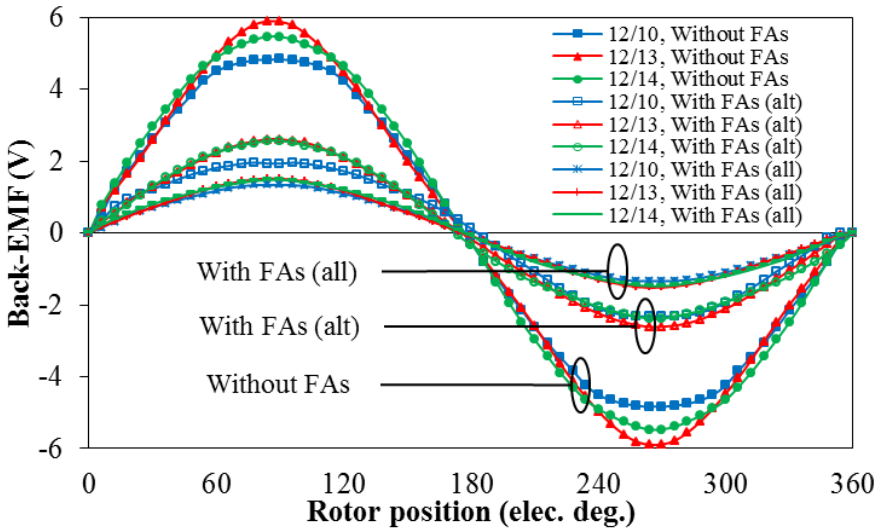

(a) Back-EMF waveform

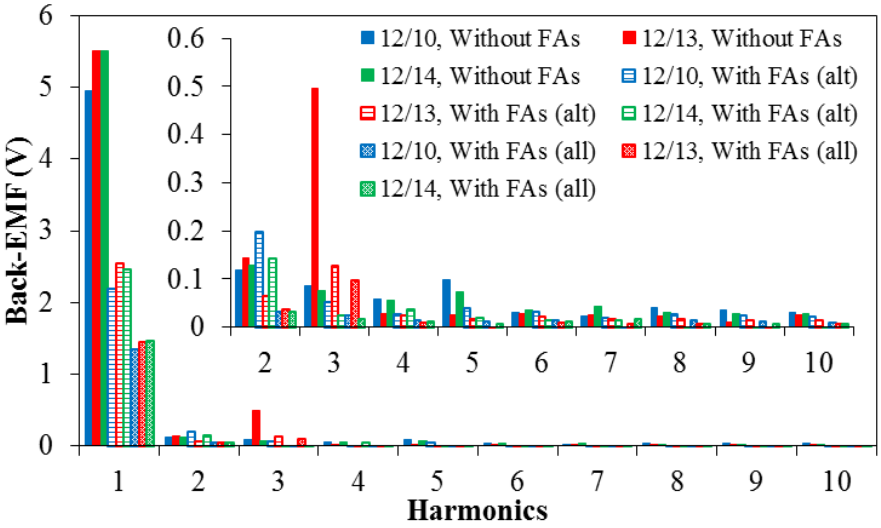

(b) Back-EMF harmonics

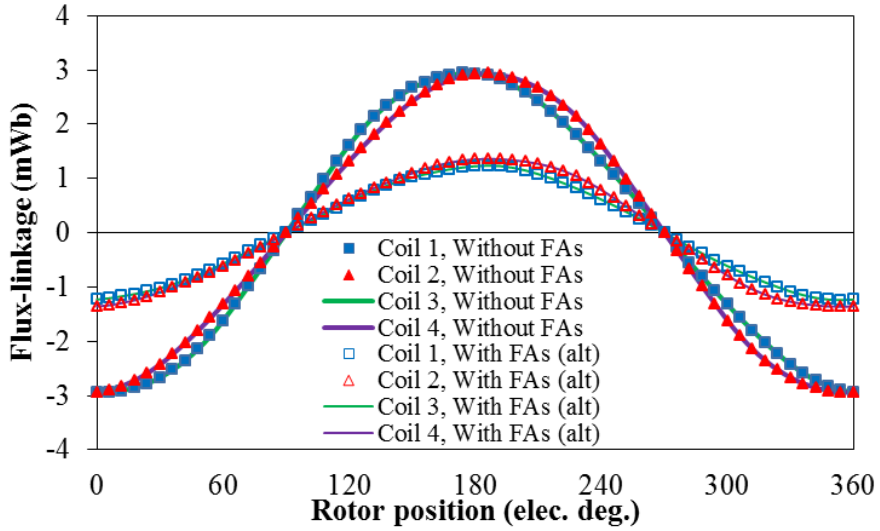

(c) 12/10 machine coils flux linkage

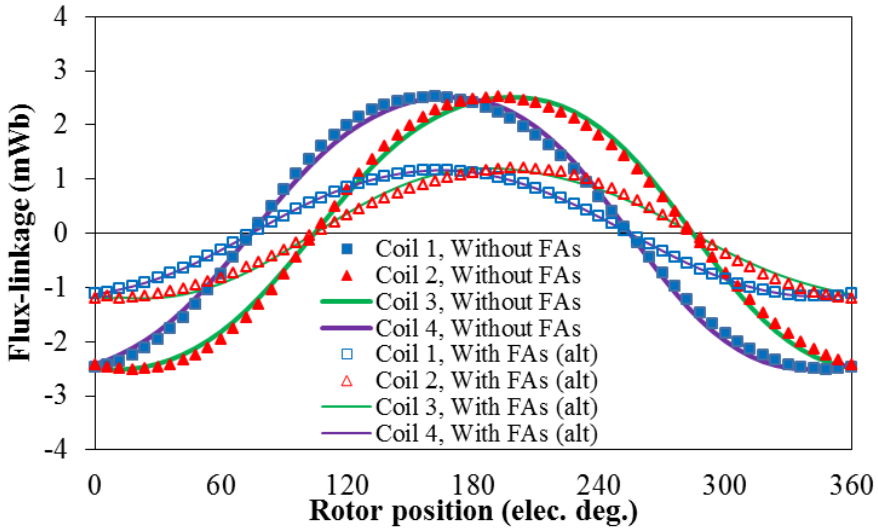

(d) 12/13 machine coils flux linkage

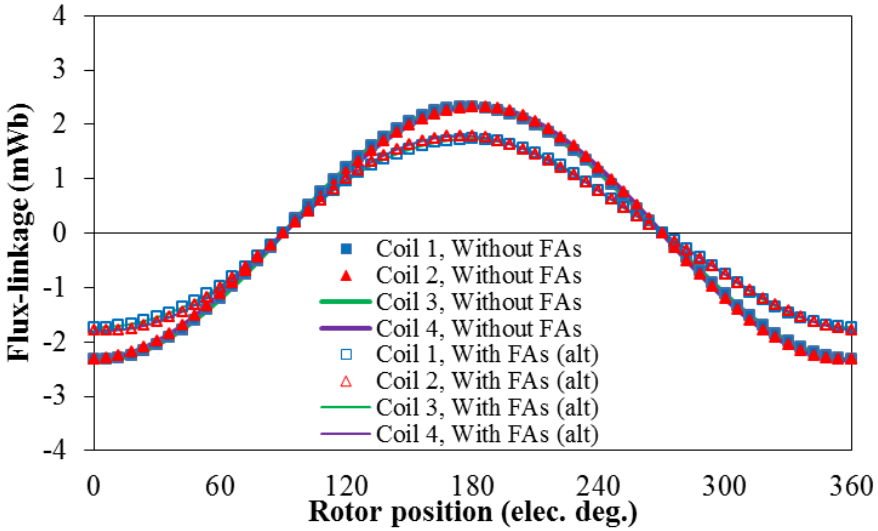

(e) 12/14 machine coils flux linkage

Fig. 5.3 Comparison of back-EMF waveforms and harmonics of 12/10, 12/13 and 12/14 SFPM machines without and with flux adjusters in all stator poles (all) and alternative stator poles (alt).

5.3.2. Electromagnetic torque

The electromagnetic torque waveform of the three SFPM machines are calculated under load condition of 15A phase current and zero current angle, i.e. (I_q=15, I_d=0). The electromagnetic torque of the three machines without and with FAs in all and alternative FAs are compared in Fig. 5.4. Since the same current (I_q) is used, the reduction in average torque when FAs are used is the same as the reduction of the back-EMF. On the other hand, it can be seen the torque ripple is significant in the machines with alternative FAs. As mentioned before, the torque ripple in SFPM machines is mainly produced by the cogging torque and back-EMF

harmonics. Therefore, in order to investigate the behaviour of the torque ripple, the cogging torques of the three machines are calculated and compared in Fig. 5.5. The cogging torque reduces significantly when FAs are added to all stator poles as shown in Fig. 5.5 (b), the reduction being more than half of the original value due to the reduction in the airgap flux density. On the other hand, the use of alternative FAs results in larger cogging torque for the 12/13 and 12/14 machines and small reduction in the 12/10 machine, although the airgap flux density of the all machines is reduced when the FAs are alternatively employed, Fig. 5.5 (c). It can be seen that in 12/10 and 12/14 machines the first cycle of the cogging torque waveforms rises to a larger value compared to the second, while in the 12/13 machine the second cogging torque cycle disappears. The reason of high and imbalanced cogging torque waveform is due to alternative FAs which form uneven flux distribution in the machine and thus cause higher interaction between the rotor poles and the stator poles without FAs but lower with the poles with FAs, i.e. higher flux density and reluctance variations around the airgap. Therefore, the cogging torque cycle is doubled since the full cycle covers one stator pole without FA and the next stator pole with FA. Furthermore, the torque ripple increases when FAs are used in alterative stator poles due to the increase in both cogging torque and back-EMF harmonics. Overall, the lowest cogging torque is observed in 12/13 machine without and with all and alternative FAs. Additionally, due to the low cogging torque and no distortion in the back-EMF waveform occurs when FAs are used both in all and alterative stator poles, the lowest torque ripple is observed in 12/13 machine.

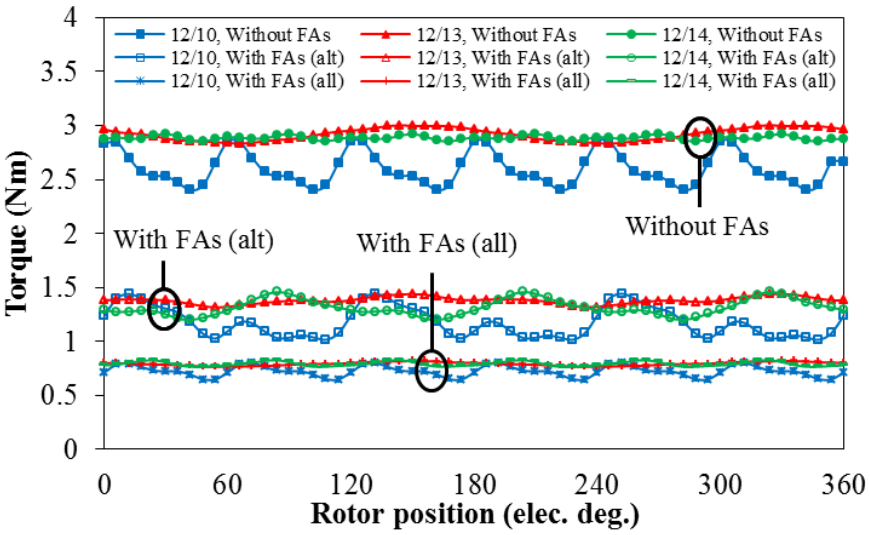

Fig. 5.3 Comparison of electromagnetic torque waveforms of 12/10, 12/13 and 12/14 SFPM machines under load condition of (I_q=15A, I_d=0) without and with flux adjusters in all stator teeth (all) and alternative stator teeth (alt).

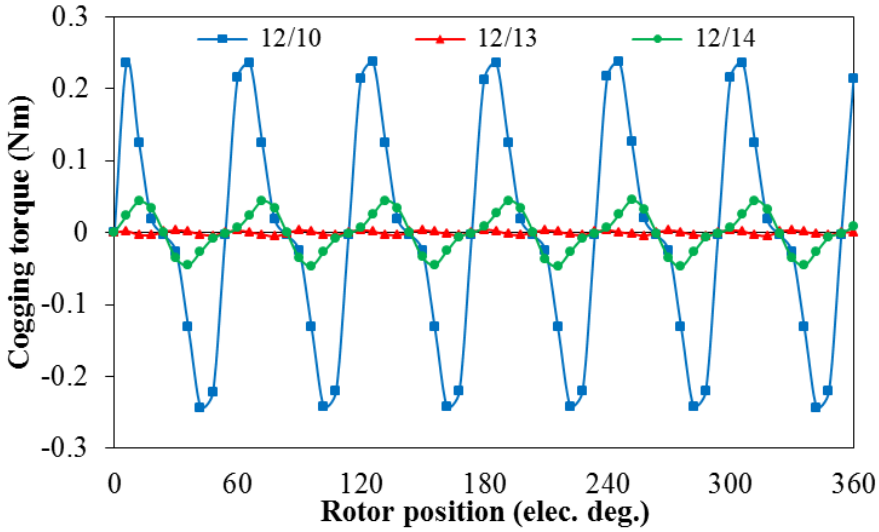

(a) Without flux adjusters

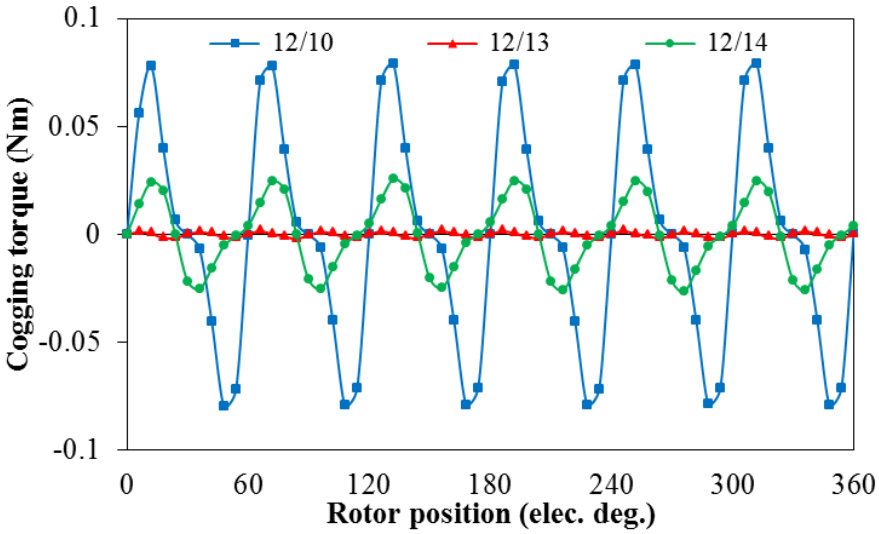

(b) With flux adjusters in all stator poles

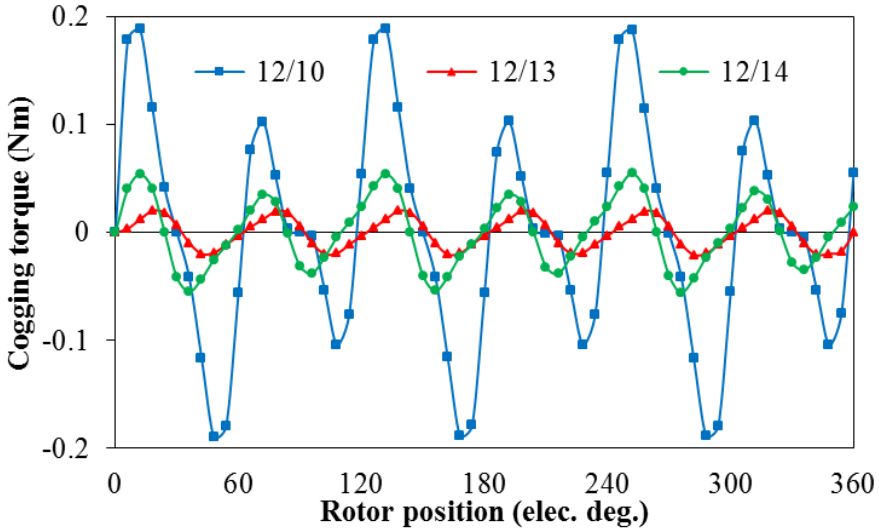

(c) With flux adjusters in alternative stator poles

Fig. 5.4 Cogging torque of 12/10, 12/13, and 12/14 SFPM machines without and with flux adjusters in all stator teeth and alternative stator teeth.

5.3.3. Torque-speed characteristics

The influence of alternative and all FAs on the torque-speed characteristic in the three SFPM machines is investigated and compared with the results of the original machines without FAs.

The PM flux-linkage reduces slightly at high q-axis current levels due to the effect of the magnetic saturation, Fig. 5.6. However, this saturation effect appears at higher current levels when FAs used in all and alternative stator poles, since the majority of PM flux is short-circuited thus less PM flux flow through the machine. On the other hand, the PM short-circuited flux creates a high magnetic saturation level in the near PM side back iron, Fig. 5.9 (a). This magnetic saturation reduces the armature flux passing through leading to significant

reduction in the inductances, Fig. 5.7. As in the majority of PM machines, the d-axis inductance values are lower than the q-axis inductance due to the present of the PMs. However, it can be seen that d-axis inductances are larger than q-axis inductances when FAs are applied to all and alterative stator poles, since the PM flux-linkage is reduced significantly leading to lower magnetic saturation along the d-axis path as well as the FAs provide new path for the d-axis flux-linkage as it can be seen in Fig 5.9 (b). Moreover, at high d-axis current both d- and q-axis inductances reduce, since the d-axis flux pushes the PM flux toward the FA which leads to increase of the magnetic saturation in the near PM side back iron and stator pole. Moreover, since the same stator and FA size are used in three machines, similar saturation level in the near PM side back-iron is created when the FAs are used. Therefore, the inductance values in the three machines are similar when the FAs are used for alternative and all stator poles, Fig. 5.7.

By using the predicted inductances and PM flux-linkage together with (1-6) and (1-10), the torque-speed curves of the three machines with/without FAs are calculated and compared in Fig. 5.8. If the alternative FAs on the stator poles are used, the constant torque region reduces but on the other hand both base and maximum speeds increase significantly due to the reduction of PM flux-linkage. However, by using the FAs in all stator poles, such influence becomes more significant. Although the d-axis inductance reduces when the FAs are used, the significant reduction in the PM flux-linkage leads to higher flux weakening factor and maximum speed as shown in Tables II and III. However, it is possible to employ a combined technique to adjust the flux and operation speed range by employing no FAs, alternative FAs and all FAs by moving the FAs in sequential steps.

On the other hand, the constant power region is relatively narrow in the machines without FAs. Therefore, by increasing the flux weakening factor by using alternative FAs, the same maximum power of 0.5kW is observed but over relatively long constant power region. However, 12/10 machine with all FAs exhibits 0.5kW maximum power over further extended constant power region. Using all FAs in 12/13 and 12/14 machines, theoretically infinite speed range is observed, while the maximum power reduces since the flux weakening factor is larger than 1 due to the large inductances and low PM flux-linkage.

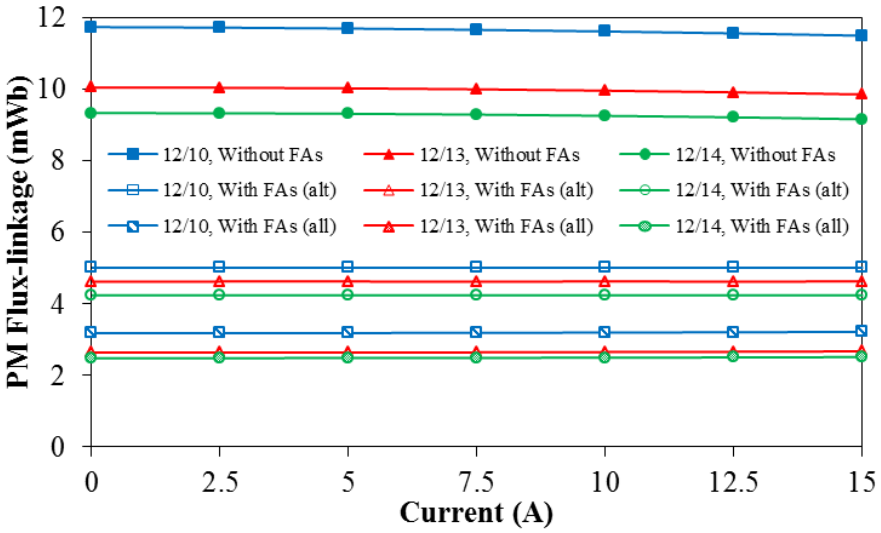

Fig. 5.19 PM flux linkage at different q-axis current levels in SFPM machines without and with flux adjusters in all stator teeth (all) and alternative stator teeth (alt).

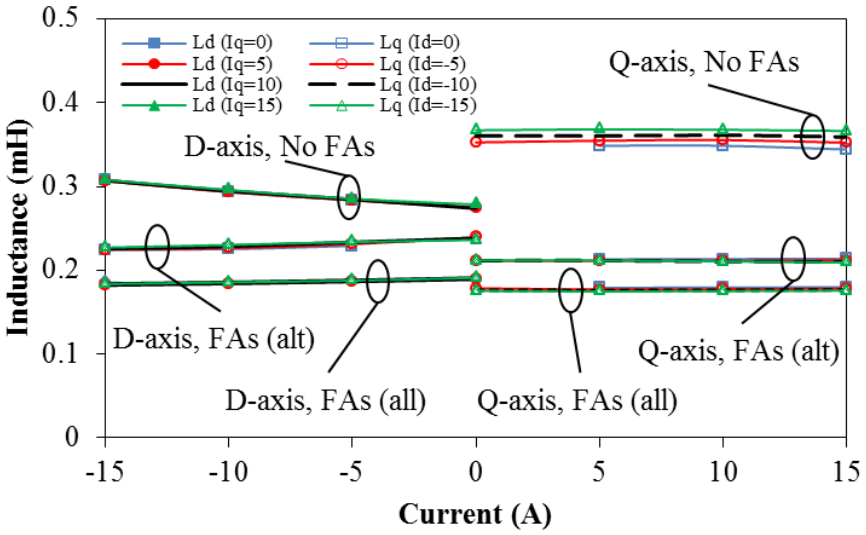

(a) 12/10 machine

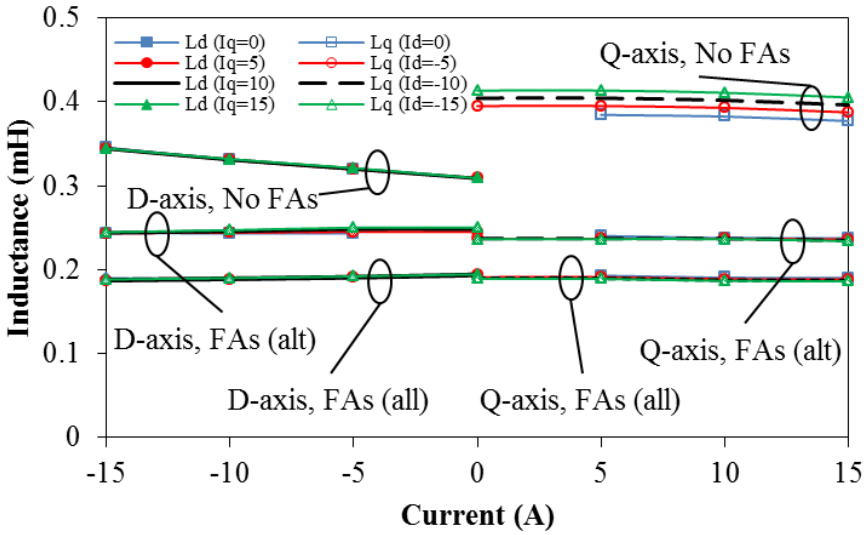

(b) 12/13 machine

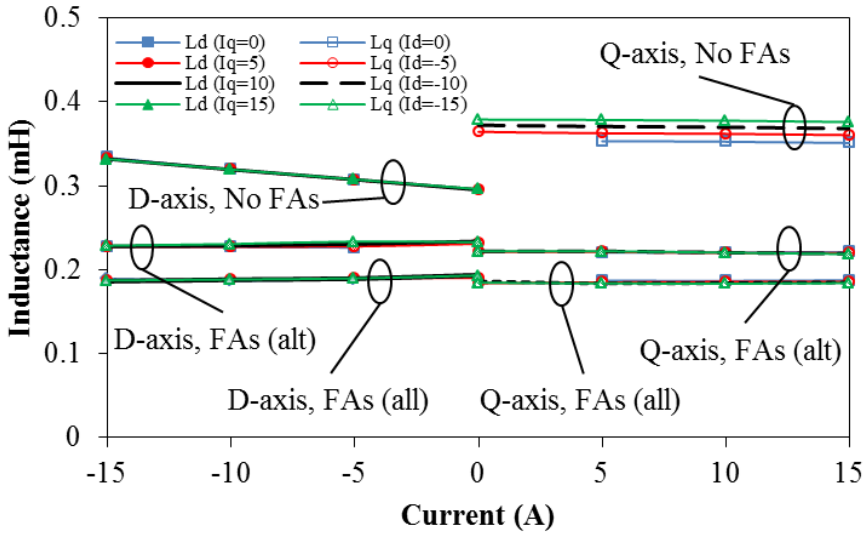

(c) 12/14 machine

Fig. 5.6 Comparison of d- and q-axis inductances of SFPM machines without and with flux adjusters in all stator teeth (all) and alternative stator teeth (alt).

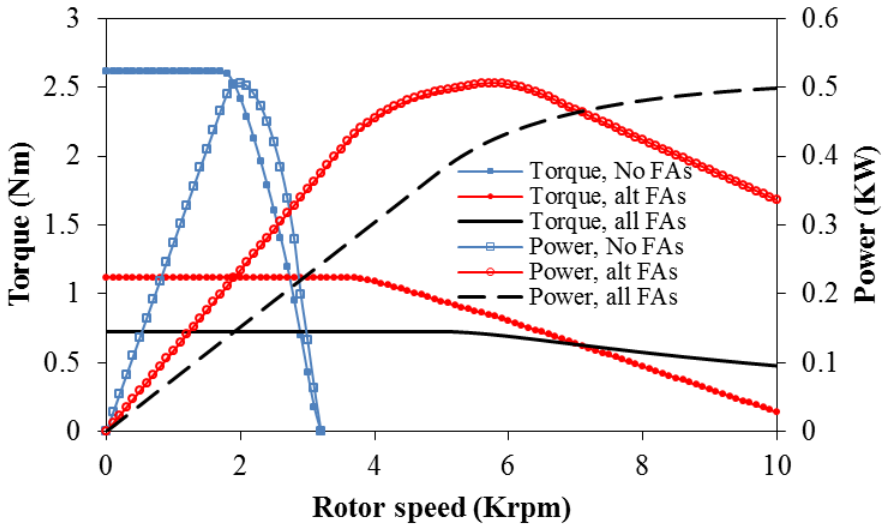

(a) 12/10 machine

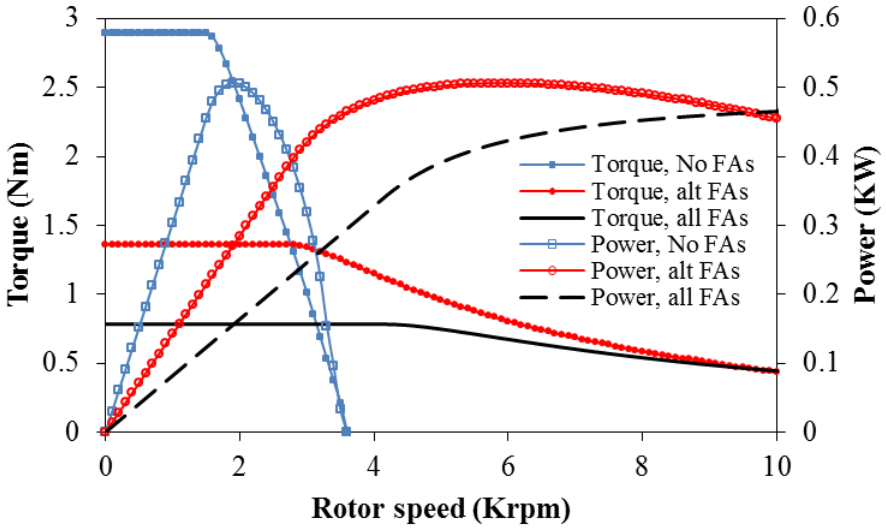

(b) 12/13 machine

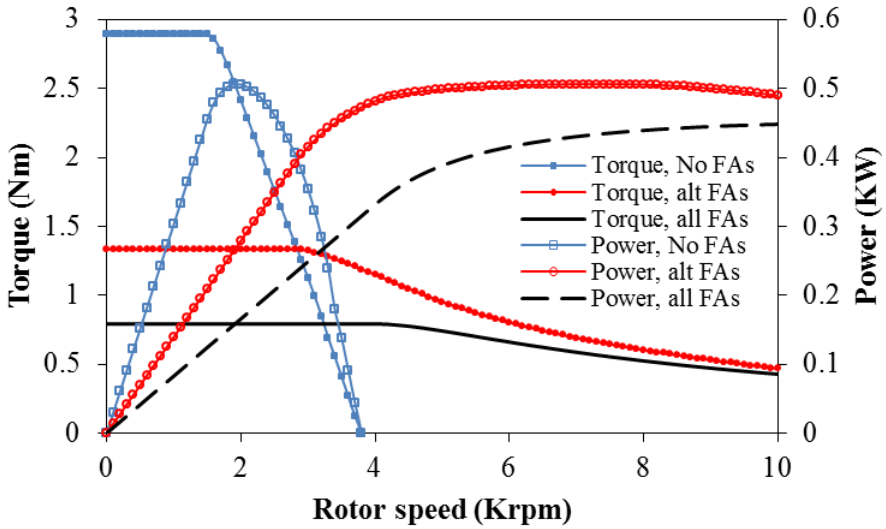

(c) 12/14 machine

Fig. 5.7 Torque- and power-speed curves of SFPM machines without and with flux adjusters in all stator teeth (all) and alternative stator teeth (alt).

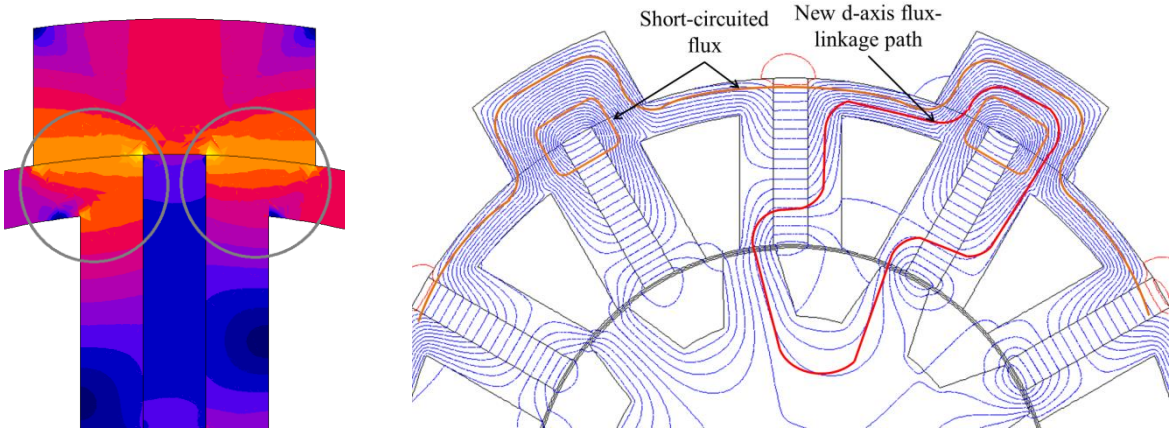

(a) Magnetic saturation in the near PM side back-iron

(b) D-axis flux linkage path

Fig. 5.8 Flux distributions in SFPM machine with FAs.

Table 5.1 Comparison of d-axis inductance, PM flux-linkage and flux weakening factor in SFPM machines without and with all and alterative flux adjusters

Machines		L_d (mH)	Ψ_{pm} (mWb)	K_{fw}	Base speed (rpm)	Max. speed (rpm)	Max. torque (Nm)	Max. power (KW)
12/10	Without FAs	0.307	11.73	0.39	1800	3200	2.6	0.5
	With FAs (all)	0.224	5	0.67	3600	15000	1.11	0.5
	With FAs (alt)	0.185	3.18	0.87	5000	37000	0.72	0.5
12/13	Without FAs	0.345	10.04	0.51	1600	3600	2.89	0.5
	With FAs (all)	0.243	4.62	0.79	2800	16500	1.35	0.5
	With FAs (alt)	0.191	2.63	1.08	4200	∞	0.78	0.47
12/14	Without FAs	0.333	9.33	0.53	1500	3800	2.89	0.5
	With FAs (all)	0.227	4.23	0.81	2700	18000	1.33	0.5
	With FAs (alt)	0.189	2.47	1.14	4100	∞	0.79	0.45

5.4. Experimental Validation

Fig. 5.10 (a) shows the prototypes of 12-pole SFPM stator and three rotors with 12, 13, and 14 rotor poles. The FAs are made smaller and designed to be inserted axially to the machine, in order to reduce the effort and ease the movement. Fig. 5.10 (b) and (c) shows the SFPM stator with the FAs inserted to all and alternative stator poles, respectively. Due to the large end-effect in SFPM machines, 3D-FEA predicted results accounting for the end-effect are compared with the measured results.

Fig. 5.11 compares the measured and the 2D-/3D-FEA predicted back-EMF waveforms of the three machines. It can be seen that a good agreement is obtained between measured and

3D-FEA predicted results. On the other hand, the machines with all FAs exhibit low back-EMF, which is lower than the values when alternative FAs are used.

As in Chapter 4 the corresponding torque-current angle curves are measured and compared in Fig. 5.12. By applying DC current of I_a=0, I_b=-I_c, the rotor is moved to the d-axis position, i.e. 0 degree current angle. Then by locking the rotor, the stator will then be rotated corresponding to the current angle, from 0 to 90 degrees, at load condition of I_a=10A, I_b=I_c=-5A. Torque-current angle curve of the 12/10 machine is distorted significantly by the cogging torque since this machine has the largest cogging torque, as shown in Fig. 5.5. In general, a good agreement is obtained between the measured and 3D-FEA predicted results.

Using flux weakening control method under maximum current of 7.5A and DC-link voltage of 26V, the torque-speed curves of the three machines are tested. The control algorithm accounts for phase resistance, voltage drop, and dead time on the inverter and it is tested by using 3D-FEA predicted PM-flux-linkage and inductance values. Figs. 5.13 and 5.14 present the torque- and power-speed curves of the 12/10, 12/13 and 12/14 machines without and with all and alternative FAs. It can be seen the measured and 3D-FEA predicted results show good agreement. Overall, the measured torque-speed curves of the three machines validate the predicted results, since the base speed and flux weakening capability increase when FAs are used in alternative stator poles and further increases are observed when all FAs are used.

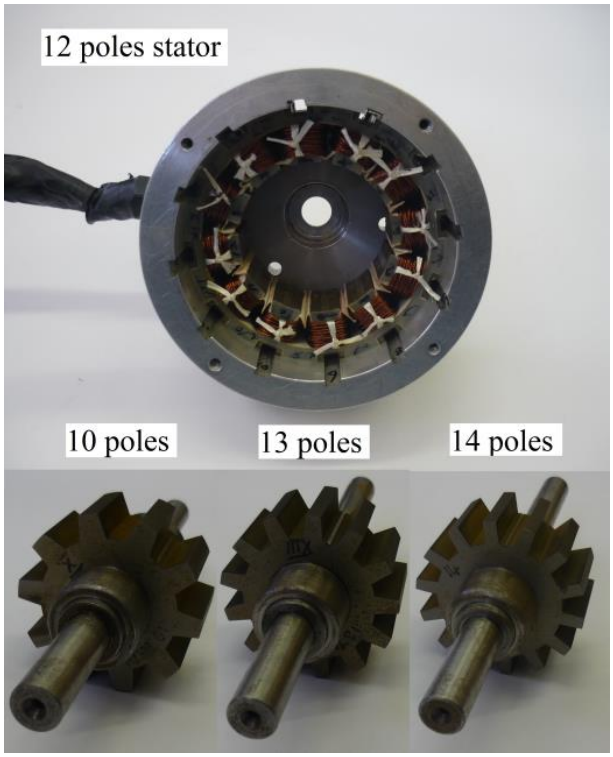

(a) 12 pole stator and 10, 13 and 14 pole rotors

(b) SFPM stator with FAs in all stator teeth

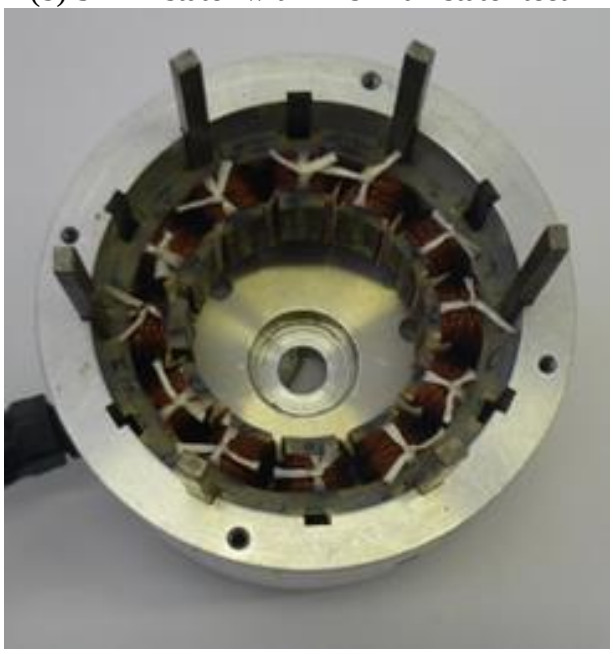

(c) SFPM stator with FAs in alternative stator teeth

Fig. 5.9 Prototype of SFPM machine with flux adjusters.

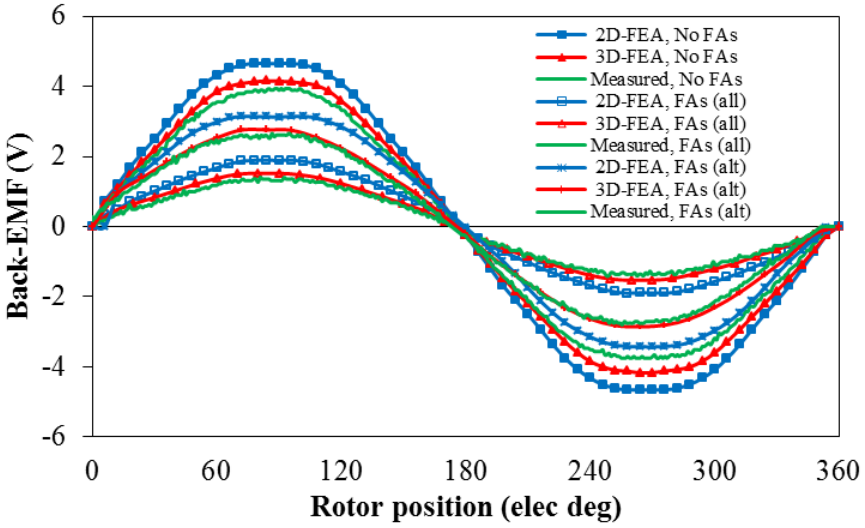

(a) 12/10 machine

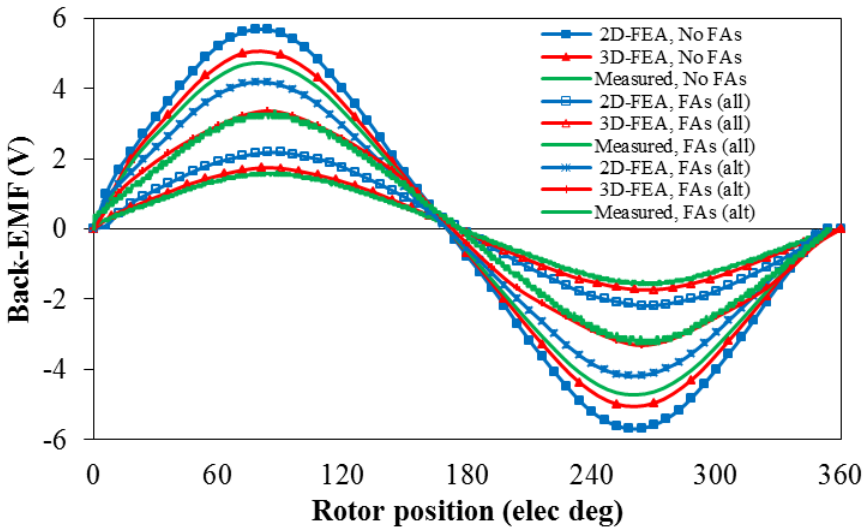

(b) 12/13 machine

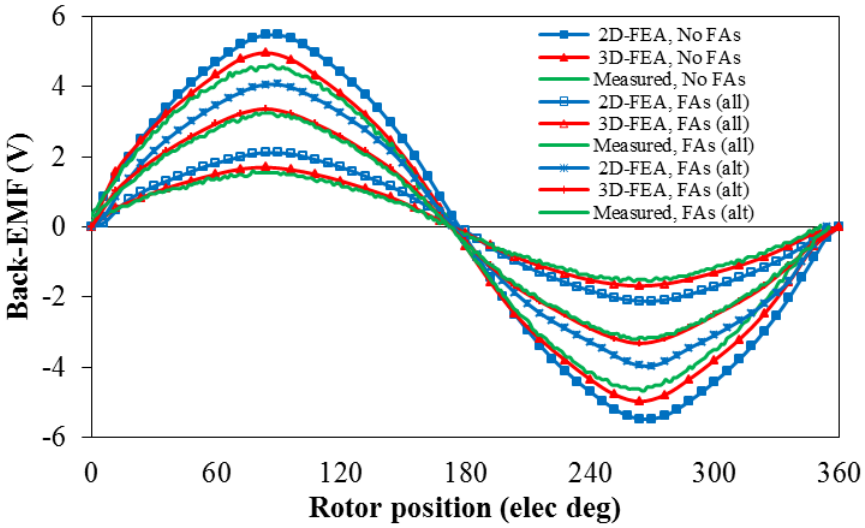

(c) 12/14 machine

Fig. 5.10 Comparison of 2D and 3D-FEA predicted, and measured back-EMF waveforms of SFPM machines without and with all and alternative FAs.

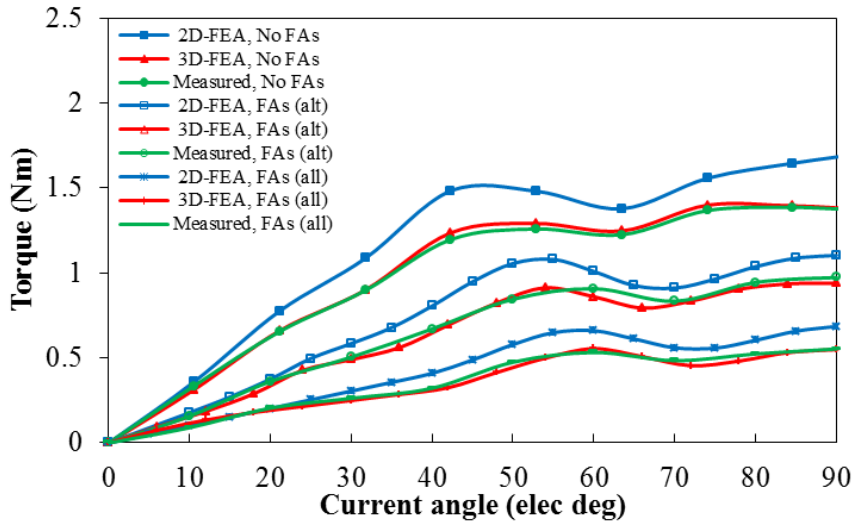

(a) 12/10 machine

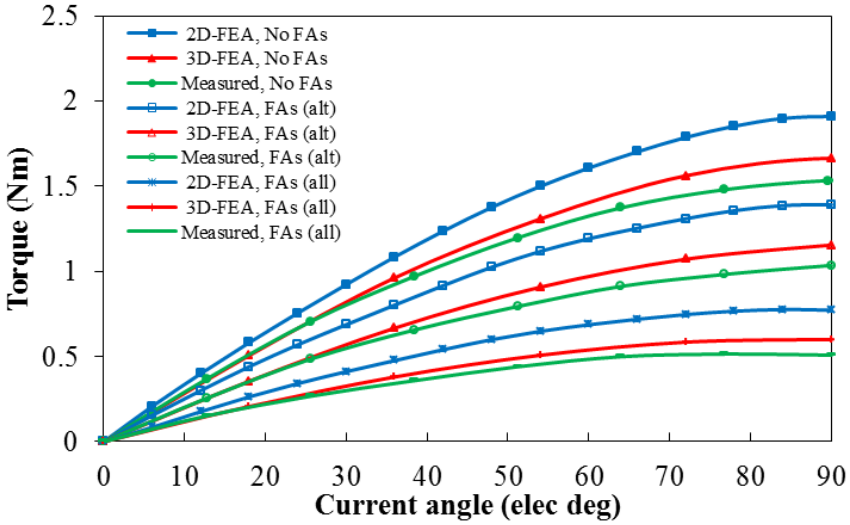

(b) 12/13 machine

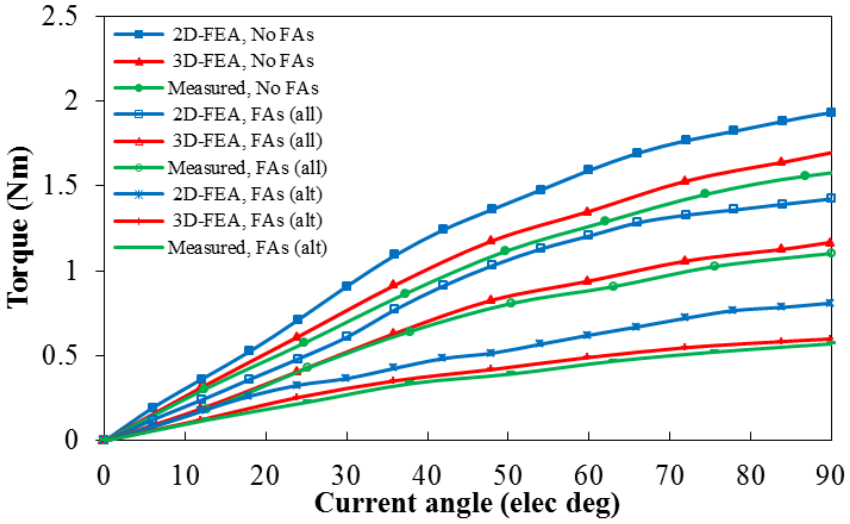

(c) 12/14 machine

Fig. 5.11 2D and 3D predicted and measured torque-current angle curves of SFPM machines without and with all and alterative FAs at load condition of (I_a=10A, I_b=I_c= -5A).

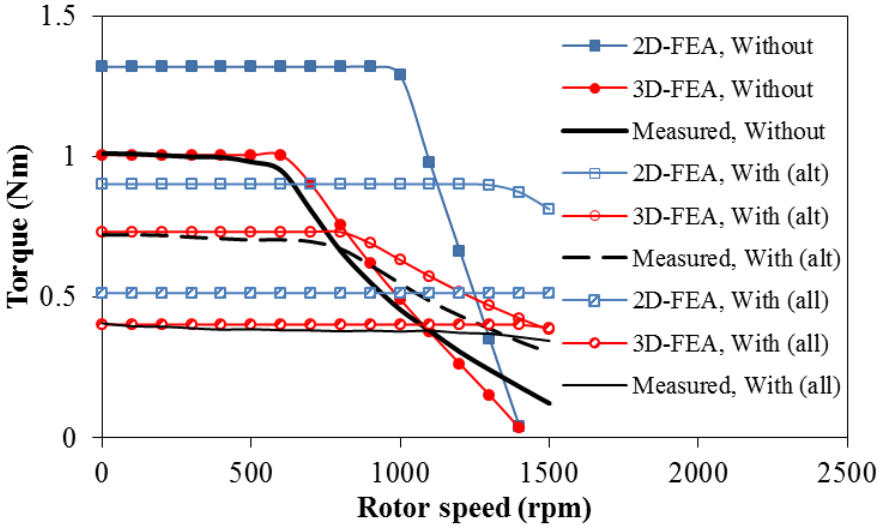

(a) 12/10 machine

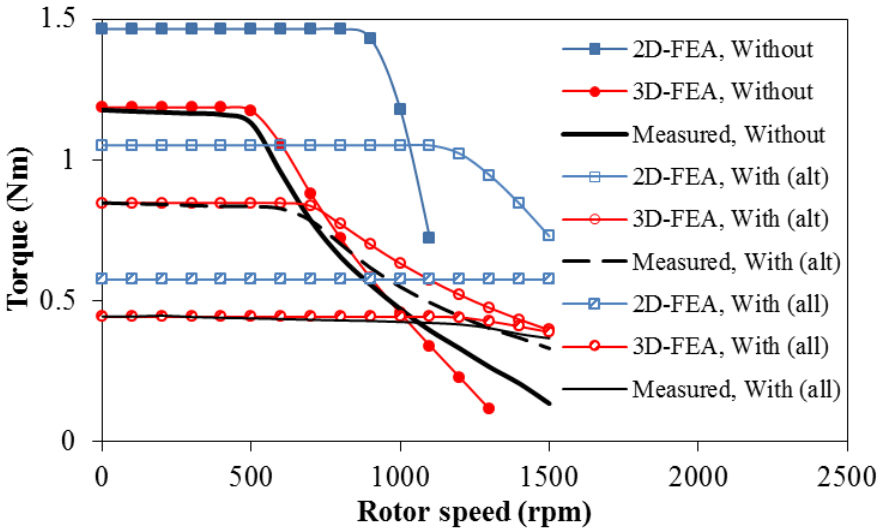

(b) 12/13 machine

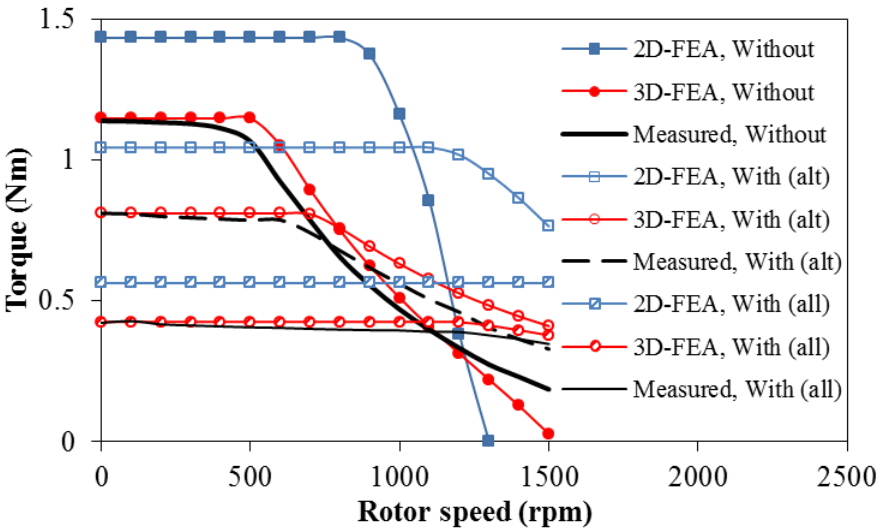

(c) 12/14 machine

Fig. 5.12 Measured, and 2D and 3D-FEA predicted torque-speed curves of SFPM machines without and with all and alternative FAs.

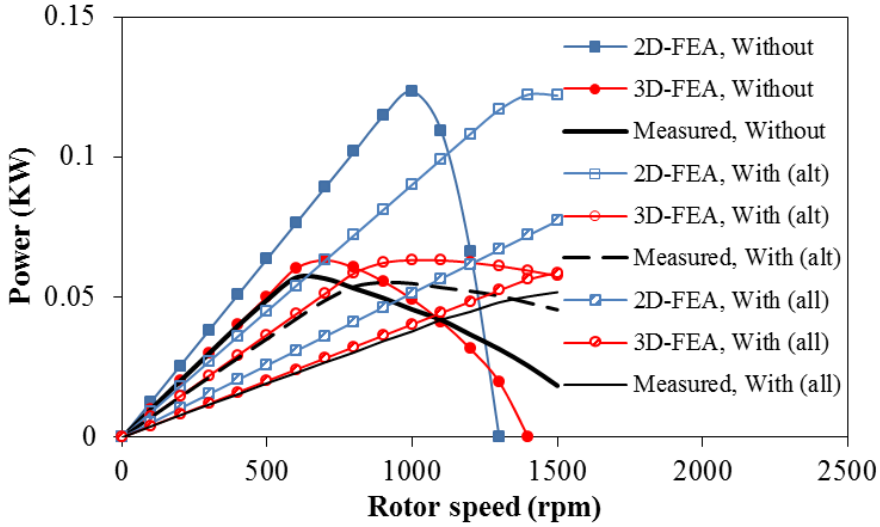

(a) 12/10 machine

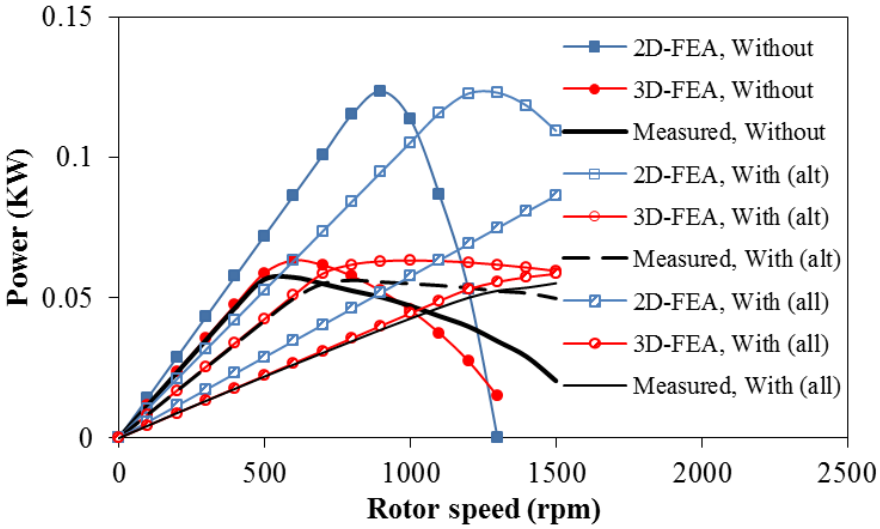

(b) 12/13 machine

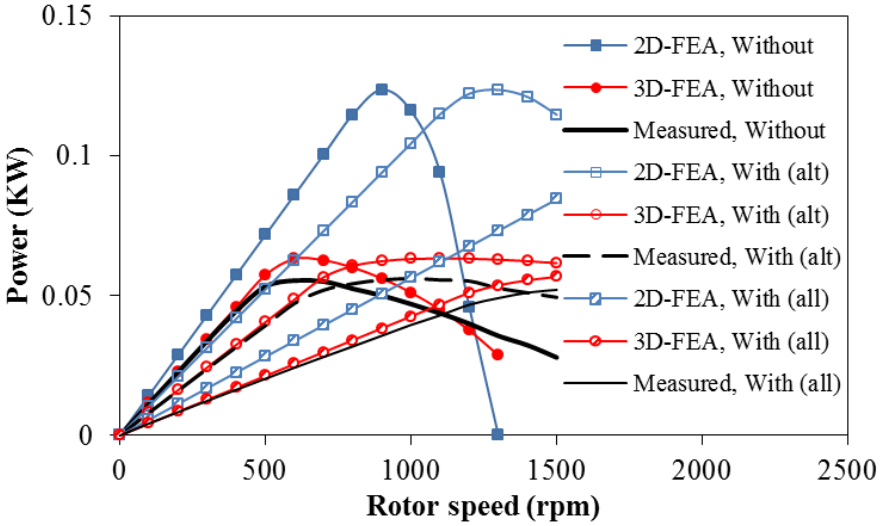

(c) 12/14 machine

Fig. 5.13 Measured, and 2D and 3D-FEA predicted power-speed curves of SFPM machines without and with all and alternative FAs.

5.5. Conclusion

In this chapter, SFPM machines with mechanically movable flux adjusters for all or alternative stator poles are developed and analyzed in order to extend the operation speed range and improve the flux weakening capability. The electromagnetic performance and torque-speed characteristics of 12/10, 12/13 and 12/14 stator/rotor pole SFPM machines with all and alternative FAs are investigated and compared. It shows that using FAs in all stator poles can extend the speed range of SFPM machines extensively. However, reducing the number of flux adjusters to half by applying the flux adjusters alternatively, a significant improvement can be exhibited albeit with a drawback of high torque ripple. A combined method to adjust the flux and operation speed range by employing no FAs, alternative FAs and all FAs by moving the FAs in sequential steps can be utilized. Moreover, it has been found that the higher the rotor poles, the better the flux weakening improvement when FAs are used. Finally, it has been concluded the 12/13 machine is the most suitable candidate for alternative FAs since no distortion on the back-EMF is observed and small cogging torque is exhibited.

6. Novel SFPM Machine with Radial and Circumferential Permeant Magnets

6.1. Introduction

Many investigations and studies on the SFPM machine have been reported in the past 10 years [10, 31, 40, 139, 145, 158]. An overall examination of the topology and performance of the SFPM machine is presented in [3, 158]. Moreover, lumped parameter circuit is designed to investigate the performance of the conventional SFPM machine as shown in [31]. Furthermore, in [10] several stator/rotor pole combinations are investigated with the objective to explore the optimum combination. Finally, since the end-effect is relatively large, in the SFPM machine due to the spoke location of the PMs, several studies on the influence of the end-effect have been reported [40, 139, 145].

On the other hand, SFPM machine topologies having multi-sandwiched PMs stator poles in parallel and V-shaped are proposed to increase the flux focusing effect [60, 159]. Low cost ferrite magnets are used instead of the rare earth, although lower performance is exhibited [60]. A modular rotor is used in SFPM machine, and an investigation on the iron loss is presented in [70]. For linear motion applications, several linear and tubular SFPM machine topologies are proposed and designed [74, 80, 160]. Moreover, SFPM machines with external rotor have been designed for direct-drive applications [71, 161]. Furthermore, as stated in Chapter 1 and 2, several SFPM machine topologies are proposed to reduce the magnetic materials and maintain the torque performance by decreasing the PMs size, i.e. using thinner PM, thus larger slot area can be employed, whereas in the multi-tooth, E-core and C-core topologies the slot area increased by reducing the total number of PMs.

In [9, 139] the magnetic flux distribution in the conventional SFPM (CSFPM) machine is modelled and analysed. Moreover, it is stated that in addition to the stator-rotor pole flux leakage, there are two magnetic flux leakage components occur in the stator of SFPM machine: 1) the end-region leakage; 2) the stator-outer region leakage.

Therefore, in order to reduce the stator-outer region leakage and achieve higher magnetic material utilization, a novel SFPM topology with circumferential PMs (PMc) and radial PMs (PMr) (SFRCPM) is proposed. The influence of the design parameters on the machine performance is investigated. Moreover, using Genetic Algorithm (GA) the SFRCPM machine

is globally optimized. Additionally, internal and external rotor SFRCPM machine topologies are presented, optimized and their results are compared with those of CSFPM machine having the same size, rotor configuration, copper loss and stator/rotor pole combination.

6.2. Topology of SFRCPM Machine

In CSFPM machine the stator is made of laminated cores shaped like 'U' sandwiched with circumferentially magnetized PMs in alternative opposite direction (PMc set) as shown in Fig. 6.1 (a). In the SFRCPM topology, the same structure as that of CSFPM machine is adopted albeit with a new PMs set made of radially magnetized magnets (PMr set) in alternative opposite direction, situated around the back iron, separated by airgaps and surrounded by a laminated ring frame, Fig. 6.1 (b).

Therefore, in addition to the original flux-linkage generated by the PMc set, Fig. 6.2 (a), a new flux-linkage provided by the PMr set is introduced as shown in Fig. 6.2 (b). Moreover, the location of the PMr set reduces the flux-leakage in the stator-outer region and enhances the PM flux-linkage, and therefore high magnetic utilization can be exhibited.

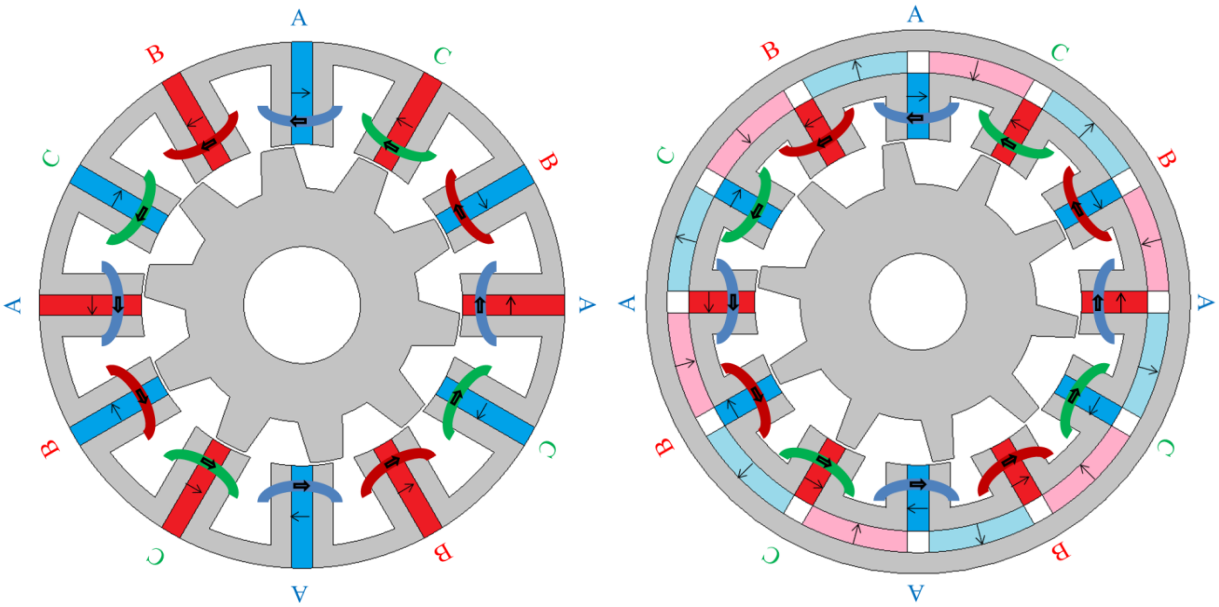

(a) CSFPM (b) SFRCPM

Fig. 6.1 Cross-sections and winding layouts of CSFPM and SFRCPM machine topologies.

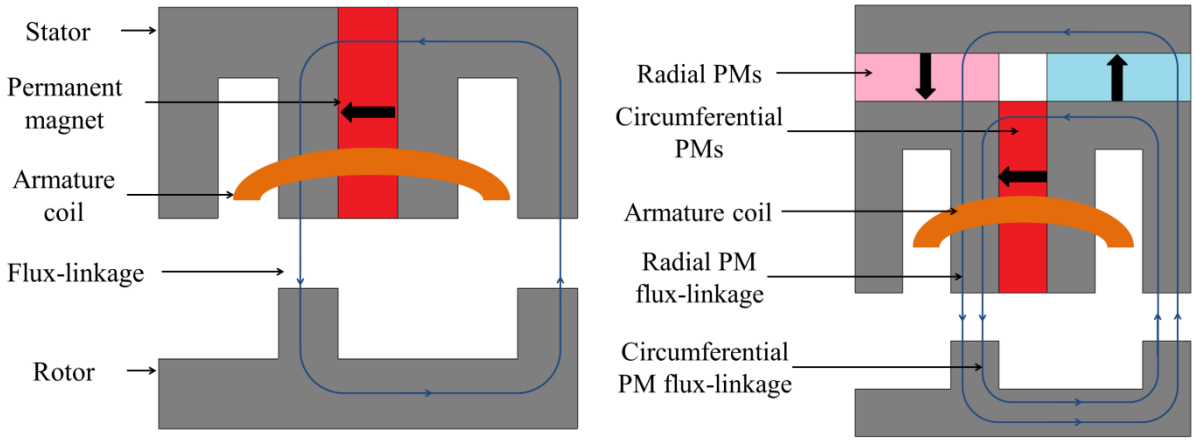

(a) CSFPM machine (b) SFRCPM machine

Fig. 6.2 Concept of CSFPM and SFRCPM machine topologies.

6.3. Parametric Investigation and Optimization of SFRCPM Machine

6.3.1. Parametric investigation

In order to fully utilize both the PMc and PMr to maximize the flux linkage and torque, and to avoid any potential demagnetization, the ratio of the PMc to PMr height (h_{PMc} to h_{PMr} ratio, Fig. 6.3) is investigated. Therefore, the average flux densities of the PMc and PMr are monitored while the PMc height varies from 1.5 to 3mm, whereas the PMr height changes from 0.5 to 3mm as shown in Fig. 6.4 (a). It is found that when the PMc height is equal to twice the PMr height ($h\_{PMc}=2h\_{PMr}$), both magnets contribute the most flux and no demagnetization risk occurs. However, high magnetic saturation leads to lower flux contribution and slightly different optimum height ratio as it can be seen when the PMc height is 3mm, Fig. 6.4 (a).

Moreover, in order to obtain the contribution of each PM set on the phase PM flux-linkage separately, frozen permeability (FP) calculations are used [162]. Fig. 6.4 (b) presents the PM flux-linkages of the PMc and PMr, respectively, it can be seen that the PMc contributes 2/3 of the total PM flux-linkage while the rest 1/3 is generated by the PMr which is consistent with their total volume when their optimum height ratio is used.

Fig. 4 presents one stator pole of SFRCPM machine with the flux-linkage paths together with its simplified equivalent magnetic circuit. Since both PMc and PMr flux-linkages are in parallel, in order to balance the magnetic flux contribution of both magnet sets and avoid any

potential demagnetization, assuming the core has infinite permeability, the following equation needs to be satisfied:

$$H_{cm}l_{cm} = H_{rmp}l_{rmp} + H_{rmc}l_{rmc} \tag{6-1}$$

Since both PMrn and PMrp have the same geometry, Fig. 4, (1) can be rewritten as:

$$H_{cm}l_{cm} = 2H_{rm}l_{rm} \tag{6-2}$$

where H_{cm}, H_{rm}, l_{cm}, and l_{rm} are the coercivity and the magnetic excitation height of the PMc and PMr, respectively. However, the same magnet material is used in both PM sets, i.e. same coercivity, therefore the height of the PMc is equal to twice the PMr height.

Furthermore, in order to find the optimum thickness of the laminated ring frame (h_{fr}), the optimum ratio of the PMc to PMr height is used and the average flux densities of both PMs are calculated at different laminated ring frame thicknesses as shown in Fig. 6.6. It is found that the optimum thickness of the frame ring is equal to about twice the PMr height. When the frame ring thickness is larger than the optimum value, the flux contribution of both PMs does not change as shown in Fig. 6.6. However, the saturation in the frame ring causes lower PMr contribution and on the other hand the thicker back iron (h_{bi}) and the increase in the PMc width (w_{PMc}) results in higher PMc flux contribution when the frame ring thickness is smaller than the optimum. Therefore, the total phase PM flux-linkage and consequently the torque do not significantly vary with the frame ring height.

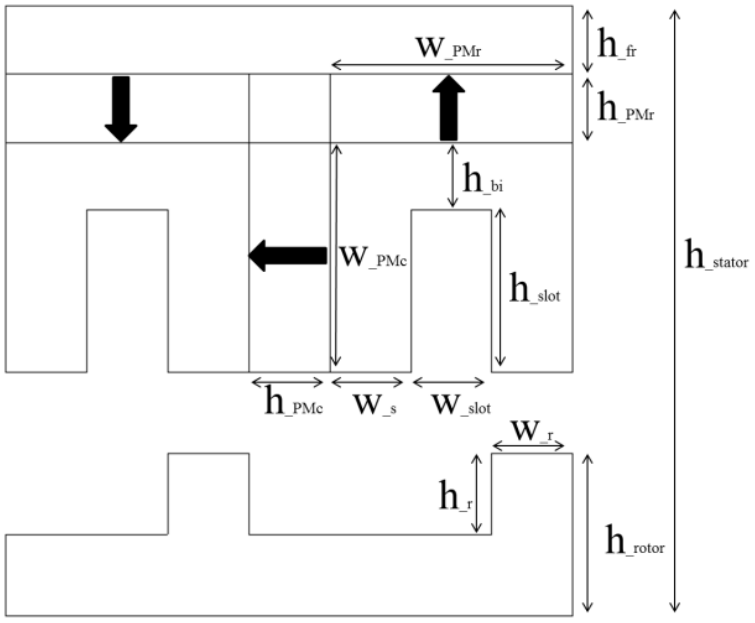

Fig. 6.3 Design parameters of DPMS machine topology.

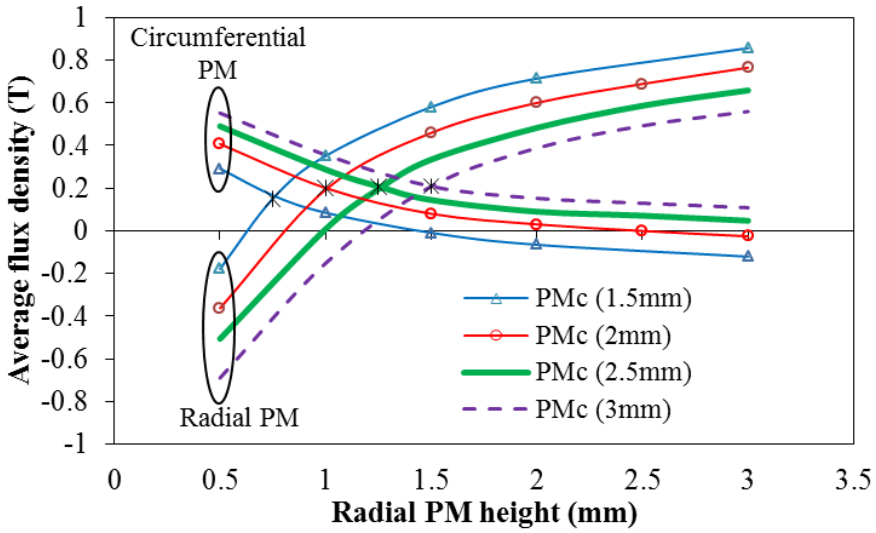

(a) Flux contribution of PMc and PMr at different heights

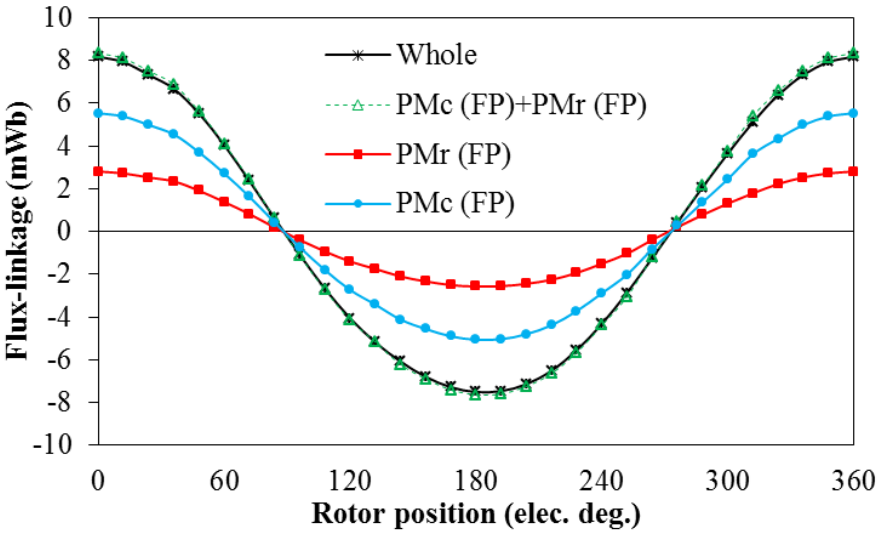

(b) Flux-linkage contributions of PMc (height=2mm) and PMr (height=1mm) using frozen permeability method

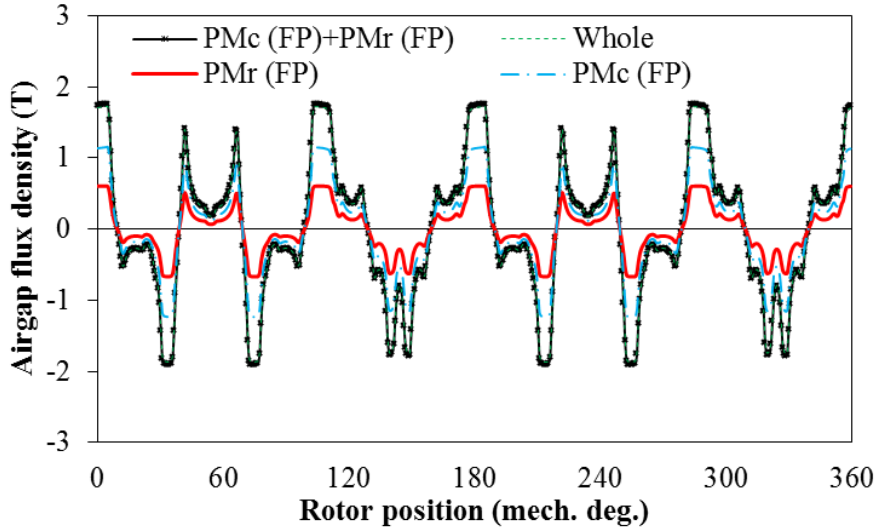

(c) Airgap flux density contributions of PMc (height=2mm) and PMr (height=1mm) using frozen permeability method

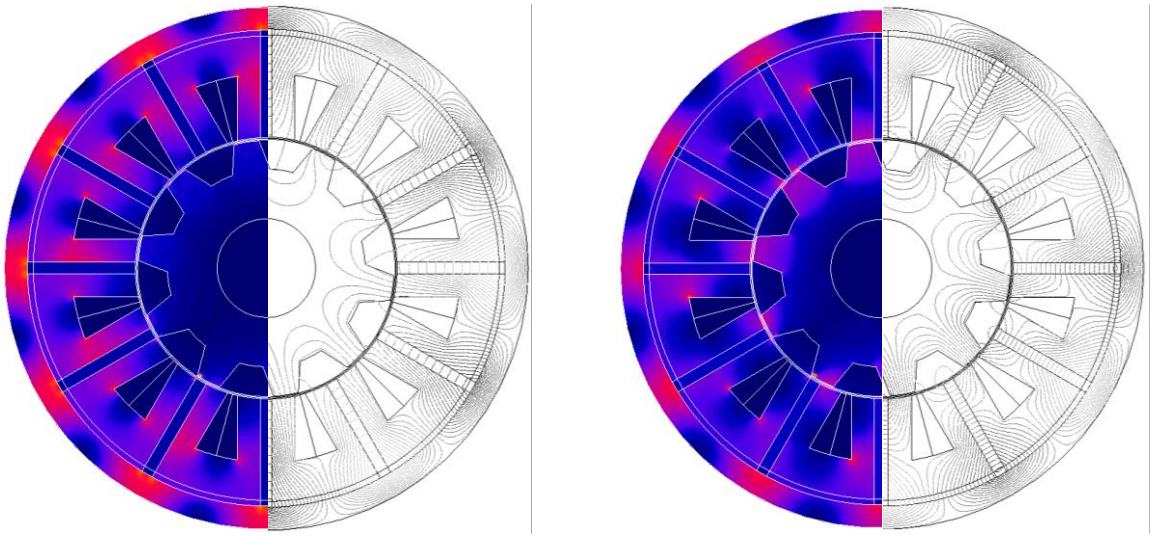

PMc (FP) PMr (FP)

(d) Equipotential and flux density distributions of PMc (height=2mm) and PMr (height=1mm) using frozen permeability method

Fig. 6.4 Influence of PMc and PMr height.

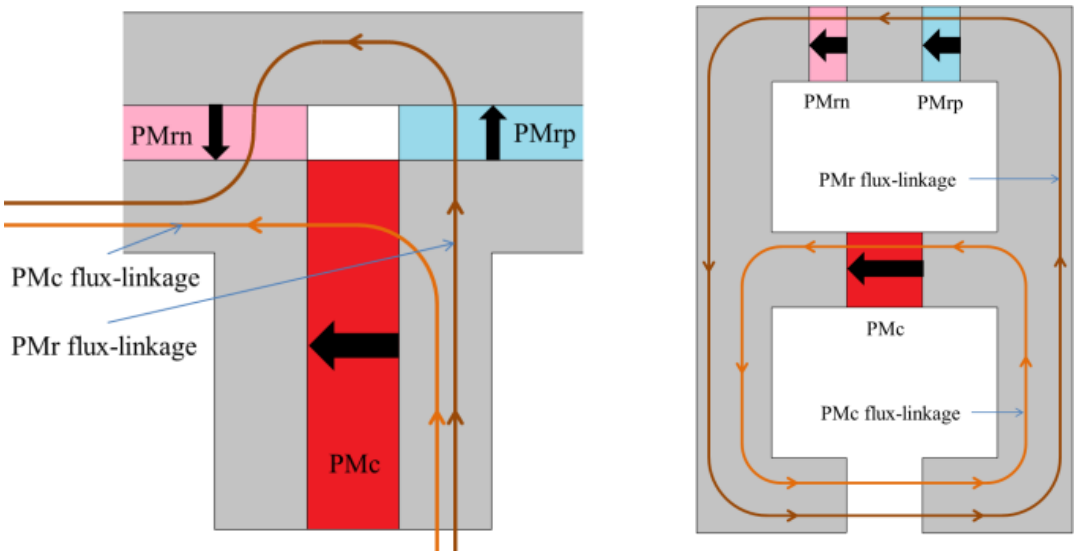

(a) Stator pole (b) Equivalent magnetic circuit

Fig. 6.5 Stator pole and its equivalent simplified magnetic circuit of SFRCPM machine.

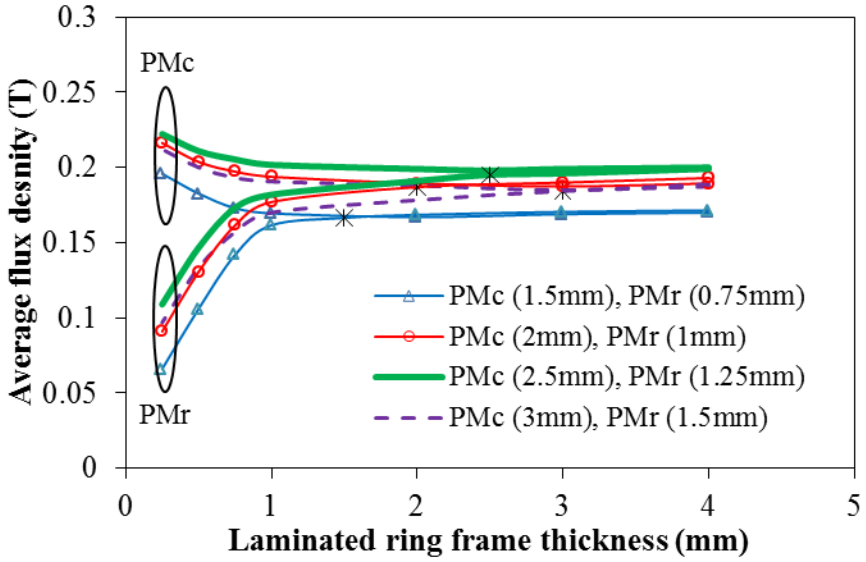

Fig. 6.6 Influence of laminated ring frame thickness.

6.3.2. Optimization of SFRCPM machine

In order to perform an effective optimization, a global optimization approach combining FEA with GA is used. The optimization is carried out with fixed copper loss, outer diameter, airgap and axial length. The GA settings are presented in Table 6.1, whereas the design parameters of the SFRCPM machine are illustrated in Fig. 6.3. Moreover, based on the previous parametric investigation, four different GA optimization scenarios are used:

Scenario 1: Without parameter restriction

Scenario 2: With restriction of (h_{PMr}=0.5h_{PMc}=h_{ib})

Scenario 3: With restriction of (PMc_{avefd}= PMr_{avefd})

Scenario 4: With restriction of (h_{PMr}=0.5h_{PMc}=h_{ib}) and (PMc_{avefd}= PMr_{avefd})

where PMc_{avefd}, and PMr_{avefd} stands for the average flux density of the PMc and PMr, respectively.

Fig. 6.7 shows the cross-sections of the optimum designs of the four GA optimization scenarios together with their torque and torque per magnet volume (T/M) ratio. The torque waveforms of the four optimum designs are compared in Fig. 6.8. It can be seen that in scenario 1 the GA attempts to reduce the PMr and frame ring, thus the PMr is fully demagnetized by the PMc and used as a shield to reduce the flux leakage. This is understandable since although the PMr is beneficial to contributing the flux linkage, it will

reduce the effective stator size of the original CSFPM machine. For the same copper loss, it is desirable to have the PMr thickness as small as possible for maximum torque. On the other hand, scenarios 2 and 4 produce similar optimum designs with small marginal difference as shown in Fig. 6.7. Moreover, scenario 3 exhibits the optimum design although scenario 1 produces higher torque than the other three, the T/M is much higher in scenario 3, since the PMr is not contributing any flux in scenario 1. It is worth mentioning that the same optimization procedure and conditions are used to optimize the CSFPM machines, i.e. with external and internal rotors, which are used in the comparisons presented in the next section. Fig. 6.9 presents the flux density and linkage distribution of the four optimum designs, whereas the cost functions of the four scenarios are shown in Fig. 6.10.

Table 6.1 Genetic algorithm optimization settings

Details	Values
Maximum number of generations	250
Parents (number of individuals)	20
Mating pool (number of individuals)	20
Mating (Individual crossover probability)	1
Mutation probability	1
Children (number of individuals)	20
Pareto front (number of survivors)	10
Torque target (T_i)	5
Weight of target (w_i)	1
Cost function	$Cost = -\sum_{1}^{N} \lvert T_i w_i \rvert$

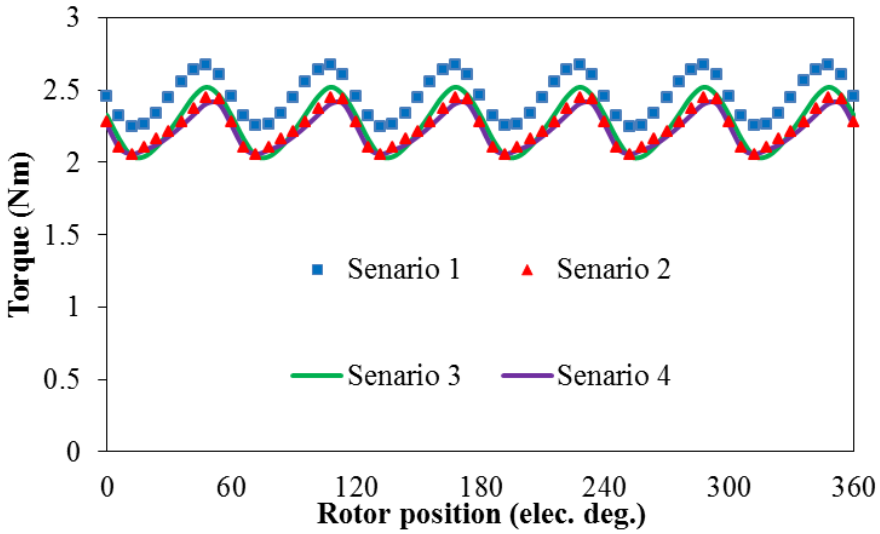

Fig. 6.7 Torque waveforms of optimum designs of different global optimization scenarios.

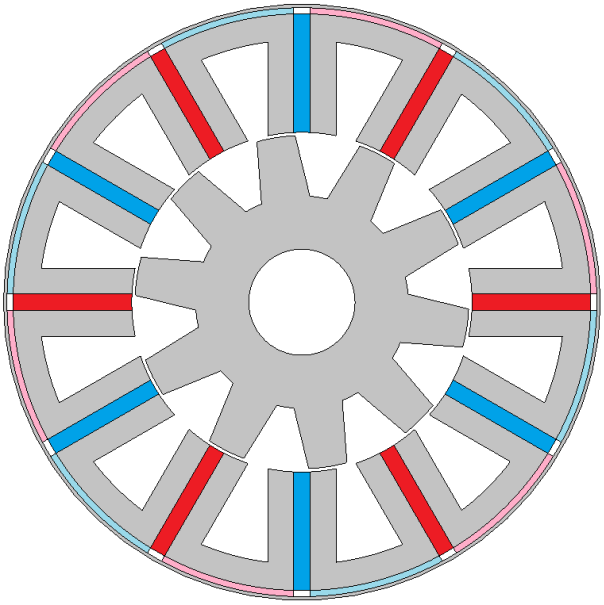

Torque=2.45Nm, T/M=1.56
(a) Scenario 1

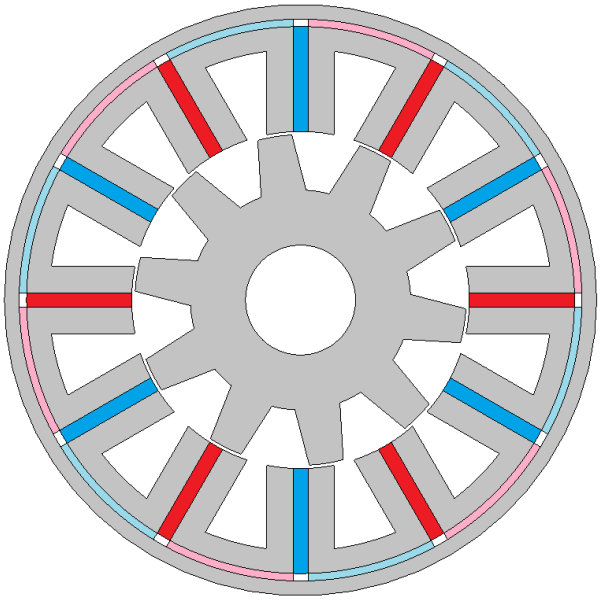

Torque=2.24Nm, T/M=1.54
(b) Scenario 2

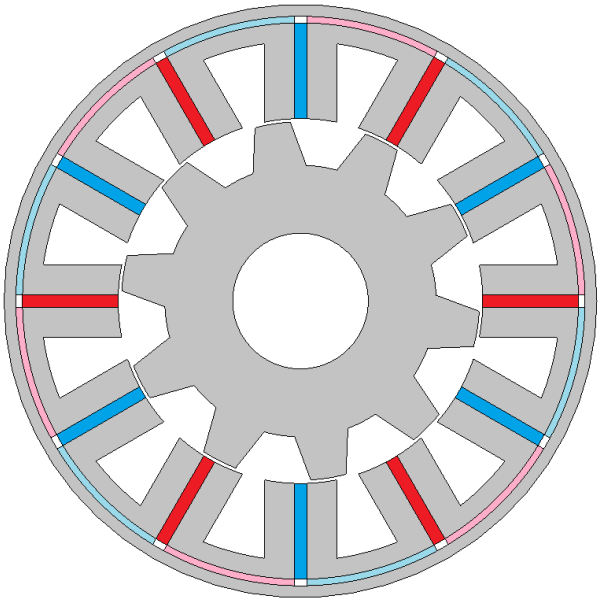

Torque=2.26Nm, T/M=1.87
(c) Scenario 3

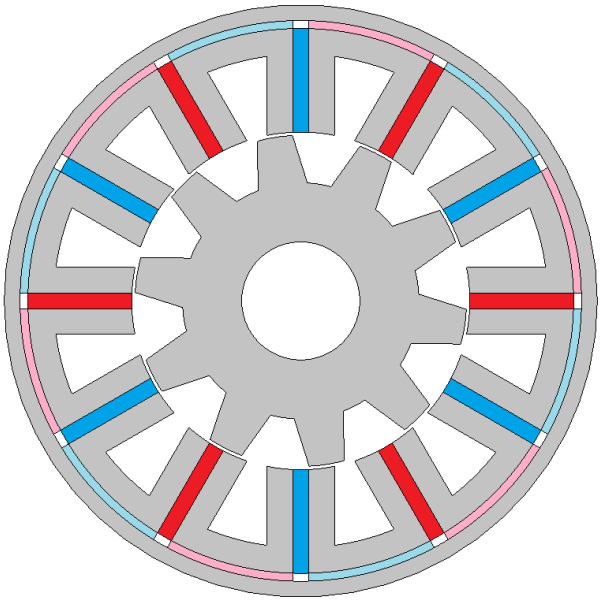

Torque=2.21Nm, T/M=1.44
(d) Scenario 4

Fig. 6.8 Optimum designs with their torque and torque per magnet volume (T/M) of global optimization scenarios of SFRCPM machine.

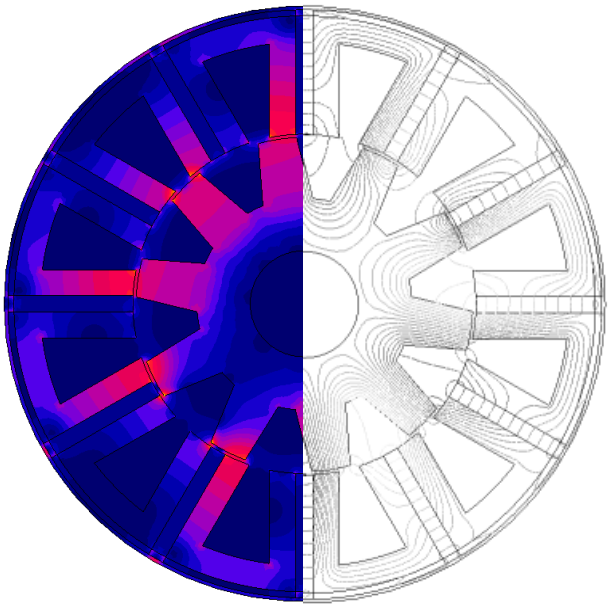

(a) Scenario 1

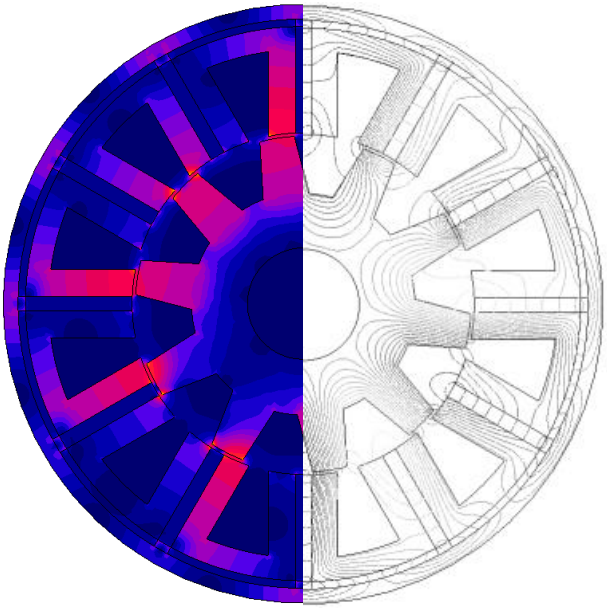

(b) Scenario 2

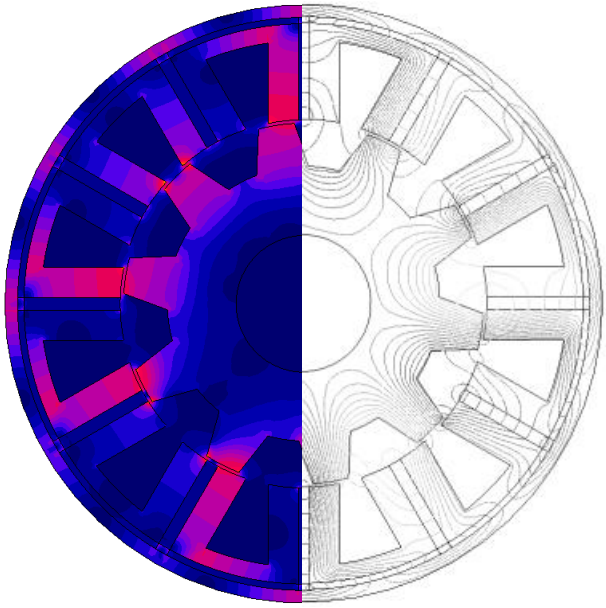

(c) Scenario 3

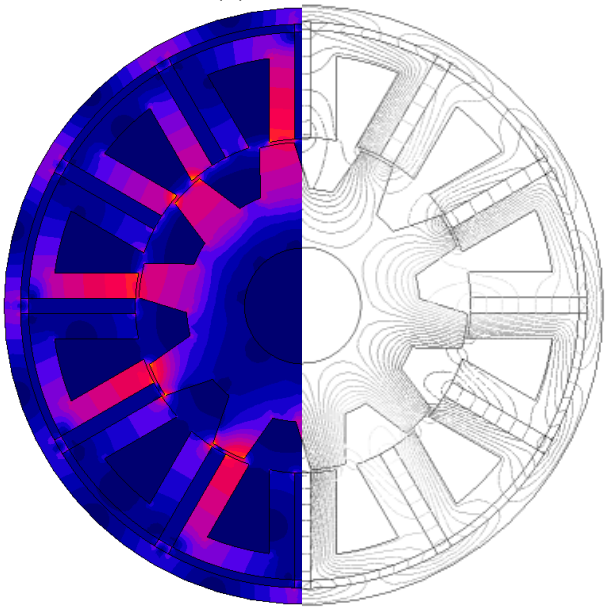

(d) Scenario 4

Fig. 6.9 Flux density and equipotential distributions of optimum designs of different global optimization scenarios.

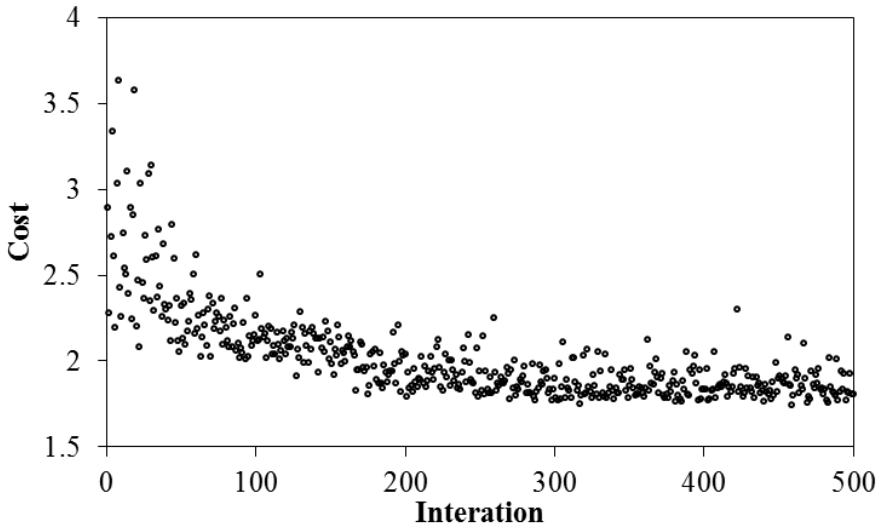

(a) Scenario 1

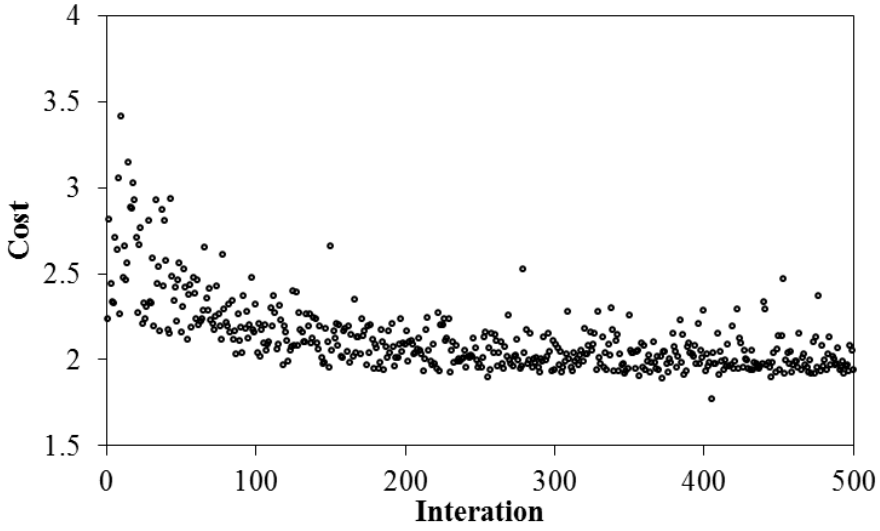

(b) Scenario 2

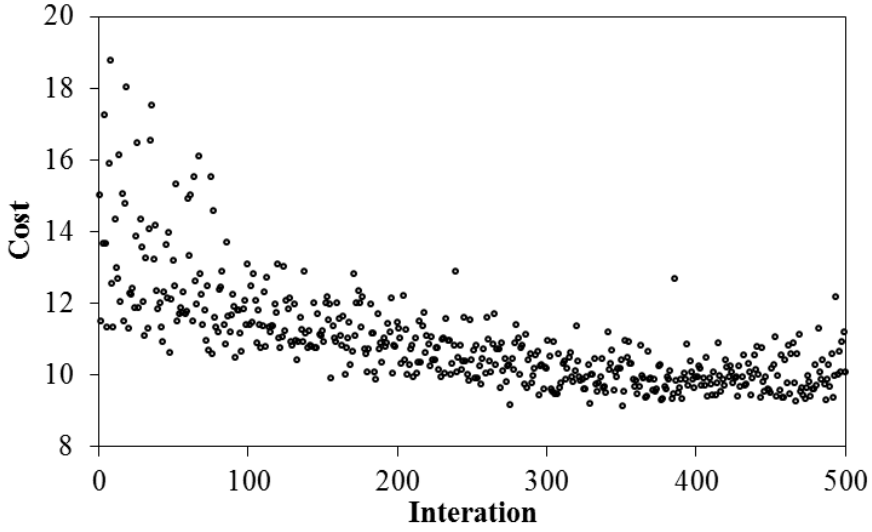

(c) Scenario 3

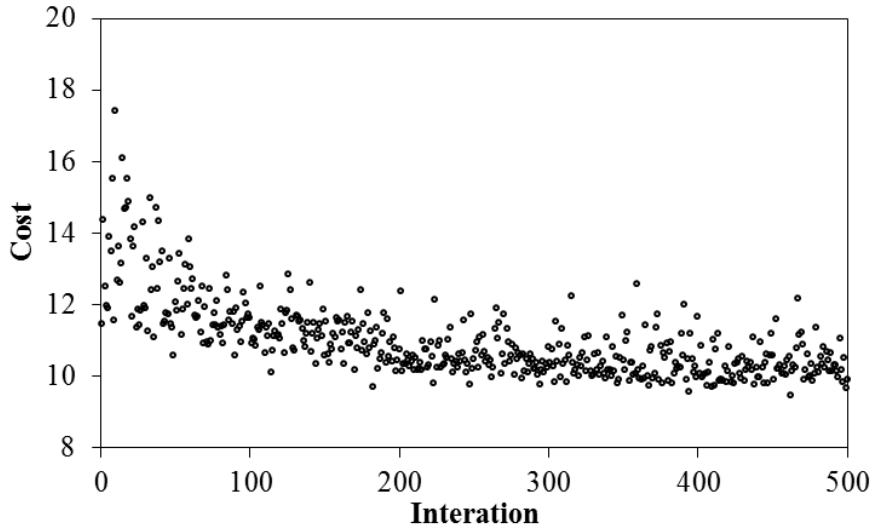

(d) Scenario 4

Fig. 6.10 Optimization procedures of four different global optimization scenarios.

6.4. Comparison of CSFPM and SFRCPM Machines with Different Rotor Configurations

6.4.1. Internal rotor SFRCPM machine

Fig. 6.11 presents the cross sections of the optimum design of CSFPM and SFRCPM machines with NdFeB and ferrite magnets, whereas the flux density and linkage distributions are presented in Fig. 12. The PM flux-linkage and torque waveforms of SFRCPM and CSFPM machines with both NdFeB and ferrite are shown in Fig. 6.13. It can be seen that when NdFeB magnets are used, the CSFPM machine produces higher flux-linkage than that of the SFRCPM machine. However, the flux-linkage per magnet volume (FL/M) is higher in the SFRCPM machine due to better PM utilization. Nevertheless, the torque and T/M are higher in the CSFPM machine due to the larger slot area since the PMr and the laminated ring frame reduce the stator size. Therefore, ferrite magnets are suggested since ferrite produces less magnetic flux thus the laminated ring frame width can be smaller and consequently more stator space is available. Similar investigation to that presented in section 6.3 is carried out with ferrite magnets. Unlike the NdFeB, it is found the laminated ring frame thickness is half the height of the PMc. Therefore, when ferrite is used the T/M in SFRCPM machine is higher than that of the CSFPM machine as shown in Fig. 6.13. However, similar to that with NdFeB the torque of the CSFPM is larger than that of the SFRCPM when ferrite magnets are used.

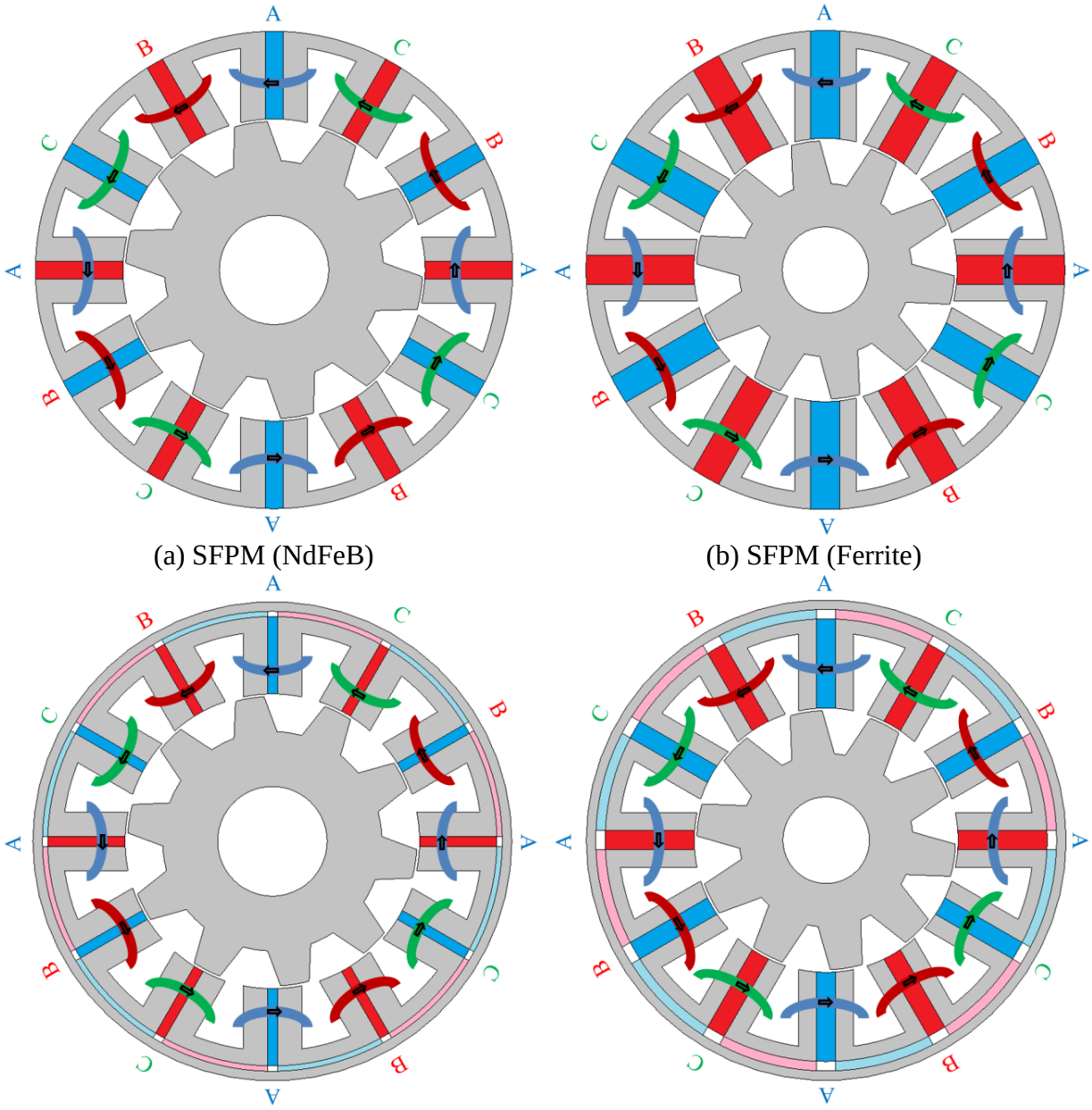

(a) SFPM (NdFeB) (b) SFPM (Ferrite)

(c) SFFCPM (NdFeB) (d) SFFCPM (Ferrite)

Fig. 6.11 Cross-sections of the optimum designs of the CSFPM and SFRCPM machines with NdFeB and ferrite magnets.

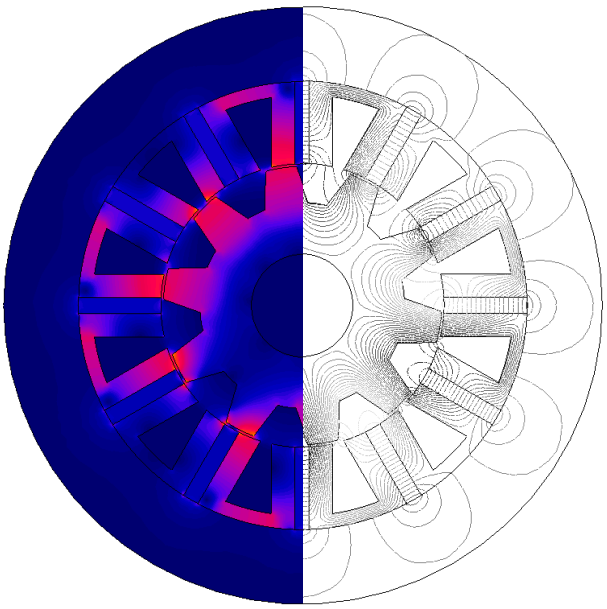

(a) SFPM (NdFeB)

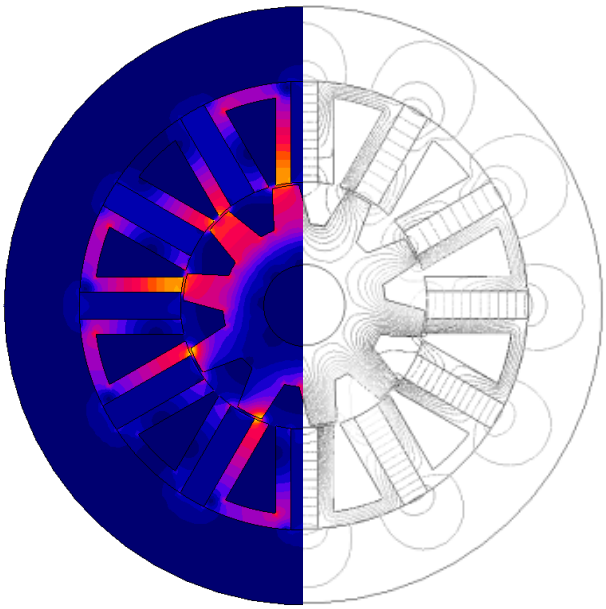

(b) SFPM (Ferrite)

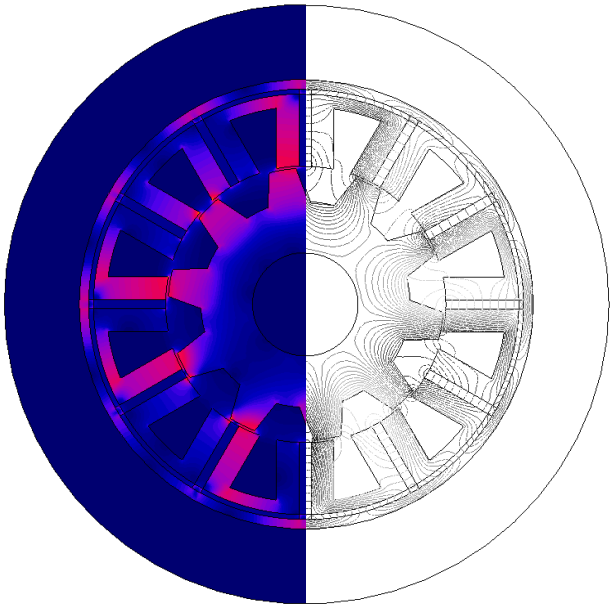

(c) SFFCPM (NdFeB)

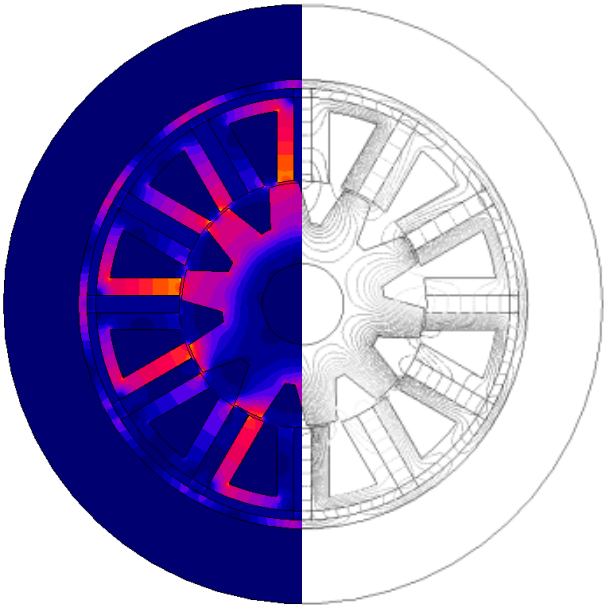

(d) SFFCPM (Ferrite)

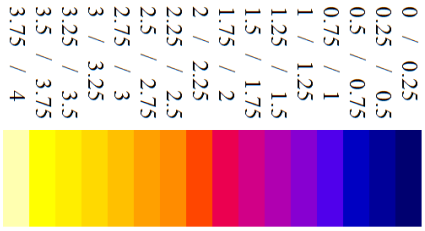

(e) Flux density (T) color scale for NdFeB machines

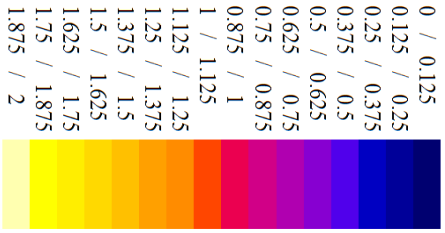

(f) Flux density (T) color scale for ferrite machines

Fig. 6. 12 Flux density and equipotential distributions of the optimum designs of the CSFPM and SFRCPM machines with NdFeB and ferrite magnets.

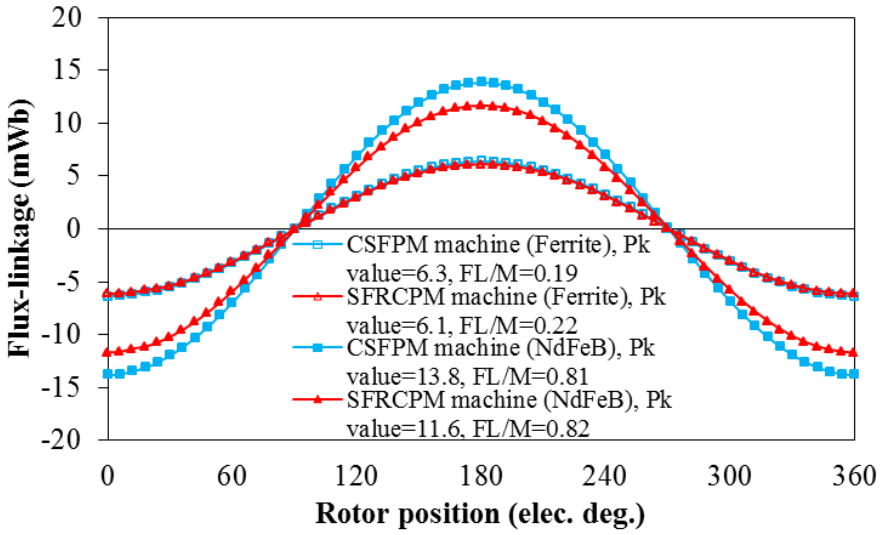

(e) PM flux-linkage with peak value (PK) and flux-linkage per magnet volume (FL/M)

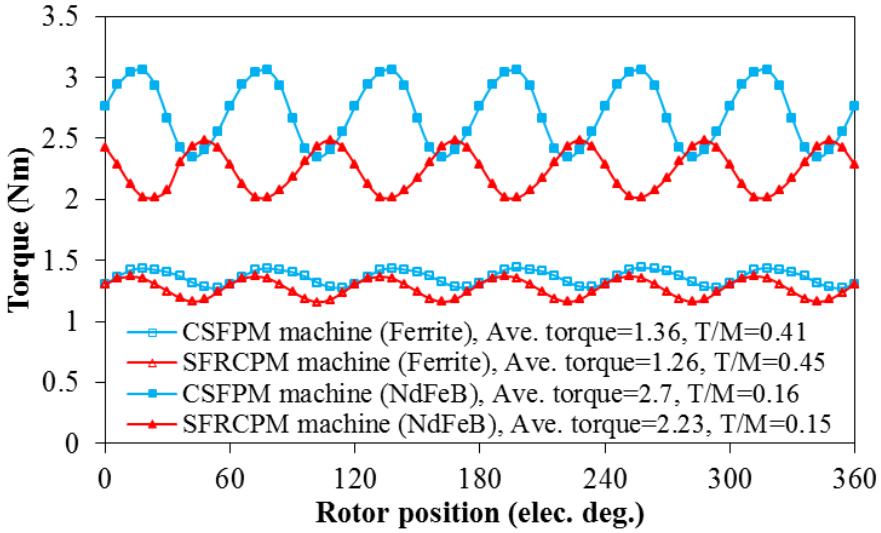

(f) Torque waveforms (I_d=0, I_q=15A) with Average torque (Ave. torque) and torque per magnet volume (T/M)

Fig. 6.13 PM flux-linkage and torque waveforms of CSFPM and SFRCPM machines with NdFeB and ferrite magnets.

6.4.2. External rotor SFRCPM machine

Since the effective stator size is reduced by the laminated ring frame and PMr in SFRCPM machine, an external rotor configuration is proposed. CSFPM and SFRCPM machine topologies with external rotor employing both NdFeB and ferrite magnets are designed, optimized and compared. It is found that the SFRCPM machine with external rotor can produce higher torque and T/M ratio than the CSFPM machine. Moreover, similar conclusion is observed when ferrite magnet is used. Therefore, a full comparison of the SFRCPM and CSFPM machines with NdFeB magnets is presented in the next section.

6.5. Comparison of External Rotor CSFPM and SFRCPM Machines

6.5.1. Topology and design parameters

In Fig. 6.14, the cross-sections of the optimum CSFPM and SFRCPM machines are shown. Table 6.2 illustrates the optimum design parameters. It is worth mentioning that both machines are optimized at fixed copper loss and phase current therefore different number of turns per phase is selected due to their different slot areas, Table 6.3. Moreover, to fully utilize the stator size, no restriction on the bore radius in the optimization is used.

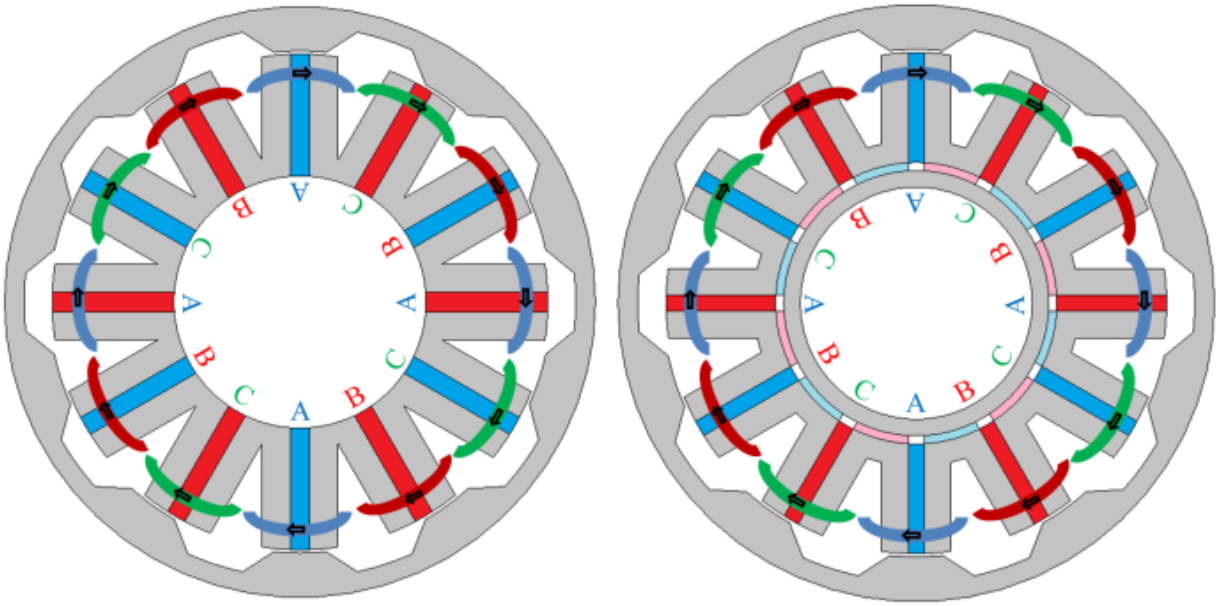

(a) SFPM (b) SFRCPM

Fig. 6.14 Cross-sections of optimized external rotor CSFPM and SFRCPM machines.

Table 6.2 Design parameters of CSFPM and SFRCPM machines with external rotor

Machines	Symbol	CSFPM	SFRCPM
Stator outer radius (mm)	h_{stator}	37.75	37.75
Stator tooth width (mm)	w_{s}	4.2	4
Rotor outer radius(mm)	h_{rotor}	45	45
Rotor tooth width(mm)	w_{r}	8	8
Rotor tooth height(mm)	h_{r}	3	3
Slot height(mm)	h_{slot}	15.3	13.7
Slot width (mm)	w_{slot}	8	9.1
PMc width (mm)	h_{PMc}	18.5	16.5
PMc height (mm)	w_{PMc}	3	2.4
Back iron (mm)	h_{bi}	3.2	2.9
PMr width (mm)	h_{PMr}	-	8.6

PMr height (mm)	w_{PMr}	-	1.2
Frame ring thickness (mm)	h_{fr}	-	2.4
Axial length (mm)	L_{a}	25	25
Airgap length (mm)	L_{gap}	0.5	0.5
Bore radius (mm)	Bo_{r}	19.2	17.5
Copper loss (W)	P_{cu}	15	15
Packing factor	K_{pa}	0.45	0.45
Turns per phase	N_a	60	68
PM remanence (T)	B_{rpm}	1.2	1.2
PM permeability	μ_r	1.05	1.05
Rated current (A)	I_{rated}	15	15

6.5.2. Open circuit performance

Fig. 6.15 presents the equipotential and flux density distributions of both CSFPM and SFRCPM machines. Moreover, the open circuit performance, i.e. airgap flux density distribution, flux-linkage, back-EMF waveforms and harmonics together with the cogging torque waveforms, of both machines are shown in Fig. 6.15. It can be seen that similar flux density distributions in the airgap are exhibited in both machines with slight differences in the peak values due to the different saturation around the airgap. On the other hand, the fundamental back-EMF in SFRCPM machine is higher than that of the CSFPM machine, whereas slightly lower Back-EMF THD as well as lower cogging torque is observed in the SFRCPM compared to the CSFPM machine. The reason is due to the wider stator tooth in the SFRCPM machine and therefore lower flux density saturation in the stator teeth is observed.

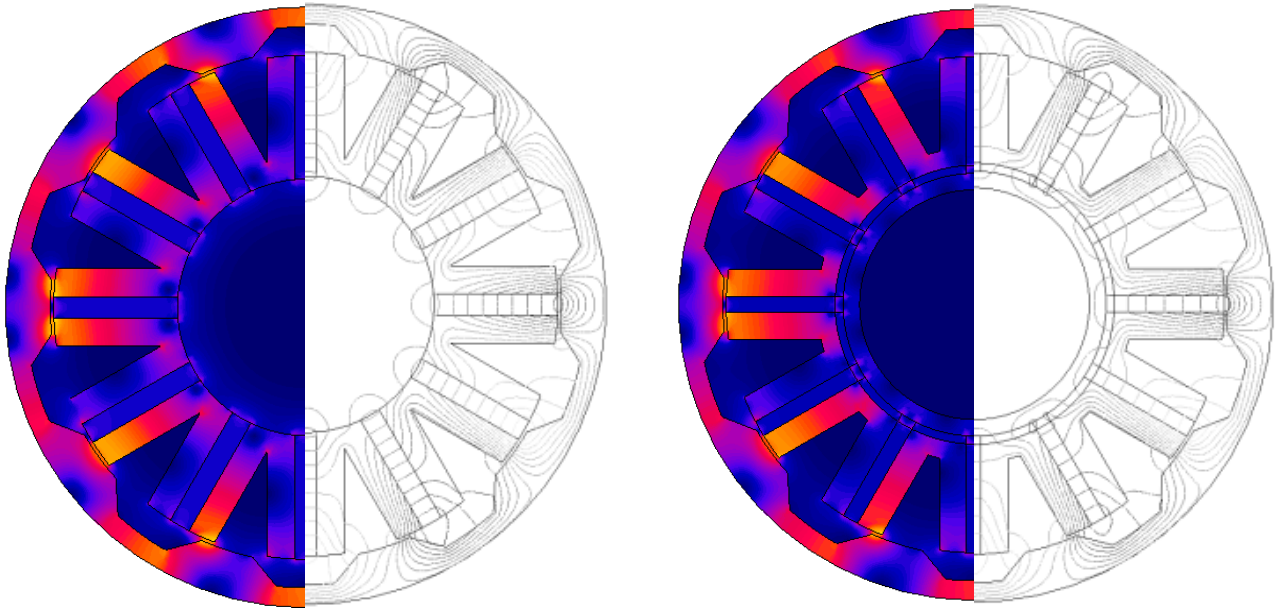

(a) CSFPM (b) SFRCPM

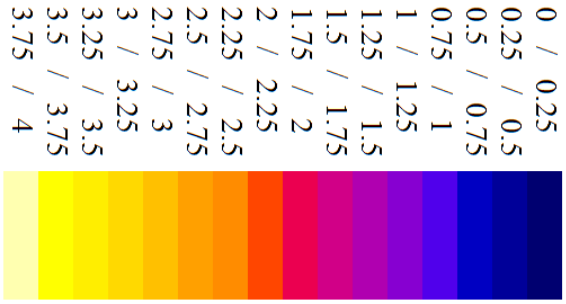

(c) Flux density colour shade (T)

Fig. 6.15 Open circuit equipotential and flux density distributions of optimized external rotor CSFPM and SFRCPM machines.

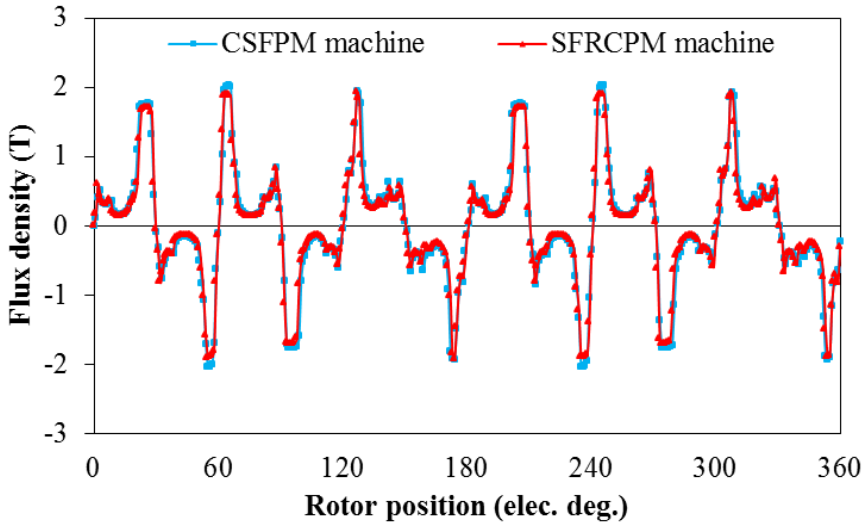

(a) Airgap flux density distributions

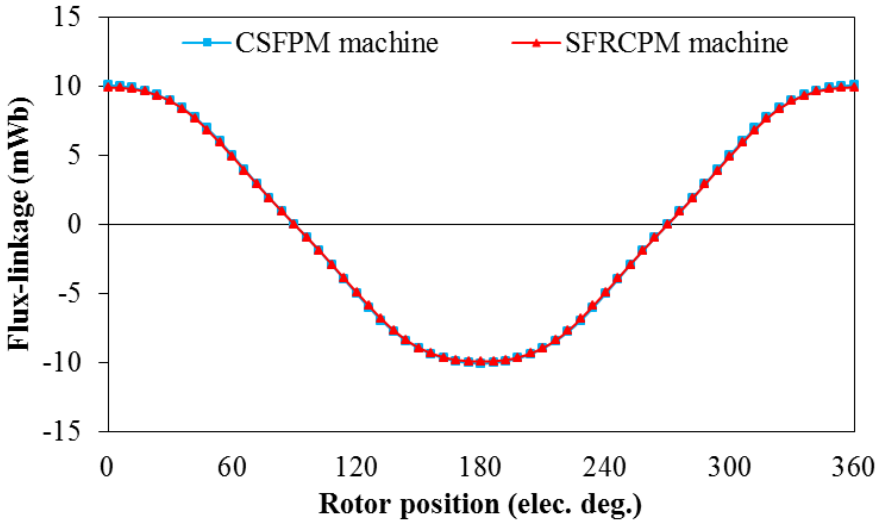

(b) Flux-linkage waveforms

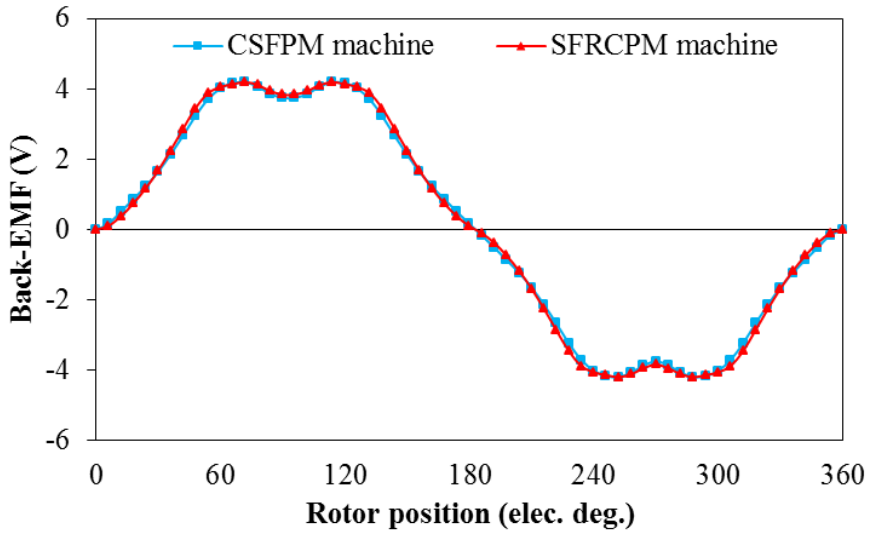

(c) Back-EMF waveforms

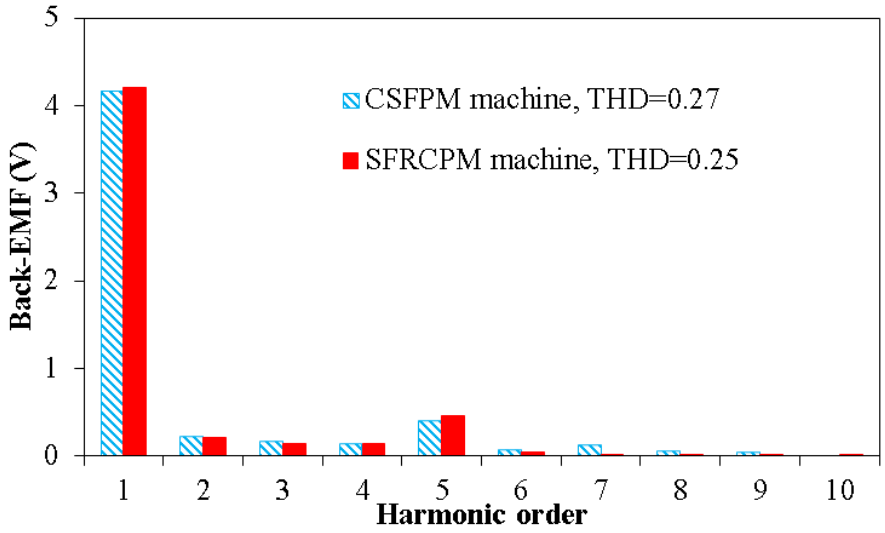

(d) Back-EMF harmonics

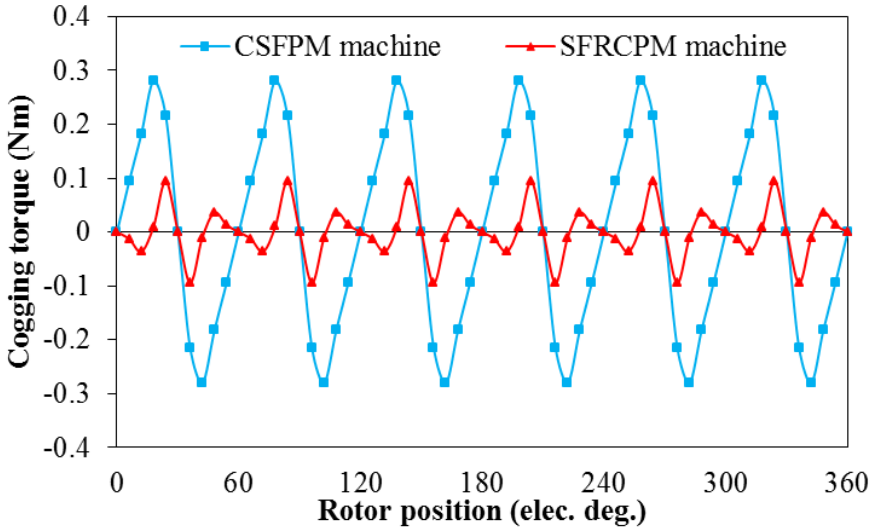

(e) Cogging torque waveforms

Fig. 6. 16 Comparison of open circuit performance of CSFPM and SFRCPM machines.

6.5.3. On-load performance

Due to better magnetic flux utilization and larger slot area, the SFRCPM machine produces higher torque and T/M than the CSFPM machine, Fig. 6.17 (a). Additionally, lower torque ripple due to low back-EMF harmonics and cogging torque is observed in the SFRCPM machine. Moreover, since the SFRCPM machine applies the concept of flux switching, the maximum torque is achieved at zero current angle, Fig. 6.17 (b). Furthermore, at high current levels the magnetic saturation is more excessive in the SFRCPM machine due to the smaller stator 'U' core size compared to that of CSFPM machine. Therefore, at high current levels the SFRCPM machine produces lower torque than the CSFPM machines as can be seen in Fig. 6.17 (c). Since less magnetic material is employed in the SFRCPM machine, the T/M is higher than that of CSFPM machine at all presented current levels, Fig. 6.17 (d).

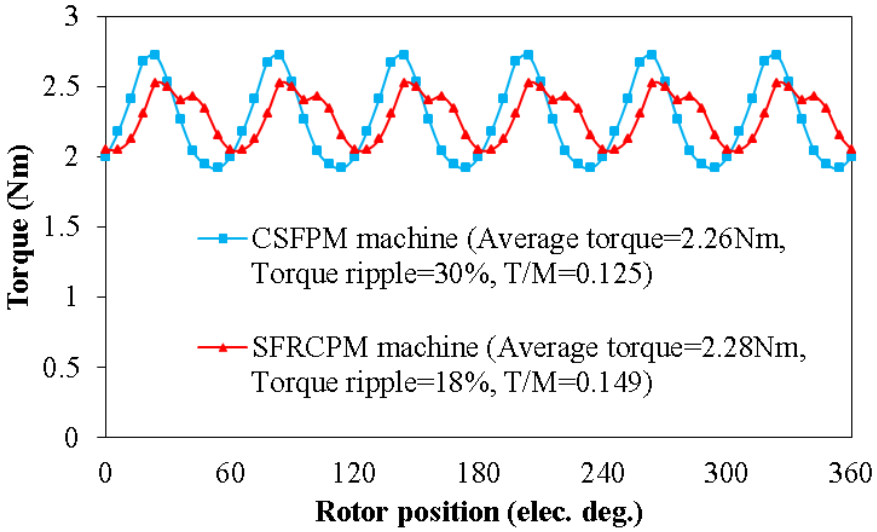

(a) Torque waveforms (I_d=0, I_q=15A) with average torque and torque ripple percentage

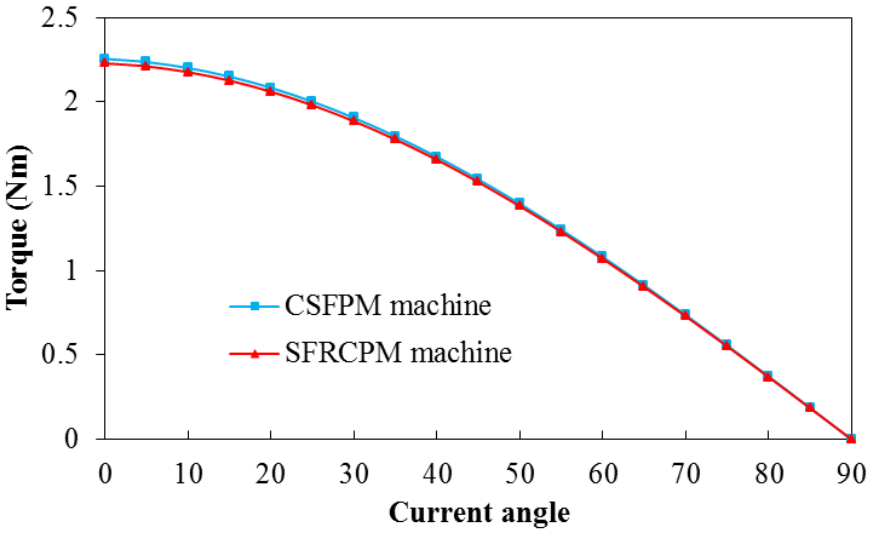

(b) Torque-current angle curve

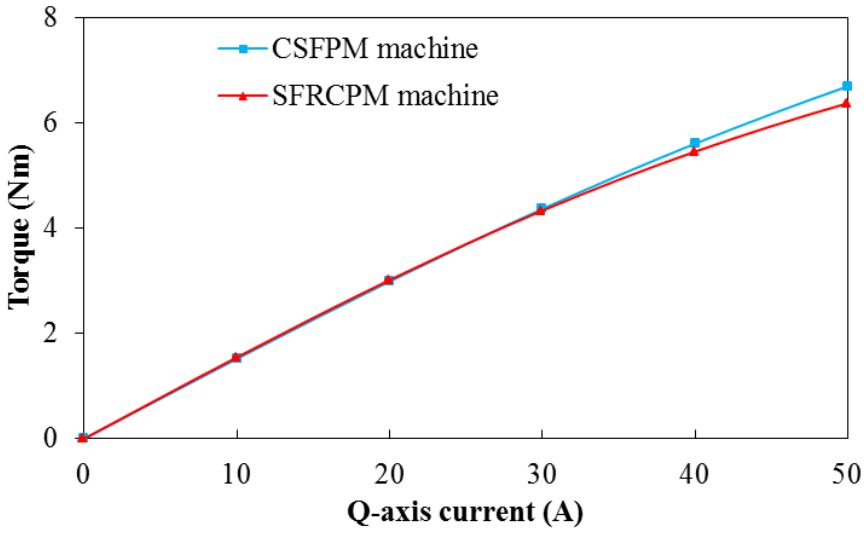

(c) Torque-current curve

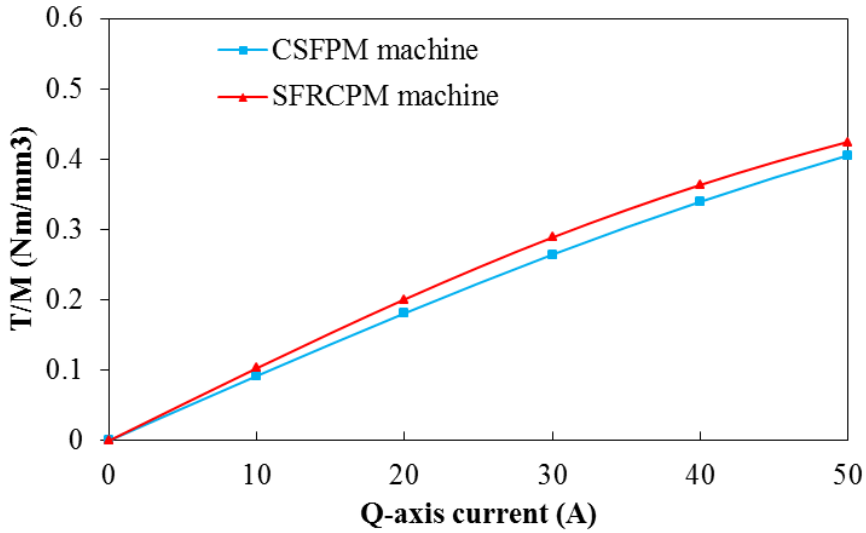

(d) T/M-current curves

Fig. 6.17 On-load performance of CSFPM and SFRCPM machines.

6.5.4. Inductances

Fig. 6.18 presents the d- and q-axis inductances at different d- and q-axis currents of the optimized external rotor CSFPM and SFRCPM machines. It can be seen that higher inductance values are exhibited in the SFRCPM machine compared to those of the CSFPM machine due to higher number of turn per phase in SFRCPM machine, Table 6.2. On the other hand, the ratio of d- to q-axis inductance is higher in the SFRCPM machine since the total magnetic material is less as well as two PMs sets are used, i.e. the PM material is more distributed.

For further investigation the same number of turns per phase of 72 is used in both machines and their inductances are compared in Fig. 6.19. It is understandable that since the same copper loss is used in both machines the phase current will be different in each machine when the same number of turns per phase is used. However, for the reason of comparison the inductances are calculated at the same current values shown in Fig. 6.18. Nevertheless, CSFPM machine produces slightly higher inductances compared to the SFRCPM machine when the same number of turns per phase is used in both machines since CSFPM machine has larger size 'U' core compared to the SFRCPM machine.

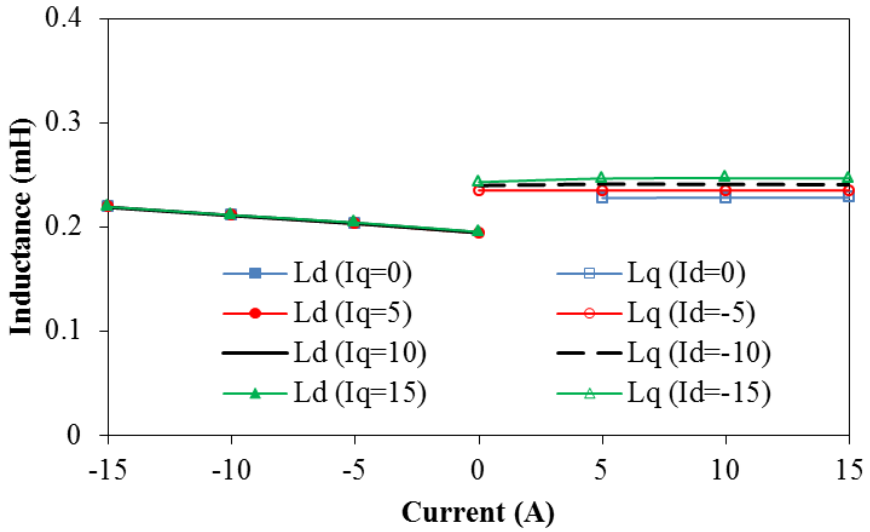

(a) CSFPM machine (turns per phase 60)

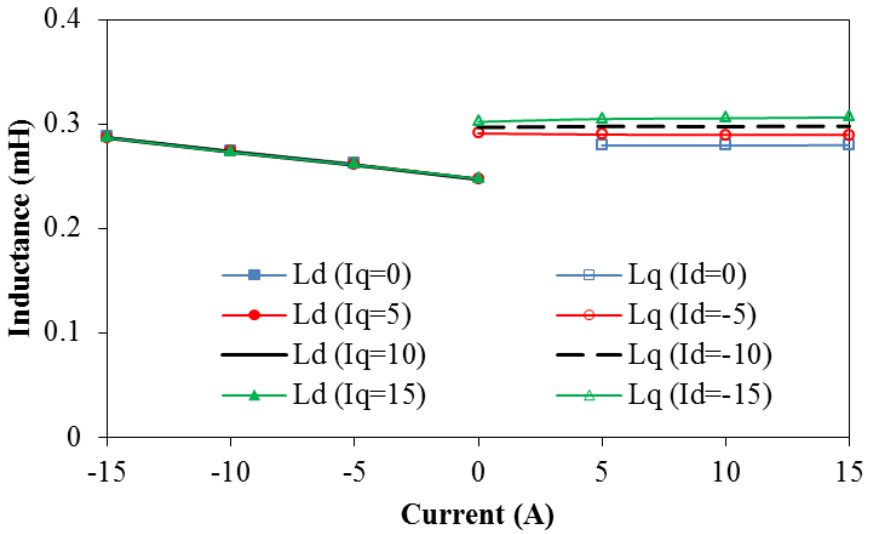

(b) SFRCPM machine(turns per phase 68)

Fig. 6.18 D- and q-axis inductances at different current levels of SFRCPM and CSFPM machines having different turns per phase.

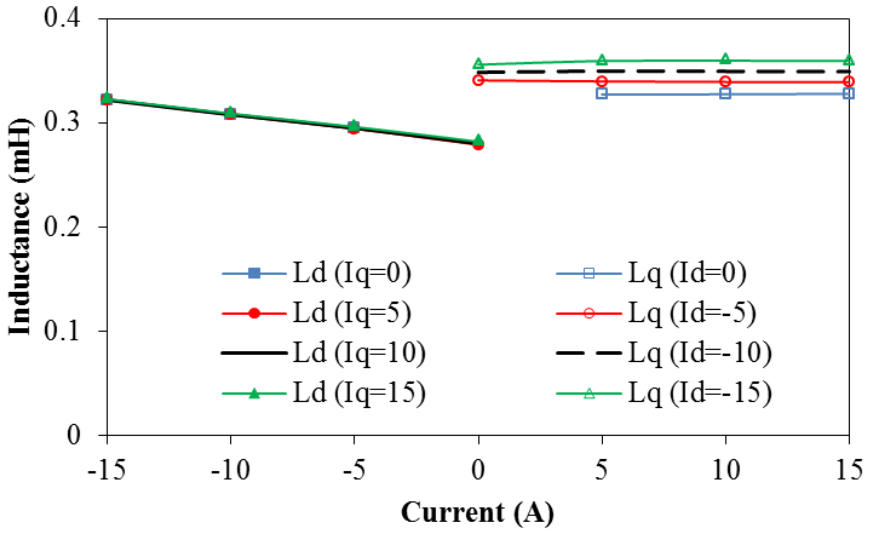

(a) CSFPM machine (turns per phase 72)

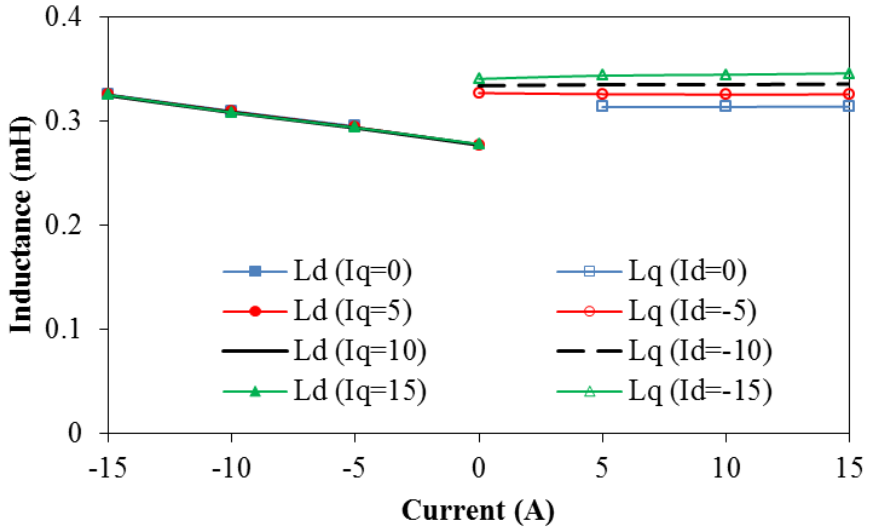

(b) SFRCPM machine (turns per phase 72)

Fig. 6.19 D- and q-axis inductances at different current levels of SFRCPM and CSFPM machines having same number of turns per phase.

6.5.5. Torque-speed characteristic

Since both machines have the same rated current and different number of turns per phase, Table 6.2, the back-EMF of SFRCPM machine is slightly higher than the CSFPM, Fig. 10. Therefore, the constant torque region and base speed of SFRCPM machine is slightly higher than the CSFPM. Moreover, since the number of turns per phase is higher in the SFRCPM machine, wider flux weakening region and higher maximum speed is observed in this machine due to large inductances, Fig. 6.18. Therefore, SFRCPM machine exhibits better torque-speed characteristics than the CSFPM machine, as shown in Fig. 12.

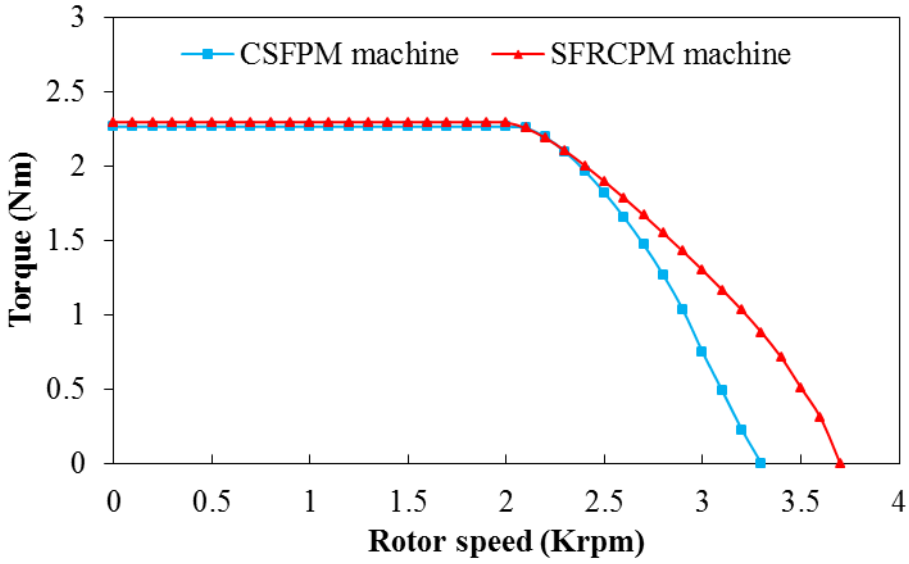

(a) Torque-speed curves

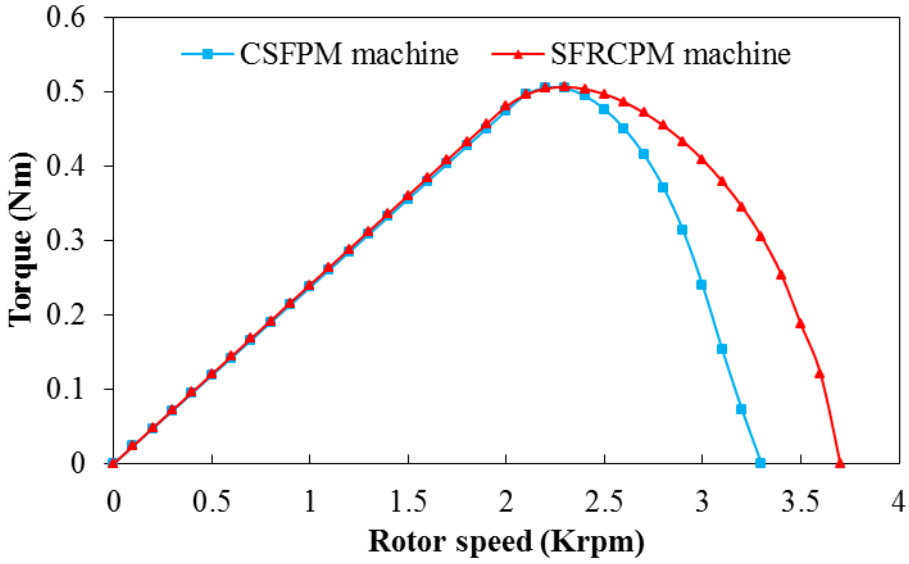

(b) Power-speed curves

Fig. 6.20 Torque-speed characteristics of CSFPM and SFRCPM machines under load condition of (I_q=15A) and ($V_{dc\text{-}link}$=36V).

6.5.6. Losses and Efficiency

Under open circuit condition, the CSFPM machine has higher total flux density compared with the SFRCPM machine, Fig. 6.15, thus the iron loss is larger in CSFPM machine, Fig. 6.21. Fig. 6.22 presents one stator pole core of both CSFPM and SFRCPM machine with external rotor. The 'U' core of the SFRCPM machine is smaller than that of the CSFPM machine. However, by including the size of the frame ring the total core size of the SFRCPM machine is larger than the CSFPM machine since both have the same rotor. Nevertheless, since the majority of the flux variation occurs in the 'U' core (highlighted in purple) and the

rotor, and on the other hand the CSFPM machine has higher overall flux density, the iron loss is higher in CSFPM machine.

Although larger amount of magnet material is used in the CSFPM machine, lower magnet loss is observed in this machine compared with SFRCPM machine. Due to the use of two PM sets in SFRCPM machine, higher eddy current loss occurs in the magnets since in SFPM machine such loss is concentrated in the edges of the PMs as illustrated in [46]. Nevertheless, the total electromagnetic losses, i.e. iron, magnet and copper, are higher in the CSFPM machine. Therefore, the efficiency is higher in SFRCPM compared to the CSFPM machine as shown in Fig. 6.23.

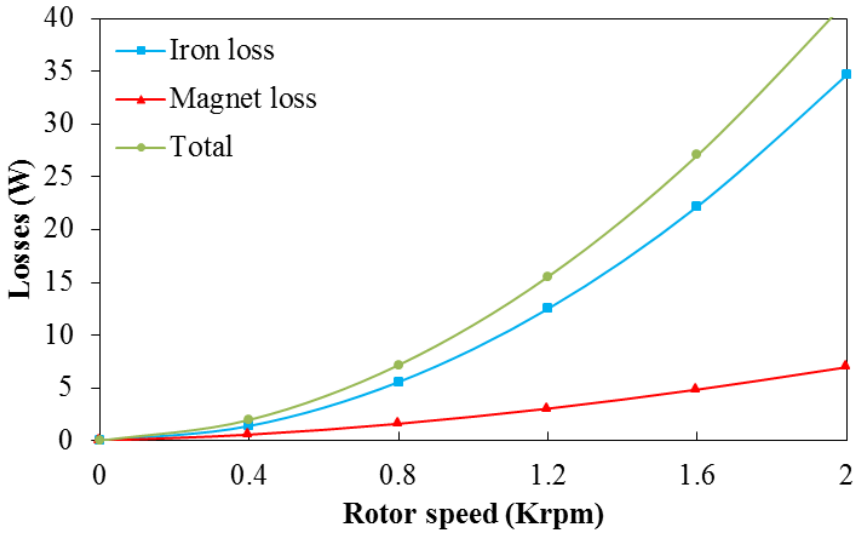

(a) CSFPM

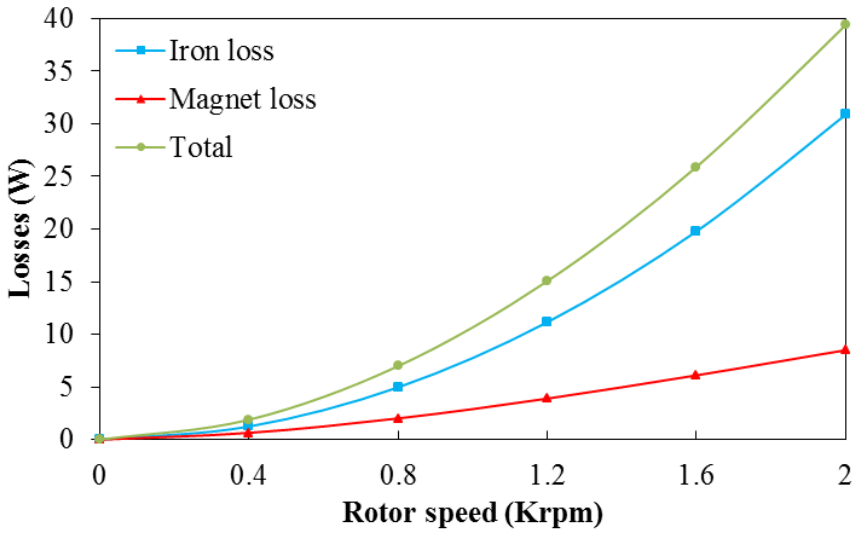

(b) SFRCPM

Fig. 6.21 Iron and magnet losses in CSFPM and SFRCPM machines under open circuit condition.

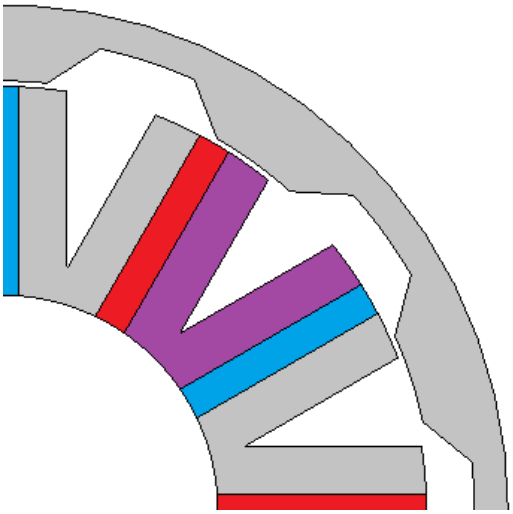

Stator ‘U’ core size (highlighted in purple)=154mm^2
non
Stator total core size=1848mm^2
Rotor total core size =1301mm^2
Machine total core size =3149mm^2
(a) CSFPM

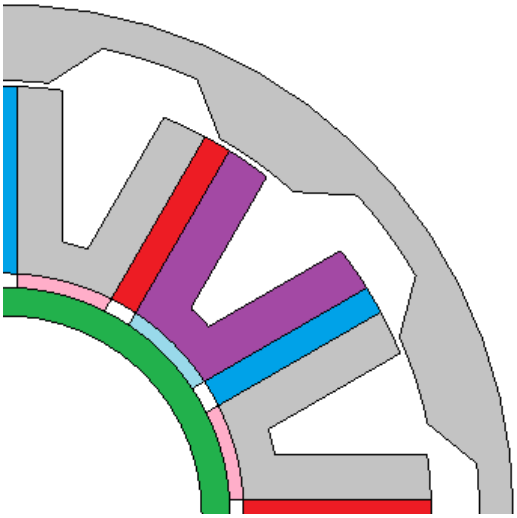

Stator ‘U’ core size (highlighted in purple)=138mm^2
Frame ring (highlighted in green)=292mm^2
Stator total core size =1948mm^2
Rotor total core size =1301mm^2
Machine total core size =3249mm^2
(b) SFRCPM

Fig. 6.22 Comparison of core size in CSFPM and SFRCPM machines.

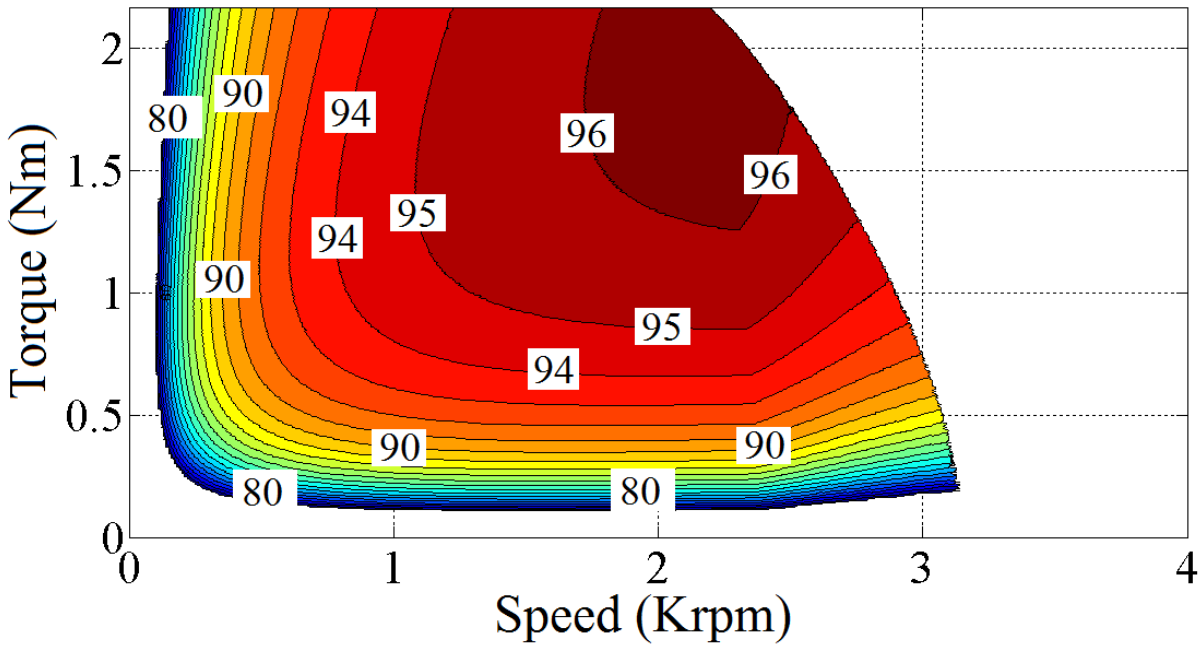

(a) CSFPM

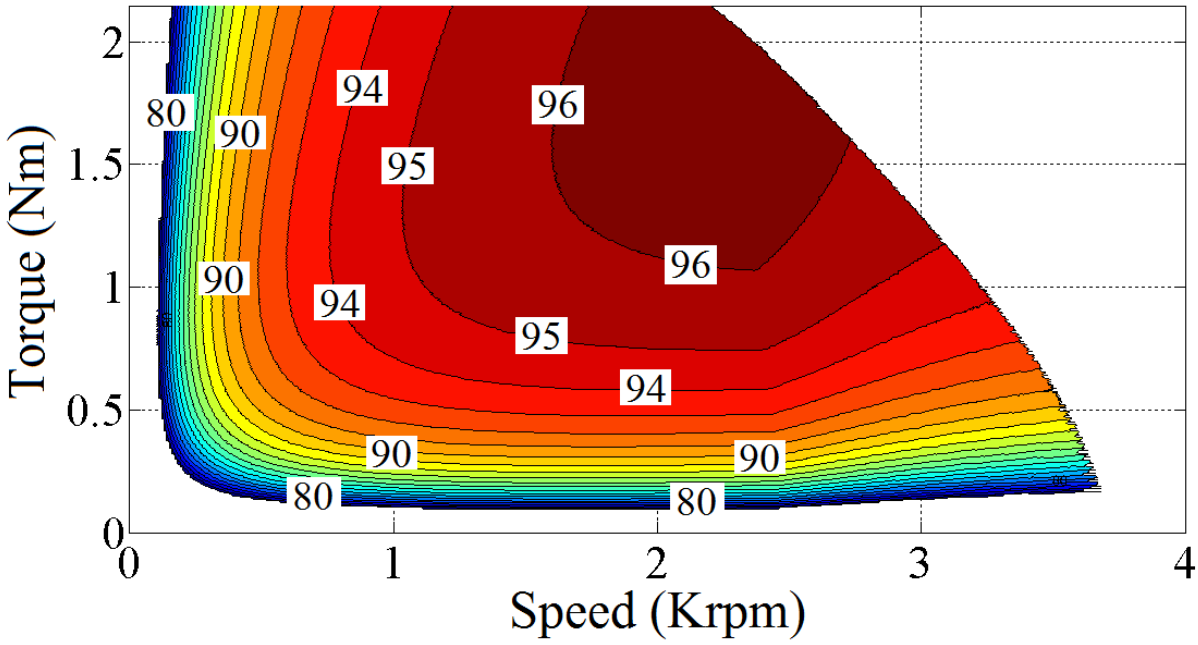

(b) SFRCPM

Fig. 6.23 Efficiency map of CAFPM and SFRCPM machines under load condition of (I_q=15A) and ($V_{dc\text{-}link}$=36V).

6.6. Different stator/rotor pole combinations of SFRCPM machine with internal and external rotors

For a multi-phase SFPM machine with internal rotor configuration, the feasible combinations of stator/rotor pole can be found by (1-1) and (1-2). On the other hand, in the external rotor SFPM machine the number of stator poles can be found by (3) where the rotor poles can be found by:

$$N_r = N_s(2 \pm \frac{K_2}{2m}) \tag{6-1}$$

Similar to (1-1) and (1-2), N_s and N_r stands for the stator and rotor number, respectively. m is number of phases and K is an integer.

Moreover, the number of phases is selected to be 3, whereas integer K_1 in (1-1) is chosen to be 4 since this gives the most feasible stator poles number for SFPM machine [31]. Table 6.3 presents the possible rotor pole numbers for N_s equal to 12. However, the bolded rotor pole values in Table 6.3 are selected for investigation since close stator and rotor pole numbers are preferred in SFPM machines due to their high winding factor, low cogging torque and unbalanced magnetic force (UMF) as stated in [30, 57].

Table 6.3 Possible rotor poles number for 3-phase 12 pole stator of SFRCPM machine

Internal rotor machine			External rotor machine		
K_2	+	-	K_2	+	-
1	**13**	**11**	1	**26**	**22**
2	**14**	**10**	2	**28**	**20**
3	15	9	3	30	18
4	16	8	4	32	16
5	17	7	5	34	14
6	18	6	6	36	12
7	19	5	7	38	10
8	20	4	8	40	8
9	21	3	9	42	6
10	22	2	10	44	4

Furthermore, in order to find the influence of the rotor pole on the performances of SFRCPM machine, the selected stator/rotor pole combinations of internal and external rotor SFRCPM machines are investigated in this section. Fig. 15 presents the cross-section of the selected machines. In order to maintain the symmetry of the machine, the design parameters are selected in internal rotor machines as follows: $w\_{r}=w\_{s}=w\_{slot}=h\_{PMc}=h\_{bi}=h\_{fr}=0.5h\_{PMr}$ and $w\_{r}=w\_{s}= 5w\_{slot}=h\_{PMc}=h\_{bi}=h\_{fr}=0.5h\_{PMr}$ in external rotor machines. The split ratio is optimized at fixed copper loss. It is found that the internal rotor SFRCPM machine has an optimum split ratio of 0.55 whereas the external rotor machine is 0.85. Moreover, the design parameters of these machines are presented in Table 6.4.

Table 6.4 Design parameters of CSFPM and SFRCPM machines

Machines	Symbol	Internal rotor	External rotor
Stator outer radius (mm)	h_{stator}	45	38.25
Stator tooth width (mm)	w_{s}	3.23	2.47
Rotor outer radius(mm)	h_{rotor}	24.25	45
Rotor tooth width(mm)	w_{r}	3.23	2.47
Rotor tooth height(mm)	h_{r}	7	3.375
Slot height(mm)	h_{slot}	12.18	11.77
Slot width (mm)	w_{slot}	3.23	12.35
PMc width (mm)	h_{PMc}	3.23	2.47
PMc height (mm)	w_{PMc}	15.4	14.3
Back iron (mm)	h_{bi}	3.23	2.47
PMr width (mm)	h_{PMr}	1.62	1.23
PMr height (mm)	w_{PMr}	17.8	9.8
Frame ring thickness (mm)	h_{fr}	3.23	2.47
Axial length (mm)	L_{a}	25	25
Airgap length (mm)	L_{gap}	0.5	0.5

Copper loss (W)	P_{cu}	15	15
Packing factor	K_{pa}	0.45	0.45
Turns per phase	N_a	72	72
PM remanence (T)	B_{rpm}	1.2	1.2
PM permeability	μ_r	1.05	1.05
Rated current (A)	I_{rated}	13.4	15.75

The cross-sections of the selected stator/rotor pole combinations of the SFRCPM machine with internal and external rotor configurations is presented in Fig. 6.24. Moreover, the phase and coil flux-linkage and back-EMF waveforms of the SFRCPM machines with different rotor pole numbers are presented in Figs. 6.25 and 6.26, respectively. It can be seen that the external rotor SFPM machines with combinations of 12/20 and 12/28 do not produce symmetrical back-EMF since the condition for symmetrical back-EMF waveform is not satisfied [30]:

$$\frac{\mathrm{N_s}}{\mathrm{GCD(N_s\&N_r)}} = \text{even number} \tag{6-2}$$

GCD stands for the greatest common divider.

Figs. 6.27 and 6.28 present a comparison of the open circuit and on-load performances of the internal and external SFRCPM machines with different rotor pole numbers, respectively. In internal rotor SFRCPM machines, Fig. 6.27, the 12/13 has the highest back-EMF peak. However, due to the influence of harmonics the fundamental back-EMF value is lower than that of the 12/14, which makes 12/14 have the highest back-EMF. In terms of back-EMF harmonics, both 12/11 and 12/13 have significant 3rd harmonic due to their winding connection, whereas a large 5th harmonic is observed in 12/10 and 12/14. The internal SFRCPM machines with odd rotor pole numbers, i.e. 12/11 and 12/13, produce low cogging torque. Finally, the electromagnetic torque waveforms of the four different machines at rated current of 13.4A are compared, since same current and number of turns are used, same conclusion with that of the back-EMF is observed.

On the other hand, 12/26 and 12/22 machines produce the highest back-EMF with significantly low harmonics, respectively, compared with the other machines which has asymmetric back-EMF waveform. Moreover, 12/20 produces the highest cogging torque compared with the other external rotor SFPM machines. Similar to that of internal rotor machines, the electromagnetic torque waveforms at rated current of 15.75A are compared and similar conclusion is observed.

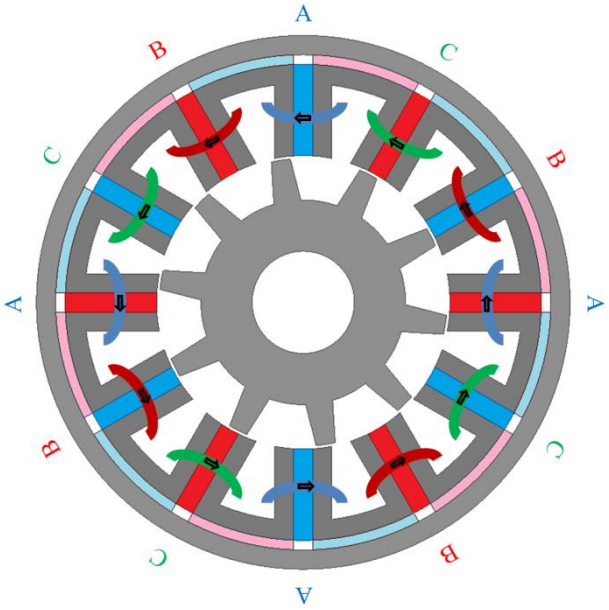

(a) 12/10 stator/rotor pole combination

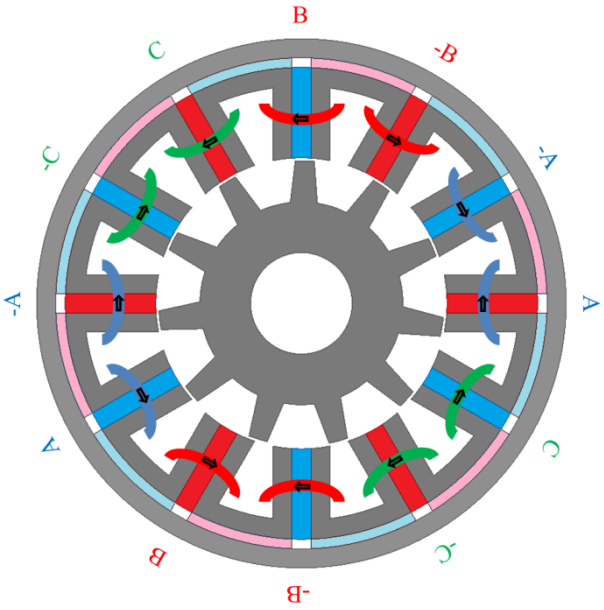

(b) 12/11 stator/rotor pole combination

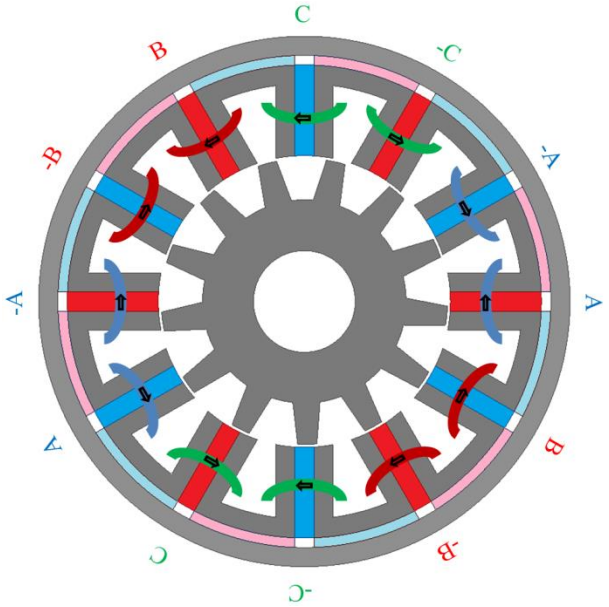

(c) 12/13 stator/rotor pole combination

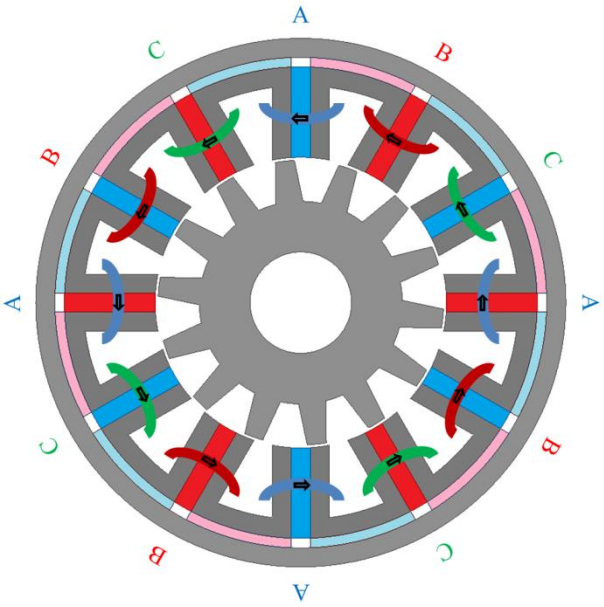

(d) 12/14 stator/rotor pole combination

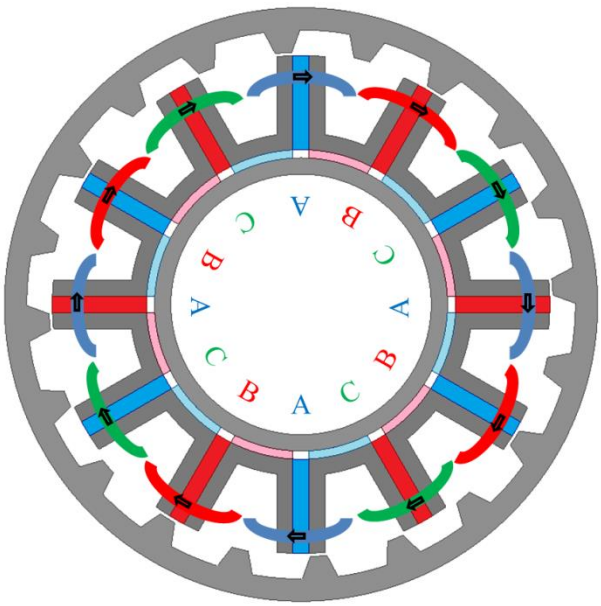

(e) 12/20 stator/rotor pole combination

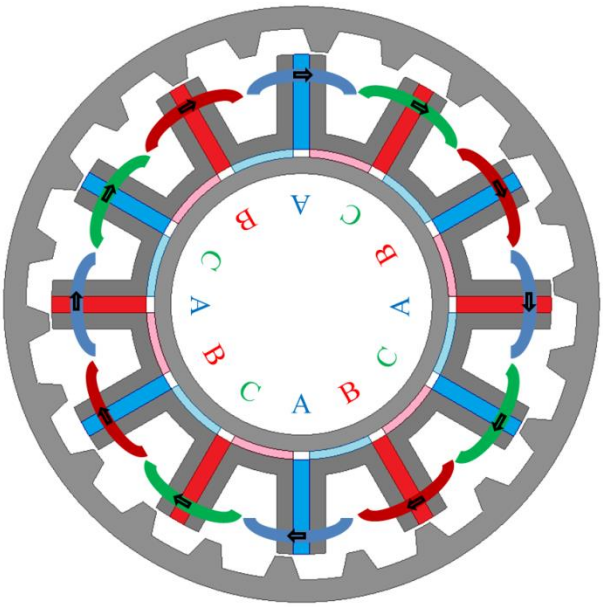

(f) 12/22 stator/rotor pole combination

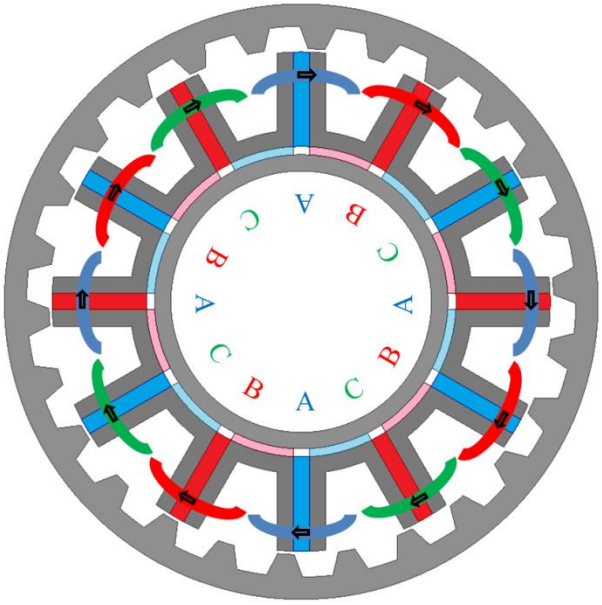

(g) 12/26 stator/rotor pole combination

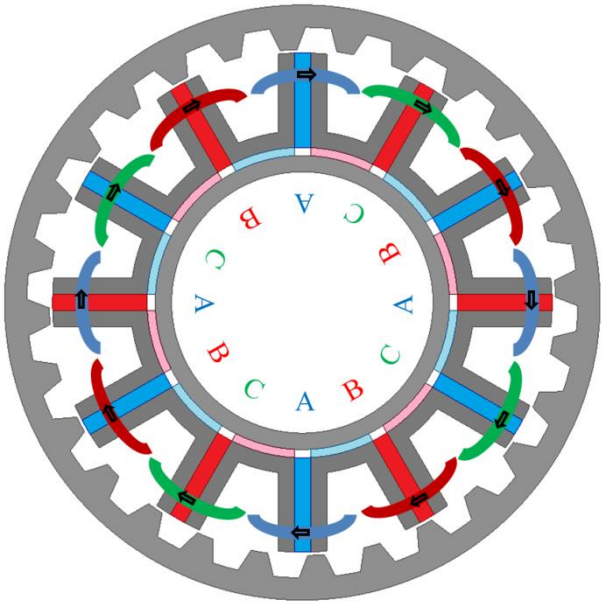

(h) 12/28 stator/rotor pole combination

Fig. 6.24 Cross-sections of SFRCPM machine with different stator/rotor pole number combinations and rotor configurations.

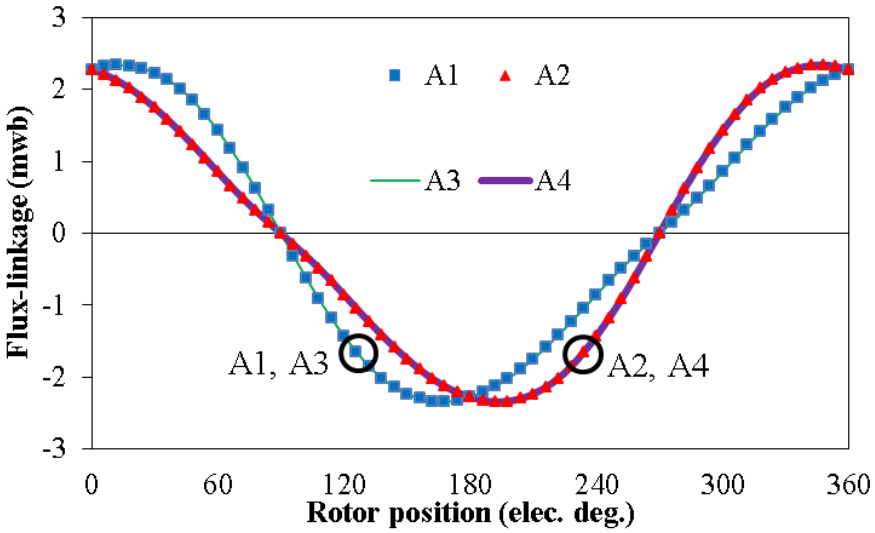

(a) 12/10 stator/rotor pole combination (internal rotor)

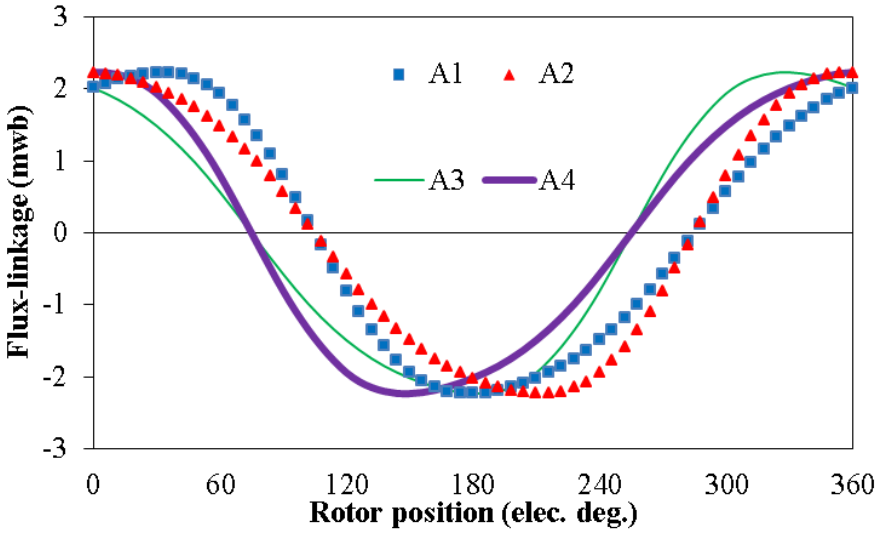

(b) 12/11 stator/rotor pole combination (internal rotor)

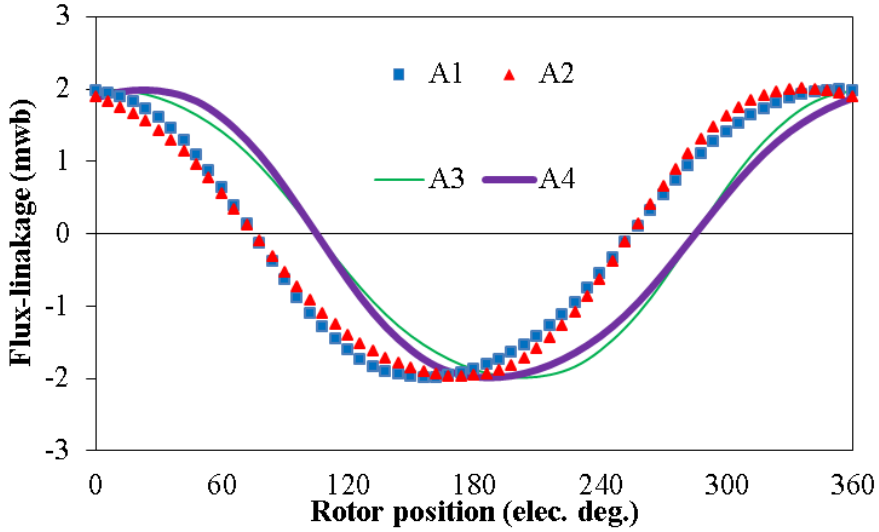

(c) 12/13 stator/rotor pole combination (internal rotor)

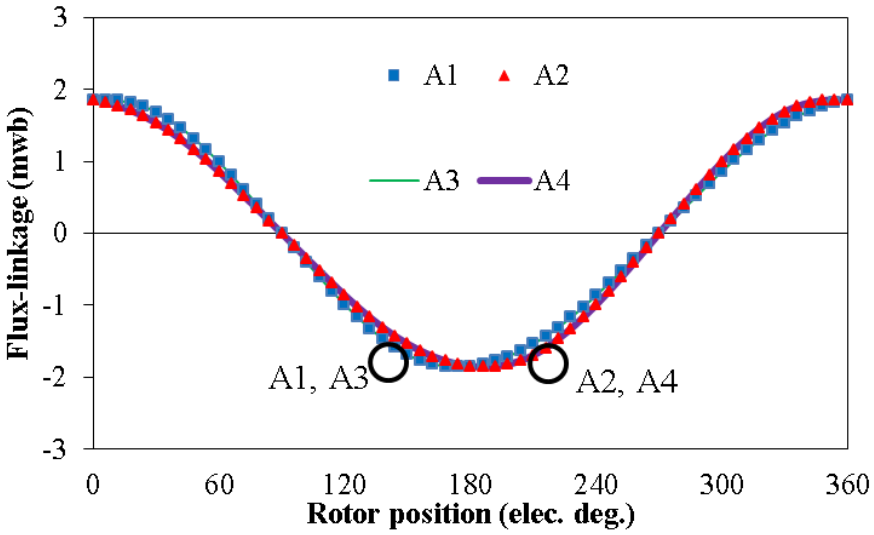

(d) 12/14 stator/rotor pole combination (internal rotor)

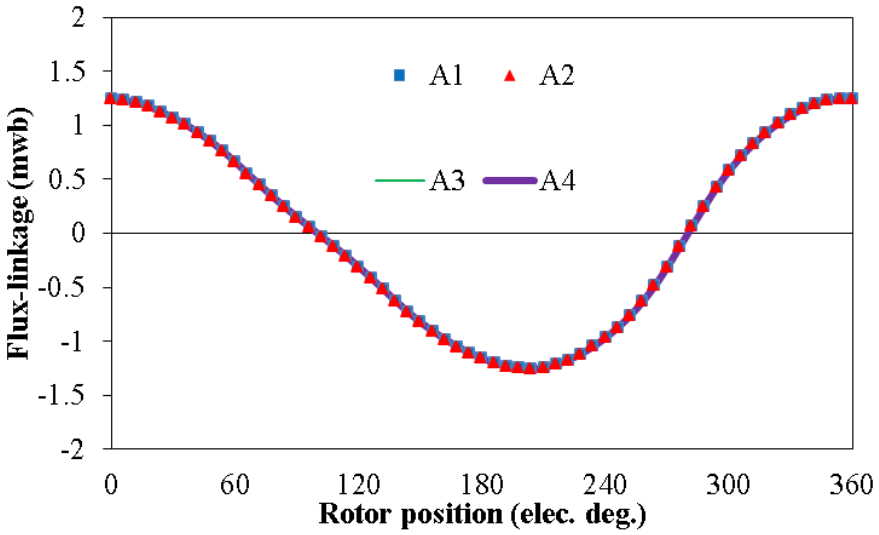

(e) 12/20 (external rotor)

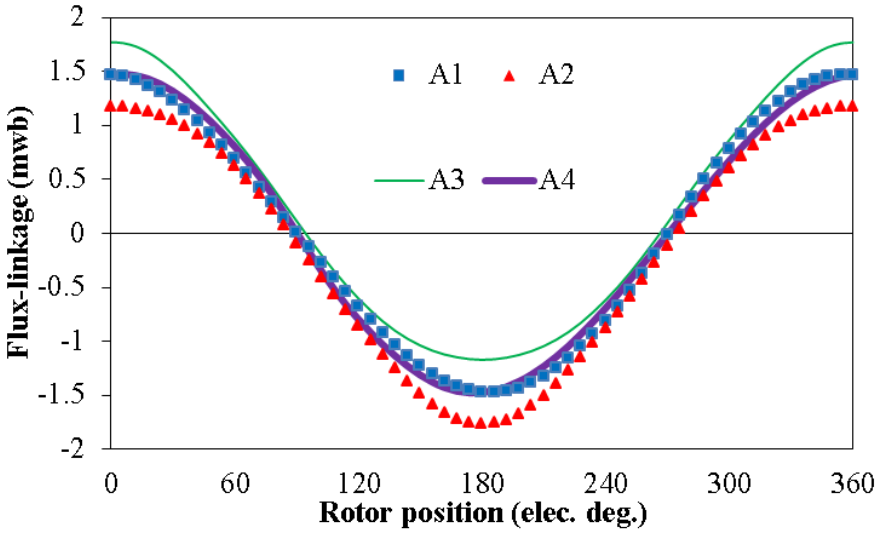

(f) 12/22 stator/rotor pole combination (external rotor)

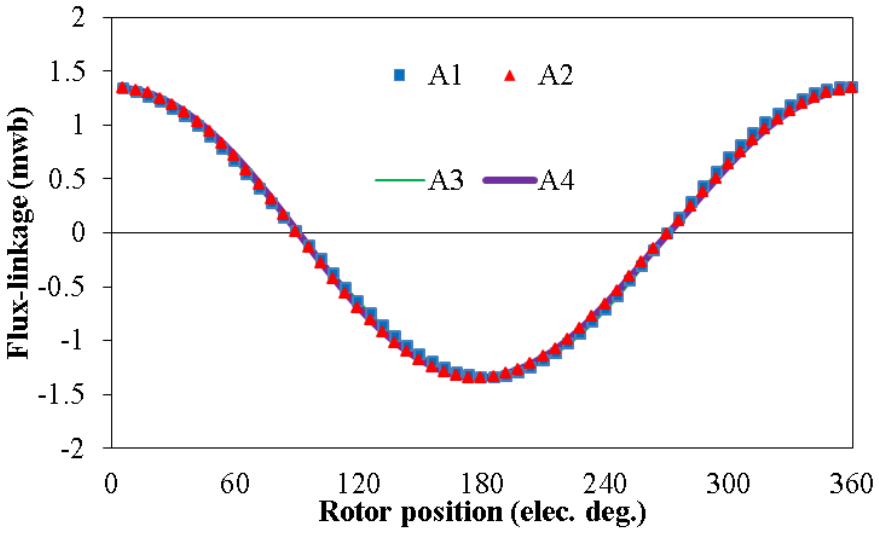

(g) 12/26 stator/rotor pole combination (external rotor)

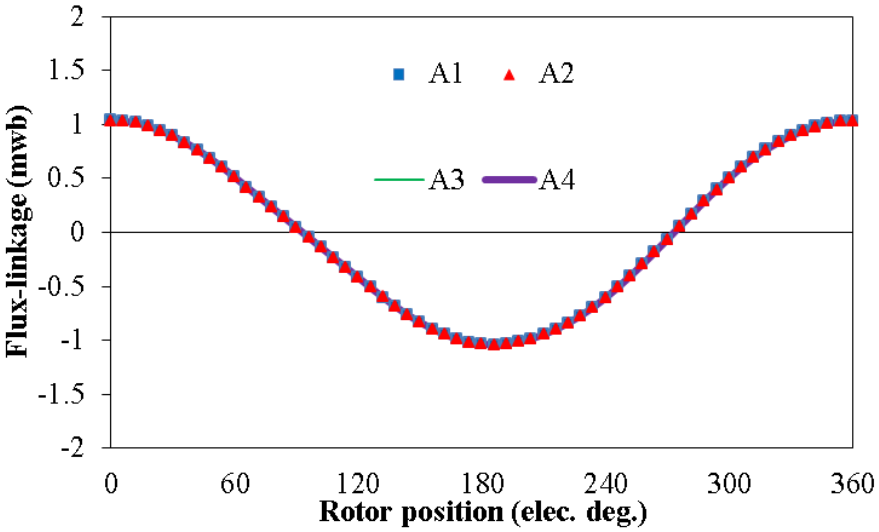

(h) 12/28 stator/rotor pole combination (external rotor)

Fig. 6.25 Coil flux-linkages of SFRCPM machines with different rotor configuration and pole numbers.

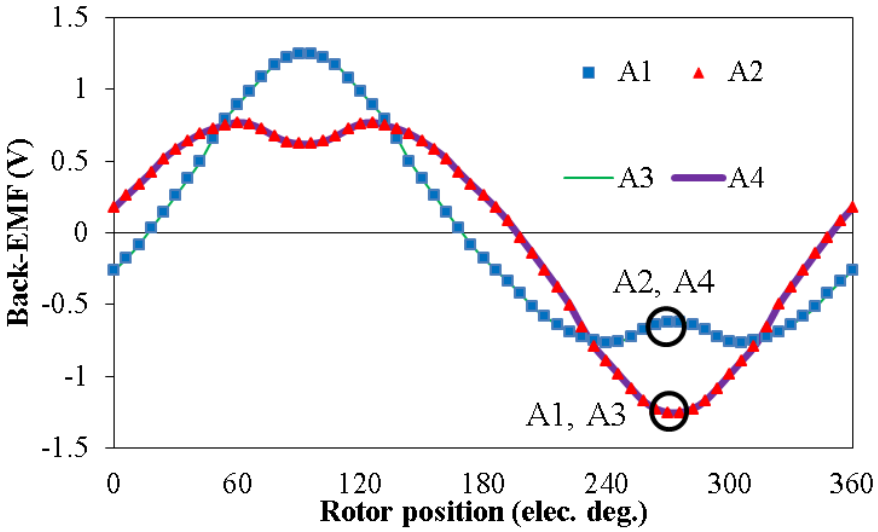

(a) 12/10 stator/rotor pole combination (internal rotor)

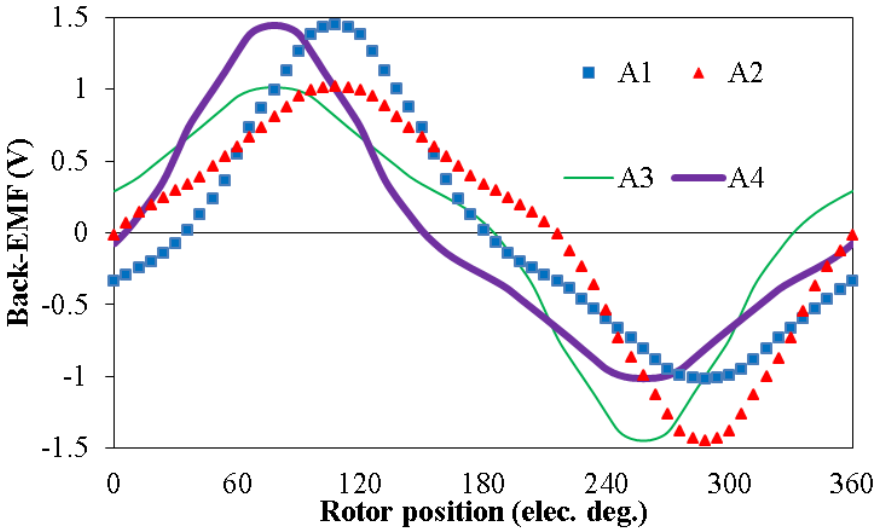

(b) 12/11 stator/rotor pole combination (internal rotor)

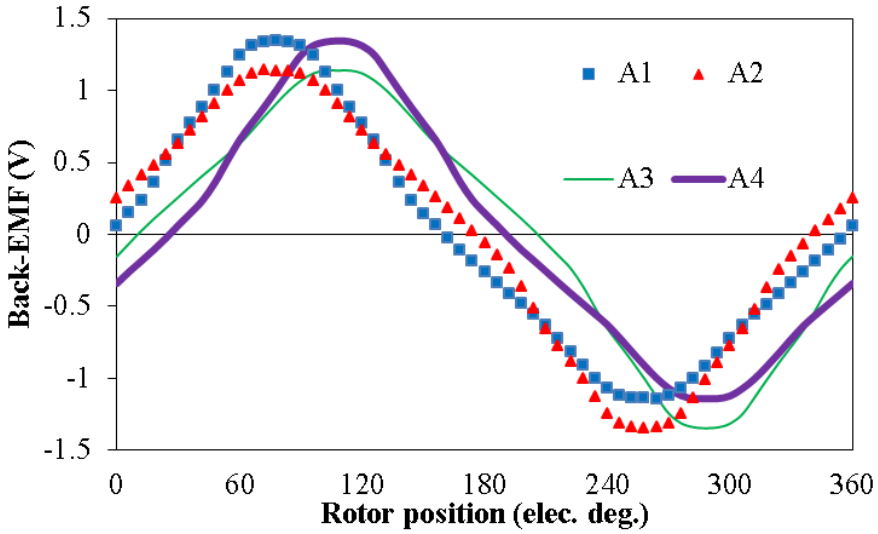

(c) 12/13 stator/rotor pole combination (internal rotor)

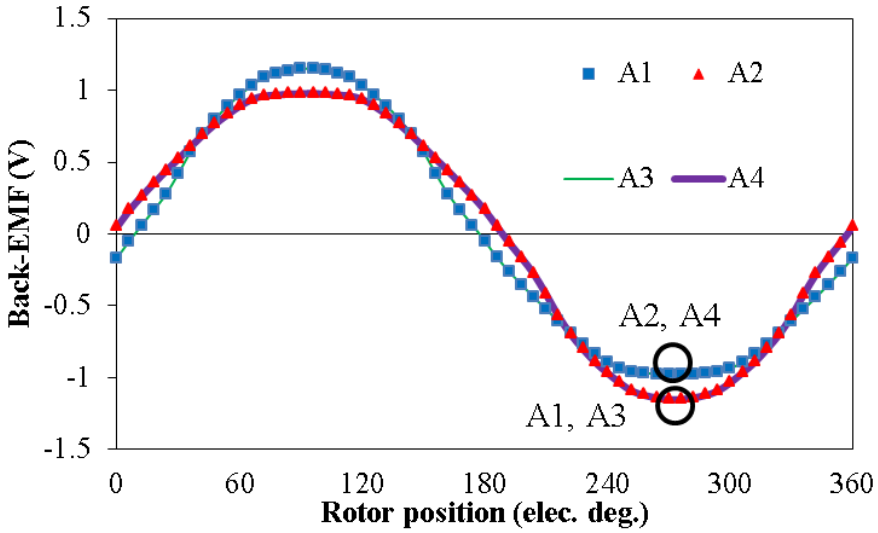

(d) 12/14 stator/rotor pole combination (internal rotor)

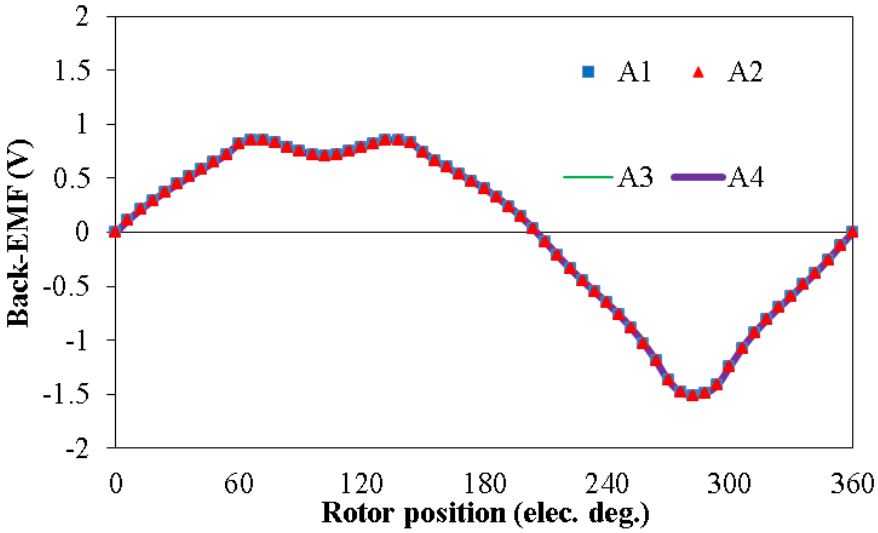

(e) 12/20 stator/rotor pole combination (external rotor)

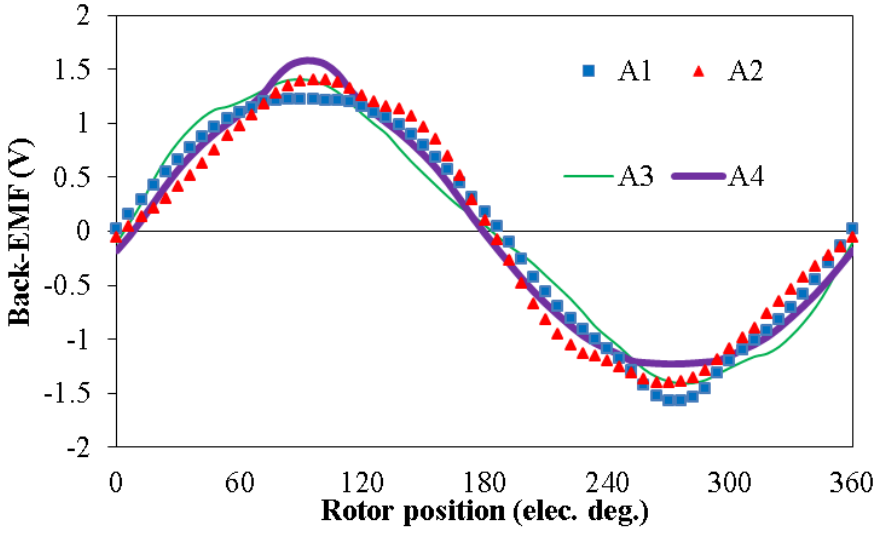

(f) 12/22 stator/rotor pole combination (external rotor)

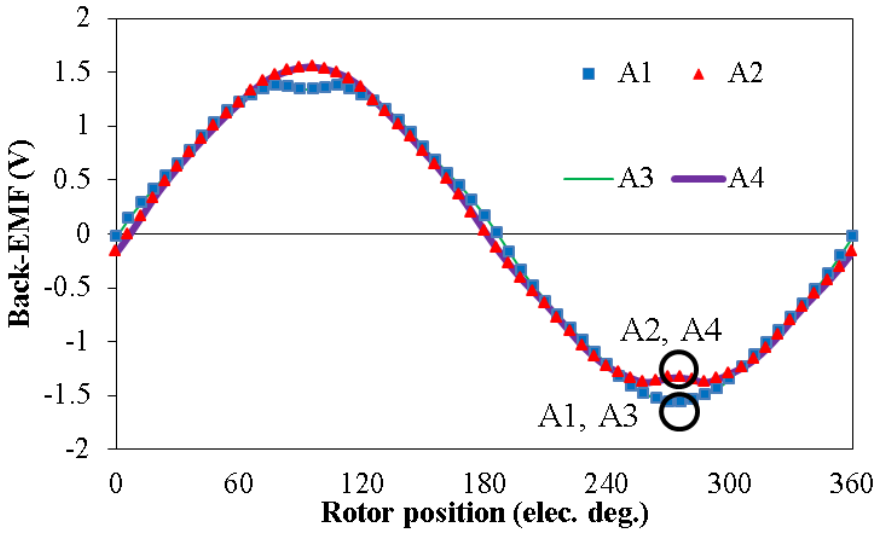

(g) 12/26 stator/rotor pole combination (external rotor)

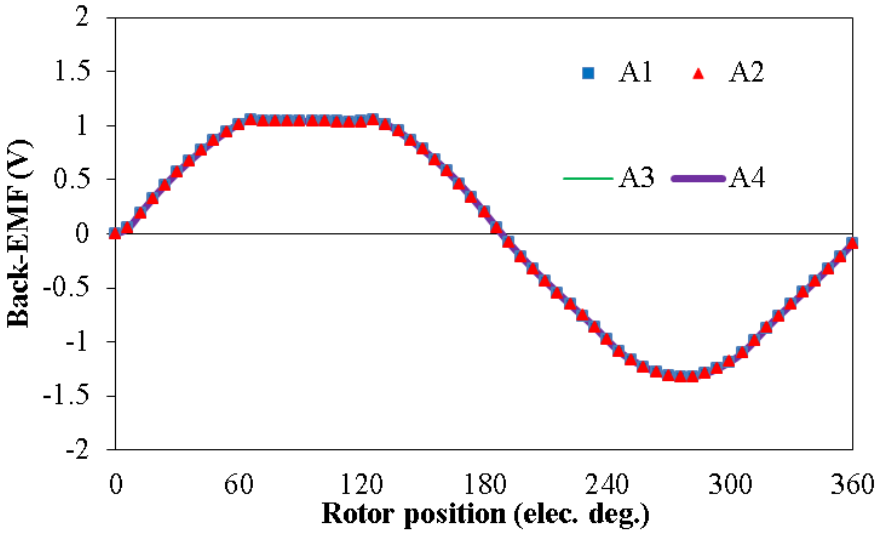

(h) 12/28 stator/rotor pole combination (external rotor)

Fig. 6.26 Coil back-EMF of SFRCPM machines with different rotor configurations and pole numbers (400rpm).

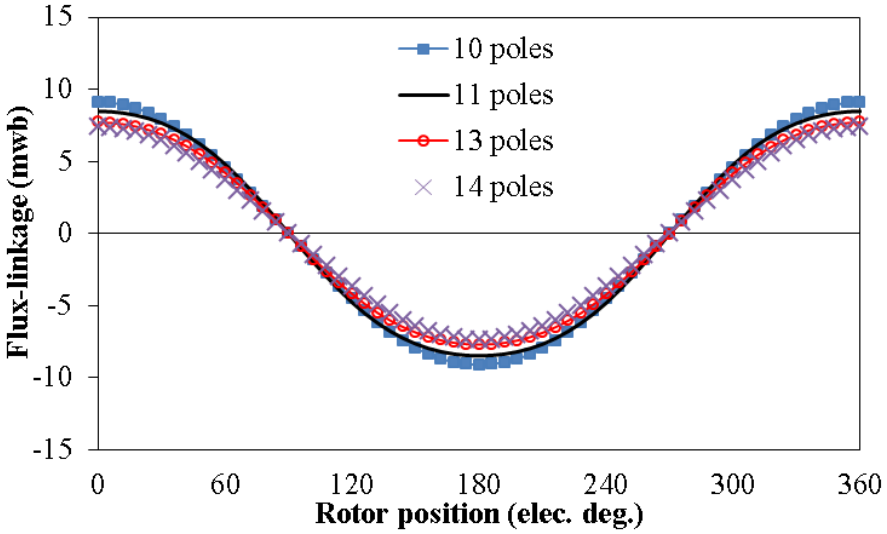

(a) Flux-linkage waveforms

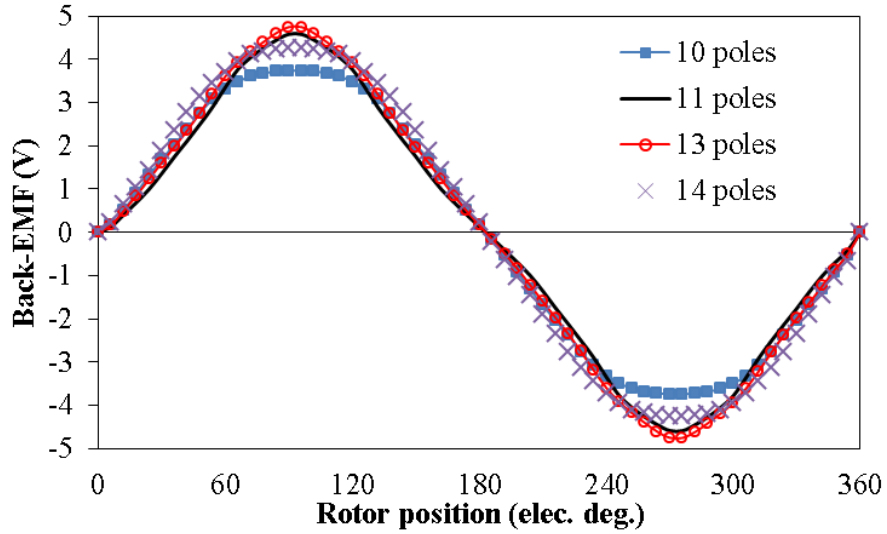

(b) Back-EMF waveforms (400rpm)

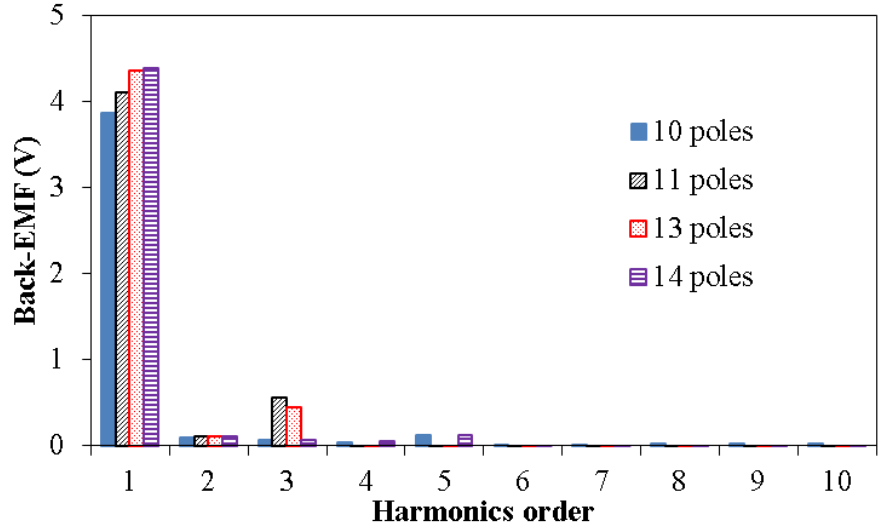

(c) Back-EMF harmonics

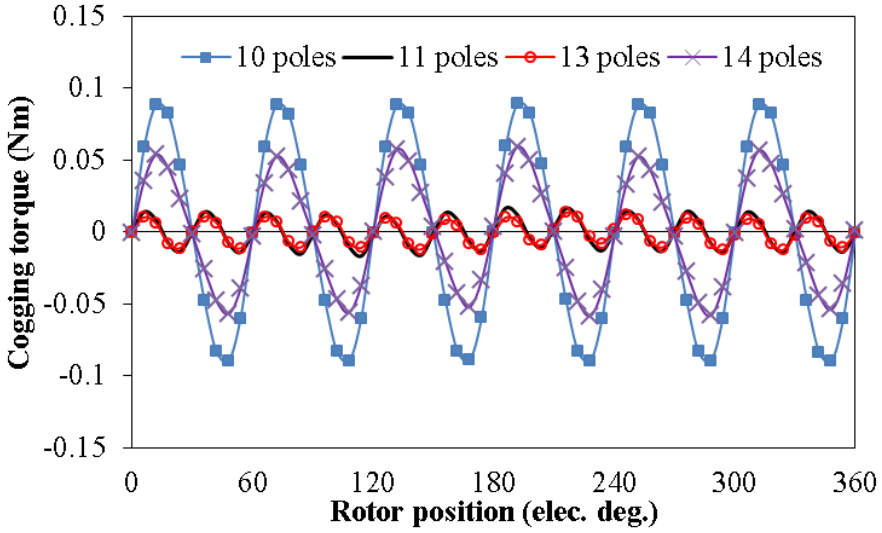

(d) Cogging torques

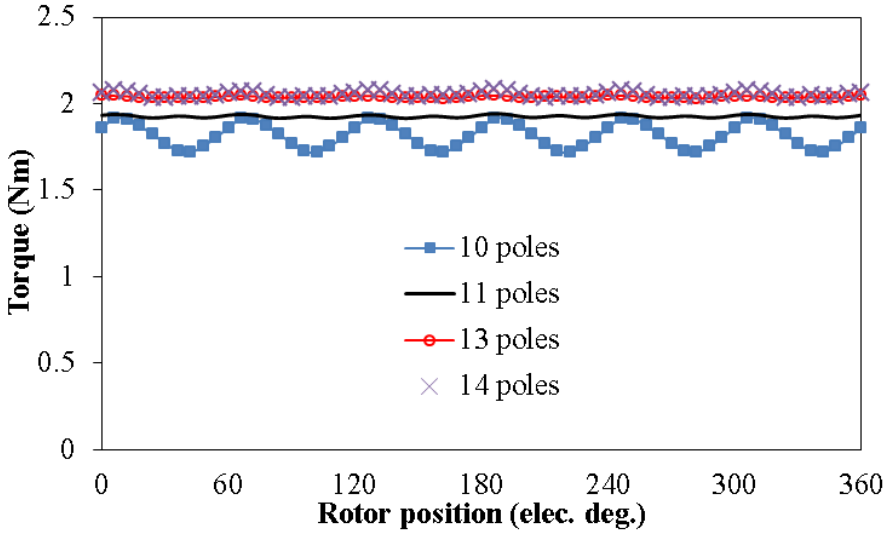

(g) Electromagnetic torques (I_q=13.4A, I_d=0)

Fig. 6.27 Comparison of open-circuit and on-load performance of internal rotor SFRCPM machines with different rotor pole numbers.

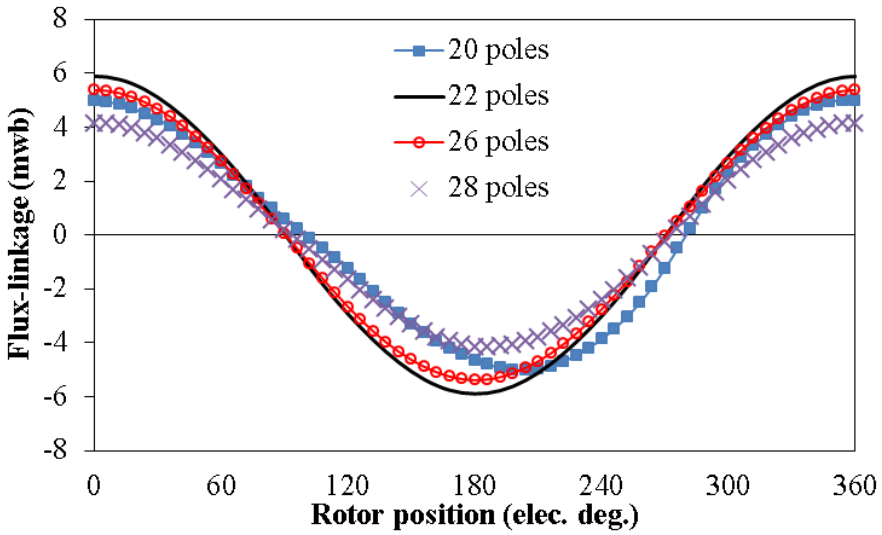

(a) Flux-linkage waveforms

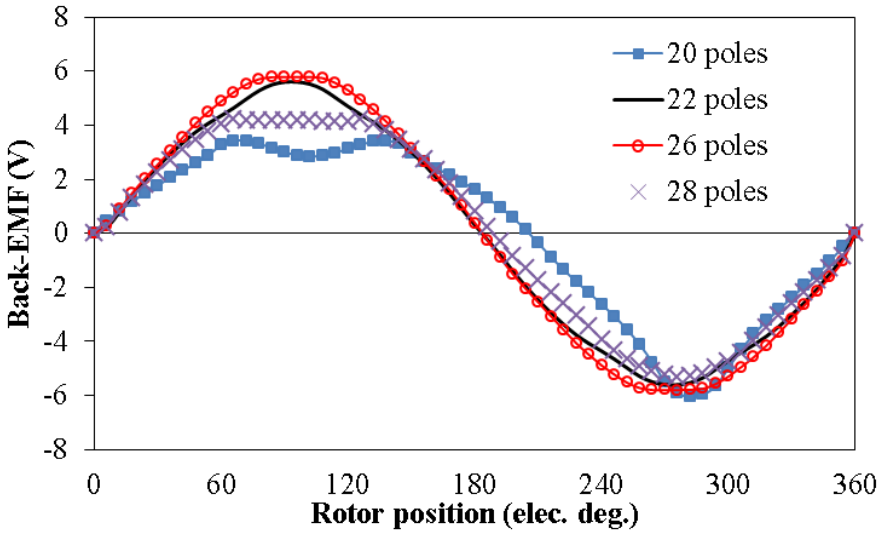

(b) Back-EMF waveforms (400rpm)

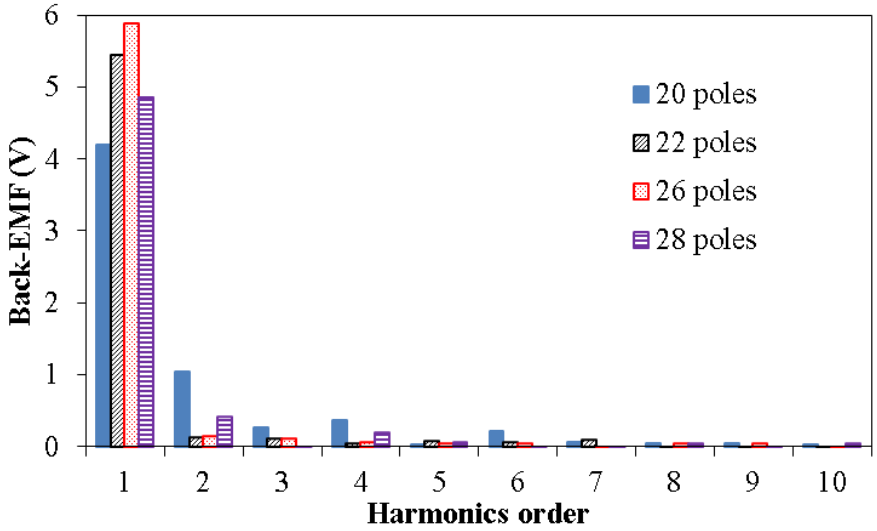

(c) Back-EMF harmonics

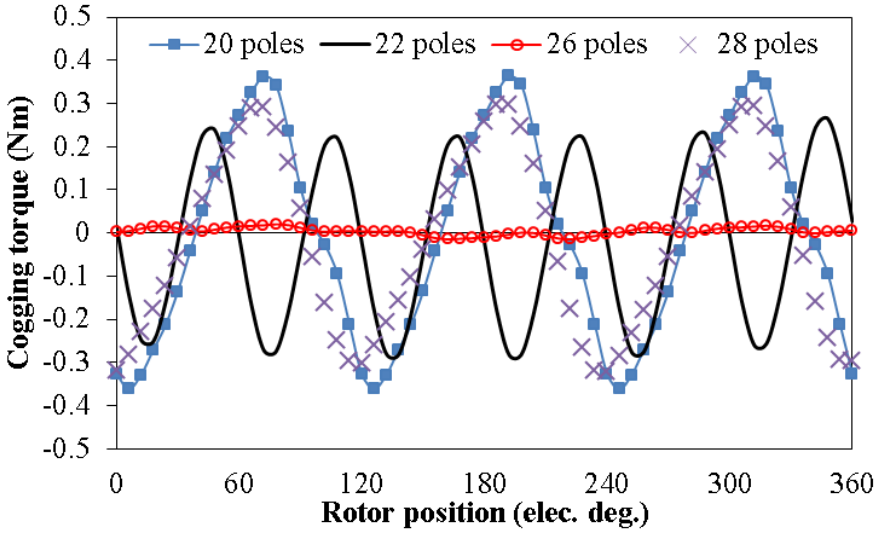

(d) Cogging torques

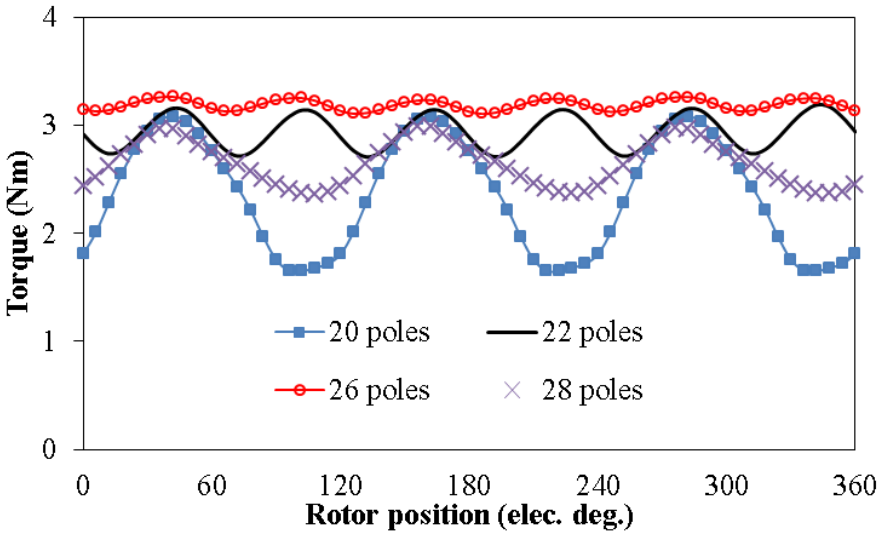

(e) Electromagnetic torques (I_q=15.75A, I_d=0)

Fig. 6.28 Comparison of open-circuit and on-load performance of external rotor SFRCPM machines with different rotor pole numbers.

6.7. Rectangular Shaped Radial Permanent Magnet

In order to utilize the magnet material efficiently in the manufacturing process, the arc shaped radially magnetized PMs can be replaced by rectangular PMs. Moreover, by examining the flux density distribution in the laminated ring frame and the back iron, it can be seen that the highly saturated areas are at the top of the PMc, i.e. circle 2 in Fig. 6.29, in the laminated ring frame and at the top of the slot area, i.e. circle 1 in Fig. 6.29, in the back iron. Therefore, in internal rotor SFRCPM machine replacing the arc shaped PMr with rectangular leads to a reduction in the size of the saturated area in the back iron and thus forces the slot area to reduce. In contrast, using rectangular PMr in the external rotor SFRCPM machine results in

thinner laminated ring frame in the low saturated area, and wider back iron in the high saturated area and thus larger slot area is available. Moreover, using rectangular PMr in an external rotor SFRCPM machine permits the slot area height to increase and therefore larger slot area can be employed and consequently higher current can be used.

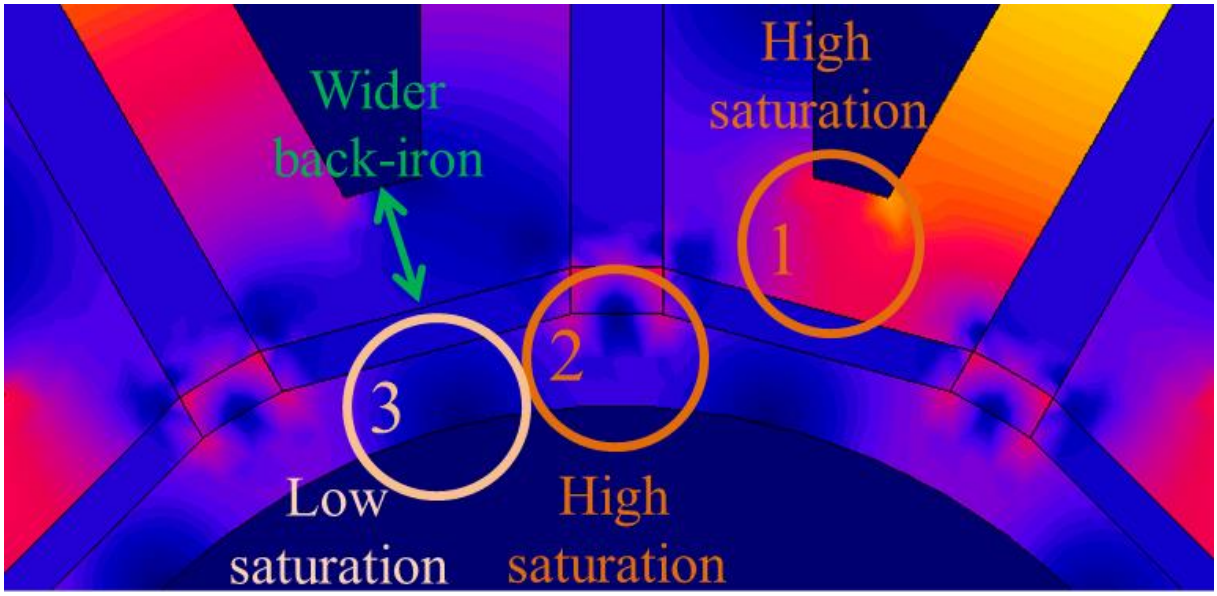

(a) External rotor SFRCPM machine with rectangular PMr

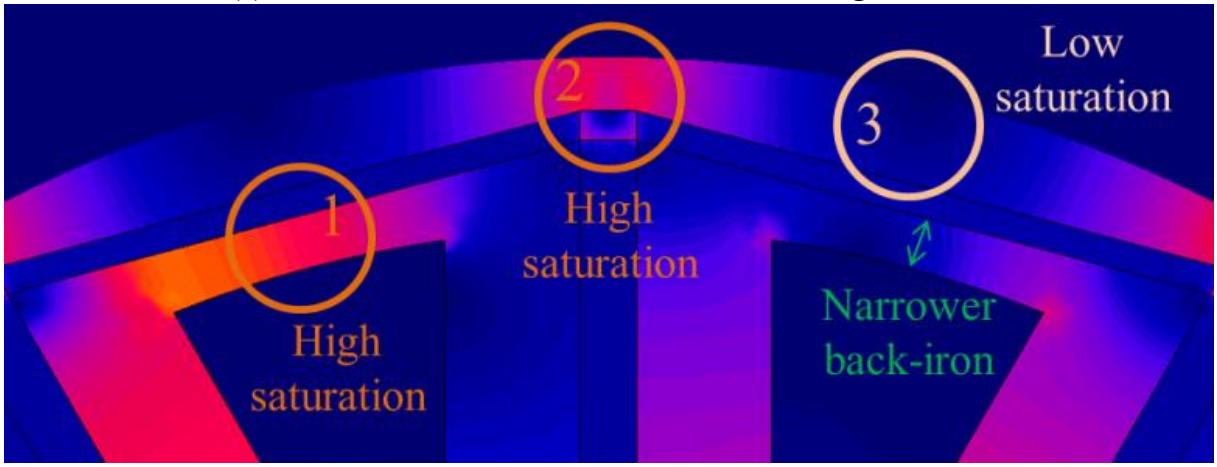

(b) Internal rotor SFRCPM machine with rectangular PMr

Fig. 6.29 Magnetic saturation in the back-iron and laminated ring frame of SFRCPM machine.

6.8. Conclusion

In order to reduce the flux leakage in the stator-outer region and thus achieve better magnetic utilization, as well as to potentially enhance the PM flux linkage and torque, a new SFPM machine topology has been proposed. It consists of radial PMs located around the back-iron and surrounded by laminated ring frame. Parametric investigation is performed in order to design an effective optimization method for such a topology. Moreover, external and internal rotor SFRCPM machines are designed, optimized and investigated. It is found that the internal rotor SFRCPM machine has high magnetic flux utilization. However, the low effective stator area leads to smaller slot area and consequently lower torque compared to the CSFPM machine. On the other hand, the external rotor SFRCPM machine can produce higher torque and torque per magnet volume as well as better torque-speed characteristics and efficiency compared to that of the CSFPM machine. Moreover, unlike the internal rotor SFRCPM, the external rotor counterpart is more preferred since the arc shaped PMr can be replaced with rectangular without having any negative influence of the performance. Furthermore, the PMr set and the laminated ring frame can be set to mechanically rotate and accordingly the SFRCPM machine can be used as variable flux machine. Therefore, in the next chapter the SFRCPM machine is proposed as variable flux machine and a comparison with other variable flux SFPM machines is presented.

7. Comparison of Different SFPM Machine Topologies with Variable Flux Techniques

7.1. Introduction

As mentioned previously, due to constant and high permanent magnets flux, SFPM machines often suffer from limited speed range and low efficiency at high speeds. Conventionally, flux weakening control methods are used to drive the PM machines in order to achieve high speed range and wide flux weakening capability. However, the inverter limitations, i.e. maximum current and voltage, can be an obstacle to achieve acceptable flux weakening capability for applications that require high speed, such as automotive. Therefore, mechanical, electrical and other approaches have been proposed to introduce variable flux ability in the PM machines in order to achieve wider speed range and higher flux weakening capability.

However, these types of machines employ same concept as the flux weakening control method by either producing d-axis flux as in the hybrid excitation machines or reduce the PM flux as in the mechanical variable flux machines and memory motors. Therefore, the magnetic working point reduces temporarily, putting the magnets in vulnerable region where the risk of irreversible demagnetization might be an issue. Moreover, in order to inject DC flux to short circuit the PM flux an amount of power is needed for the DC winding or to move the mechanical parts, these powers have no contribution in the energy conversion process.

In this chapter, three switched flux permanent magnet (SFPM) machine topologies with flux variation techniques, i.e. the mechanically movable flux adjusters (MMFA) presented in Chapter 4, mechanically rotatable magnet set (MRMS), a modification of the SFRCPM machine presented in Chapter 6 and hybrid excitation SFPM with backside DC coils (HEBC), reviewed in Chapter 1, are presented and compared. Their electromagnetic performance with emphasis on the torque-speed characteristics are investigated and compared using FEA. Moreover, the flux weakening capability and the demagnetization withstand capability are investigated when the machines are under flux strengthening state (FSS) and flux weakening state (FWS). Furthermore, the required power for switching between FSS and FWS is investigated. Fig. 7.1 shows the cross-sections of the three SFPM machines.

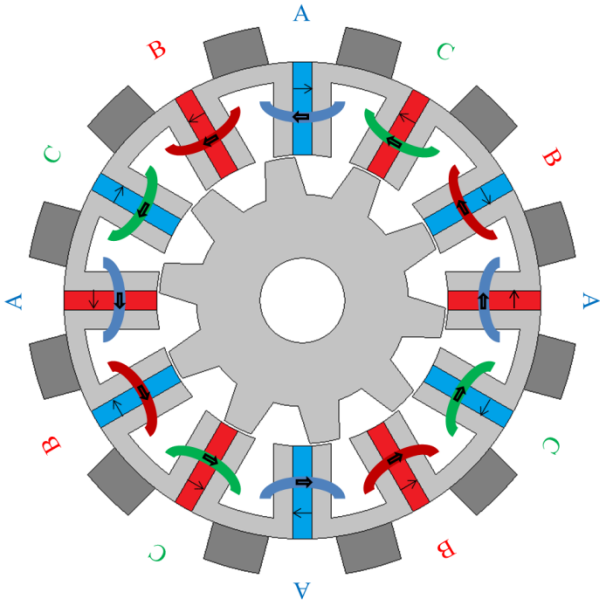

(a) MMFA

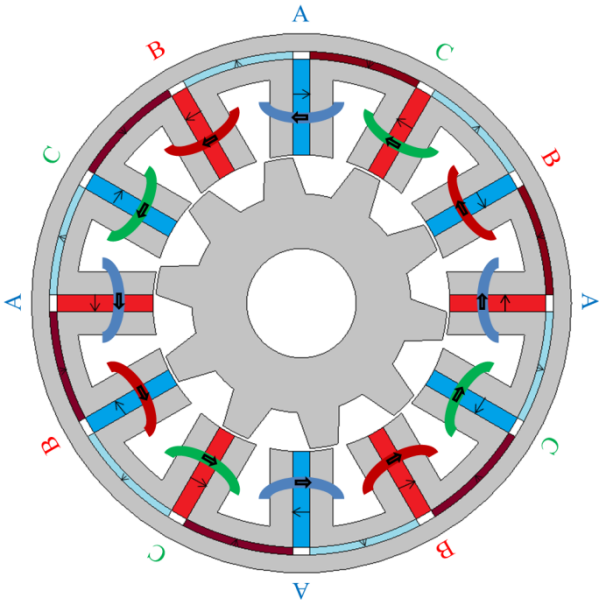

(b) MRMS

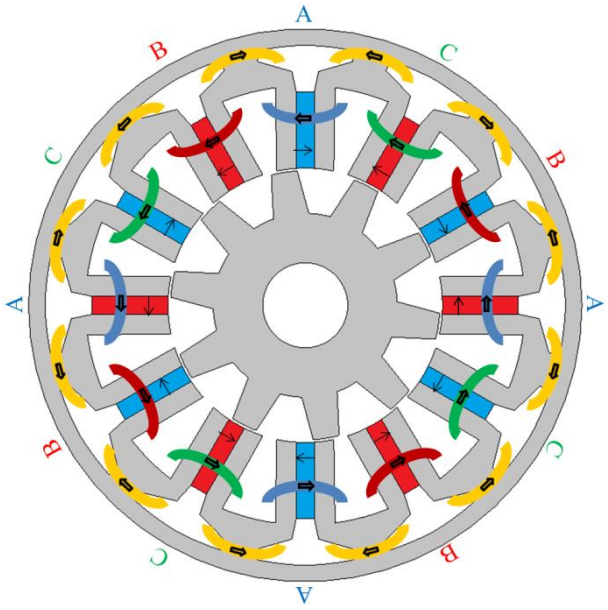

(c) HEBC

Fig. 7.1 Cross-sections of SFPM machines with variable flux techniques.

7.2. SFPM Machine Topologies

7.2.1. Mechanically movable flux adjusters (MMFA)

This topology illustrated in Chapter 4, it consists of movable ferromagnetic pieces, i.e. flux adjusters (FAs), located on the outside surface of the stator at each stator pole. The PM flux of this machine can be controlled by the relative position of these FAs. When the machine is set to FSS, the FAs are moved away from the PMs, Fig. 7.2 (a). Therefore, the PM flux flows through the stator, airgap and rotor, and the FAs have no effect on the machine and the flux distribution is the same as that of the conventional machine without the FAs. Moreover, at high speed, i.e. constant power region, the FAs move to the top of the PMs, Fig. 7.2 (b). Therefore, part of the PM flux will be short-circuited through the FA which leads to lower PM flux-linkage and therefore higher flux weakening capability and higher speed range.

7.2.2. Mechanically rotatable magnet set (MRMS)

A new set of arc shaped radially magnetized PMs in alternative opposite direction located around the back iron, separated by airgaps and surrounded by ferromagnetic ring frame are employed in the MRMS machine topology (Chapter 6). In constant torque region, i.e. FSS, the magnetization direction of three adjacent PMs, i.e. two consecutive stator PMs and their neighbouring PM from the radial PM set, are either toward or outward the stator slot, Fig. 7.2 (c). Therefore, the PM flux flows through two circuits created by the stator PMs and the PMs

from the new set. Moreover, to achieve higher flux weakening capability when the machine operates in the constant power region, the radial PM set together with the laminated ring frame can be used as mechanical rotatable variable flux component. Therefore, by rotating this mechanical component as shown in Fig. 7.2 (d), the radial PM set magnets will create short circuit path for the stator PMs. Thus, the PM flux flow through the stator PMs into the two adjacent new PM set magnets and thus low PM flux-linkage will be exhibited.

7.2.3. Hybrid excitation with backside DC coils (HEBC)

Additional ferromagnetic yoke is added to the SFPM machine with DC excitation coils wound around. The armature winding and permanent magnet configurations remain the same as the conventional SFPM machine. The DC coils strengthen or weaken the PM flux according to the current direction. At positive current, the DC coils produce flux flowing in parallel with the armature flux resulting high saturation in the back iron yoke of the DC excitation which forces the PMs flux to flow toward the airgap, Fig. 7.2 (e). Moreover, when the DC coils are set to open circuit, the additional ferromagnetic yoke will provide a short circuit path for the PM flux and therefore lower PM flux-linkage can be exhibited. When negative DC current is applied, further PM flux-linkage reduction can be observed and consequently higher flux weakening capability can be achieved, Fig. 7.2 (f).

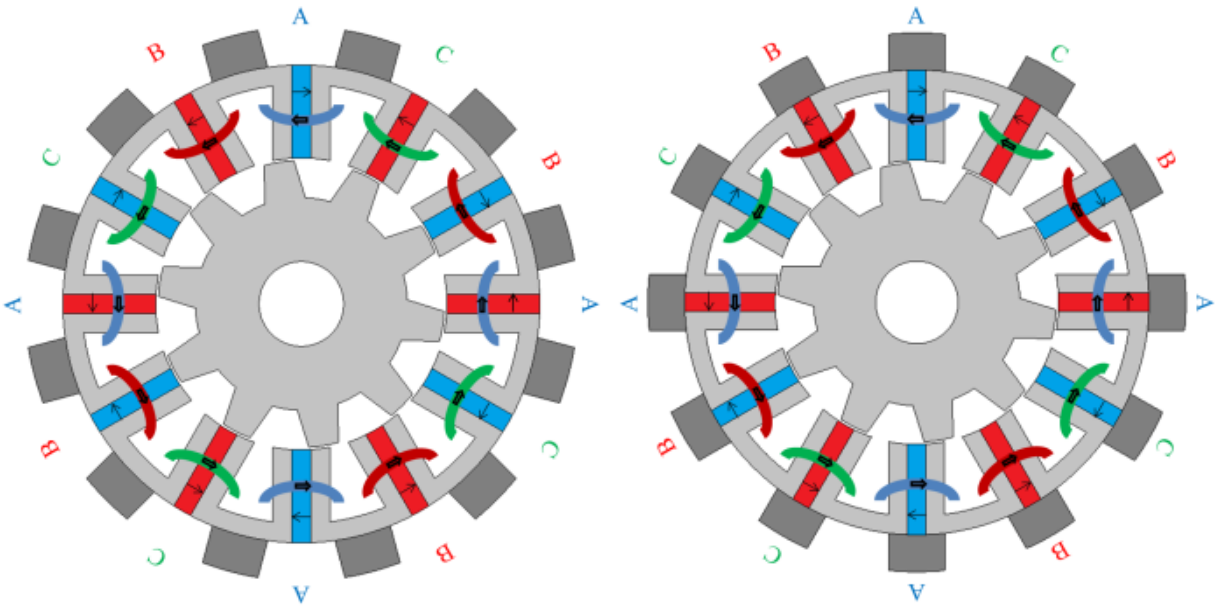

(a) MMFA, flux strengthening state (b) MMFA, flux weakening state

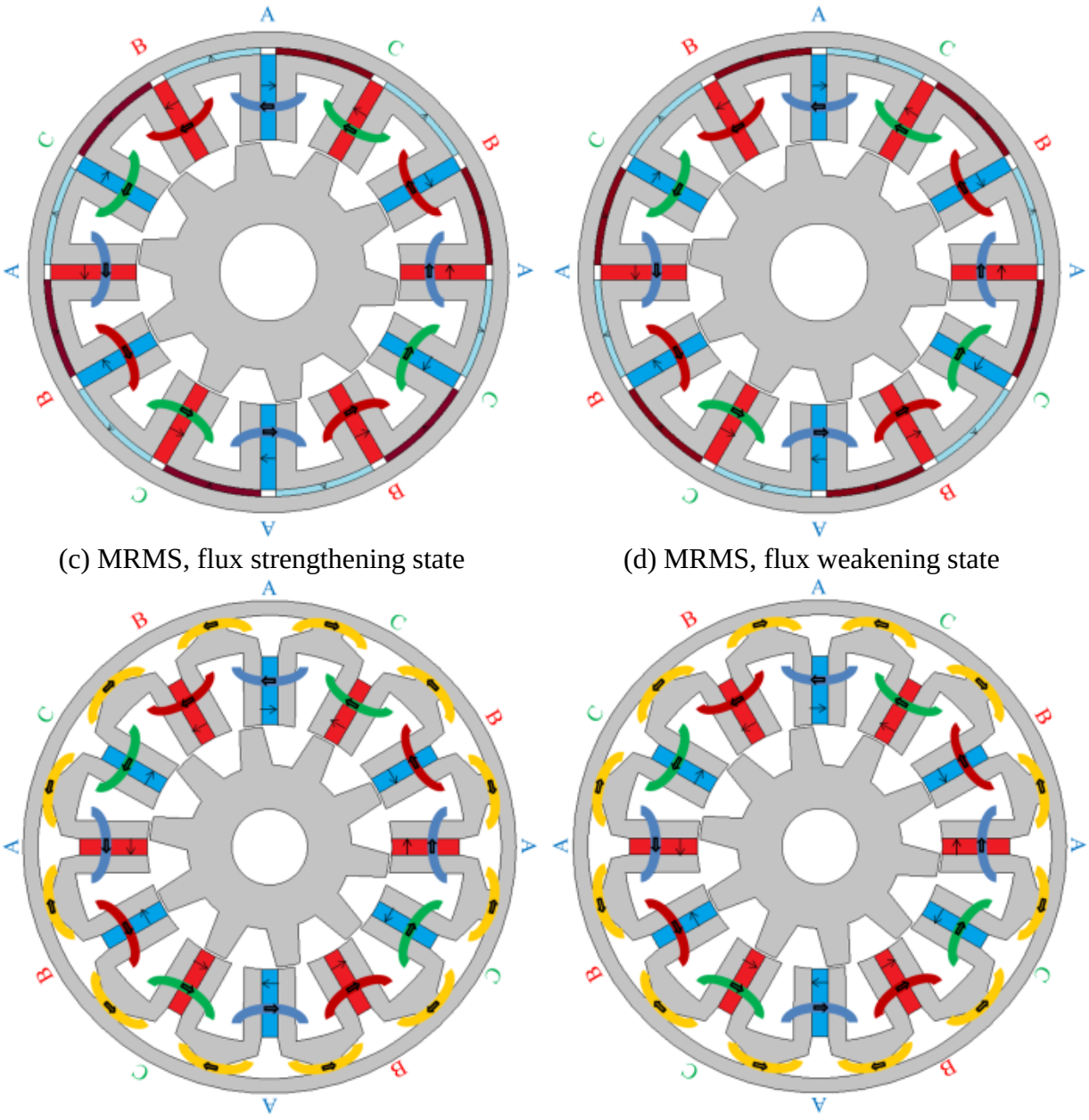

(c) MRMS, flux strengthening state (d) MRMS, flux weakening state

(e) HEBC, flux strengthening state (f) HEBC, flux weakening state

Fig. 7.2 SFPM machine topologies with variable flux technique under flux strengthening and weakening states.

7.2.4. Design parameters

For fair comparison, the same outer diameter, airgap length, axial length, copper loss and winding packing factor, as well as stator and rotor pole combination are used. Moreover, the material properties of PMs, stator and rotor iron, and the armature and DC windings of the three machines are all the same. The major design parameters of the three SFPM machines are listed in Table 7.1.

Table 7.1 Major design parameters of SFPM machines

Machines	MMFA	MRMS	HEBC
Number of rotor poles	10	10	10
Number of stator poles	12	12	12
Rotor outer radius (mm)	27	30.7	25.3
Stator outer radius (mm)	52	52	52
Stator tooth width	3.6	4.8	3.7
Stator back iron thickness (mm)	3.6	3	2.7
Magnet height (mm)	17.5	17	14.2
Magnet width (mm)	3.6	3	3.3
Airgap length (mm)	0.5	0.5	0.5
Axial length (mm)	25	25	25
Number of turns per phase (AC)	72	72	72
Number of turns (DC)	-	-	216
Total AC slot area (mm^2)	1212	1200	1221
Total DC slot area (mm^2)	-	-	823.2
Total PM volume (mm^3)	18900	15420	14364
Total back PM volume (mm^3)	-	10110	-
PM remanence (T)	1.2	1.2	1.2
PM permeability	1.05	1.05	1.05
Flux adjuster height (mm)	7	-	-
Flux adjuster width (mm)	11	-	-
Back PM width (mm)	-	1.5	-
Stator outer iron thickness (mm)	-	2.5	3.6
DC coils slot pitch (mm)	-	-	23.5
Iron bridge thickness (mm)	-	-	-
Copper loss (W)	15	15	15

7.3. Comparison of Electromagnetic Performance

7.3.1. Open circuit results

Fig. 7.3 presents the open circuit flux linkage and flux density distributions of the three SFPM machines under FSS and FWS. It is worth mentioning that in HEBC machine the FWS is set when the DC current is -5A (I_{DC}=-5A), whereas the FSS is selected when the DC current is 45A (I_{DC}=45A).

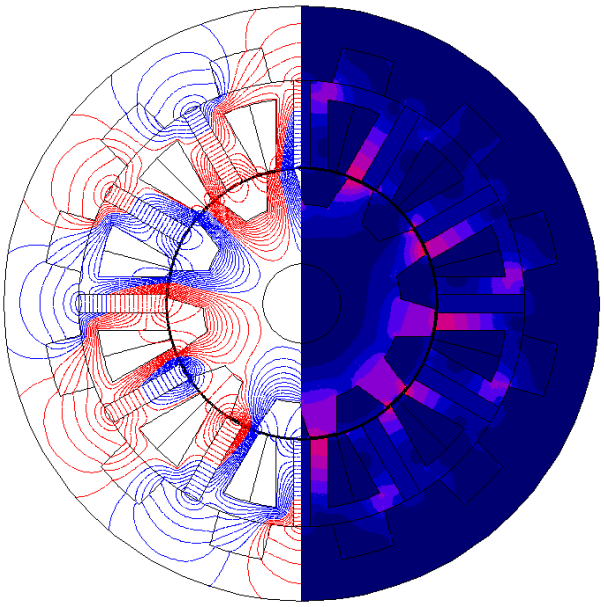

(a) MMFA, flux strengthening state

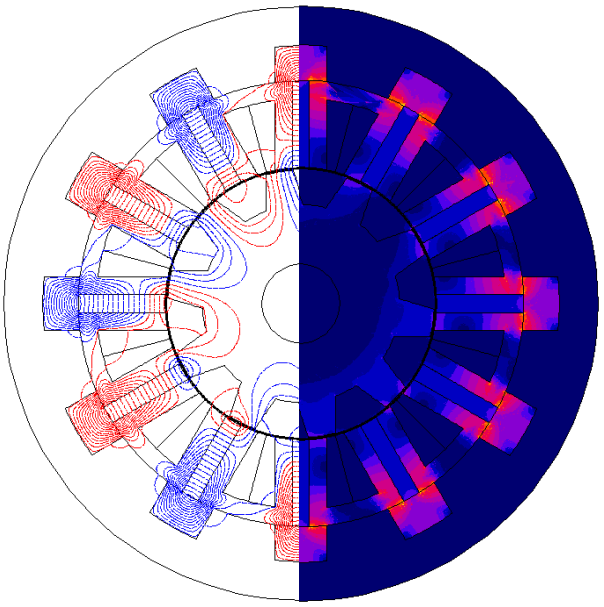

(b) MMFA, flux weakening state

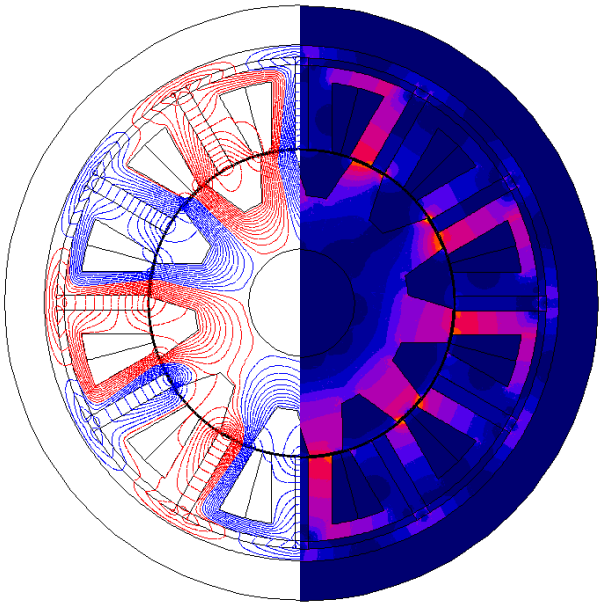

(c) MRMS, flux strengthening state

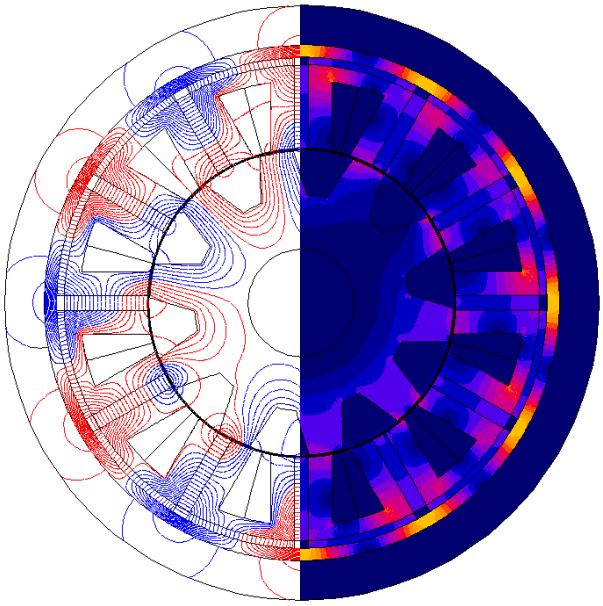

(d) MRMS, flux weakening state

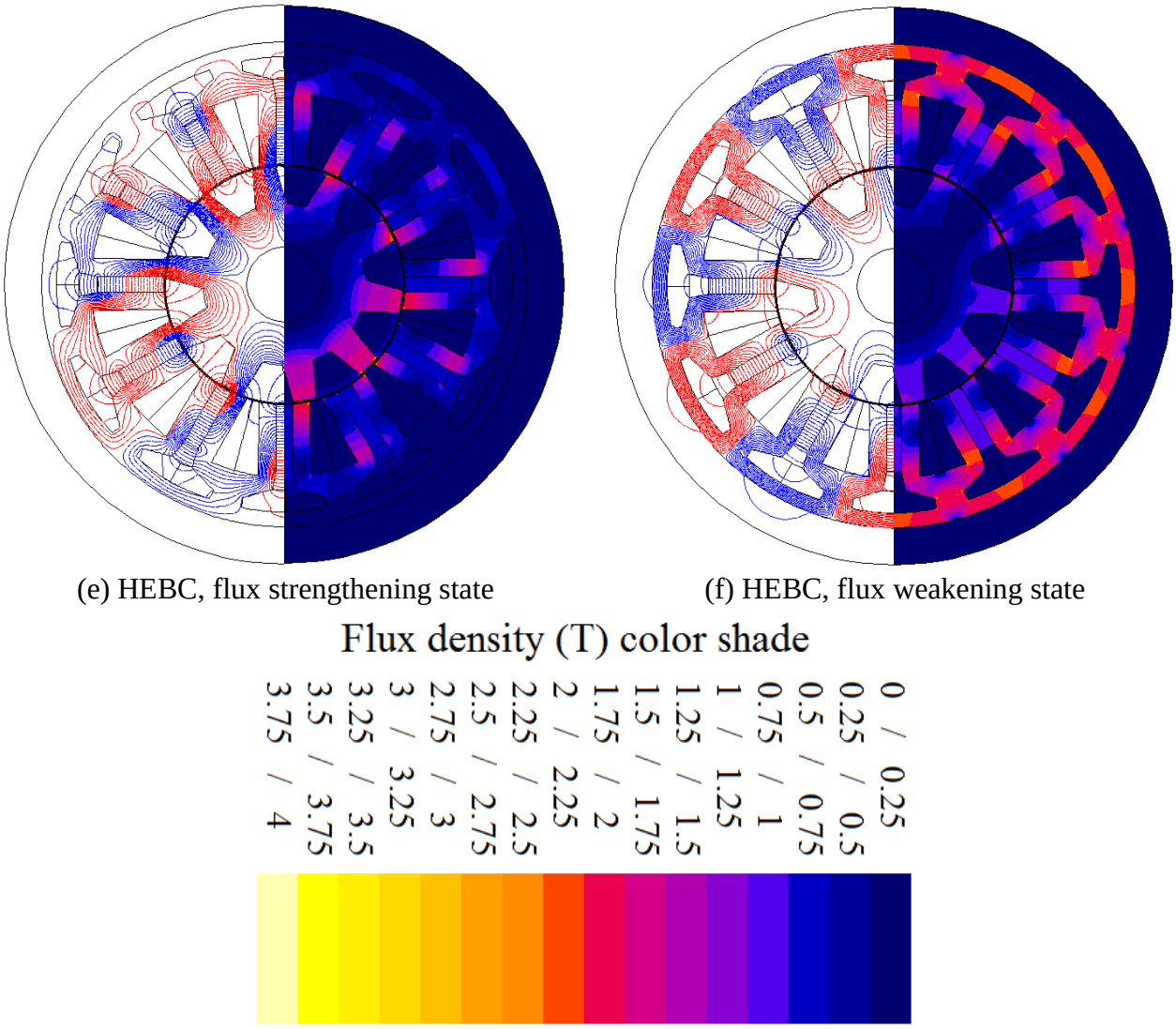

(e) HEBC, flux strengthening state (f) HEBC, flux weakening state

Fig. 7.3 Open circuit flux linkage and flux density distributions of SFPM machines with variable flux techniques.

The airgap flux density distribution of the MMFA, MRMS and HEBC under FSS and FWS are presented in Figs. 7.4 (a) and (b), respectively. Since the three machines have the same stator and rotor pole number, similar flux density distributions are predicted, whereas different peak values are observed due to different stator and rotor pole widths and local saturated spots around the airgap. Nevertheless, when the three machines are set to FWS, the flux density peak value reduces to about the half in the MMFA and around 40% in the MRMS and HEBC machines due to the short circuited PM flux.

On the other hand, the back-EMF waveforms of the three SFPM machines are compared in Fig. 7.5. It can be seen that under FSS, the MRMS machine has the highest back-EMF amplitude, whereas the lowest back-EMF is observed in MMFA and HEBC machines which

both achieved same fundamental component of back-EMF under FSS. However, by short circuiting the PM flux, i.e. FWS, the reduction in back-EMF amplitude is almost half in the MRMS machines and 60% in MMFA machine. However, the HEBC machine exhibits reduction of about 75%. The difference between the reduction in the airgap flux density and back-EMF is due to different stator-rotor flux-leakages under FSS and FWS.

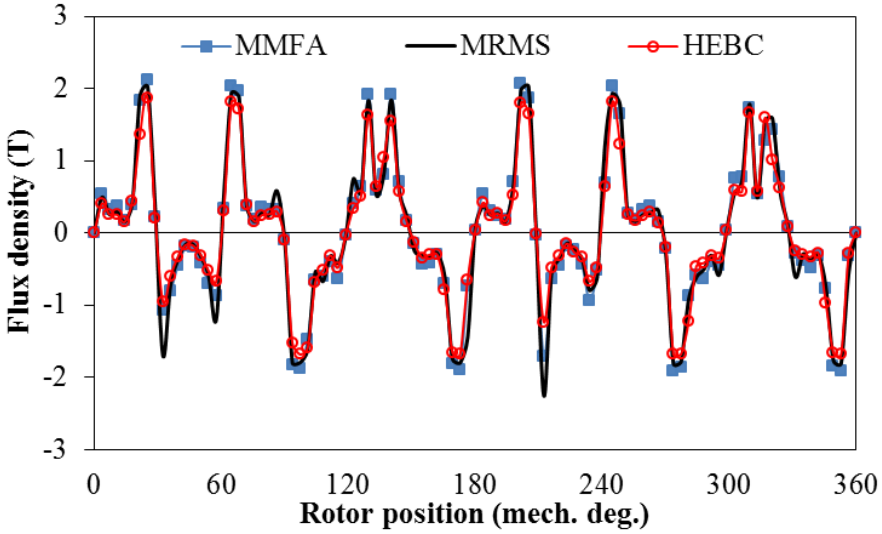

(a) Flux strengthening state

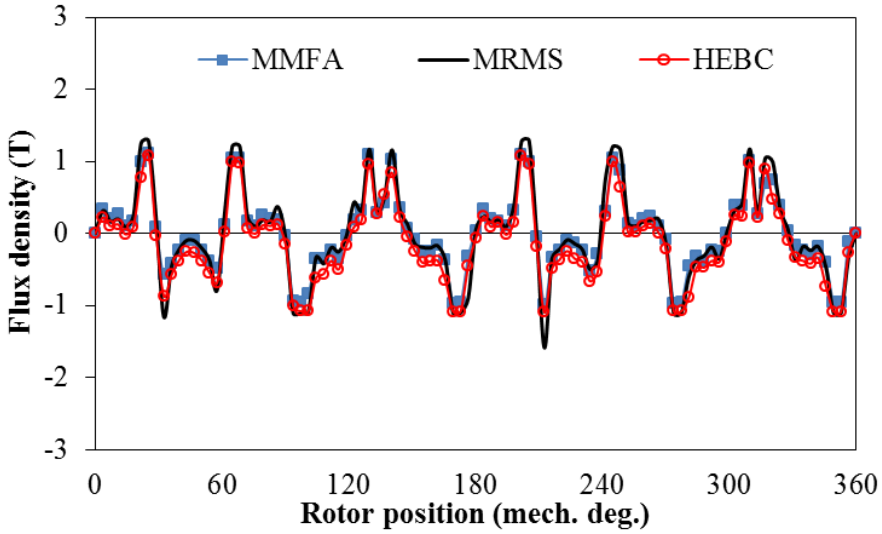

(b) Flux weakening state

Fig. 7.4 Airgap flux density of MMFA, MEMS and HEBC machine topologies.

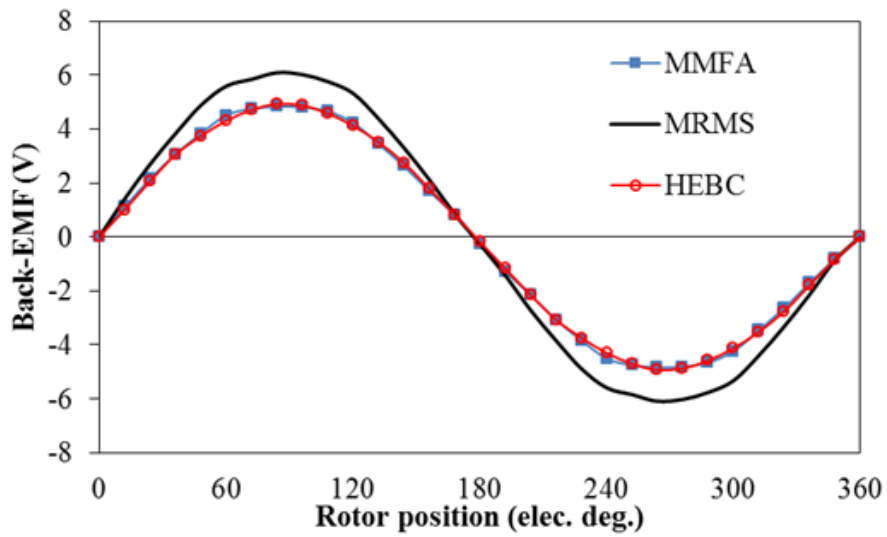

(a) Flux strengthening mode

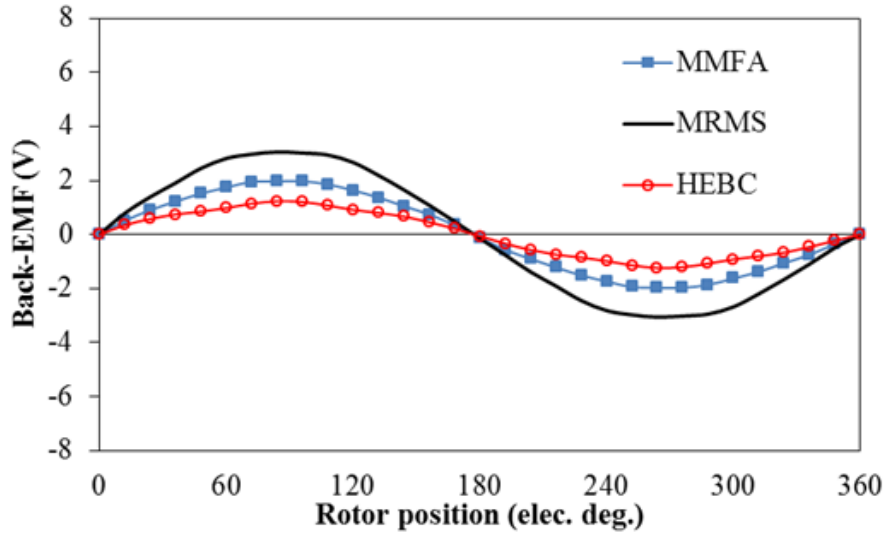

(b) Flux weakening mode

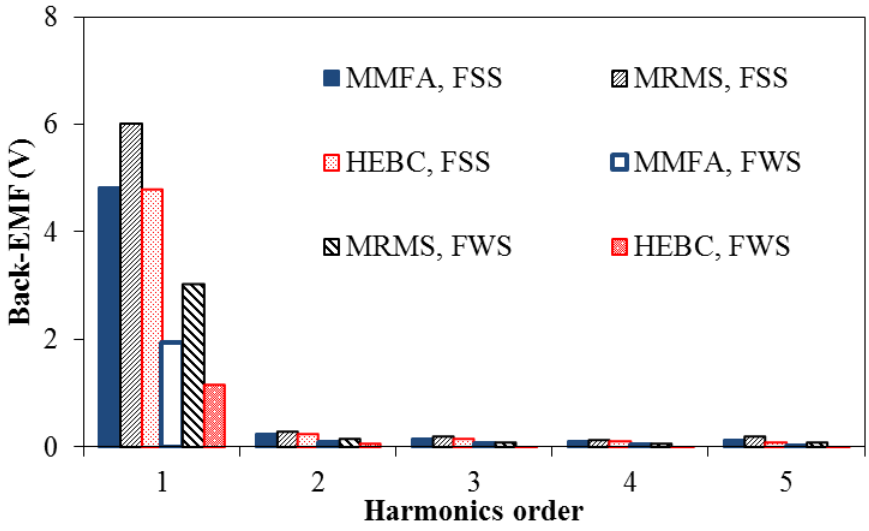

(c) Back-EMF harmonics

Fig. 7.5 Comparison of back-EMF waveforms of SFPM machines with variable flux techniques.

7.3.2. Electromagnetic torque

The electromagnetic torque in SFPM machine can be found by (1-7). However, in the HEBC machine the equivalent component of Ψ_{pm} is a combination of the PM flux-linkage and the DC flux-linkage therefore (1-7) can be presented as:

$$T_e = \frac{3}{2} N_r (\Psi_{pm} + \Psi_{DC}) I_q \tag{7-1}$$

where Ψ_{DC} is the DC flux-linkage and can be presented as the product of DC inductance L_{DC} and DC current I_{DC} assuming the flux leakage is neglected.

Nevertheless, the electromagnetic torque waveforms of the three machines under FSS and FWS are presented in Fig. 7.6 (a). However, since the torque is proportional to the product of the back-EMF and q-axis current, the average torque values are consistent with the back-EMF since same phase current is used. Moreover, under FWS the torque reduces at the same rate of the back-EMF.

Furthermore, the torque ripple in SFPM machine is mainly produced by the back-EMF harmonics and cogging torque, since the reluctance torque is negligible in SFPM machines. However, the predicated back-EMF waveforms are almost sinusoidal with relatively small harmonics, Fig. 7.5, thus the cogging torque is the main source of the torque ripple in the three machines. Therefore, the cogging torque under FSS and FWS are presented in Figs. 7.6 (b) and (c), respectively.

Under FSS, MRMS machine produces the highest cogging torque followed by the MMFA machine due to their wide stator and rotor teeth. In addition, significant second harmonic is observed in cogging torque waveform of the MMFA machine due to the stator to rotor teeth angle [163-165]. On the other hand, under FWS, similar cogging torque is exhibited by the three machines due to reduction in the airgap flux density. Therefore, the highest reduction in the torque ripple when the FWS is utilized is observed in the MRMS machine, whereas higher torque ripple is exhibited by the HEBC machine due to small reduction in the cogging torque.

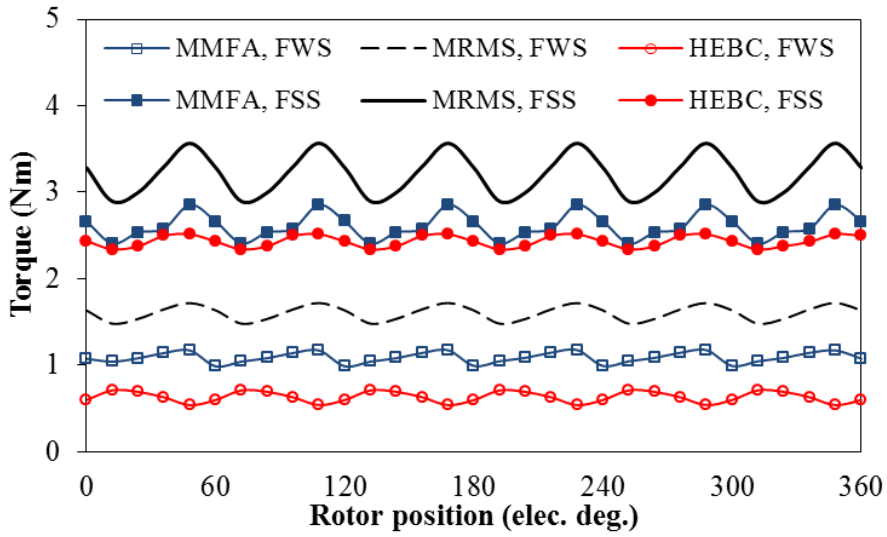

(a) Torque waveforms

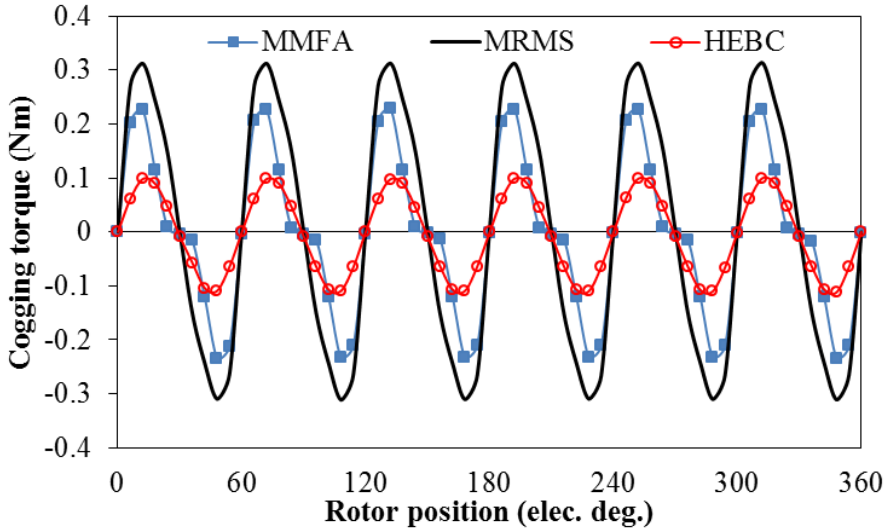

(b) Cogging torque, flux strengthening state

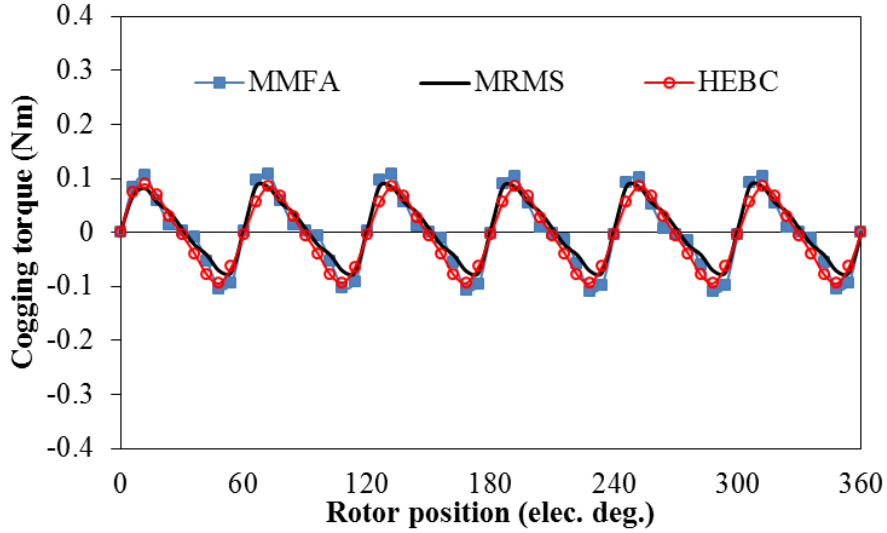

(c) Cogging torque, flux weakening state

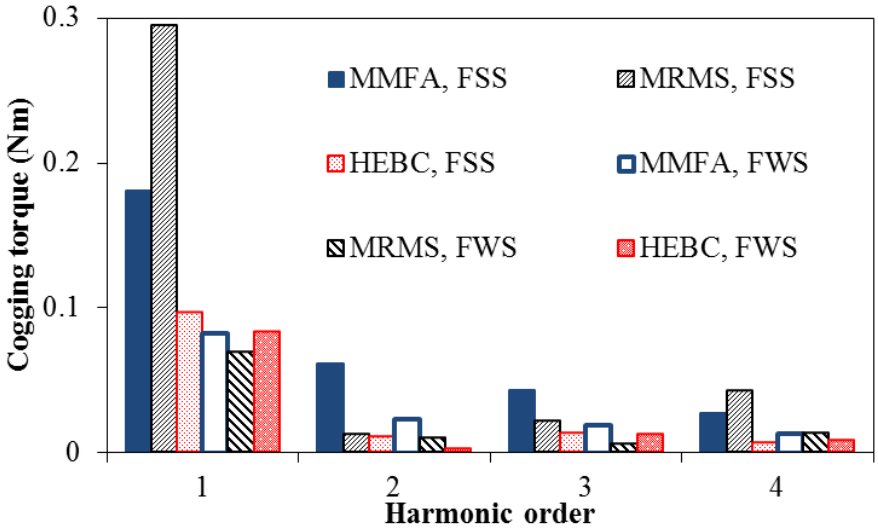

(d) Cogging torque harmonics

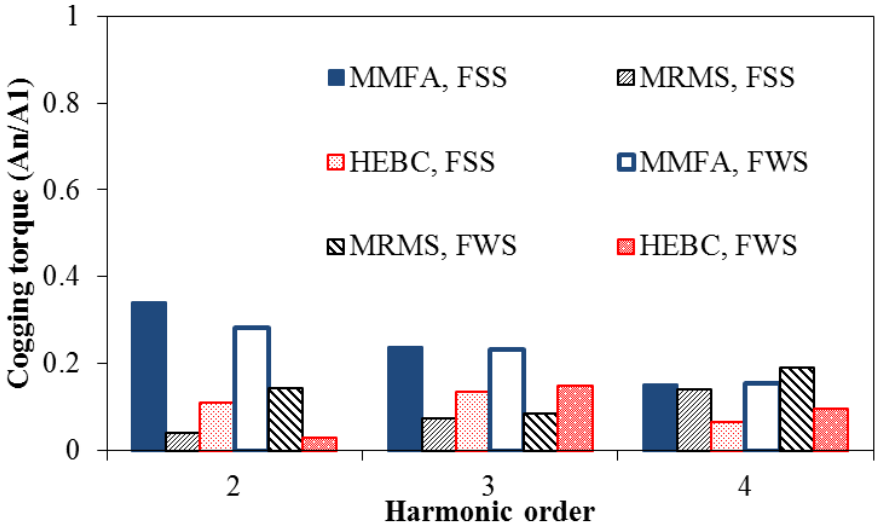

(e) Cogging torque harmonics (An/A1)

Fig. 7.6 Electromagnetic torque and cogging torque of MMFA, MRMS and HEBC machines under flux strengthening state (FSS) and weakening state (FWS).

7.3.3. Torque-speed characteristic

The d- and q-axis inductances at different d- and q-axis currents as well as the PM flux-linkage at different q-axis current levels are predicted by FEA and used in the above equation in order to analytically calculate the torque-speed curves account for the magnetic saturation and cross-coupling effect. Fig. 7.7 presents the PM flux-linkage and d- and q-axis inductances of the three SFPM machines under FSS and FWS. Moreover, the torque-speed characteristics of the three SFPM machine under FSS and FWS are presented in Fig. 7.8.

By observing the PM flux-linkage, when the machines are set to FSS, it can be seen that slight reduction at high current, i.e. 15A, occurs due to the influence of magnetic saturation.

However, by short circuiting the PM flux, i.e. FWS, lower flux level flowing through the machine can be observed and therefore the saturation effect appears at higher current levels.

Moreover, it can be seen that under FSS, the HEBC machine which has relatively high inductances due to its large magnetic circuit. Moreover, the low inductances are observed in MRMS and MMFA machines due to their small magnetic circuit and large size of the PMs.

When the machines are set to FWS, the inductances reduce in HEBC and MMFA machines due to high magnetic saturation around the backiron and the outer side of the stator pole, i.e. around the flux variation components. However, the reduction is more excessive in the HEBC machine due to the high level of saturation, Fig. 7.3. Moreover, when d-axis current is applied, the saturation influence increases since the d-axis flux forces the PM flux to move toward the short circuiting components leading to higher saturation level and therefore lower permeability for the armature flux. On the other hand, it can be seen that the inductance increases in the MRMS machine due to the low saturation level around the PM short circuited flux path. However, the saturation influence on the inductance can be observed at high d-axis current, i.e. 15A.

Fig. 10 shows the torque- and power-speed curves of the three machines when the FSS and FWS are utilized. Under FSS, the highest constant torque region is observed in MRMS machine. However, it exhibits the lowest flux weakening capability due to its low inductances. Furthermore, same torque levels are produced by the MMFA and HEBC machines at low speeds, whereas the high d-axis inductances of the HEBC machine leads to higher flux weakening capability compared to that of the MMFA machine.

On the other hand, although the d-axis inductance has reduced significantly, and the highest flux weakening capability is produced by the HEBC machine due to the significant reduction in the PM flux-linkage when the FWS is employed. Furthermore, the high d-axis inductance and low PM flux-linkage are exhibited by the MRMS machine when the FWS is applied, leading to significant improvement in the flux weakening capability. Moreover, wide speed range is observed in the MMFA machine when FWS is utilized.

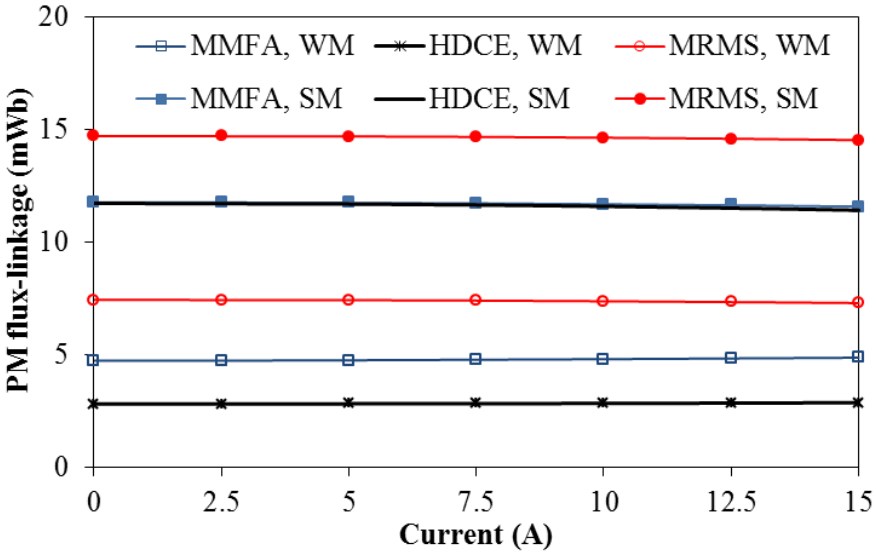

(a) PM flux linkage

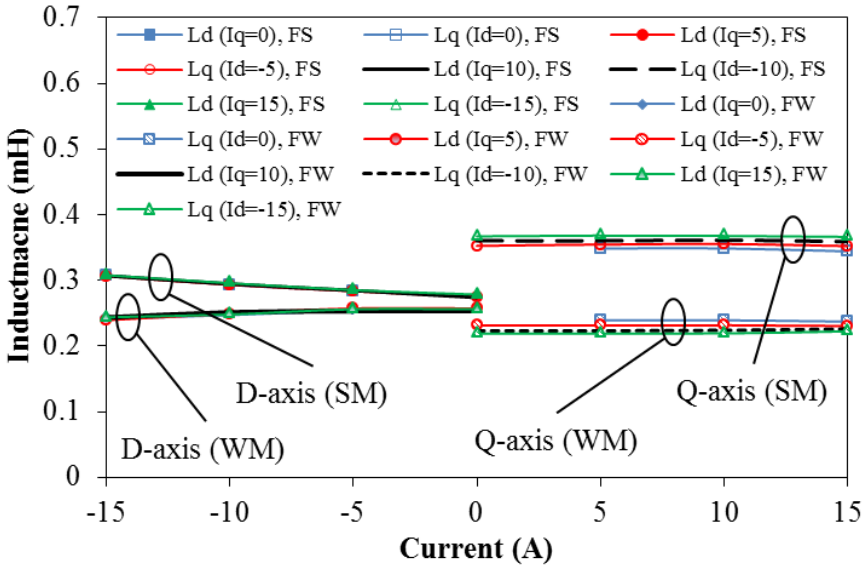

(b) MMFA inductances

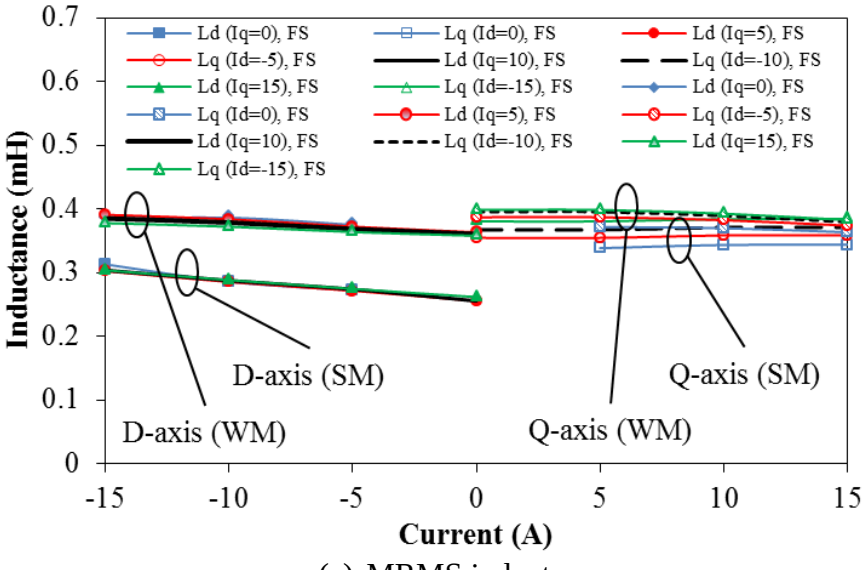

(c) MRMS inductances

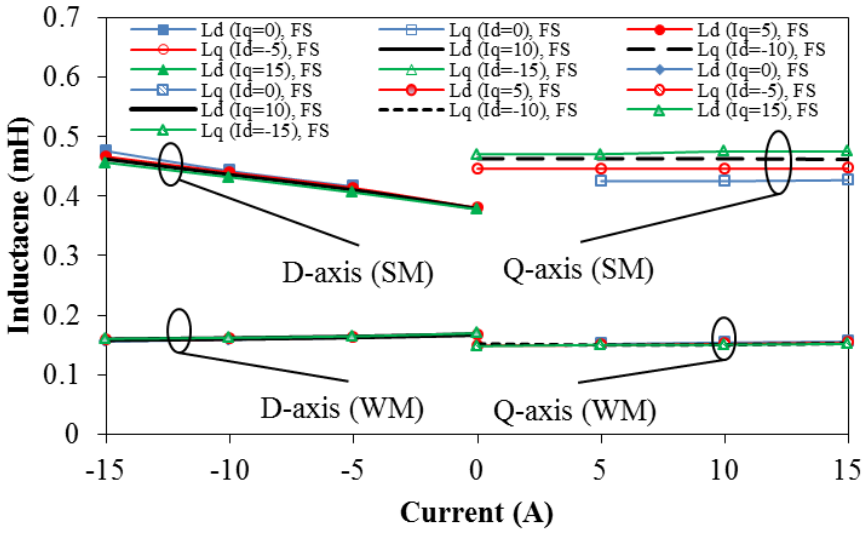

(d) HEBC inductance

Fig. 7.7 PM flux-linkage and d- and q-axis inductances of three SFPM machines under flux strengthening and weakening states.

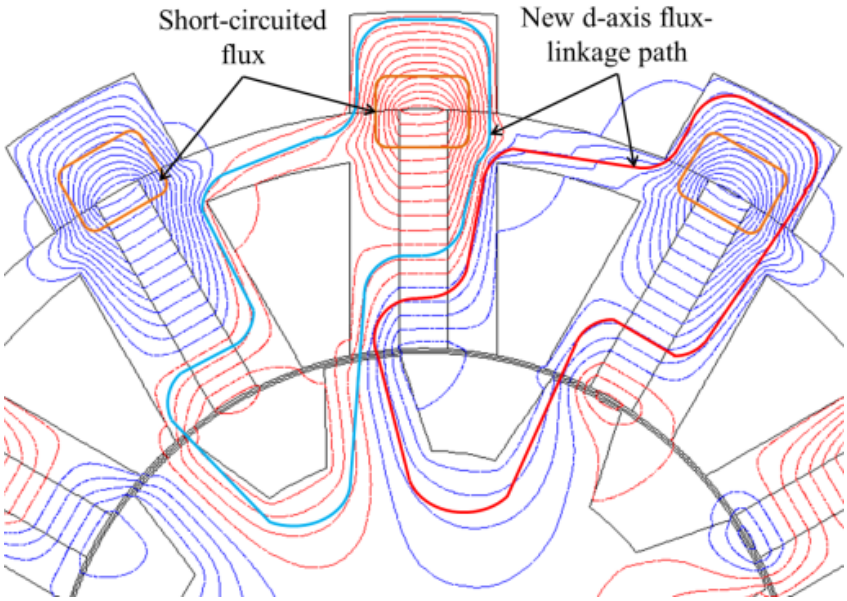

(a) MMFA

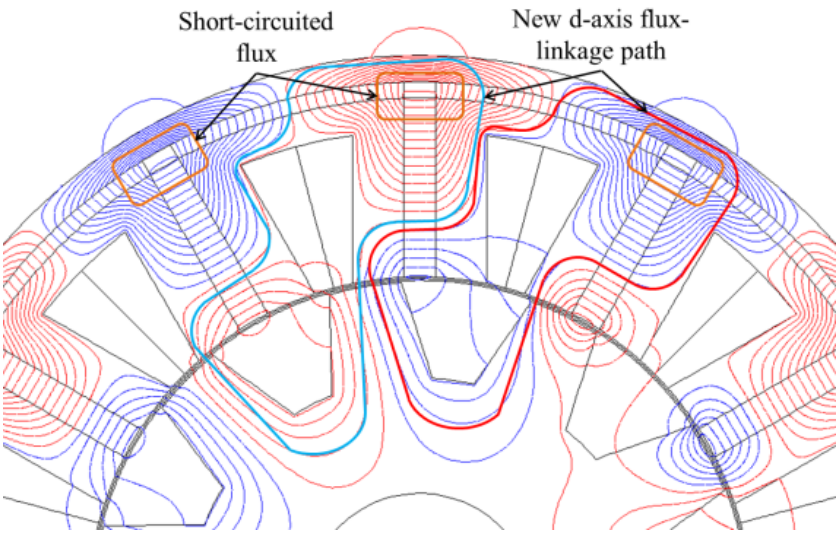

(b) MRMS

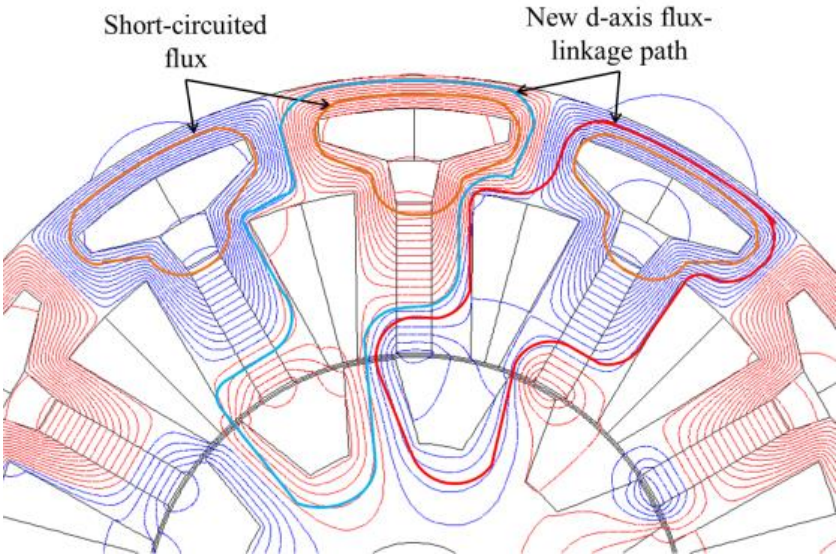

(c) HEBC

Fig. 7.8 Short circuit flux and new d-axis flux paths in the three SFPM machines under flux weakening state.

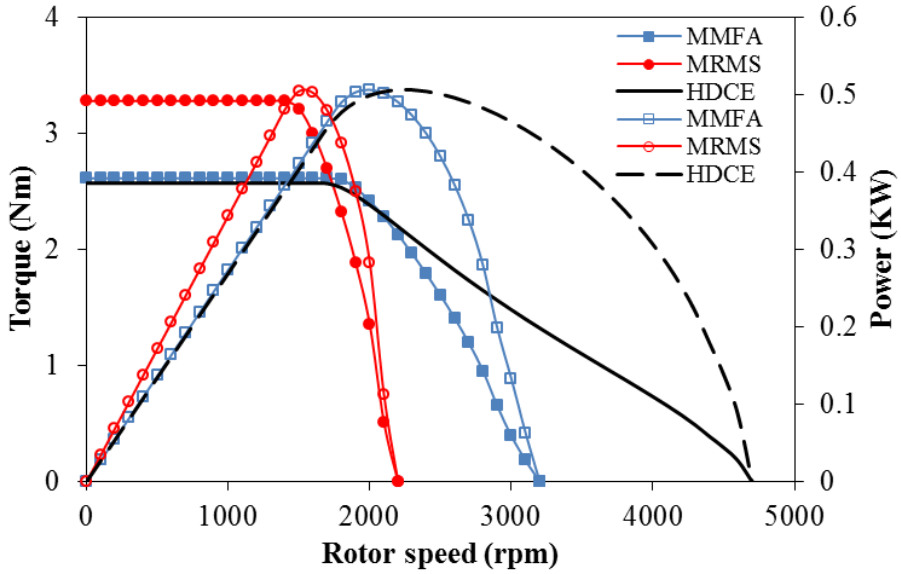

(a) Flux strengthening state

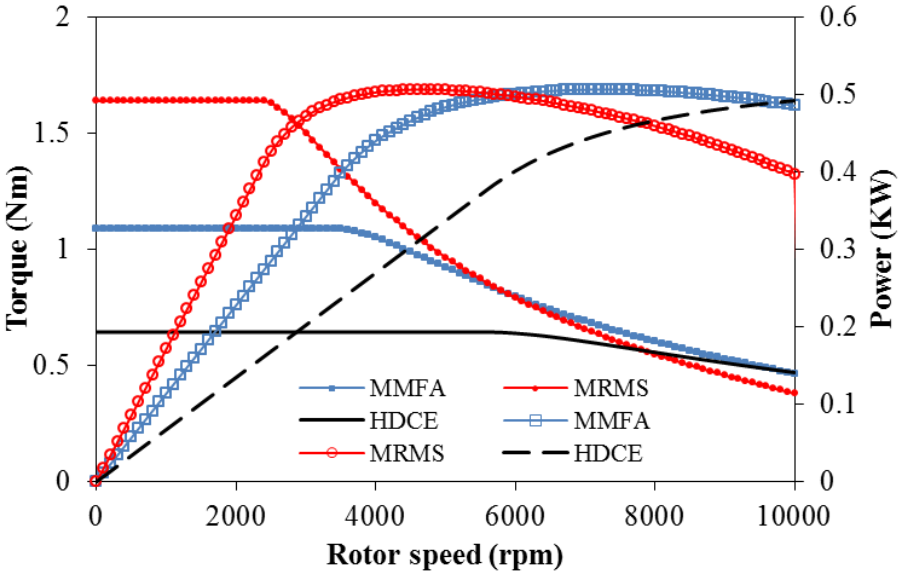

(b) Flux weakening state

Fig. 7.9 Torque- and power-speed curves of three SFPM machines.

7.4. Comparison of Flux Weakening Capabilities

7.4.1. Flux weakening capability

Table 7.2 presents the flux weakening factor and its components as well as the base speed and the maximum speed, torque and power of the three machines under FSS and FWS together with their changing percentages. It can be seen that under FSS, HEBC produces the highest flux weakening factor. However, the highest increase in the flux weakening factor is observed in the MRMS machine due to the increase in the d-axis inductances. On the other hand, the torque is reduced significantly in the HEBC machine, whereas the lowest torque

reduction is exhibited in MRMS machine when the FWS is utilized. Moreover, the same maximum power value is maintained in all three machines when the FWS is applied compared to its counter part of FSS.

Table 7.2 Comparison of flux weakening capability of SFPM machines

Machines		MMFA	MRMS	HEBC
Flux strengthening mode	L_d	0.307	0.313	0.475
	Ψ_{PM}	0.0117	0.0146	0.0116
	K_{fw}	0.39	0.32	0.61
	Max. torque	2.6	3.2	2.55
	Max. power	506	506	506
	Base speed	1800	1500	1700
	Max. speed	3200	2200	4700
Flux weakening mode	L_d	0.243	0.383	0.156
	Ψ_{PM}	0.0046	0.0074	0.0027
	K_{fw}	0.8	0.77	0.86
	Max. torque	1.08	1.6	0.64
	Max. power	506	506	506
	Base speed	3500	2400	5700
	Max. speed	20000	14600	37000
Level of changing	L_d	21%↓	21%↑	67%↓
	Ψ_{PM}	60%↓	50%↓	76%↓
	K_{fw}	48%↑	60%↑	30%↑
	Max. torque	58%↓	50%↓	75%↓
	Max. power	-	-	-
	Base speed	48%↑	37%↑	70%↑
	Max. speed	84%↑	85%↑	87%↑

7.4.2. Required power for switching between states

In order to switch between FSS and FWS an amount of power is needed to move the mechanical parts in MMFA and MRMS machines, whereas in the HEBC machine electrical power is needed for the DC winding to generate the required DC flux for either strengthening or weakening state. However, the mechanical power to switch between states in MMFA and MRMS machines and the electrical power in the HEBC machine under FWS do not contribute in the energy conversion process and can be considered as losses.

Therefore, in order to predict such powers, the movable parts in the MMFA and MRMS machines are set to rotate (movable mechanical frame) while the rotor is locked and the armature winding is set to open circuit, Fig. 7.10. Furthermore, by considering the DC excitation winding as separated source supplied by external power supply, i.e. not included in

the power inverter of the armature windings, the required power for the DC excitation winding can be found by:

$$P_{DC} = I_{DC}^2 R_{DC} \tag{7-2}$$

where R_{DC} is the DC winding resistance and can be found by:

$$R_{DC} = \frac{N_{DC}^2 \rho_{cu} l_{DC}}{A_{DC} K_{paDC}} \tag{7-3}$$

where N_{DC}, ρ_{cu}, l_{DC}, A_{DC} and K_{paDC} stand for the total number of DC excitation turns, copper resistivity, length of DC coil, total DC excitation slot area and packing factor of the DC winding. The influence of the temperature rise on the resistance is neglected.

Figs. 7.11 (a) and (b) present the torque waveform of the movable mechanical frame of MMFA and MRMS machines, respectively. Although high torque is needed to rotate the movable mechanical frame in the MMFA and MRMS machines, the average torque for one full cycle is zero. Therefore, by using a mean of potential power source, i.e. tension springs or PMs, the large amount of torque can be overcome. Figs. 7.12 (a) and (b) present a proposed mechanical system to move and control the motion of the movable mechanical frame of MMFA and MRMS machines. The mechanical frame of MMFA can be made of the FAs surrounded by non-ferromagnetic material. Moreover, a tension spring can be used as shown in Fig. 7.12 (a) to overcome the large required torque, whereas the motion can be controlled by external actuator. On the other hand, similar method can be employed in the MRMS machine as presented Fig. 7.12 (b), the movable frame can be attached to tension springs to overcome the large torque and an actuator is used to control the motion.

On the other hand, Table 7.3 shows the flux weakening factor, average torque and required DC power for different stages of flux strengthening and weakening states, i.e. different DC current levels. Relatively high power is required in the HEBC machine due to the need of high DC current levels to achieve significant flux strengthening stages. In addition, the DC power is required to maintain the state therefore it is considered continues power needed to be supplied to the machine throughout the entire operation duration.

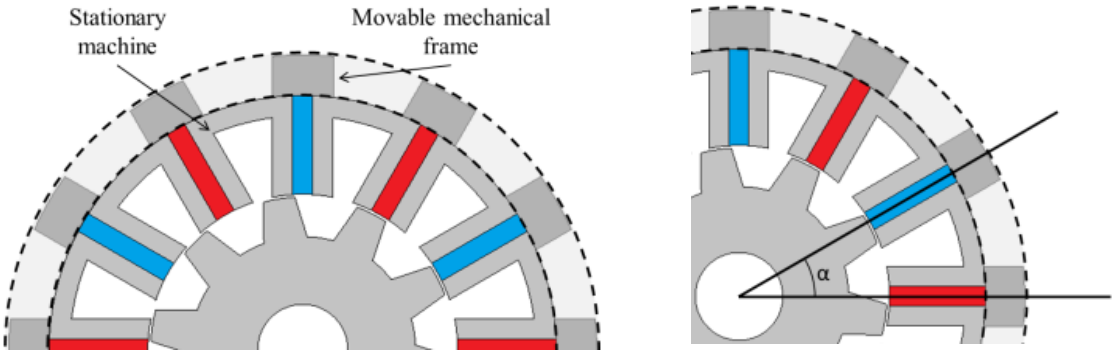

(a) MMFA

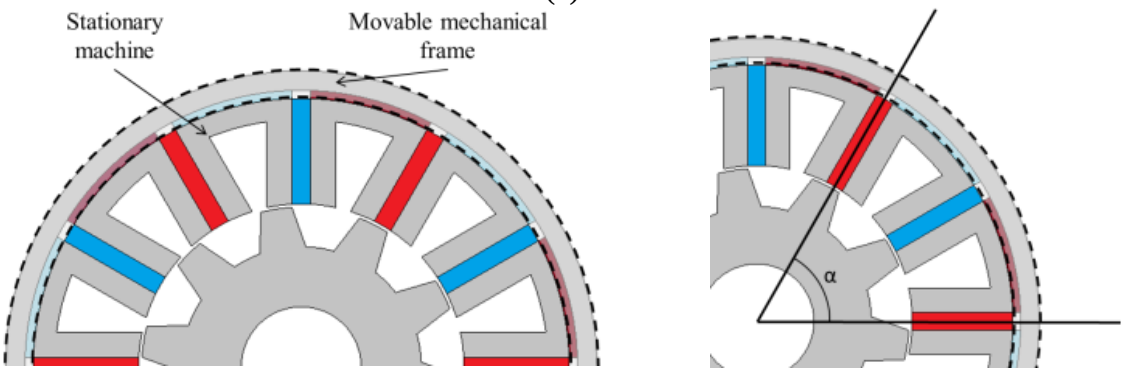

(b) MRMS

Fig. 7.10 Mechanically movable frame and its rotation angle in MMFA and MRMS machines.

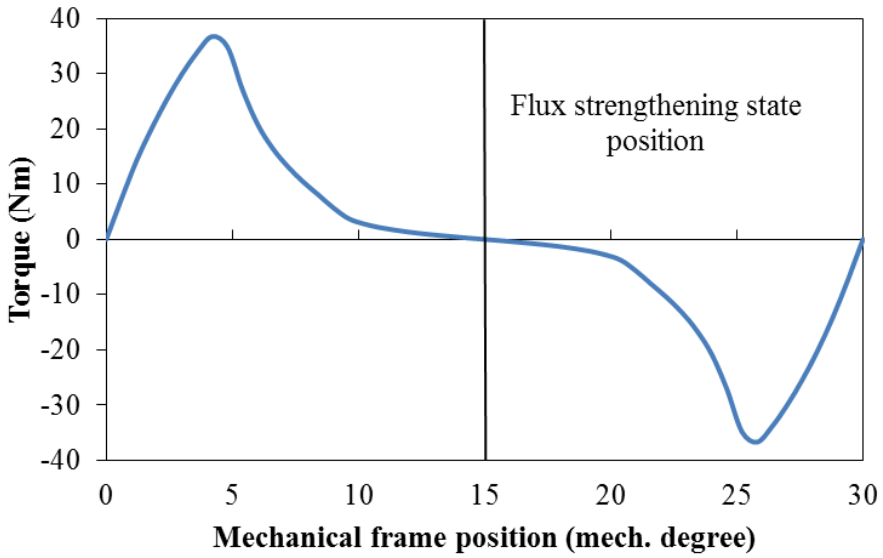

(a) MMFA

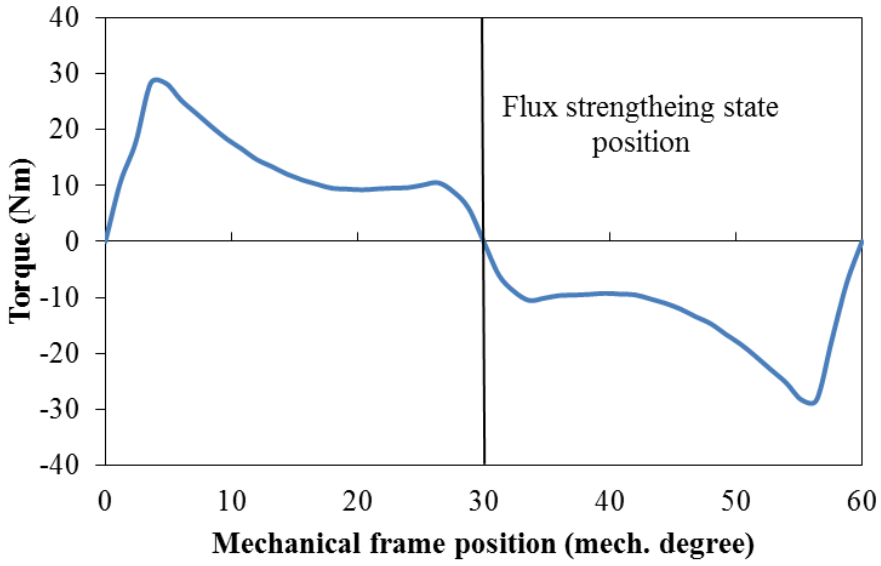

(b) MRMS

Fig. 7.11 Torque waveform of the movable mechanical frame.

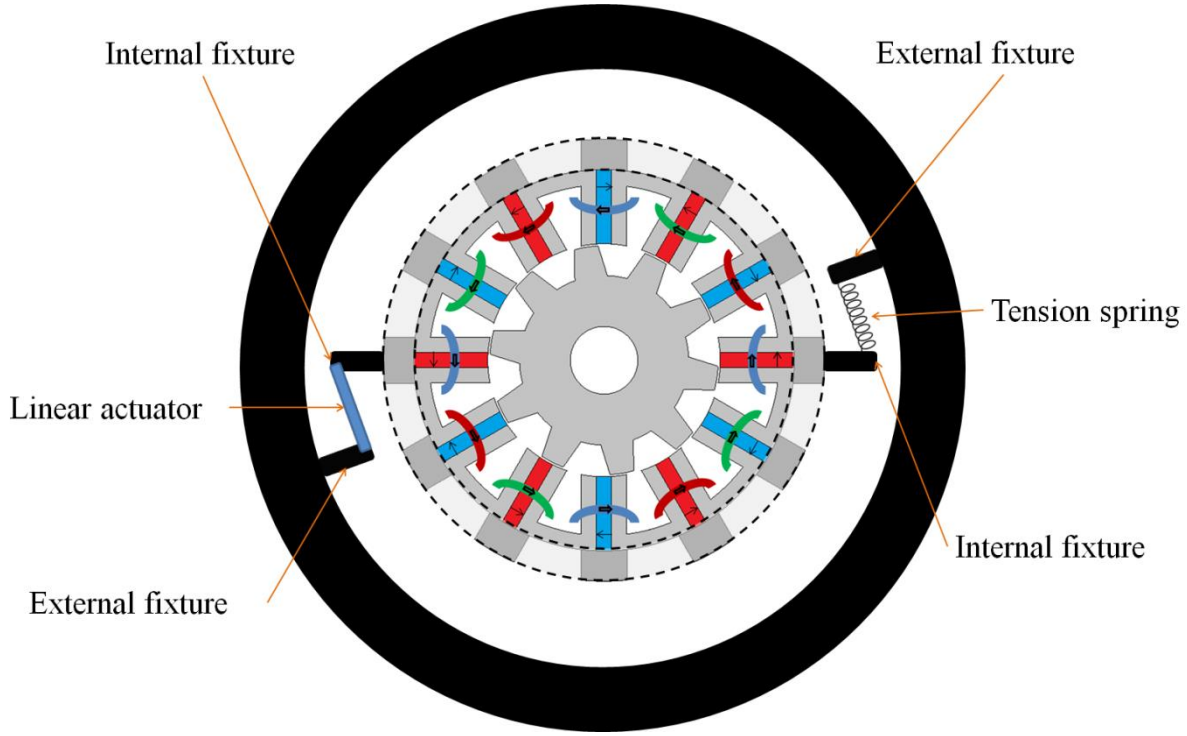

(a) MMFA

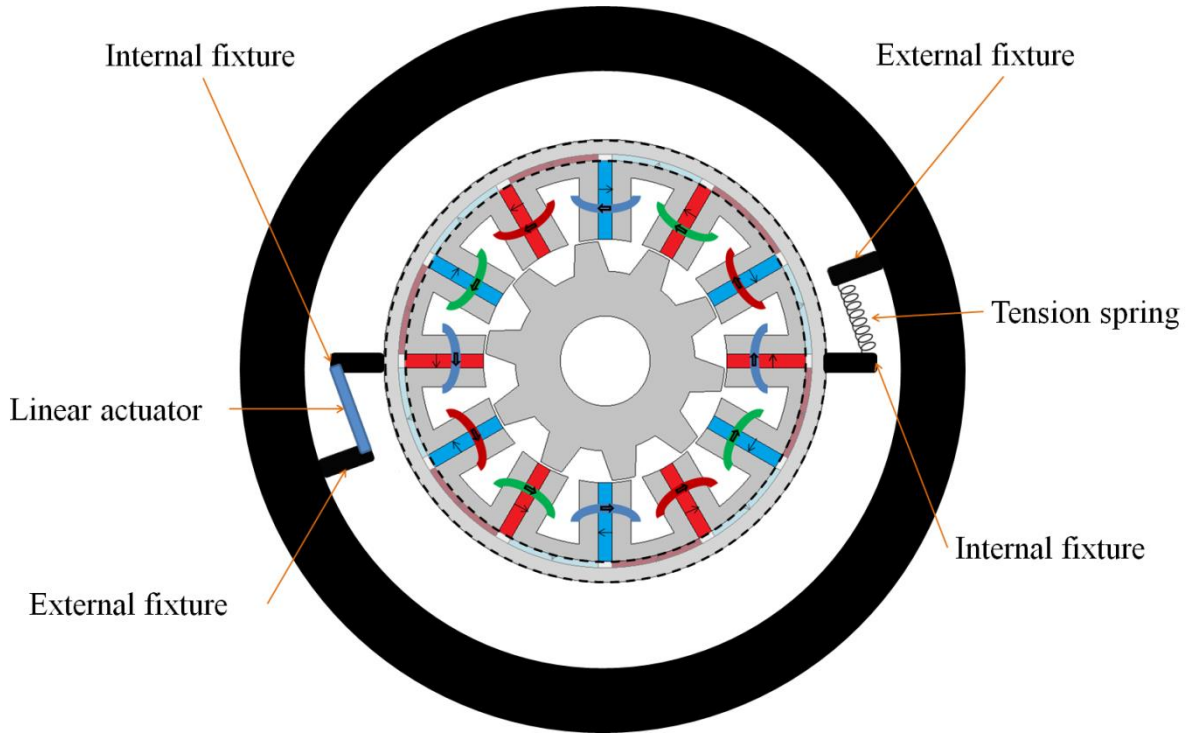

(b) MRMS

Fig. 7.12 Mechanical system in MMFA and MRMS machines.

Table 7.3 Comparison of DC power, flux weakening factor and average torque at different DC currents of HEBC machine

Current (A)	RPFW (W)	K_{fw}	Torque (Nm)
45	240	0.59	2.59
35	145	0.62	2.23
25	75	0.68	1.45
15	25	0.73	0.94
5	3	0.81	0.76
-5	3	0.85	0.66

7.4.3. Demagnetization withstand capability

Generally, in PM machines the d-axis current is implemented to overcome the PM flux when the machine is operating in the flux weakening region. The d-axis flux opposes the magnetization direction of the PM which leads to a temporary reduction in the PM working point. Moreover, the flux weakening techniques apply similar principle. Therefore, under both FWS and armature d-axis current the working points of the magnets have to be monitored and examined in order to avoid any risk of irreversible PM demagnetization.

In conventional SFPM machine the d-axis flux opposes the PM flux. However, such flux does not go through the PM, but it forces the PM flux to move toward the inactive magnetic circuits, i.e. stator-rotor leakage and stator outside leakage. Therefore, the PM working point reduces slightly when d-axis current is applied to the machine. Fig. 7.13 (a) presents the PM flux density and field intensity along the mid line of the PM of MMFA machine under FSS. It can be seen that slight reduction in the working point of the PM can be exhibited when d-axis current is applied. On the other hand, the variable flux components contain extra ferromagnetic parts and/or generate DC flux flows in the PM magnetization direction when FWS is utilized. Therefore, these components create high permeability path for the PM, resulting in higher PM working point and consequently high PM flux and high saturation around these components, as illustrated in section (7.3.3). Therefore, with such phenomena the PM working point increases when the FWS is applied, Figs. 7.13 (a) and (b).

Unlike other PM machines with variable flux techniques, in SFPM machine the variable flux components are theoretically in parallel with the PM and the armature d-axis source as shown in Fig. 7.14. Therefore, when the short circuit component, i.e. FWS, as well as rated d-axis current are applied, the working point of the PM increases. Fig. 7.13 (b) shows the working point of the PM in the MMFA machine which is set to FWS under maximum d-axis current and under open circuit. It can be seen that the working point overall increases when d-axis current is applied. However, small reduction is observed in the near airgap side of the PM due to the stator-rotor leakage which increases when d-axis current is applied.

Furthermore, the PM working point along the mid line of the PM is calculated when the three machines are set to FWS and maximum d-axis current, i.e. 15A, is injected, and compared with its FSS counterpart, Fig. 7.15. Fig. 7.16 presents the PM average working point of the three SFPM machines under FSS and FWS. In general, the working point has increased in the three machines when FWS is applied. Therefore, SFPM machines with variable flux techniques under FWS are far from any demagnetization risk.

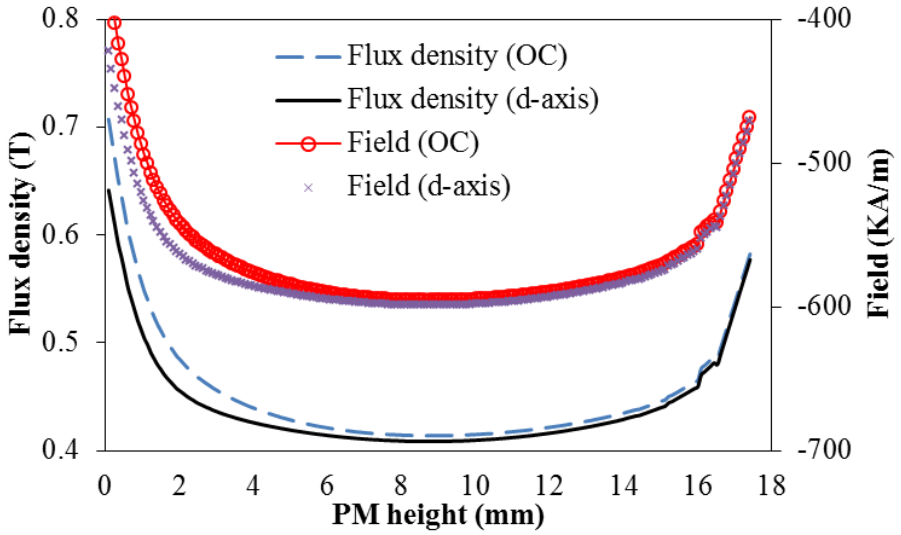

(a) Flux strengthening state

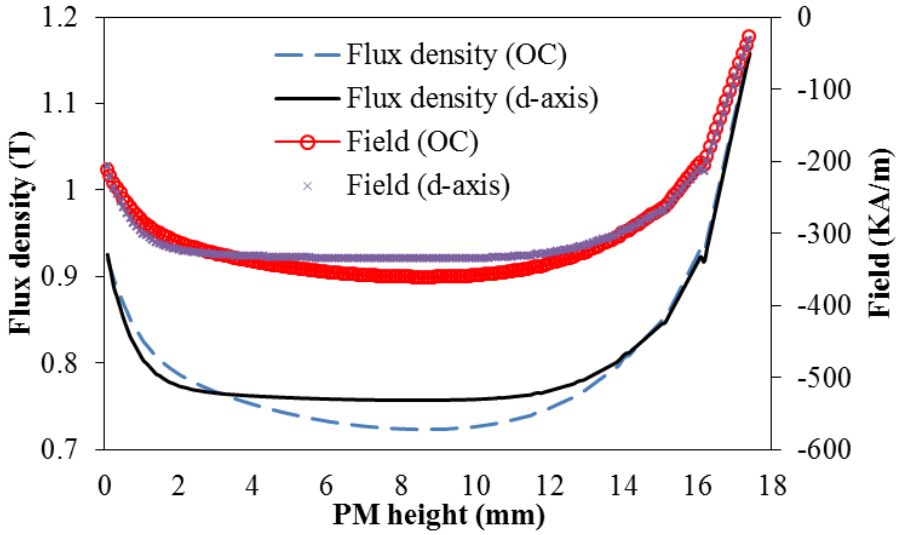

(b) Flux weakening state

Fig. 7.13 Flux density and field intensity of the mid line of PM in MMFA machine.

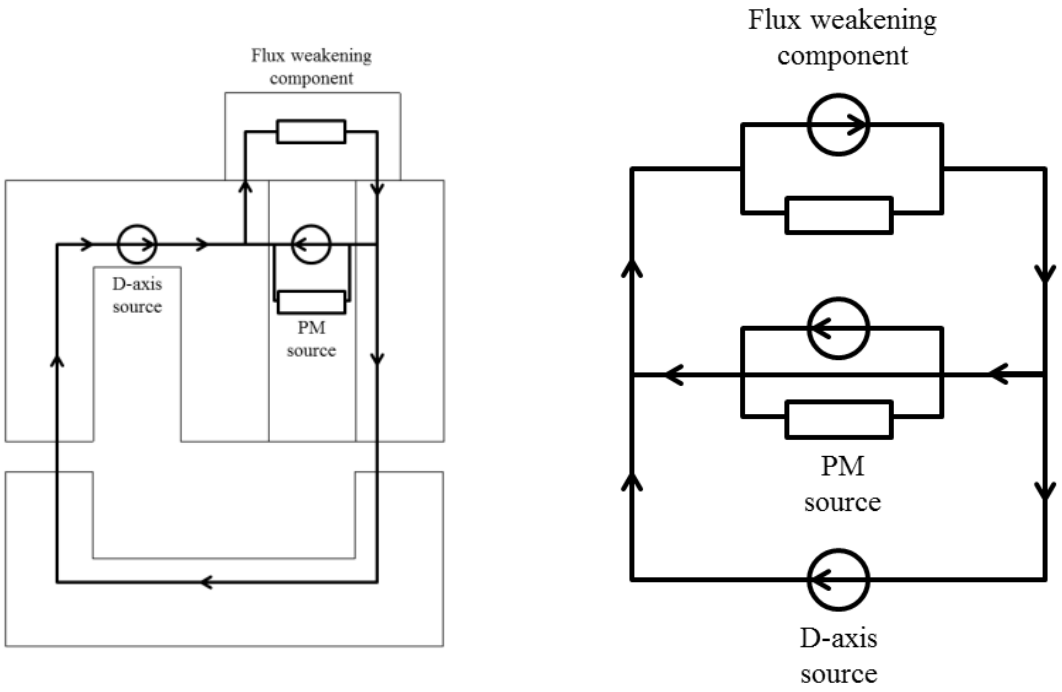

Fig. 7.14 Equivalent magnetic circuit of the PM, d-axis and flux weakening component in SFPM machine.

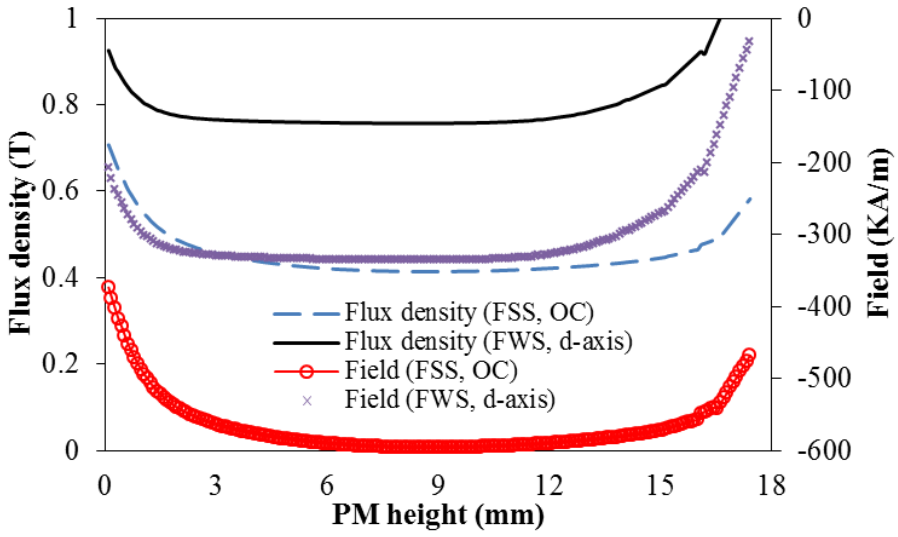

(a) MMFA

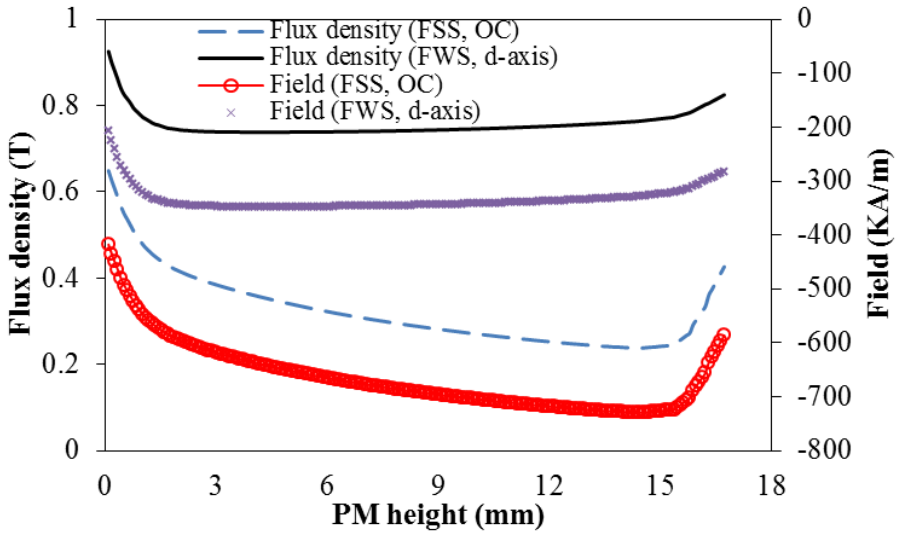

(b) MRMS

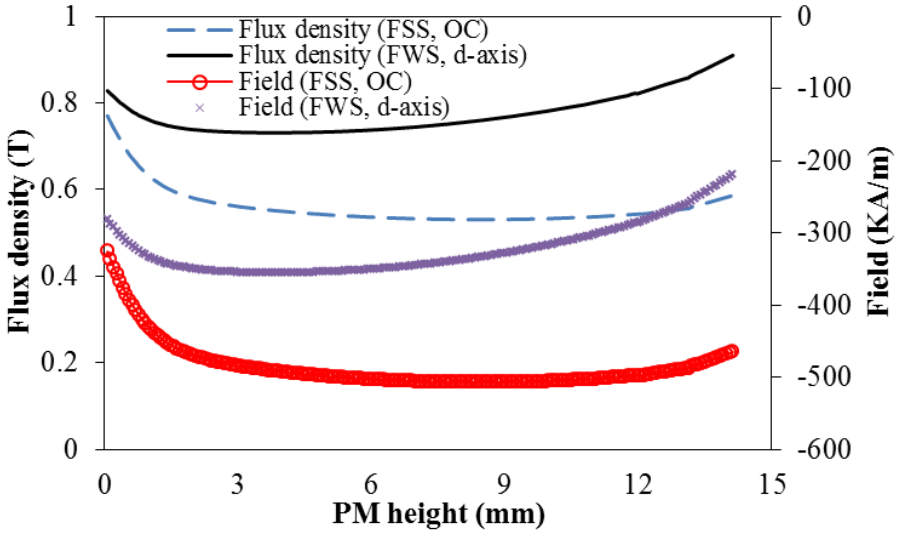

(c) HEBC

Fig. 7.15 Flux density and field intensity of mid line of the PM in the three SFPM machines

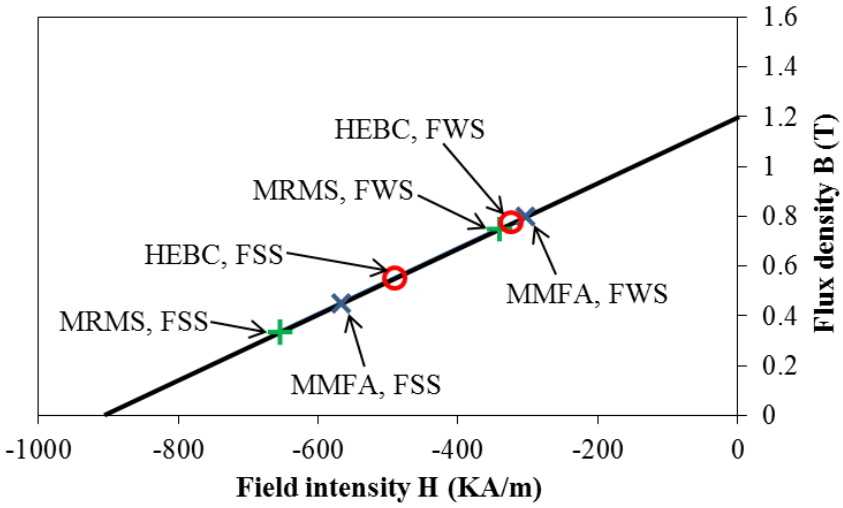

Fig. 7.16 PM working point of the three SFPM machines under FSS and FWS.

7.5. Conclusion

In this chapter, a comparative study of three SFPM machine topologies with variable flux techniques, i.e. mechanically movable flux adjusters (MMFA), mechanically rotatable magnet set (MRMS) and hybrid excitation with backside DC coils (HEBC) is presented. In addition to the electromagnetic performances, the comparison includes the required power to interchange between flux strengthening and weakening states as well as the flux weakening capability and demagnetization withstand capability of the three machines under flux strengthening and weakening states.

It has been concluded that, when flux weakening state is applied, the highest flux weakening improvement is observed in MRMS machine due to inductance increase. On the other hand, MRMS machine has the highest torque performance under both flux strengthening and weakening states. However, HEBC machine requires large power to achieve considerable flux strengthening state, whereas the required powers to switch between flux strengthening and weakening states in the MRMS and MMFA machines depend on the switching speed between states. Moreover, it is found that the three SFPM machines with variable flux techniques do not have any demagnetization risk when flux weakening state is utilized.

8. General Conclusions

8.1. Conclusions

This thesis has investigated and compared the electromagnetic performance and torque-speed characteristic of several SFPM and VFPM machine topologies for electric vehicle applications. The research focused on the evaluating topologies of SFPM machine with emphases on their speed range as well as proposes variable flux techniques to extend the speed range in order to satisfy the requirements of electric vehicles. In summary, the investigation areas included:

- Comparative study of several SFPM machine topologies with different number of rotor poles and magnets.
- Mechanical variable flux SFPM machine topologies.
- Novel SFPM machine topology with circumferential and radial PM sets.
- Comparison of three different SFPM machine topologies with variable flux techniques.

This chapter provides a general conclusion for the work that has been undertaken in this thesis. Additionally, the potential work that might be carried out to extend the finding of this thesis is presented.

8.2. Comparative Study of Several SFPM Machine Topologies

A comparative study of electromagnetic performance of different SFPM machine topologies, i.e. multi-tooth, E-core and C-core, together with conventional SFPM machines having different stator/rotor pole combinations, has been presented. In addition to open circuit and electromagnetic torque performances their torque-speed characteristics are investigated and compared. It has been found that:

- For conventional SFPM machines having stator/rotor pole combinations of 12/10, 12/13 and 12/14, the higher the rotor pole number, the better the flux weakening capability, as well as higher maximum speed can be achieved.
- Compared with conventional SFPM machines, multi-tooth, E-core and C-core machines exhibit significantly wider speed range, i.e. theoretically infinite maximum speed.
- The multi-tooth machine has the highest flux weakening factor, while the E-core machine exhibits the largest power capability.

- Overall, the conventional SFPM machines are more suitable for low speed and high electric loading applications, while the multi-tooth, E-core and C-core machines are characterized by their wide constant power region and low cost.

8.3. Comparison of Electromagnetic Performance of SFPM Machines with Mechanical Flux Adjusters

The main focus of this thesis has been the mechanical variable flux method of flux adjusters. The flux adjusters are used in either all or alternative stator pole. Moreover, a comparison of different machines equipped with flux adjusters has been completed. Overall, the concept of mechanical flux adjusters can be summarised as:

- It consists of using ferromagnetic material pieces, i.e. flux adjusters, located on the outside surface of the stator at every stator poles or every alternative.
- The position of these pieces can be mechanically adjusted to weaken the airgap flux density by short circuiting the PM flux.

The influence of using all or alternative FAs on the open circuit results, electromagnetic performance and torque-speed characteristics of the SFPM machine is investigated. A comparison has been made between different SFPM machine topologies with flux adjusters. The comparison objective is exploring the most suitable machine topologies for flux adjusting technique and to investigate the influence of all and alternative flux adjusters on the electromagnetic performance of the different SFPM machines. From this comparison it has been concluded that:

- The maximum speed and flux weakening capability of the conventional SFPM machines can be significantly increased if FAs are used.
- The multi-tooth, E-core and C-core SFPM machines have inherently large inductance, thus the flux adjusting technique has hardly any positive influence on their flux weakening performance.
- Using FAs in all stator poles can significantly improve the flux weakening capability. However, alternative FAs can also achieve remarkable improvement with drawback of higher torque ripple is observed.
- The 12/13 combination is considered to be the most suitable candidate for alternative FAs technique although unbalanced magnetic force should be taken into consideration.

8.4. Novel SFPM Machine Topology with Circumferential and Radial Permanent Magnets

Novel SFPM machine topology with circumferential and radial permanent magnet sets is proposed, optimized and compared with the conventional SFPM machine topology. In addition to the original circumferential PMs, a new set of radially magnetized PMs located around the back iron, separated by airgaps and surrounded by laminated ring frame is employed in the SFRCPM machine topology in order to reduce the flux leakage and increase the magnetic utilization. Moreover, parametric investigation is performed and based on such investigation global optimization procedure is designed. However, from the parametric investigation it has been found that:

- 2:1 is the optimum circumferential to radial magnet height ratio.
- A balanced flux distribution from both PM sets is achieved when the laminated ring frame thickness is equal to twice the radial PM height.

Furthermore, due to the small stator size, the torque performance of internal rotor SFRCPM machine is not compatible with its counterpart of conventional SFPM machine. Therefore, external rotor configuration is proposed. By comparing this machine with conventional SFPM machine with external rotor it is found that SFRCPM machine has:

- Relatively high flux-linkage and consequently high output torque due to high utilization of the magnetic material.
- Large inductance leads to wide speed range and high flux weakening capability.
- Low overall flux density distribution and therefore low iron loss and high efficiency.

Moreover, the radial PM set and the laminated ring frame can be set as a mechanically rotatable flux variation component. Therefore, this machine can be proposed as VFPM machine.

8.5. Comparison of Different SFPM Machines with Variable Flux Techniques

A comparative study of three SFPM machine topologies with variable permanent magnet flux techniques, i.e. mechanically movable flux adjusters (MMFA), mechanically rotatable magnet set (MRMS) and hybrid excitation with backside DC coils (HEBC), is presented. The comparison includes:

- The open circuit results, electromagnetic performance and torque-speed characteristics.
- The flux weakening capability, required power for switching between flux strengthening and weakening states and the demagnetization withstand capability.

From the comparison it has been concluded that:

- The MRMS machine exhibits the highest torque performance and requires relatively low power to achieve flux weakening state.
- Under flux weakening state, the best speed range and flux weakening capability achieved by HEBC machine.
- MMFA machine compromises between high torque and relatively wide speed range.
- Overall, the highest improvement in the flux weakening capability as well as highest torque performance is observed in the MRMS machine.

8.6. Future Work

Several research areas could be investigated further to extend the conclusions of this thesis:

- Further investigate the influence of the flux weakening techniques on the d-axis inductance, in particular the size of the component and level/stage of flux weakening.
- Study the influence of the alternative flux adjuster size on the cogging torque in different SFPM machine topologies and stator/rotor pole combinations.
- Investigate the effect of using all and alternative flux adjusters on the unbalanced magnetic force, cogging torque and THD in the back-EMF.
- Study the optimization procedure of variable flux machines considering the level of flux weakening capability.
- Comparatively study the required power for switching between flux strengthening and weakening states in different variable flux machines.
- Investigate influence of the magnetic saturation on the torque-speed characteristics.

References

[1] S. E. Rauch and L. J. Johnson, "Design Principles of Flux-Switch Alternators " *Transactions of the American Institute of Electrical Engineers, Power Apparatus and Systems, part iii,* vol. 74, 1955.

[2] H. R. Bolton and Y. Shakweh, "Performance prediction of Laws's relay actuator," *IEE Proceedings Electric Power Applications,* vol. 137, pp. 1-13, 1990.

[3] W. Hua, Z. Q. Zhu, M. Cheng, Y. Pang, and D. Howe, "Comparison of flux-switching and doubly-salient permanent magnet brushless machines," in *Proceedings of the Eighth International Conference on Electrical Machines and Systems (ICEMS)* 2005, pp. 165-170 Vol. 1.

[4] L. Yuefeng, F. Liang, and T. A. Lipo, "A novel permanent magnet motor with doubly salient structure," in *Conference Record of the 1992 IEEE Industry Applications Society Annual Meeting,* 1992, pp. 308-314 vol.1.

[5] R. P. Deodhar, S. Andersson, I. Boldea, and T. J. E. Miller, "The flux-reversal machine: a new brushless doubly-salient permanent-magnet machine," in *IEEE Industry Applications Conference, Thirty-First IAS Annual Meeting,* 1996, pp. 786-793 vol.2.

[6] K. Tae Heoung and L. Ju, "A study of the design for the flux reversal machine," *IEEE Transactions on Magnetics,* vol. 40, pp. 2053-2055, 2004.

[7] C. Wang, S. A. Nasar, and I. Boldea, "Three-phase flux reversal machine (FRM)," *IEE Proceedings Electric Power Applications,* vol. 146, pp. 139-146, 1999.

[8] Y. Amara, E. Hoang, M. Gabsi, M. Lécrivain, and S. Allano, "Design and comparison of different flux-switch synchronous machines for an aircraft oil breather application," *European Transactions on Electrical Power,* vol. 15, pp. 497-511, 2005.

[9] Z. Q. Zhu, Y. Pang, D. Howe, S. Iwasaki, R. Deodhar, and A. Pride, "Analysis of electromagnetic performance of flux-switching permanent-magnet Machines by nonlinear adaptive lumped parameter magnetic circuit model," *IEEE Transactions on Magnetics,* vol. 41, pp. 4277-4287, 2005.

[10] J. T. Chen and Z. Q. Zhu, "Winding Configurations and Optimal Stator and Rotor Pole Combination of Flux-Switching PM Brushless AC Machines," *IEEE Transactions on Energy Conversion,* vol. 25, pp. 293-302, 2010.

[11] C. Sanabria-Walter, H. Polinder, J. A. Ferreira, P. Janker, and M. Hofmann, "Torque enhanced Flux-Switching PM machine for aerospace applications," in *International Conference on Electrical Machines (ICEM),* 2012, pp. 2585-2595.

[12] H. Wei, C. Ming, Z. Q. Zhu, and D. Howe, "Design of Flux-Switching Permanent Magnet Machine Considering the Limitation of Inverter and Flux-Weakening Capability," in *41st Industry Applications Conference (IAS) Annual Meeting,* 2006, pp. 2403-2410.

[13] A. M. El-Refaie, D. W. Novotny, and T. M. Jahns, "A simple model for flux weakening in surface PM synchronous machines using back-to-back thyristors," *IEEE Power Electronics Letters,* vol. 2, pp. 54-57, 2004.

[14] S. Morimoto, Y. Takeda, T. Hirasa, and K. Taniguchi, "Expansion of operating limits for permanent magnet motor by optimum flux-weakening," in *Industry Applications Society Annual Meeting,* 1989, pp. 51-56 vol.1.

[15] J. Yan, P. Qingyun, H. Shoudao, X. Zhenyu, H. Keyuan, and X. Lei, "Improved method on flux-weakening control of permanent magnet synchronous motor in electric vehicles," in *International Conference on Electrical Machines and Systems (ICEMS)* 2011, pp. 1-4.

[16] W. L. Soong, S. Han, and T. M. Jahns, "Design of interior PM machines for field-weakening applications," in *International Conference on Electrical Machines and Systems (ICEMS)* 2007, pp. 654-664.

[17] W. L. Soong and N. Ertugrul, "Field-weakening performance of interior permanent magnet motors," in *IEEE Industry Applications Conference,* 2000, pp. 416-423 vol.1.

[18] W. L. Soong and T. J. E. Miller, "Field-weakening performance of brushless synchronous AC motor drives," *IEE Proceedings Electric Power Applications,* vol. 141, pp. 331-340, 1994.
[19] W. L. Soong and T. J. E. Miller, "Practical field-weakening performance of the five classes of brushless synchronous AC motor drive," in *Fifth European Conference on Power Electronics and Applications* 1993, pp. 303-310 vol.5.
[20] D. M. Ionel, J. F. Eastham, T. J. E. Miller, and E. Demeter, "Design considerations for permanent magnet synchronous motors for flux weakening applications," *IEE Proceedings Electric Power Applications,* vol. 145, pp. 435-440, 1998.
[21] X. Xingyi and D. W. Novotny, "Selection of the flux reference for induction machine drives in the field weakening region," *IEEE Transactions on Industry Applications,* vol. 28, pp. 1353-1358, 1992.
[22] X. Xingyi, R. De Doncker, and D. W. Novotny, "Stator flux orientation control of induction machines in the field weakening region," in *IEEE Industry Applications Society Annual Meeting*, 1988, pp. 437-443 vol.1.
[23] S. Morimoto, M. Sanada, and Y. Takeda, "Effects and Compensation of Magnetic Saturation in Flux-Weakening Controlled Permanent Magnet Synchronous Motor Drives," *IEEE Transactions on Industry Applications,* vol. 30, p. 1632, 1994.
[24] Z. Q. Zhu, Y. S. Chen, and D. Howe, "Online optimal flux-weakening control of permanent-magnet brushless AC drives," *IEEE Transactions on Industry Applications,* vol. 36, pp. 1661-1668, 2000.
[25] Y. F. Shi, Z. Q. Zhu, and D. Howe, "Torque-Speed Characteristics of Interior-Magnet Machines in Brushless AC and DC Modes, with Particular Reference to Their Flux-Weakening Performance," in *CES/IEEE 5th International Power Electronics and Motion Control Conference (IPEMC)*, 2006, pp. 1-5.
[26] J. T. Chen, Z. Q. Zhu, and D. Howe, "A dual-lumped parameter magnetic circuit model accounting for the cross-coupling effect, with particular reference to flux-switching permanent magnet machines," in *4th IET Conference on Power Electronics, Machines and Drives (PEMD)*, 2008, pp. 111-115.
[27] Z. Q. Zhu, Y. Pang, J. T. Chen, Z. P. Xia, and D. Howe, "Influence of design parameters on output torque of flux-switching permanent magnet machines," in *IEEE Vehicle Power and Propulsion Conference (VPPC)*, 2008, pp. 1-6.
[28] Z. Q. Zhu and X. Liu, "Individual and global optimization of switched flux permanent magnet motors," in *International Conference on Electrical Machines and Systems (ICEMS)*, 2011, pp. 1-6.
[29] A. Thomas, Z. Q. Zhu, G. W. Jewell, and D. Howe, "Flux-switching PM brushless machines with alternative stator and rotor pole combinations," in *International Conference on Electrical Machines and Systems (ICEMS)*, 2008, pp. 2986-2991.
[30] J. T. Chen, Z. Q. Zhu, A. S. Thomas, and D. Howe, "Optimal combination of stator and rotor pole numbers in flux-switching PM brushless AC machines," in *International Conference on Electrical Machines and Systems (ICEMS)*, 2008, pp. 2905-2910.
[31] J. T. Chen and Z. Q. Zhu, "Influence of rotor pole number on optimal parameters in flux-switching PM brushless AC machines by lumped parameter magnetic circuit model," in *IEEE International Electric Machines and Drives Conference (IEMDC)* 2009, pp. 1216-1223.
[32] Z. Q. Zhu, A. S. Thomas, J. T. Chen, and G. W. Jewell, "Cogging Torque in Flux-Switching Permanent Magnet Machines," *IEEE Transactions on Magnetics,* vol. 45, pp. 4708-4711, 2009.
[33] J. Hongyun, C. Ming, H. Wei, Y. Zhengzhuan, and Z. Yunqian, "Compensation of cogging torque for flux-switching permanent magnet motor based on current harmonics injection," in *IEEE International Electric Machines and Drives Conference (IEMDC)*, 2009, pp. 286-291.
[34] X. Wei, Z. Jianguo, Z. Yongchang, and H. Jiefeng, "Cogging torque reduction for radially laminated flux-switching permanent magnet machine with 12/14 poles," in *37th Annual Conference on IEEE Industrial Electronics Society (IECON)*, 2011, pp. 3590-3595.
[35] J. Hongyun, C. Ming, H. Wei, Z. Wenxiang, and L. Wenlong, "Torque Ripple Suppression in Flux-Switching PM Motor by Harmonic Current Injection Based on Voltage Space-Vector Modulation," *IEEE Transactions on Magnetics,* vol. 46, pp. 1527-1530, 2010.

[36] W. Fei, P. C. K. Luk, B. Xia, Y. Wang, and J. X. Shen, "Permanent magnet flux switching integrated-starter-generator with different rotor configurations for cogging torque and torque ripple mitigations," in *IEEE Energy Conversion Congress and Exposition (ECCE)*, 2010, pp. 1715-1722.

[37] H. Wei and M. Chen, "Inductance characteristics of 3-phase flux-switching permanent magnet machine with doubly-salient structure," in *CES/IEEE 5th International Power Electronics and Motion Control Conference (IPEMC)*, 2006, pp. 1-5.

[38] E. Ilhan, M. F. J. Kremers, E. T. Motoasca, J. J. H. Paulides, and E. A. Lomonova, "Sensitivity analysis for phase inductances in Flux-Switching PM machines," in *International Conference on Electrical Machines (ICEM)*, 2012, pp. 763-768.

[39] Z. Q. Zhu, J. T. Chen, Y. Pang, D. Howe, S. Iwasaki, and R. Deodhar, "Modeling of end-effect in flux-switching permanent magnet machines," in *International Conference on Electrical Machines and Systems (ICEMS), 2007.* , 2007, pp. 943-948.

[40] Z. Q. Zhu and Z. Azar, "Influence of end-effect and cross-coupling on torque-speed characteristics of switched flux permanent magnet machines," in *IEEE 8th International Conference on Power Electronics and ECCE Asia (ICPE & ECCE)*, 2011, pp. 145-152.

[41] W. Hua, M. Cheng, X. Zhu, and J. Zhang, "Investigation of End-Effect in Brushless Machines Having Magnets in The Stator with Doubly Salient Structure," in *IEEE International Magnetics Conference (INTERMAG)*, 2006, pp. 197-197.

[42] S. Iwasaki, R. Deodhar, Y. Liu, A. Pride, Z. Q. Zhu, and J. Bremner, "Influence of PWM on the Proximity Loss in Permanent Magnet Brushless AC Machines," in *IEEE Industry Applications Society Annual Meeting*, 2008, pp. 1-8.

[43] A. S. Thomas, Z. Q. Zhu, and G. W. Jewell, "Proximity Loss Study In High Speed Flux-Switching Permanent Magnet Machine," *IEEE Transactions on Magnetics*, vol. 45, pp. 4748-4751, 2009.

[44] Y. Pang, Z. Q. Zhu, D. Howe, S. Iwasaki, R. Deodhar, and A. Pride, "Investigation of iron loss in flux-switching PM machines," in *4th IET Conference on Power Electronics, Machines and Drives (PEMD)*, 2008, pp. 460-464.

[45] Y. Pang, Z. Q. Zhu, D. Howe, S. Iwasaki, R. Deodhar, and A. Pride, "Eddy Current Loss in the Frame of a Flux-Switching Permanent Magnet Machine," *IEEE Transactions on Magnetics*, vol. 42, pp. 3413-3415, 2006.

[46] Z. Q. Zhu, Y. Pang, J. T. Chen, R. L. Owen, D. Howe, S. Iwasaki, R. Deodhar, and A. Pride, "Analysis and reduction of magnet eddy current loss in flux-switching permanent magnet machines," in *4th IET Conference on Power Electronics, Machines and Drives (PEMD)* 2008, pp. 120-124.

[47] J. T. Chen, Z. Q. Zhu, S. Iwasaki, and R. Deodhar, "Comparison of losses and efficiency in alternate flux-switching permanent magnet machines," in *International Conference on Electrical Machines (ICEM)*, 2010, pp. 1-6.

[48] K. Wang, J. X. Shen, and S. Z. Dong, "Sensorless control and initial position estimation of permanent magnet flux switching motor," in *International Conference on Electrical Machines and Systems (ICEMS)*, 2007, pp. 487-491.

[49] J. Hongyun, C. Ming, H. Wei, W. Lu, and F. Xiaofan, "Investigation and Implementation of Control Strategies for Flux-Switching Permanent Magnet Motor Drives," in *IEEE Industry Applications Society Annual Meeting*, 2008, pp. 1-6.

[50] H. Wei, C. Ming, W. Lu, and J. Hongyun, "A new stator-flux orientation strategy for flux-switching permanent magnet motor based on current-hysteresis control," *Journal of Applied Physics*, vol. 105, pp. 07F112-07F112-3, 2009.

[51] Y. Pang, Z. Q. Zhu, D. Howe, S. Iwasaki, R. Deodhar, and A. Pride, "Comparative study of flux-switching and interior permanent magnet machines," in *International Conference on Electrical Machines and Systems (ICEMS)*, 2007, pp. 757-762.

[52] C. Ruiwu, C. Mi, and C. Ming, "Quantitative Comparison of Flux-Switching Permanent-Magnet Motors With Interior Permanent Magnet Motor for EV, HEV, and PHEV Applications," *IEEE Transactions on Magnetics*, vol. 48, pp. 2374-2384, 2012.

[53] W. Hua., M. Cheng., Z. Q. Zhu., and W. X. Zhao., "Comparison of electromagnetic performance of brushless motors having magnets in stator and rotor " *J. Appl. Phys.*, vol. 103, pp. 07F124–1–07F124–3, 2008.

[54] J. T. Chen, Z. Q. Zhu, S. Iwasaki, and R. Deodhar, "A novel E-core flux-switching PM brushless AC machine," in *IEEE Energy Conversion Congress and Exposition (ECCE)*, 2010, pp. 3811-3818.

[55] J. T. Chen, Z. Q. Zhu, S. Iwasaki, and R. P. Deodhar, "Influence of Slot Opening on Optimal Stator and Rotor Pole Combination and Electromagnetic Performance of Switched-Flux PM Brushless AC Machines," *IEEE Transactions on Industry Applications*, vol. 47, pp. 1681-1691, 2011.

[56] Z. Q. Zhu, J. T. Chen, Y. Pang, D. Howe, S. Iwasaki, and R. Deodhar, "Analysis of a Novel Multi-Tooth Flux-Switching PM Brushless AC Machine for High Torque Direct-Drive Applications," *IEEE Transactions on Magnetics*, vol. 44, pp. 4313-4316, 2008.

[57] J. T. Chen, Z. Q. Zhu, and D. Howe, "Stator and Rotor Pole Combinations for Multi-Tooth Flux-Switching Permanent-Magnet Brushless AC Machines," *IEEE Transactions on Magnetics*, vol. 44, pp. 4659-4667, 2008.

[58] J. T. Chen, Z. Q. Zhu, and D. Howe, "Optimization of multi-tooth flux-switching PM brushless ac machines," in *18th International Conference on Electrical Machines (ICEM)*, 2008, pp. 1-6.

[59] E. M. Yang Tang, Johannes J.H. Paulides, and Elena A. Lomonova,, "Comparison of flux-switching machines and permanent magnet synchronous machines in an in-wheel traction application," *COMPEL: The International Journal for Computation and Mathematics in Electrical and Electronic Engineering*, vol. 32, pp. 153 - 165, 2013.

[60] W. Z. Fei and J. X. Shen, "Novel Permanent Magnet Switching Flux Motors," in *Proceedings of the 41st International Universities Power Engineering Conference (UPEC)*, 2006, pp. 729-733.

[61] Y. Tang, J. J. H. Paulides, T. E. Motoasca, and E. A. Lomonova, "Flux-Switching Machine With DC Excitation," *IEEE Transactions on Magnetics*, vol. 48, pp. 3583-3586, 2012.

[62] J. T. Chen, Z. Q. Zhu, S. Iwasaki, and R. Deodhar, "Low cost flux-switching brushless AC machines," in *IEEE Vehicle Power and Propulsion Conference (VPPC)*, 2010, pp. 1-6.

[63] R. L. Owen, Z. Q. Zhu, A. S. Thomas, G. W. Jewell, and D. Howe, "Fault-Tolerant Flux-Switching Permanent Magnet Brushless AC Machines," in *IEEE Industry Applications Society Annual Meeting*, 2008, pp. 1-8.

[64] T. Raminosoa and C. Gerada, "Fault tolerant winding technology comparison for Flux Switching Machine," in *International Conference on Electrical Machines (ICEM)*, 2010, pp. 1-6.

[65] Z. Wenxiang, C. Ming, K. T. Chau, J. Jinghua, H. Wei, and C. Ruiwu, "A new modular flux-switching permanent-magnet machine using fault-tolerant teeth," in *14th Biennial IEEE Conference on Electromagnetic Field Computation (CEFC)*, 2010, pp. 1-1.

[66] A. S. Thomas, Z. Q. Zhu, R. L. Owen, G. W. Jewell, and D. Howe, "Multi-Phase Flux-Switching Permanent Magnet Brushless Machine for Aerospace Application," in *IEEE Industry Applications Society Annual Meeting*, 2008, pp. 1-8.

[67] A. Zulu, B. C. Mecrow, and M. Armstrong, "A Wound-Field Three-Phase Flux-Switching Synchronous Motor With All Excitation Sources on the Stator," *IEEE Transactions on Industry Applications*, vol. 46, pp. 2363-2371, 2010.

[68] A. Zulu, B. C. Mecrow, and M. Armstrong, "Prediction of performance of a wound-field segmented-rotor flux-switching synchronous motor using a dq-equivalent model," in *International Conference on Electrical Machines (ICEM)*, 2010, pp. 1-6.

[69] A. Zulu, B. C. Mecrow, and M. Armstrong, "Topologies for wound-field three-phase segmented-rotor flux-switching machines," in *5th IET International Conference on Power Electronics, Machines and Drives (PEMD)*, 2010, pp. 1-6.

[70] A. S. Thomas, Z. Q. Zhu, and L. J. Wu, "Novel Modular-Rotor Switched-Flux Permanent Magnet Machines," *IEEE Transactions on Industry Applications*, vol. 48, pp. 2249-2258, 2012.

[71] W. Fei, P. C. K. Luk, J. Shen, and Y. Wang, "A novel outer-rotor permanent-magnet flux-switching machine for urban electric vehicle propulsion," in *3rd International Conference on Power Electronics Systems and Applications (PESA)*, 2009, pp. 1-6.

[72] M. Z. Ahmad, E. Sulaiman, Z. A. Haron, and T. Kosaka, "Preliminary studies on a new outer-rotor permanent magnet flux switching machine with hybrid excitation flux for direct drive EV applications," in *IEEE International Conference on Power and Energy (PECon)*, 2012, pp. 928-933.

[73] J.-X. S. Wei-Zhong Fei, Can-Fei Wang, Patrick Chi-Kwong Luk, "Design and analysis of a new outer-rotor permanent-magnet flux-switching machine for electric vehicle propulsion," *COMPEL: The International Journal for Computation and Mathematics in Electrical and Electronic Engineering*, vol. 30, pp. 48-61, 2011.

[74] W. Min, J. T. Chen, Z. Q. Zhu, Y. Zhu, M. Zhang, and G. H. Duan, "Optimization and Comparison of Novel E-Core and C-Core Linear Switched Flux PM machines," *IEEE Transactions on Magnetics*, vol. 47, pp. 2134-2141, 2011.

[75] A. Gandhi and L. Parsa, "Double-sided flux-switching linear synchronous machine with yokeless translator," in *IEEE Energy Conversion Congress and Exposition (ECCE)*, 2012, pp. 2676-2680.

[76] J. Meng-Jia, W. Can-Fei, S. Jian-Xin, and X. Bing, "A Modular Permanent-Magnet Flux-Switching Linear Machine With Fault-Tolerant Capability," *IEEE Transactions on Magnetics*, vol. 45, pp. 3179-3186, 2009.

[77] Z. Q. Zhu, X. Chen, J. T. Chen, D. Howe, and J. S. Dai, "Novel linear flux-switching permanent magnet machines," in *International Conference on Electrical Machines and Systems (ICEMS)*, 2008, pp. 2948-2953.

[78] D. C. J. Krop, L. Encica, and E. A. Lomonova, "Analysis of a novel double sided flux switching linear motor topology," in *International Conference on Electrical Machines (ICEM)*, 2010, pp. 1-5.

[79] J. F. Eastham, "Novel synchronous machines: linear and disc," *IEE Proceedings Electric Power Applications*, vol. 137, pp. 49-58, 1990.

[80] W. Jiabin, W. Weiya, K. Atallah, and D. Howe, "Design Considerations for Tubular Flux-Switching Permanent Magnet Machines," *IEEE Transactions on Magnetics*, vol. 44, pp. 4026-4032, 2008.

[81] K. Mei, J. Jinghua, L. Guohai, and Z. Wenxiang, "A new tubular fault-tolerant permanent-magnet motor for active vehicle suspension," in *38th Annual Conference on IEEE Industrial Electronics Society (IECON)*, 2012, pp. 4082-4086.

[82] Z. Q. Zhu, P. J. Hor, D. Howe, and J. Rees-Jones, "Novel linear tubular brushless permanent magnet motor," in *Eighth International Conference on Electrical Machines and Drives*, 1997, pp. 91-95.

[83] E. Spooner, S. A. W. Khatab, and N. G. Nicolaou, "Hybrid excitation of AC and DC machines," in *Fourth International Conference on Electrical Machines and Drives*, 1989, pp. 48-52.

[84] J. F. Eastham, P. D. Evans, P. C. Coles, and M. Ibrahim, "Double disc alternators with hybrid excitation," *IEEE Transactions on Magnetics*, vol. 28, pp. 3039-3041, 1992.

[85] J. A. Tapia, M. Aydin, H. Surong, and T. A. Lipo, "Sizing equation analysis for field controlled PM machines: a unified approach," in *IEEE International Electric Machines and Drives Conference (IEMDC)*, 2003, pp. 1111-1116 vol.2.

[86] W. Yu and D. Zhiquan, "Comparison of Hybrid Excitation Topologies for Flux-Switching Machines," *IEEE Transactions on Magnetics*, vol. 48, pp. 2518-2527, 2012.

[87] H. Wei, C. Ming, and Z. Gan, "A Novel Hybrid Excitation Flux-Switching Motor for Hybrid Vehicles," *IEEE Transactions on Magnetics*, vol. 45, pp. 4728-4731, 2009.

[88] R. L. Owen, Z. Q. Zhu, and G. W. Jewell, "Hybrid-Excited Flux-Switching Permanent-Magnet Machines With Iron Flux Bridges," *IEEE Transactions on Magnetics*, vol. 46, pp. 1726-1729, 2010.

[89] B. Gaussens, E. Hoang, M. Lecrivain, P. Manfe, and M. Gabsi, "A new hybrid-excited flux-switching machine with excitation coils in stator slots," in *Electrical Machines and Systems (ICEMS), 2012 15th International Conference on*, 2012, pp. 1-6.

[90] E. Hoang, M. Lecrivain, and M. Gabsi, "A new structure of a switching flux synchronous polyphased machine with hybrid excitation," in *European Conference on Power Electronics and Applications*, 2007, pp. 1-8.
[91] E. Hoang, M. Lecrivain, S. Hlioui, and M. Gabsi, "Hybrid excitation synchronous permanent magnets synchronous machines optimally designed for hybrid and full electrical vehicle," in *IEEE 8th International Conference on Power Electronics and ECCE Asia (ICPE & ECCE)*, 2011, pp. 153-160.
[92] J. T. Chen, Z. Q. Zhu, S. Iwasaki, and R. Deodhar, "A novel hybrid excited flux-switching brushless AC Machines for EV/HEV applications," in *IEEE Vehicle Power and Propulsion Conference (VPPC)*, 2010, pp. 1-6.
[93] L. Vido, M. Gabsi, M. Lecrivain, Y. Amara, and F. Chabot, "Homopolar and bipolar hybrid excitation synchronous machines," in *IEEE International Conference on Electric Machines and Drives (ICEMD)*, 2005, pp. 1212-1218.
[94] L. Vido, Y. Amara, M. Gabsi, M. Lecrivain, and F. Chabot, "Compared performances of homopolar and bipolar hybrid excitation synchronous machines," in *Conference Record of the 2005 Industry Applications Conference, Fourtieth IAS Annual Meeting*, 2005, pp. 1555-1560 Vol. 3.
[95] C. Bekhaled, S. Hlioui, L. Vido, M. Gabsi, M. Lecrivain, and Y. Amara, "3D magnetic equivalent circuit model for homopolar hybrid excitation synchronous machines," in *International Aegean Conference on Electrical Machines and Power Electronics (ACEMP)*, 2007, pp. 575-580.
[96] Z. Zhuoran, Y. Yangguang, Y. Shanshui, and B. Zhou, "Principle of Operation and Feature Investigation of a New Topology of Hybrid Excitation Synchronous Machine," *IEEE Transactions on Magnetics*, vol. 44, pp. 2174-2180, 2008.
[97] H. Wang, Z. An, R. Tang, and Y. Niu, "Design of a hybrid excitation permanent magnet synchronous with low voltage regulation," in *Proceedings of the Eighth International Conference on Electrical Machines and Systems (ICEMS)*, 2005, pp. 480-483 Vol. 1.
[98] C. Yang, H. Lin, X. Liu, S. Fang, and J. Guo, "Analysis and Experimental Investigation for Field-Control Capability of a Novel Hybrid Excitation Claw-Pole Synchronous Machine," in *7th International Conference on Power Electronics and Drive Systems (PEDS)*, 2007, pp. 196-201.
[99] C. Yang, H. Lin, and J. Guo, "Magnetic field analysis of hybrid excitation brushless claw-pole motor with three-dimensional finite element method," in *Proceedings of the Eighth International Conference on Electrical Machines and Systems (ICEMS)* 2005, pp. 664-666 Vol. 1.
[100] N. Youyuan, B. Xiaohua, and Q. Zhe, "Magnetic leakage analysis and computation of claw-pole alternators," in *International Conference on Electrical Machines and Systems (ICEMS)*, 2009, pp. 1-4.
[101] N. Youyuan, W. Qunjing, B. Xiaohua, and Z. Weiguo, "Optimal design of a hybrid excitation claw-pole alternator based on a 3-D MEC method," in *Proceedings of the Eighth International Conference on Electrical Machines and Systems (ICEMS)*, 2005, pp. 644-647 Vol. 1.
[102] D. Fodorean, A. Djerdir, l. A. Viorel, and A. Miraoui, "A Double Excited Synchronous Machine for Direct Drive Application-Design and Prototype Tests," *IEEE Transactions on Energy Conversion*, vol. 22, pp. 656-665, 2007.
[103] T. Finken and K. Hameyer, "Study of Hybrid Excited Synchronous Alternators for Automotive Applications Using Coupled FE and Circuit Simulations," *IEEE Transactions on Magnetics*, vol. 44, pp. 1598-1601, 2008.
[104] Y. Li and T. A. Lipo, "A doubly salient permanent magnet motor capable of field weakening," in *IEEE Power Electronics Specialists Conference (PESC)*, 1995, pp. 565-571 vol.1.
[105] F. Leonardi, T. Matsuo, Y. Li, T. A. Lipo, and P. McCleer, "Design considerations and test results for a doubly salient PM motor with flux control," in *IEEE Industry Applications Conference, Thirty-First IAS Annual Meeting*, 1996, pp. 458-463 vol.1.

[106] F. Ying and K. T. Chau, "Design, modeling and analysis of a brushless doubly-fed doubly-salient machine for electric vehicles," in *Conference Record of the 2005 Industry Applications Conference, Fourtieth IAS Annual Meeting*, 2005, pp. 2712-2719 Vol. 4.
[107] Z. Zhuoran, T. Yangyang, and Y. Yangguang, "A new hybrid excitation doubly salient brushless DC generator with dual terminal output," in *International Conference on Electrical Machines (ICEM)*, 2010, pp. 1-5.
[108] F. Caricchi, F. Crescimbini, F. Giulii Capponi, and L. Solero, "Permanent-magnet, direct-drive, starter/alternator machine with weakened flux linkage for constant-power operation over extremely wide speed range," in *IEEE Industry Applications Conference, Thirty-Sixth IAS Annual Meeting*, 2001, pp. 1626-1633 vol.3.
[109] L. Del Ferraro, F. Giulii Capponi, R. Terrigi, F. Caricchi, and O. Honorati, "Ironless Axial Flux PM Machine With Active Mechanical Flux Weakening For Automotive Applications," in *IEEE Industry Applications Conference, 41st IAS Annual Meeting*, 2006, pp. 1-7.
[110] M. Aydin, H. Surong, and T. A. Lipo, "A new axial flux surface mounted permanent magnet machine capable of field control," in *Conference Record of the Industry Applications Conference, 37th IAS Annual Meeting*, 2002, pp. 1250-1257 vol.2.
[111] G. Zhou, T. Miyazaki, S. Kawamata, D. Kaneko, and N. Hino, "Development of variable magnetic flux motor suitable for electric vehicle," in *International Power Electronics Conference (IPEC)*, 2010, pp. 2171-2174.
[112] "I. Kazuyuki, "Patent: P2007-244020a.."
[113] M. Lei, M. Sanada, S. Morimoto, Y. Takeda, and N. Matsui, "High efficiency adjustable speed control of IPMSM with variable permanent magnet flux linkage," in *IEEE Industry Applications Conference, Thirty-Fourth IAS Annual Meeting.*, 1999, pp. 881-887 vol.2.
[114] M. Lei, M. Sanada, S. Morimoto, and Y. Takeda, "Advantages of IPMSM with adjustable PM armature flux linkage in efficiency improvement and operating range extension," in *Proceedings of the Power Conversion Conference (PCC-Osaka)*, 2002, pp. 136-141 vol.1.
[115] B. Kou, C. Li, and S. Cheng, "A new flux weakening method of permanent magnet synchronous machine," in *Proceedings of the Eighth International Conference on Electrical Machines and Systems (ICEMS)*, 2005, pp. 500-503 Vol. 1.
[116] R. Owen, Z. Q. Zhu, J. B. Wang, D. A. Stone, and I. Urquhart, "Mechanically adjusted variable-flux concept for switched-flux permanent-magnet machines," in *International Conference on Electrical Machines and Systems (ICEMS)*, 2011, pp. 1-6.
[117] A. Shakal, L. Yuefeng, and T. A. Lipo, "A permanent magnet AC machine structure with true field weakening capability," in *IEEE International Symposium on Industrial Electronics (ISIE)*, 1993, pp. 19-24.
[118] "Y. Shibukawa, "Patent: P2006-037075a."."
[119] V. Ostovic, "Memory motors," *IEEE Industry Applications Magazine*, vol. 9, pp. 52-61, 2003.
[120] V. Ostovic, "Pole-changing permanent magnet machines," in *IEEE Industry Applications Conference, Thirty-Sixth IAS Annual Meeting*, 2001, pp. 2570-2576 vol.4.
[121] T. Niizuma and K. Sakai, "Electronic motors capable of pole-changing and variable machine constants," in *15th International Conference on Electrical Machines and Systems (ICEMS)*, 2012, pp. 1-4.
[122] V. Ostovic, "Memory motors-a new class of controllable flux PM machines for a true wide speed operation," in *IEEE Industry Applications Conference, Thirty-Sixth IAS Annual Meeting*, 2001, pp. 2577-2584 vol.4.
[123] Y. Chen, W. Pan, Y. Wang, R. Tang, and J. Wang, "Interior composite-rotor controllable-flux PMSM - memory motor," in *Proceedings of the Eighth International Conference on Electrical Machines and Systems (ICEMS)*, 2005, pp. 446-449 Vol. 1.
[124] C. Yiguang, K. Lingbing, and Z. Weigang, "Finite element analysis of interior composite-rotor controllable flux permanent magnet synchronous machine," in *International Conference on Electrical Machines and Systems (ICEMS)*, 2009, pp. 1-4.
[125] Y. Chuang, K. T. Chau, and J. Z. Jiang, "A permanent-magnet flux-mnemonic integrated-starter-generator for hybrid electric vehicles," in *IEEE Vehicle Power and Propulsion Conference (VPPC)*, 2008, pp. 1-6.

[126] L. Chunhua, K. T. Chau, J. Z. Jiang, L. Xinhua, and W. Zheng, "Design and Control of a Doubly-Excited Permanent-Magnet Brushless Integrated-Starter-Generator for Hybrid Electric Vehicles," in *IEEE Industry Applications Conference, 42nd IAS Annual Meeting*, 2007, pp. 1702-1709.
[127] Y. Chuang and G. Yu, "Multi-mode operations of DC-excited memory motors under flux regulation," in *International Conference on Power Electronics and Drive Systems (PEDS)*, 2009, pp. 1354-1359.
[128] M. M. Swamy, T. Kume, A. Maemura, and S. Morimoto, "Extended high-speed operation via electronic winding-change method for AC motors," *IEEE Transactions on Industry Applications*, vol. 42, pp. 742-752, 2006.
[129] M. V. Cistelecan, M. Popescu, L. Melcescu, and T. Tudorache, "Three phase line start claw poles permanent magnet motor with pole changing winding," in *International Symposium on Power Electronics, Electrical Drives, Automation and Motion (SPEEDAM)*, 2008, pp. 245-249.
[130] A. S. Abdel-Khalik, M. I. Masoud, B. W. Williams, A. L. Mohamadein, and M. M. Ahmed, "Steady-State Performance and Stability Analysis of Mixed Pole Machines With Electromechanical Torque and Rotor Electric Power to a Shaft-Mounted Electrical Load," *IEEE Transactions on Industrial Electronics*, vol. 57, pp. 22-34, 2010.
[131] A. Abdel-Khalik, M. I. Masoud, A. L. Mohamadein, B. W. Williams, and M. Magdy, "Control of rotor torque and rotor electric power of a shaft-mounted electrical load in a mixed pole machine," *IET Electric Power Applications*, vol. 3, pp. 265-278, 2009.
[132] J. T. Chen and Z. Q. Zhu, "Influence of rotor pole number on optimal parameters in flux-switching PM brushless AC machines by lumped parameter magnetic circuit model," in *Electric Machines and Drives Conference, 2009. IEMDC '09. IEEE International*, 2009, pp. 1216-1223.
[133] C. Pollock, H. Pollock, R. Barron, J. R. Coles, D. Moule, A. Court, and R. Sutton, "Flux-Switching Motors for Automotive Applications," *IEEE Transactions on Industry Applications*, vol. 42, pp. 1177-1184, 2006.
[134] J. T. Chen, Z. Q. Zhu, S. Iwasaki, and R. P. Deodhar, "Influence of Slot Opening on Optimal Stator and Rotor Pole Combination and Electromagnetic Performance of Switched-Flux PM Brushless AC Machines," *Industry Applications, IEEE Transactions on*, vol. 47, pp. 1681-1691, 2011.
[135] G. Qi, J. T. Chen, Z. Q. Zhu, D. Howe, L. B. Zhou, and C. L. Gu, "Influence of Skew and Cross-Coupling on Flux-Weakening Performance of Permanent-Magnet Brushless AC Machines," *IEEE Transactions on Magnetics*, vol. 45, pp. 2110-2117, 2009.
[136] L. Hesong, Z. Q. Zhu, E. Mohamed, F. Yongling, and Q. Xiaoye, "Flux-Weakening Control of Nonsalient Pole PMSM Having Large Winding Inductance, Accounting for Resistive Voltage Drop and Inverter Nonlinearities," *IEEE Transactions on Power Electronics*, vol. 27, pp. 942-952, 2012.
[137] O. de la Barriere, S. Hlioui, H. Ben Ahmed, M. Gabsi, and M. LoBue, "Three-Dimensional Analytical Modeling of a Permanent-Magnet Linear Actuator With Circular Magnets," *IEEE Transactions on Magnetics*, vol. 46, pp. 3608-3616, 2010.
[138] J. Azzouzi, G. Barakat, and B. Dakyo, "Quasi-3-D analytical modeling of the magnetic field of an axial flux permanent-magnet synchronous machine," *IEEE Transactions on Energy Conversion*, vol. 20, pp. 746-752, 2005.
[139] C. Yu, Z. Q. Zhu, and D. Howe, "Three-Dimensional Lumped-Parameter Magnetic Circuit Analysis of Single-Phase Flux-Switching Permanent-Magnet Motor," *IEEE Transactions on Industry Applications*, vol. 44, pp. 1701-1710, 2008.
[140] M. Platen and G. Henneberger, "Examination of leakage and end effects in a linear synchronous motor for vertical transportation by means of finite element computation," *IEEE Transactions on Magnetics*, vol. 37, pp. 3640-3643, 2001.
[141] Z. Chao-hui, L. Shui-liang, and Y. Yang-guang, "Influence factor analysis of PMSM air gap flux density," in *Proceedings of the Eighth International Conference on Electrical Machines and Systems (ICEMS)*, 2005, pp. 334-339 Vol. 1.

[142] M. Sanada, S. Morimoto, and Y. Takeda, "Interior permanent magnet linear synchronous motor for high-performance drives," *IEEE Transactions on Industry Applications*, vol. 33, pp. 966-972, 1997.
[143] H. Polinder, J. G. Slootweg, M. J. Hoeijmakers, and J. C. Compter, "Modeling of a linear PM Machine including magnetic saturation and end effects: maximum force-to-current ratio," *IEEE Transactions on Industry Applications*, vol. 39, pp. 1681-1688, 2003.
[144] Z. Xiaoyong, C. Ming, H. Wei, and Z. Jianzhong, "Investigation of End-Effect and Experimental Validation for Hybrid Excited Doubly Salient Machine," in *12th Biennial IEEE Conference on Electromagnetic Field Computation*, 2006, pp. 320-320.
[145] Z. Q. Zhu, J. T. Chen, Y. Pang, D. Howe, S. Iwasaki, and R. Deodhar, "Modeling of end-effect in flux-switching permanent magnet machines," in *International Conference on Electrical Machines and Systems (ICEMS)* 2007, pp. 943-948.
[146] Y. P. Z. Q. Zhu, W. Hua, M. Cheng, and D. Howe "Investigation of end effect in permanent magnet brushless machines having magnets on the stator " *J. Appl. Phys.*, vol. 99, pp. 319-321, 2007.
[147] B. Gaussens, E. Hoang, M. Lecrivain, P. Manfe, and M. Gabsi, "A new hybrid-excited flux-switching machine with excitation coils in stator slots," in *15th International Conference on Electrical Machines and Systems (ICEMS)*, 2012, pp. 1-6.
[148] Y. Amara, L. Vido, M. Gabsi, E. Hoang, A. Hamid Ben Ahmed, and M. Lecrivain, "Hybrid Excitation Synchronous Machines: Energy-Efficient Solution for Vehicles Propulsion," *IEEE Transactions on Vehicular Technology, ,* vol. 58, pp. 2137-2149, 2009.
[149] F. Giulii Capponi, G. De Donato, and F. Caricchi, "Recent Advances in Axial-Flux Permanent-Magnet Machine Technology," *IEEE Transactions on Industry Applications*, vol. 48, pp. 2190-2205, 2012.
[150] F. G. Capponi, R. Terrigi, F. Caricchi, and L. Del Ferraro, "Active Output Voltage Regulation for an Ironless Axial-Flux PM Automotive Alternator With Electromechanical Flux Weakening," *IEEE Transactions on Industry Applications*, vol. 45, pp. 1785-1793, 2009.
[151] B. Kou, C. Li, and S. Cheng, "Flux-Weakening-Characteristic Analysis of a New Permanent-Magnet Synchronous Motor Used for Electric Vehicles," *IEEE Transactions on Plasma Science*, vol. 39, pp. 511-515, 2011.
[152] C. C. Chan, K. T. Chau, J. Z. Jiang, W. Xia, M. Zhu, and R. Zhang, "Novel permanent magnet motor drives for electric vehicles," *IEEE Transactions on Industrial Electronics*, vol. 43, pp. 331-339, 1996.
[153] J. A. Tapia, F. Leonardi, and T. A. Lipo, "Consequent-pole permanent-magnet machine with extended field-weakening capability," *IEEE Transactions on Industry Applications*, vol. 39, pp. 1704-1709, 2003.
[154] L. Xiaogang and T. A. Lipo, "A synchronous/permanent magnet hybrid AC machine," *IEEE Transactions on Energy Conversion*, vol. 15, pp. 203-210, 2000.
[155] T. Kosaka, Y. Kano, N. Matsui, and C. Pollock, "A novel multi-pole permanent magnet synchronous machine with SMC bypass core for magnet flux and SMC field-pole core with toroidal coil for independent field strengthening/weakening," in *European Conference on Power Electronics and Applications*, 2005, pp. 10 pp.-P.10.
[156] L. Hengchuan, L. Heyun, Z. Q. Zhu, H. Mingming, and J. Ping, "Permanent Magnet Remagnetizing Physics of a Variable Flux Memory Motor," *IEEE Transactions on Magnetics*, vol. 46, pp. 1679-1682, 2010.
[157] Y. Chuang and K. T. Chau, "Design, Analysis, and Control of DC-Excited Memory Motors," *IEEE Transactions on Energy Conversion*, vol. 26, pp. 479-489, 2011.
[158] W. Z. Fei and J. X. Shen, "Comparative Study and Optimal Design of PM Switching Flux Motors," in *Proceedings of the 41st International Universities Power Engineering Conference (UPEC)*, 2006, pp. 695-699.
[159] L. Kaiyuan, P. O. Rasmussen, S. J. Watkins, and F. Blaabjerg, "A New Low-Cost Hybrid Switched Reluctance Motor for Adjustable-Speed Pump Applications," *IEEE Transactions on Industry Applications*, vol. 47, pp. 314-321, 2011.
[160] C. Ruiwu, C. Ming, C. Mi, H. Wei, W. Xin, and Z. Wenxiang, "Modeling of a Complementary and Modular Linear Flux-Switching Permanent Magnet Motor for Urban

Rail Transit Applications," *IEEE Transactions on Energy Conversion,* vol. 27, pp. 489-497, 2012.
[161] F. Weizhong, P. C. K. Luk, S. Jian Xin, W. Yu, and J. Mengjia, "A Novel Permanent-Magnet Flux Switching Machine With an Outer-Rotor Configuration for In-Wheel Light Traction Applications," *IEEE Transactions on Industry Applications,* vol. 48, pp. 1496-1506, 2012.
[162] Z. Azar, Z. Q. Zhu, and G. Ombach, "Influence of Electric Loading and Magnetic Saturation on Cogging Torque, Back-EMF and Torque Ripple of PM Machines," *IEEE Transactions on Magnetics*,, vol. 48, pp. 2650-2658, 2012.
[163] W. Daohan, W. Xiuhe, and J. Sang-Yong, "Reduction on Cogging Torque in Flux-Switching Permanent Magnet Machine by Teeth Notching Schemes," *IEEE Transactions on Magnetics,* vol. 48, pp. 4228-4231, 2012.
[164] N. Bianchi and S. Bolognani, "Design techniques for reducing the cogging torque in surface-mounted PM motors," *IEEE Transactions on Industry Applications,* vol. 38, pp. 1259-1265, 2002.
[165] H. Wei, C. Ming, Z. Q. Zhu, and D. Howe, "Analysis and Optimization of Back EMF Waveform of a Flux-Switching Permanent Magnet Motor," *IEEE Transactions on Energy Conversion,* vol. 23, pp. 727-733, 2008.

Appendices

A.1. Appendix 1: Windings Configuration of SFPM Machines

This section presents the coils connection of the six machines, i.e. the three combinations 12/10, 12/13 and 12/14, and the three novel topologies multi-tooth, E-core and C-core.

A.1.1. 12/10 machine

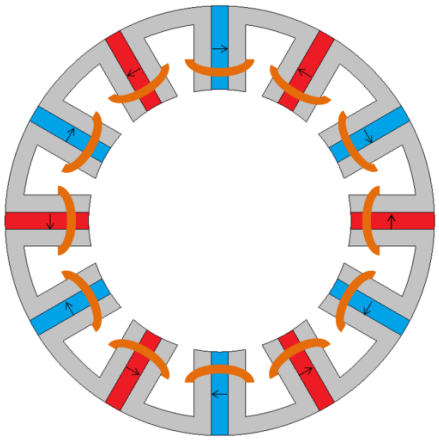

(a) Schematic of 12-stator poles and coils

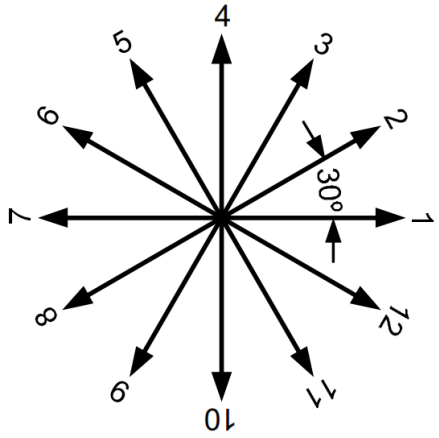

(b) Stator coils (mechanical degree)

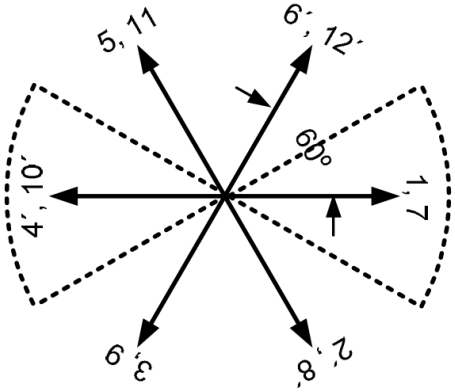

(c) EMF vectors (electrical degree) and phase sectors (dashed lines)

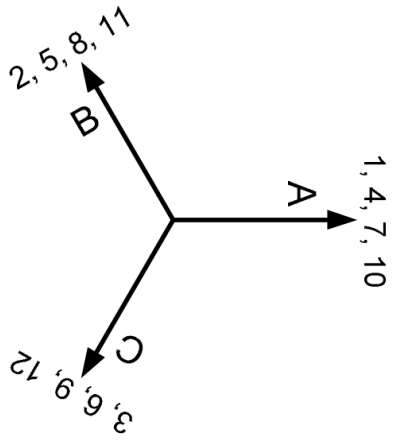

(d) Phase Coils

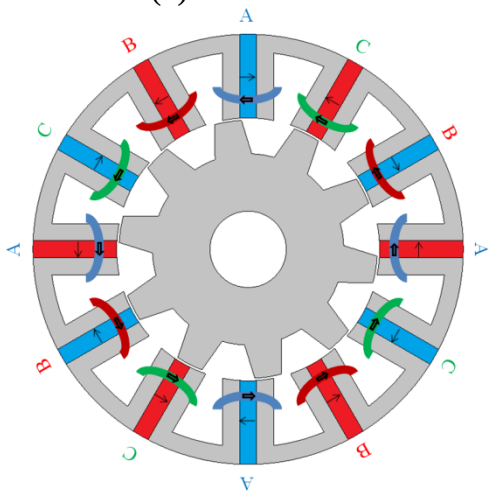

(e) Phases connections

Fig. A.1 12/10 stator/rotor pole combination SFPM machine.

A.1.2. 12/13 machine

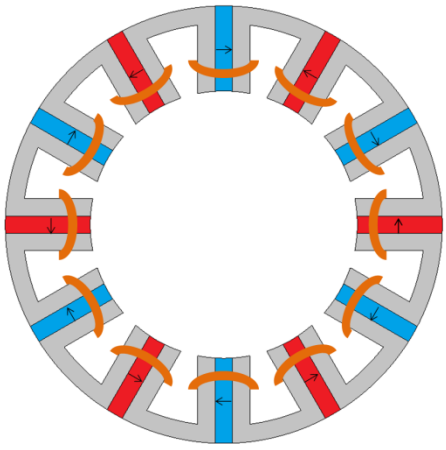

(a) Schematic of 12-stator poles and coils

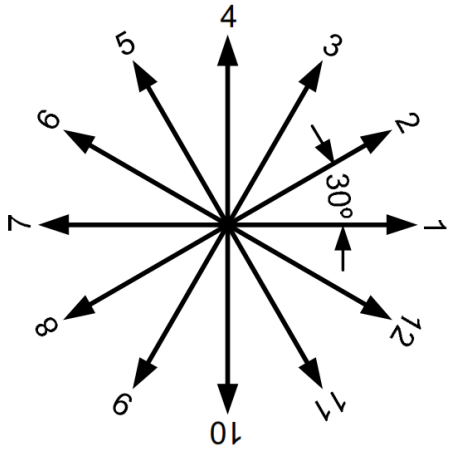

(b) Stator coils (mechanical degree)

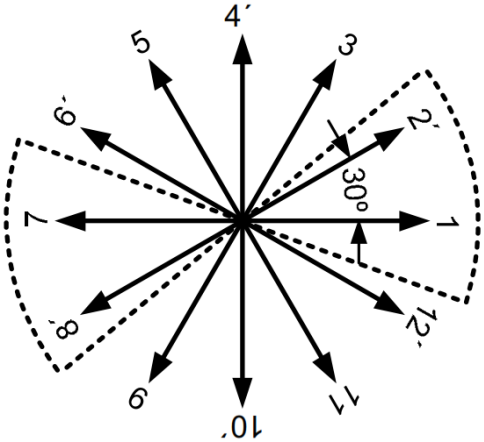

(c) EMF vectors (electrical degree) and phase sectors (dashed lines)

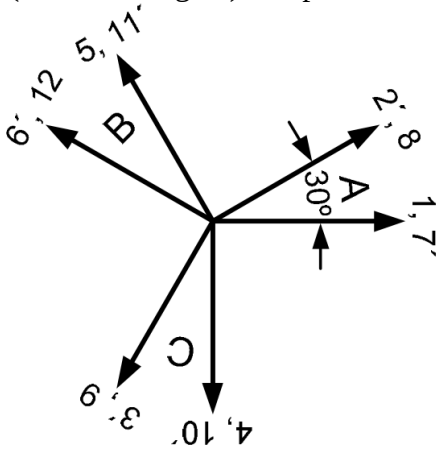

(d) Phase Coils

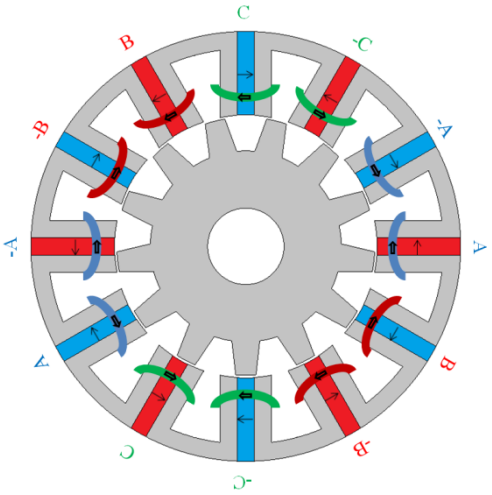

(e) Phases connections

Fig. A.2 12/13 stator/rotor pole combination SFPM machine.

A.1.3. 12/14 machine

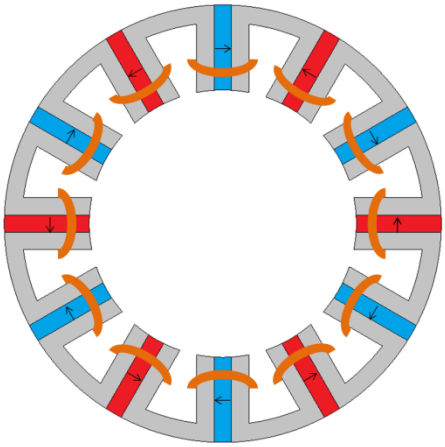

(a) Schematic of 12-stator poles and coils

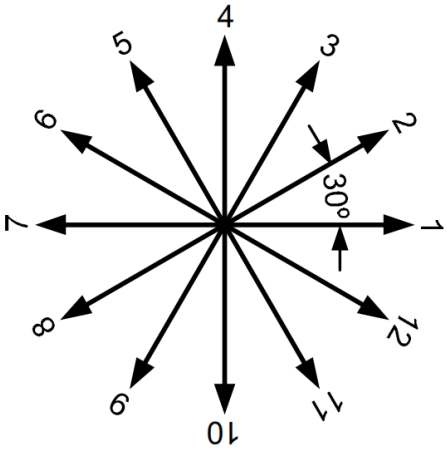

(b) Stator coils (mechanical degree)

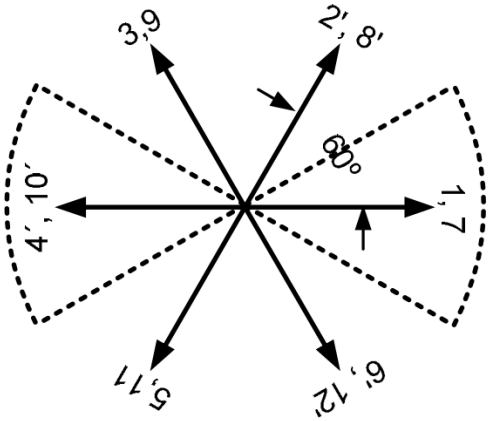

(c) EMF vectors (electrical degree) and phase sectors (dashed lines)

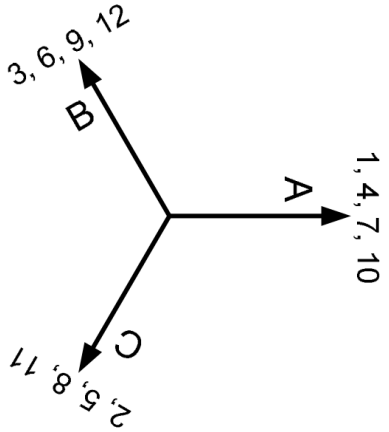

(d) Phase Coils

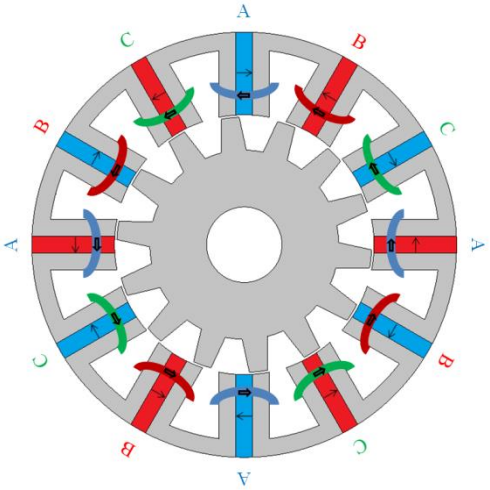

(e) Phases connections

Fig. A.3 12/14 stator/rotor pole combination SFPM machine.

A.1.4. Multi-tooth machine

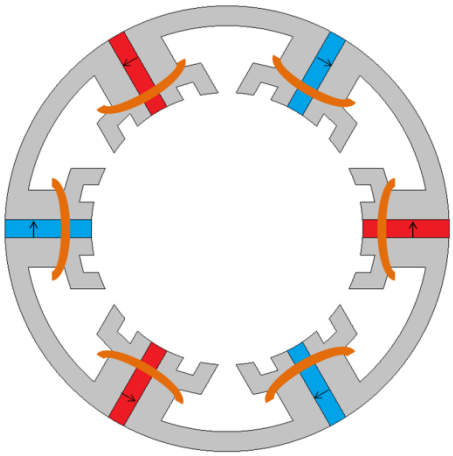

(a) Schematic of 12-stator poles and coils

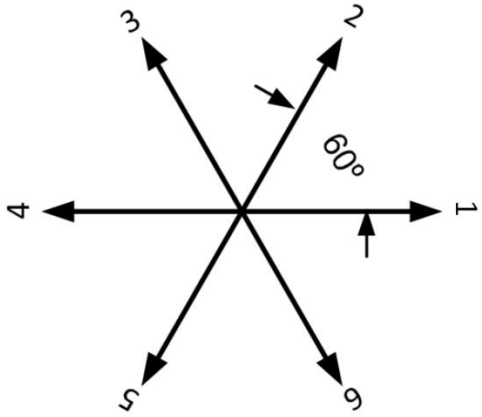

(b) Stator coils (mechanical degree)

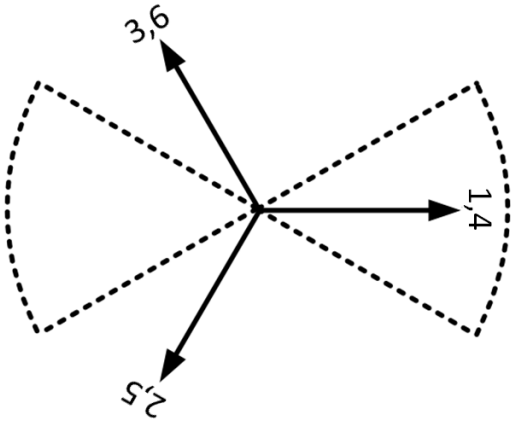

(c) EMF vectors (electrical degree) and phase sectors (dashed lines)

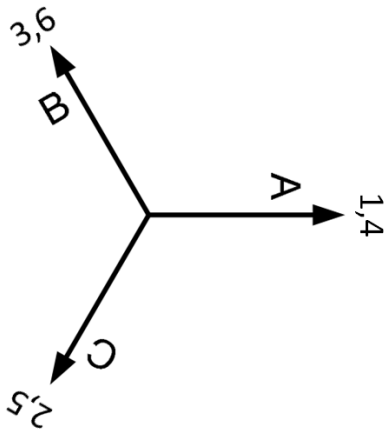

(d) Phase Coils

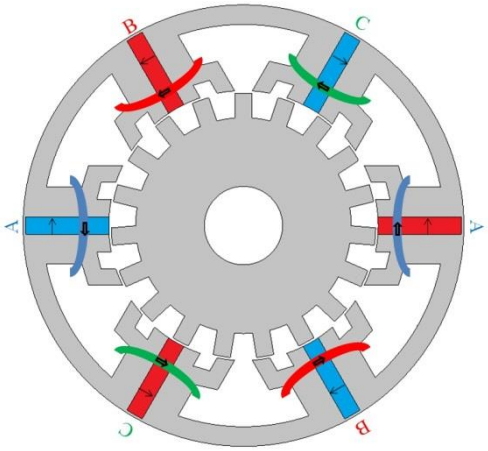

(e) Phases connections

Fig. A.4 Multi-tooth SFPM machine.

A.1.5. E-core machine

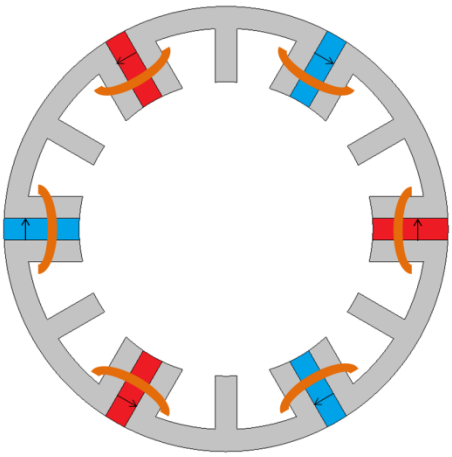

(a) Schematic of 12-stator poles and coils

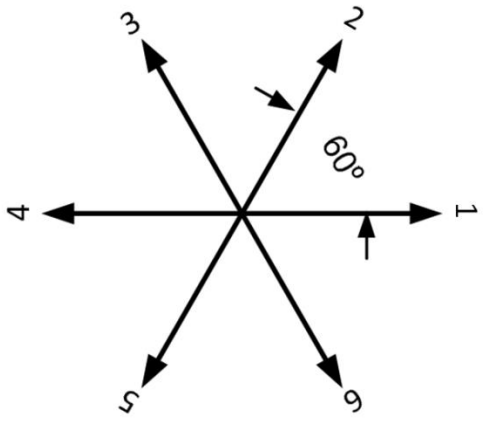

(b) Stator coils (mechanical degree)

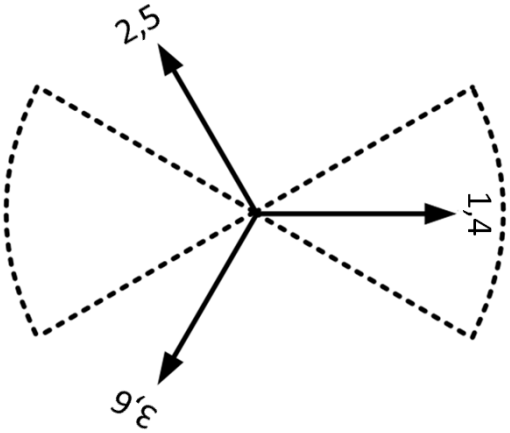

(c) EMF vectors (electrical degree) and phase sectors (dashed lines)

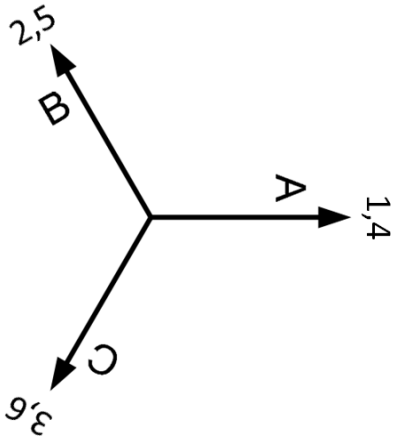

(d) Phase Coils

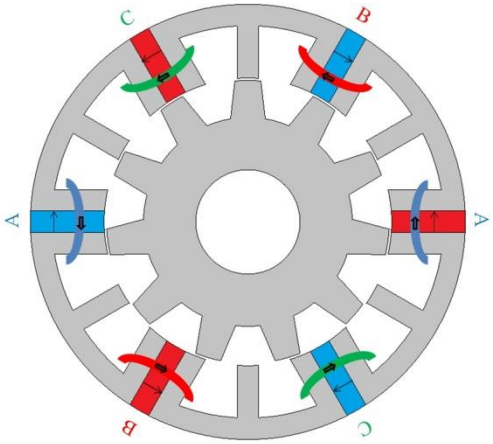

(e) Phases connections

Fig. A.5 E-core SFPM machine.

A.1.6. C-core machine

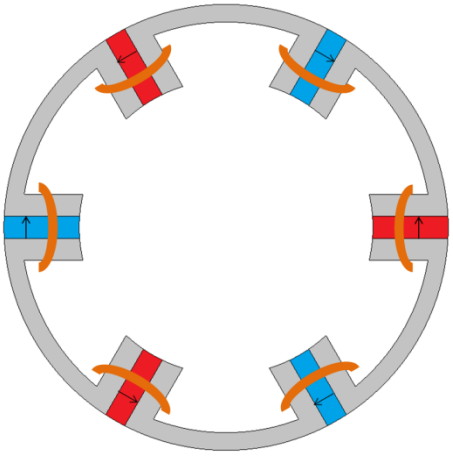

(a) Schematic of 12-stator poles and coils

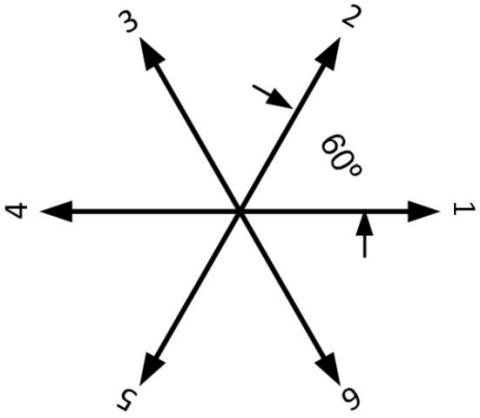

(b) Stator coils (mechanical degree)

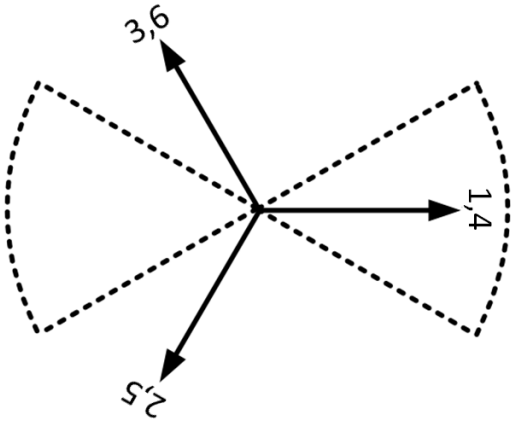

(c) EMF vectors (electrical degree) and phase sectors (dashed lines)

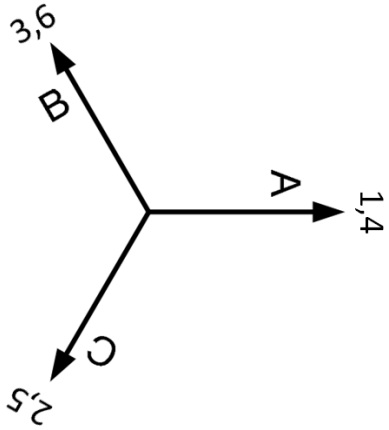

(d) Phase Coils

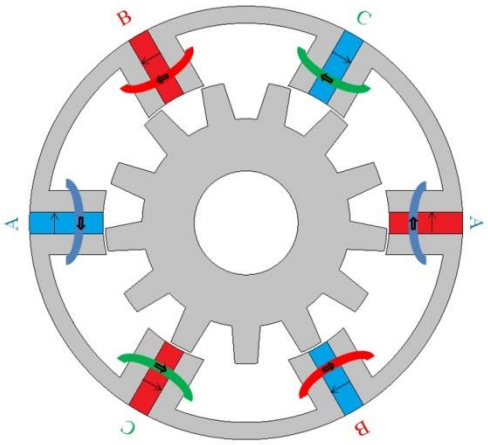

(e) Phases connections

Fig. A.6 C-core SFPM machine.

A.2. Appendix 2: Inductance Calculation Methods

In order to increase the accuracy of the torque-speed curve prediction, the influence of the magnetic saturation and cross-coupling effect on the d- and q-axis inductance is fully accounted. Therefore the d- and q-axis inductance can be found using these equations:

$$L_d = \frac{\Psi_d(I_d,I_q)-\Psi_{PM}(I_q)}{I_d} \quad \text{(A-1)}$$

$$L_q = \frac{\Psi_q(I_d,I_q)}{I_q} \quad \text{(A-2)}$$

where $\Psi_d(I_d,I_q)$, $\Psi_q(I_d,I_q)$ and $\Psi_{PM}(I_q)$ stand for the d-axis flux-linkage under the influence of d- and q-axis current, q-axis flux-linkage under the influence of d- and q-axis current and the PM flux-linkage under the influence of the q-axis current. This method is used in the calculation of the torque-speed curves presented in chapters 2, 4, 5, 6 and 7.

However, since the 3D-FEA requires long period to provide accurate results, the inductances are predicted using partial-coupling method, where the d- and q-axis inductance can be found by:

$$L_d = \frac{\Psi_d(I_d)-\Psi_{PM}(I_q)}{I_d} \quad \text{(A-3)}$$

$$L_q = \frac{\Psi_q(I_q)}{I_q} \quad \text{(A-4)}$$

In which $\Psi_d(I_d)$, $\Psi_q(I_q)$ and $\Psi_{PM}(I_q)$ stand for the d-axis flux-linkage under the influence of d-axis current, q-axis flux-linkage under the influence of q-axis current and the PM flux-linkage under the influence of the q-axis current. This method is used in the end-effect influence study in Chapter 3 as well as in the 3D-FEA torque-speed curves presented in the experimental validation of chapters 4 and 5.

A.3. Appendix 3: Coil Back-EMF Waveforms

This section presents the back-EMF of each coil in phase A of the six analysed machines in their conventional state, i.e. without FAs, and with the small size FAs placed in all stator poles, i.e. the FAs presented in Chapter 4. Moreover, the coil back-EMFs of the 12/10, 12/13 and 12/14 machines with large size FAs located on alternative and all stator poles, i.e. the FAs presented in Chapter 5 are also shown in this section.

A.3.1. 12/10 machine

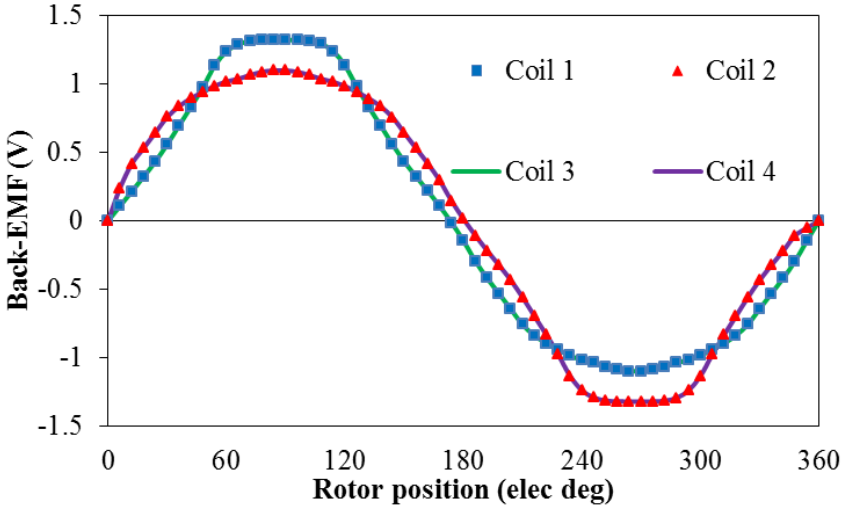

(a) 12/10 machine without FAs

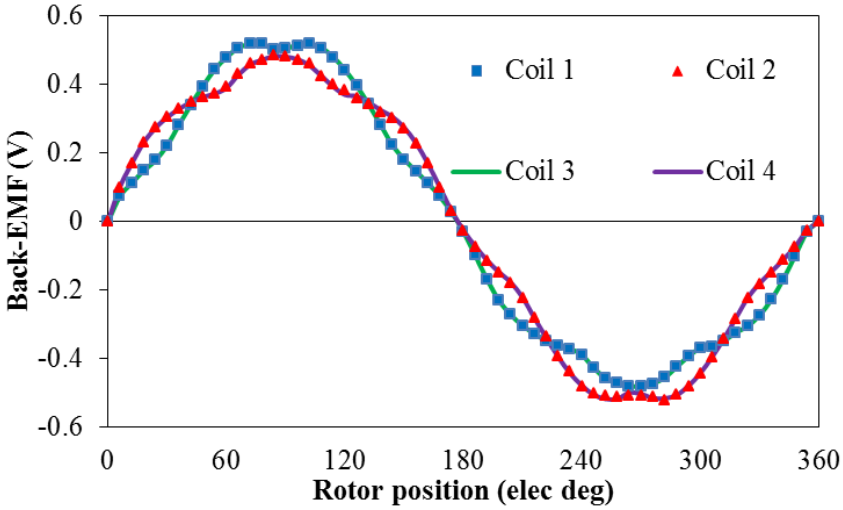

(b) 12/10 machine with FAs at all stator poles (small FA)

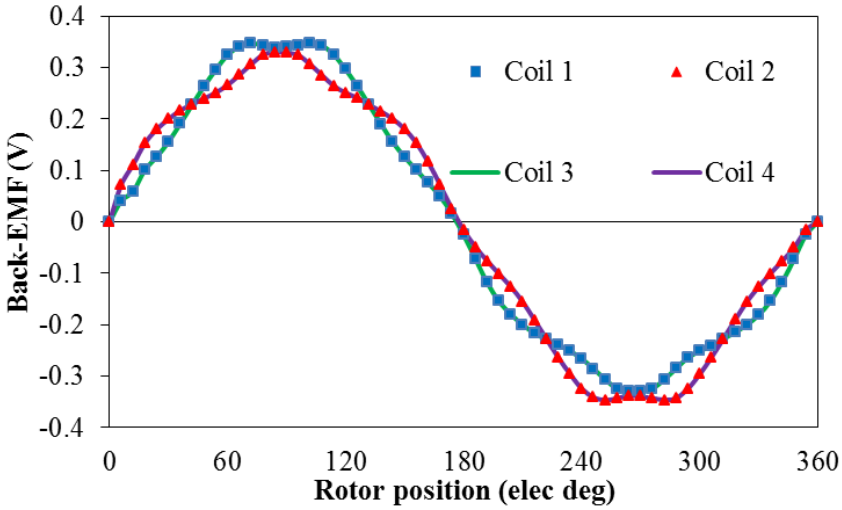

(c) 12/10 machine with FAs at all stator poles (large FA)

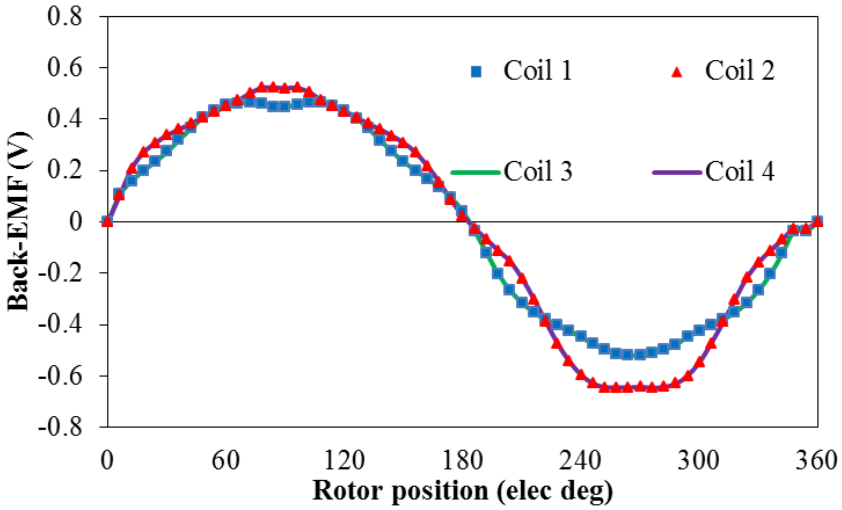

(d) 12/10 machine with FAs at alternative stator poles (large FA)

Fig. A.7 Back-EMF of 12/10 machine.

A.3.2. 12/13 machine

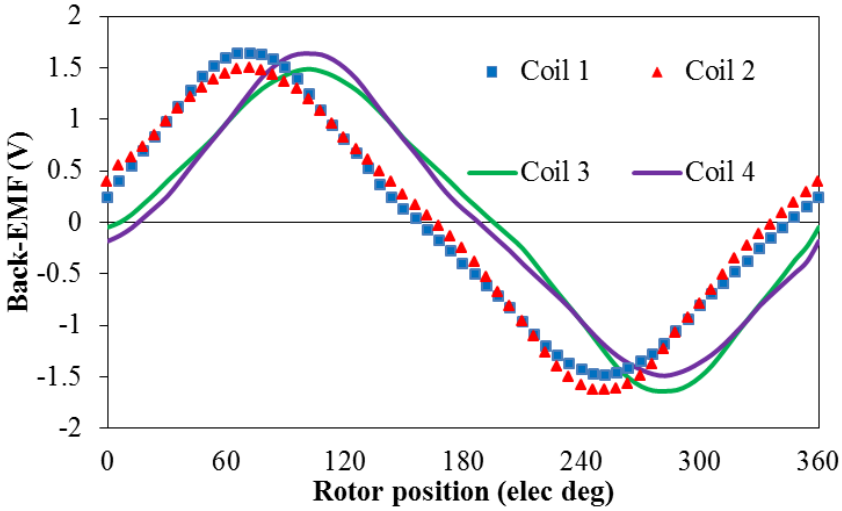

(a) 12/13 machine without FAs

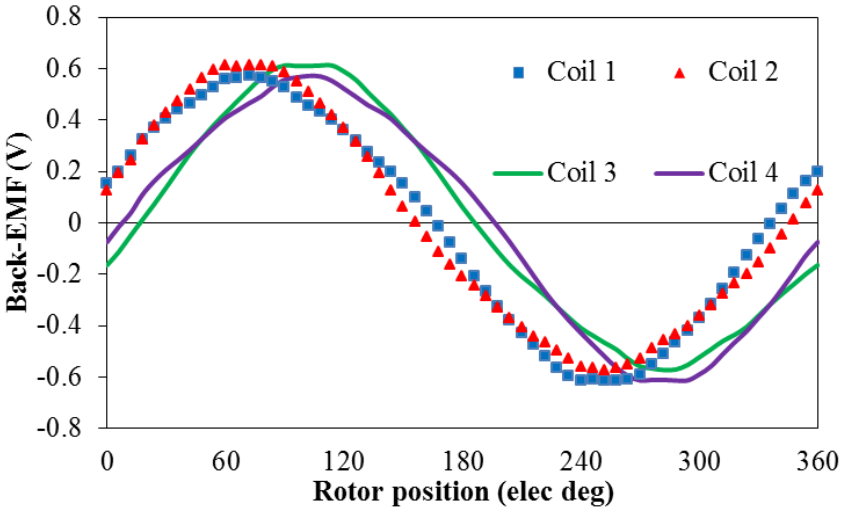

(b) 12/13 machine with FAs at all stator poles (small FA)

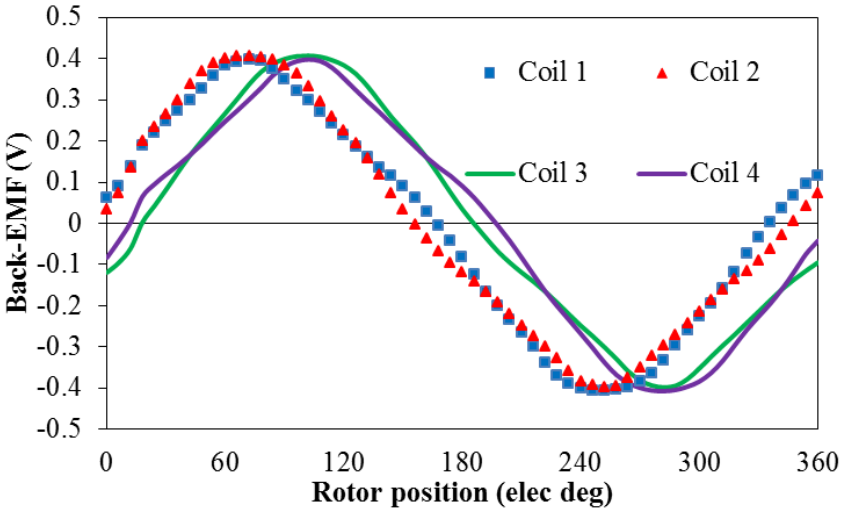

(c) 12/13 machine with FAs at all stator poles (large FA)

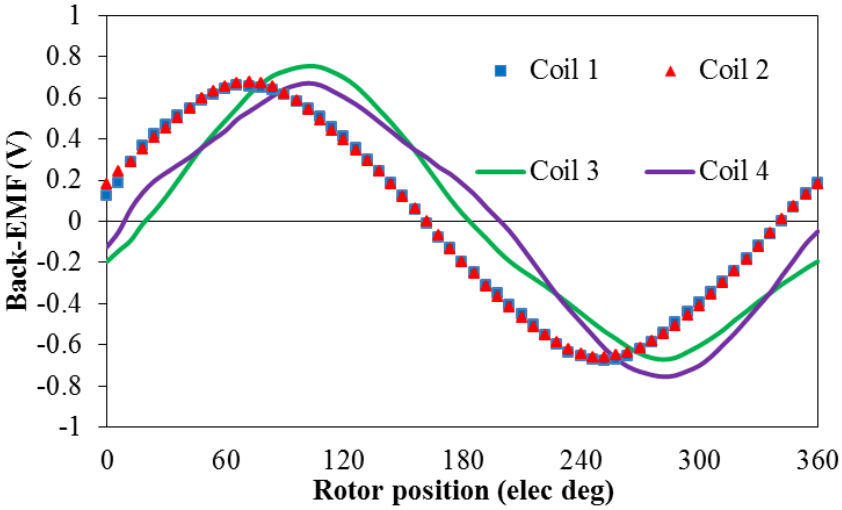

(d) 12/13 machine with FAs at alternative stator poles (large FA)

Fig. A.8 Back-EMF of 12/13 machine.

A.3.3. 12/14 machine

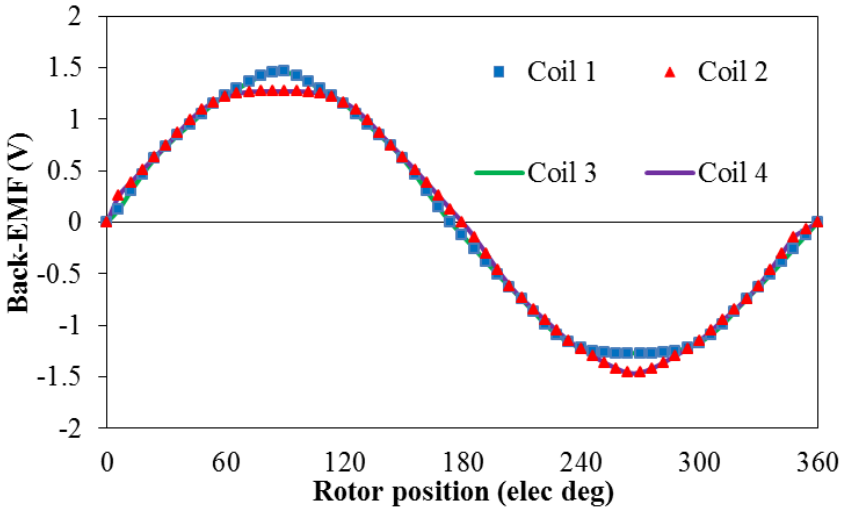

(a) 12/14 machine without FAs

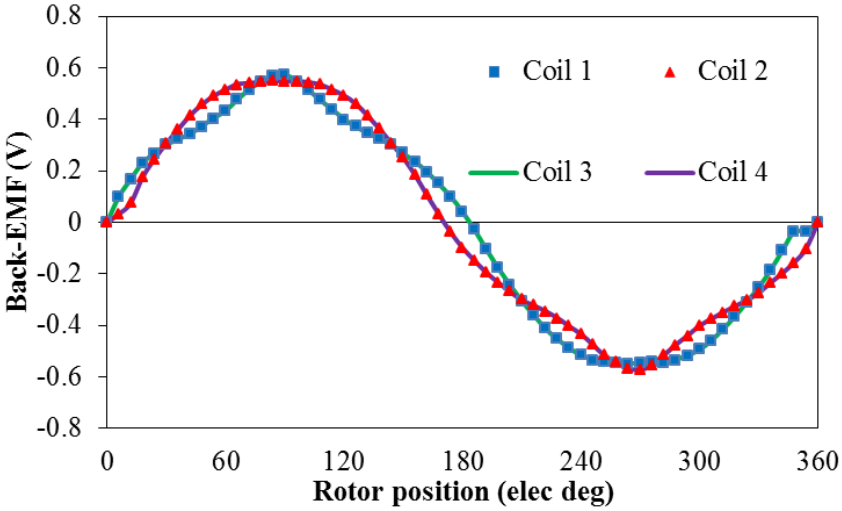

(b) 12/14 machine with FAs at all stator poles (small FA)

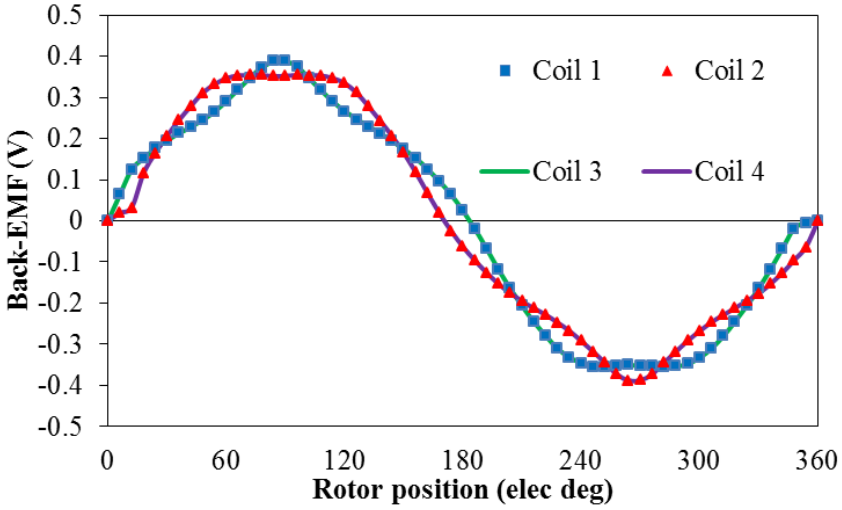

(c) 12/14 machine with FAs at all stator poles (large FA)

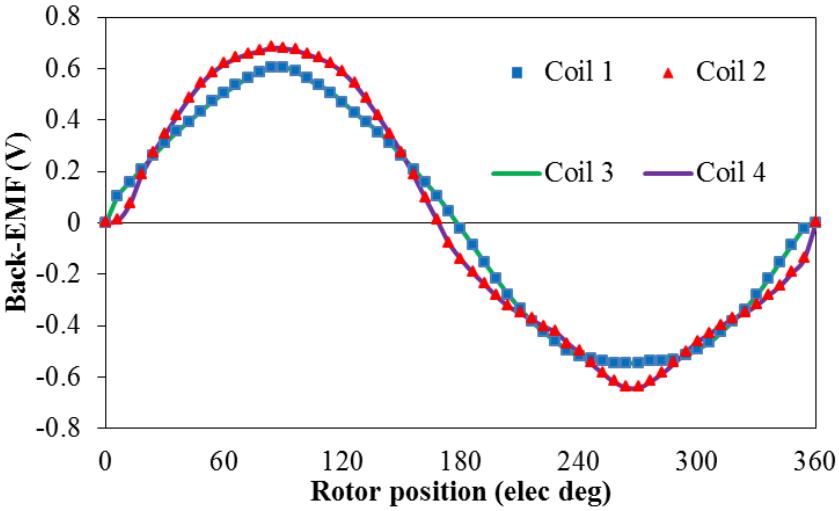

(d) 12/14 machine with FAs at alternative stator poles (large FA)

Fig. A. 9 Back-EMF of 12/14 machine.

A.3.4. Multi-tooth machine

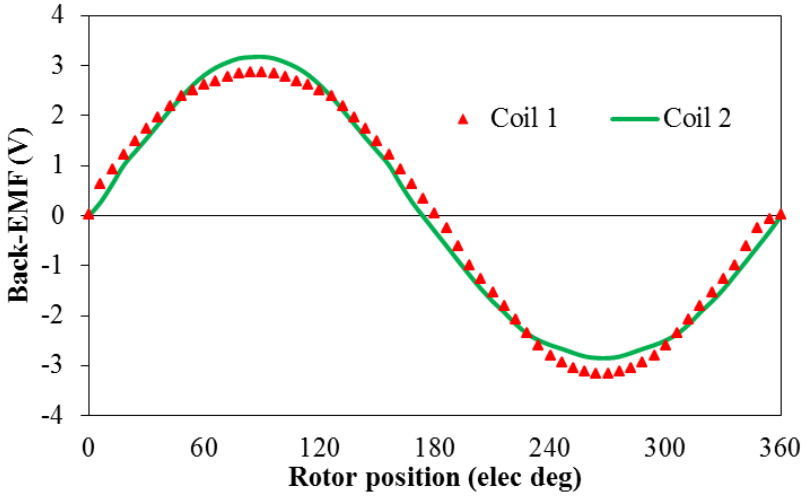

(a) 12/14 machine without FAs

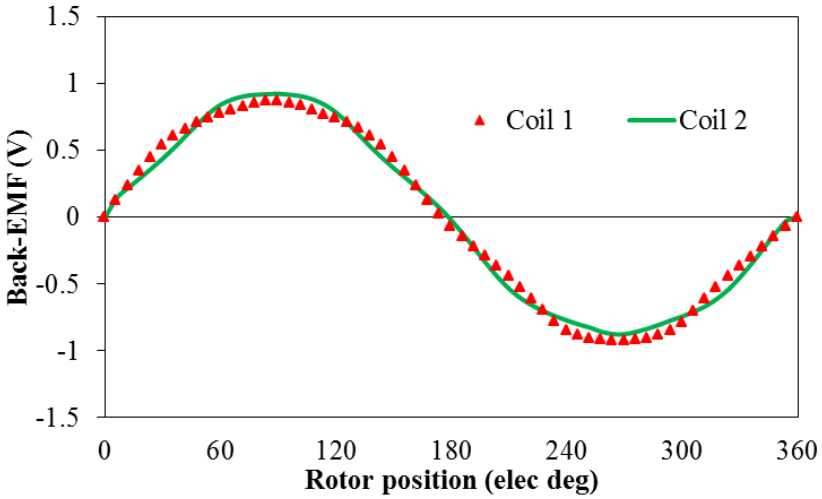

(b) 12/14 machine with FAs at all stator poles

Fig. A. 10 Back-EMF of multi-tooth machine.

A.3.5. E-core machine

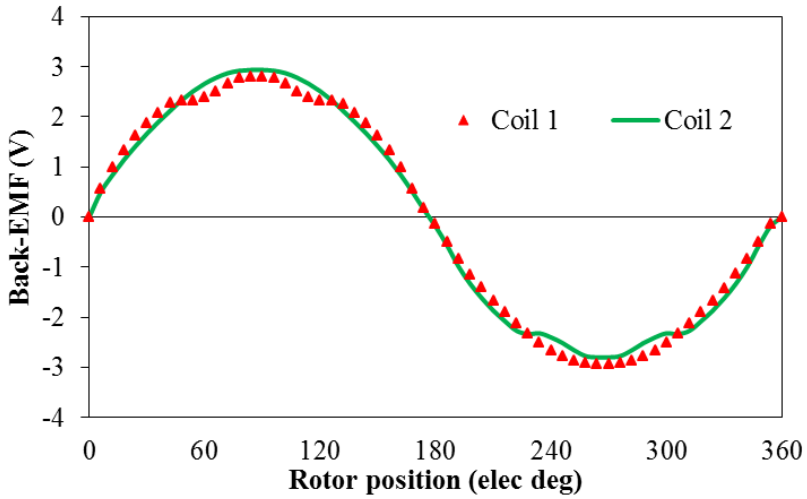

(c) 12/14 machine without FAs

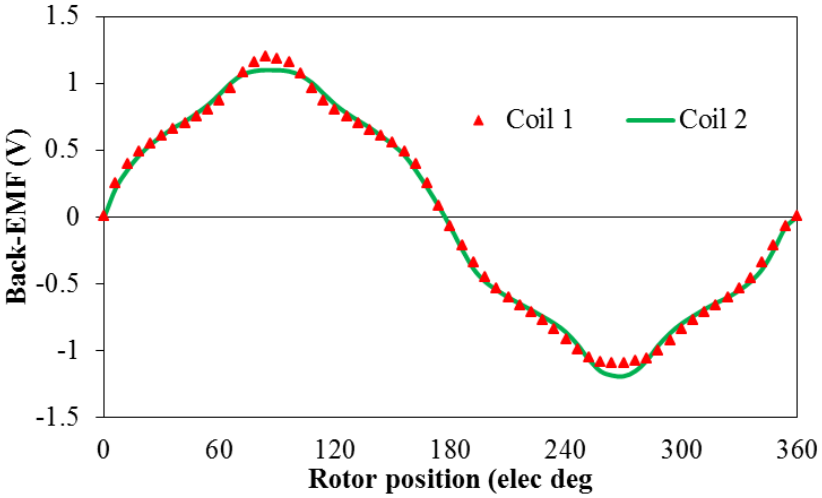

(d) 12/14 machine with FAs at all stator poles

Fig. A. 11 Back-EMF of E-core machine.

A.3.6. C-core machine

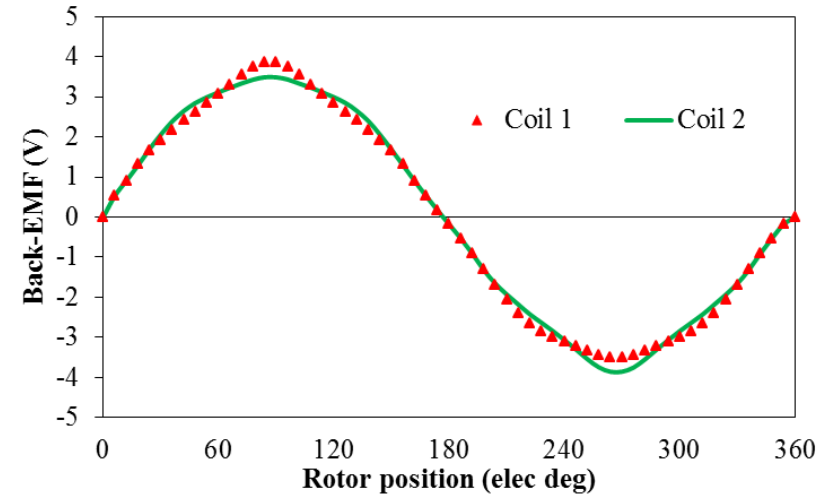

(e) 12/14 machine without FAs

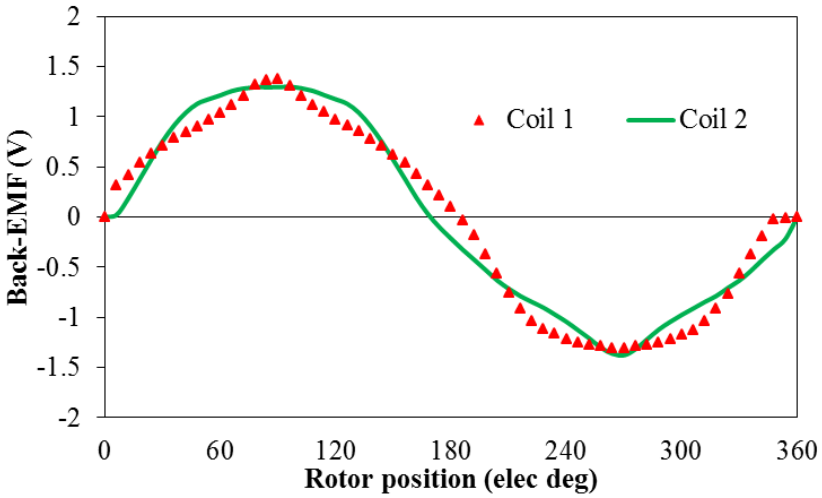

(f) 12/14 machine with FAs at all stator poles

Fig. A.12 Back-EMF of C-core machine.

A.4. Appendix 6: Publications Resulting from Study

[1] M. M. J. Al-Ani, and Z. Q. Zhu, ‘‘Influence of End-Effect on Torque-Speed Characteristics of Various Switched Flux Permanent Magnet Machines,’’ (International Conference on Electrical Machines and Systems, 22-25 October, 2014, Hangzhou, China, ICEMS2014)

[2] M. M. J. Al-Ani, and Z. Q. Zhu, ‘‘Novel SFPM Machine Topology with Radial and Circumferential Permeant Magnets,’’ (International Conference on Electrical Machines and Systems, 22-25 October, 2014, Hangzhou, China, ICEMS2014)

[3] M. M. J. Al-Ani, and Z. Q. Zhu, ‘‘Comparison of Different SFPM Machine Topologies with Variable Flux Techniques,’’ (to be submitted)

[4] Z. Q. Zhu, M. M. J. Al-Ani, B. Lee, X. Liu, and Z. Azar, ‘‘Comparative Study of Electromagnetic Performance of Switched Flux Permanent Magnet Machines,’’ (IET Electric Power Applications, accepted)

[5] Z. Q. Zhu, M. M. J. Al-Ani, B. Lee, X. Liu, and Z. Azar, ‘‘Comparison of Electromagnetic Performance of Switched Flux Permanent Magnet Machines with Mechanical Flux Adjusters,’’ (Submitted to IET Electrical Systems in Transportation)

[6] Z. Q. Zhu, M. M. J. Al-Ani, B. Lee, X. Liu, and Z. Azar, ‘‘A Novel Mechanical Flux Weakening Method for Switched Flux Permanent Magnet Machines,’’ (IEEE Transactions on Energy Conversion, accepted)

[7] Z. Q. Zhu, M. M. J. Al-Ani, X. Liu, M. Hasegawa, A. Pride and R. Deodhar, ‘‘Comparison of Alternate Mechanically Adjusted Variable Flux Switched Flux Permanent Magnet Machines,’’ *Energy Conversion Congress and Exposition (ECCE) 2012 IEEE, pp.3655-3662, 15-20 Sept.* 2012.

[8] Z. Q. Zhu, M. M. J. Al-Ani, X. Liu, M. Hasegawa, A. Pride and R. Deodhar, ‘‘Comparison of Flux Weakening Capability in Alternative Switched Flux Permanent Magnet Machines by Mechanical Adjusters,’’ *International Conference on Electrical Machine (ICEM), pp.2889-2895, 2-5 Sept.* 2012.

[9] Z. Q. Zhu, M. M. J. Al-Ani, X. Liu, M. Hasegawa, A. Pride and R. Deodhar, ‘‘Comparative Study of Torque-Speed Characteristics of Alternate Switched-Flux Permanent Magnet Machine Topologies,’’ *6th International Conference on Power Electronics, Machines and Drives (PEMD 2012), pp.16,* 27-29 March 2012.